Bioelectrochemistry by Fluorescent Cyclic Voltammetry

Giulia Mizzon

A thesis submitted for the degree of

Doctor of Philosophy

Hilary 2012

Christ Church
Inorganic Chemistry Laboratory
University of Oxford

Bioelectrochemistry by
Fluorescent Cyclic Voltammetry

Giulia Mizzon
Christ Church
Inorganic Chemistry Laboratory

A thesis submitted for the degree of Doctor of Philosophy in the University of Oxford
Hilary Term 2012

Understanding the factors influencing the ET characteristics of redox proteins confined at an electrochemical interface is of fundamental importance from both pure (fundamental science) and applied (biosensory) perspectives. This thesis reports on progress made in the emerging field of coupled electrochemical characterization and optical imaging in moving the analysis of redox-active films to molecular scales. More specifically the combination of cyclic voltammetry and wide-field Total Internal Reflection (TIRF) microscopy, here named 'Fluorescent Cyclic Voltammetry' (FCV), was applied to monitoring the response of surface-confined redox active proteins at submonolayer concentrations.

The combined submicrometre spatial resolution and photon capture efficiency of an inverted TIRF configuration enabled the redox reactions of localized populations of proteins to be directly imaged at scales down to a few hundreds of molecules. This represents a 6-9 orders of magnitude enhancement in sensitivity with respect to classical current signals observed in bioelectrochemical analysis. Importantly, measurements of redox potentials at this scale could be achieved from both natural and artificially designed bioelectrochemical fluorescent switches and shed fundamental light on the thermodynamic and kinetic dispersion within a population of surface confined metalloproteins.

The first three chapters of this thesis provide an overview of the relevant literature and a theoretical background to both the rapidly expanding fields of electroactive monolayers bioelectrochemistry and TIRF imaging.

The initial design and construction of a robust electrochemically and optically addressable fluorescent switch, crucial to the applicability of FCV is reported in chapter 5. The generation of optically transparent, and chemically modifiable electrode surfaces suitable for FCV are also described.

Chapter 6 describes the response of the surface confined azurin-based switch. Analysis of the spatially-resolved redox reaction of zeptomole samples in various conditions enables the mapping of thermodynamic dispersion across the sampled areas.

In chapter 7 the newly developed FCV detection method was extended to investigate more complex bioelectrochemical systems containing multiple electron transferring redox centres and responding optically at different wavelengths. This approach provides a platform for spectral resolution of different electrochemical processes on the same sample.

Finally in chapter 8 an electrochemical procedure is proposed for investigating the kinetic response of redox proteins using a fundamentally new methodology based on interfacial capacitance. In using variations in the surface chemistry to tune the rate of electron transfer, the approach was shown to be a robust and facile means of characterising redox active films in considerably more detail than possible through standard electrochemical methodologies. Ultimately, it can be applied to probe dispersion within protein populations and represents a powerful means of analysing molecular films more generally.

Acknowledgements

I would like to thank my supervisor, Dr Jason Davis, for giving me the opportunity to work on a very absorbing research topic. I am especially indebted to him for the ideas, inspiration and words of motivation he has contributed during this past four years.

I am extremely grateful to many of the former members of the JJD group, in particular to Dr Amol Patil for guiding me through the fundamentals of AFM imaging, optical microscopy and MatLab use, to Dr G. Orlowski, Dr M. Busby, Dr J. Tkac and Dr M. Samalova for sharing their expertise on various subjects and being great colleagues and friends. A big thank you also to Habibur Rahman, Michael Morten and Michal Siwek for sharing enthusiasm about TIRF imaging of redox reactions and for company during long hours in the dark looking at blinking spots. And to Prof Paulo Bueno for his enthusiastic introduction to the world of impedance spectroscopy and the intense cooperation, hoping to see him next time in Brazil!

I would also like to thank the EdRox FP6 Marie Curie research training network and in particular Professor Gerard. W. Canters and Professor Thjis J. Aartsma for allowing me to collaborate with their research groups and being always so welcoming in Leiden. Thanks to Alessio Andreoni, Dr L. Tabares and Lionel Nambda for supplying so many protein samples and for making my time in Leiden so productive and so much fun at the same time! Thank you to Professor E. Fort, to Karla and Olivier for their patience and help in working with surface plasmons effects and for welcoming me so warmly in their lab during my stay in Paris.

Dr. Dirk Aarts really deserves a special note for being the best college advisor ever and teaching me some valuable Dutch words.

Credits must be given to Dr Robert Jacobs for producing an infinite series of OTEs, to Dr Michael Pitcher for help with the pyrolysis of the PPFs, to Professor L. Wang and Professor F. Gilardi for flavoproteins samples and to the staff of PTCL and the workshops for daily help and for being always cheerful and smiling. Thank you also to Gemma, Luca, Josh and Radhika, and to the small group of habitués of the Christ Church GCR study room for dealing patiently with all the bizarre behaviours of a stressed writing-up DPhil student.

A whole-hearted mention goes to Kiterie for being such a great friend, for night long chats, chips&tea at four in the morning, for her frank opinions and especially for supporting me (sometimes also physically, but mostly with cakes) through the greatest highs and deepest lows of last four years.

Finally I would have never finished this thesis without the constant encouragement and trust of those who, despite being physically distant, were always there to listen and were my deepest supporters. So, 'grazie di cuore' to my parents Flavio and Leda, my 'little' sister Irene, nonna Iliana, Monia and Andrea, Jochen, Marika and Lucia.

Giulia Mizzon, April 2012

Table of Contents

List of Figures

List of Tables

Abbreviations and Symbols

C^*	Complex capacitance
i_C, i_f	Faradaic and capacitive currents
k_{ET}	Rate of Electron Transfer
k_{nr}	Rate of non-radiative decay
k_{SET}, k_{FRET}	Rate of SET and FRET
n_i	Refractive index of material
Z^*	Complex impedance
z_0	Evanescent wave decay distance
α_a, α_c	Electron transfer coefficients, anodic and cathodic
θ_c	Critical angle for TIR
θ_{NA}	Maximum angle of illumination in TIRF objective
κ^2	Orientation factor in dipole-dipole interactions
Φ_i	Fluorescence quantum yield of species *i*
λ	Wavelength
A, D	Acceptor, Donor
ABTS	2,2'-azino-bis(3-ethylbenzothiazoline-6-sulphonic acid)
A_{el}	Electrode area
ArR	Ferredoxin reductase
Az	Azurin
EM-CCD	Electron Multiplying Charge Coupled Device
CV	Cyclic Voltammetry
d, d_0	Donor-Surface distance, distance for 50% SET efficiency
DET	Direct Electron Transfer
DTT	Dithiothreitol
DT	Sodium Dithionite
E	Potential
E_{FRET}	FRET efficiency
EDC	1-ethyl-3-(3-dimethylaminopropyl)carbodiimide
EIS	Electrochemical Impedance Spectroscopy
E_{pa}, E_{pc}	Anodic and cathodic peak potential
F	Faraday constant (96 485.3415$C \times mol^{-1}$)
FAD	Flavin Adenine Dinucleotide
FCV	Fluorescent Cyclic Voltammetry
Fld	Flavodoxin
FMN	Flavin Mononucleotide
FRA	Frequency Response Analyser
FRET	Förster Resonance Energy Transfer
FWHM	Full Width at Half Maximum
GOx	Glucose Oxidase
I	Fluorescence intensity
IET	Internal Electron Transfer

J	Spectral overlap
Lc	Laccase
MUA	11-Mercaptoundecanoic acid
n	Number of electrons
N.A.	Numerical Aperture
NAD(P)H	Nicotinamide Adenine Dinucleotide (Phosphate)
NHE	Normal Hydrogen Electrode
NHS	N-Hydroxysuccinimide
OTE	Optically Transparent Electrode
PB	Phosphate Buffer
PdR, PuR	Putidaredoxin Reductase, Palustrisredoxin Reductase
Q	Observed switching efficiency
QCM	Quart Crystal Microbalance
R	Gas constant (8.31446 $J\ mol^{-1}K^{-1}$)
R, R_0	Donor-acceptor distance in FRET and Förster radius
SAM	Self Assembled Monolayer
SCE	Saturated Calomel Electrode
SHE	Standard Hydrogen Electrode
SM	Single Molecule
SPE	Surface Plasmon Enhancement
SPR	Surface Plasmon Resonance
SWV	Square Wave Voltammetry
T1, T2, T3	Type 1, Type 2 and Type 3 copper sites
TIR	Total Internal Reflection
TIRFM	Total Internal Reflection Fluorescence Microscopy
TM-AFM	Tapping-Mode Atomic Force Microscopy
TNC	Tri-Nuclear Copper Centre
UQR	Unusual Quasi Reversibility
UV-Vis.	Ultra Violet-Visible
WD	Working Distance
Γ	Radiative emission rate
ν	Scan rate
τ	Fluorescence lifetime
τ_1, τ_{ct}	Relaxation times of dielectric and charge transfer elements
ϕ	Phase shift in EIS

Chapter 1

Introduction

The conductive interface where a layer of redox active proteins is bound is a place where chemistry, physics and biology disciplines meet and overlap in a fascinating way. Interfacial redox reactions are crucial to the metabolism of energy production and consumption across all living organisms, from photosynthesis to respiration.[1] Many of these reactions are carried out and finely tuned by a pool of redox proteins and enzymes[1,2], complex biomacromolecules typically containing, embedded in the dielectric of the polypeptide folds, one or more metallic sites or organic cofactors. These facilitate the electron transfer process and typically confer characteristic spectral properties to the otherwise colourless protein structures.[2]

More than a third of the currently structurally determined polypeptides contains metals, with about 40% of these employed in redox centres[3]; nonetheless bioinformatics[4] and high throughput screening tests[5] suggest that metalloproteosomes are still largely unexplored. At the same time a whole new library of synthetic redox bio-macromolecules is being produced biotechnologically, via *de novo* design[6-8] or via engineering of existing binding centres.[7,9]

Based on this vast number of diverse samples, the development of reliable techniques for investigating small amounts of these redox active molecules is of great relevance to state of the art of biological chemistry research and to the development of large scale biosensors/diagnostics devices.

Within this larger context, the aim of this thesis project was to investigate novel methods of directly imaging electron transfer of small samples of surface confined proteins by coupling their redox state to an optical output measurable by fluorescence microscopy. Specifically, the redox state of the surface confined electron-transfer proteins was studied using a combination of two elegant and powerful techniques: electrochemistry, in the form of Cyclic Voltammetry (CV), and Total Internal Reflection Fluorescence Microscopy (TIRFM). This approach was applied to monitor the response of the simple electron-transfer protein azurin (hereafter referred to as Az) and later extended to more complex bioelectrochemical systems, with the aim to resolve electron transfer characteristics invisible with standard electrochemical approach.

1.1 Bioelectrochemistry of Surface Confined Proteins

Bioelectrochemistry is a wide field of science that investigates the electron transfer reactions in biology, and in which electroanalytical techniques are widely employed.

The idea of immobilizing electroactive molecules on the surface of electrodes was first advanced in the 1980s by Weaver *et al.*[10-12] for inorganic cobalt compounds and was later applied to protein films investigations.[13,14] Aided by the development of methods for chemical modification of the electroactive surfaces, 'protein film voltammetry' (PFV), in its various forms, soon became the chosen approach for studying the thermodynamics and kinetics of redox active proteins.[14-18] The pioneering works of Armstrong and co-workers started in this University in the late 90s[14-18] on graphite electrodes has, since then, developed into a large field of studies, with a wide range of applications.

Redox active proteins confined to electrode surfaces have drawn a lot of attention from the scientific community. One of the reasons of this large success is that the investigation of adsorbed electrochemical species offers many advantages over solution phase heterogeneous studies of electrochemical probes. Among these, surface confinement facilitates the removal of diffusion limitations in CV. At the same time it facilitates coupling with spectroscopic and gravimetric analyses of very small quantities of material (typically 10^{-11}-10^{-12} moles cm^{-2}).[19] Furthermore the characteristics of the surface can be chemically designed to attain the desired type of immobilization.

A few examples of techniques that have been integrated with interfacial electrochemical measurements include Quartz Crystal Microbalance(QCM) [20,21], contact angle[22], ellipsometry[23] and surface plasmon resonance.[24,25] Spectroscopic analyses have also been employed, in particular in the infrared frequency range. Hildebrandt, Murgida and their co-workers widely employed Surface Enhanced Raman Resonance Spectroscopy (SERRS) of cytochrome *c* at rough silver rotating disk electrodes to follow the conformational dynamics of the heme under electrochemical control.[26-30]

In this project a wide field Total Internal Reflection Fluorescence Microscope (TIRFM) was used to detect fluorescent emission of surface confined proteins in a spatially resolved way, under electrochemical control. The resulting technique is referred to as Fluorescent Cyclic Voltammetry (FCV). A schematic of this combined approach and of the phenomena we hope to be able to investigate is illustrated in Figure 1.1.

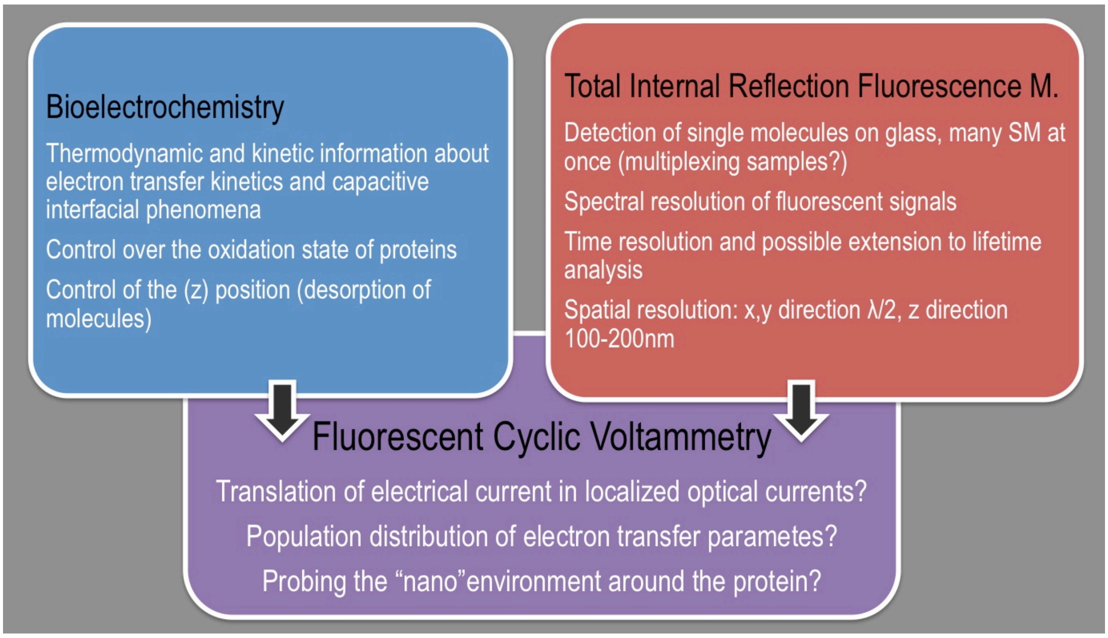

Figure 1.1: Schematic summarizing the advantages offered by combination of TIRFM and CV of surface confined films into FCV.

The investigated redox proteins were converted into fluorescent redox switches via a labelling strategy that enables a link between the rate of photon emission and the protein's redox state.[31-33] Fluorescence emission can then be observed at micrometre-sized areas thanks to the magnification offered by the microscope lenses. The optical output thus provides a tool to investigate the occurrence of the electron transfer reactions across the surface.

It was hoped that an association between optical output and redox state could be transcribed to, suitably prepared, optically transparent electrode surfaces in an inverted TIRFM objective-based setup.

1.1.1 Effects of Microheterogeneity

The established theoretical treatment of electrochemical signals for surface confined molecules assumes homogenous response from a population of equally oriented, non interacting protein molecules.[14] However evidence has been accumulated to suggest that protein layers are often deviating from this behaviour.[34-38] The current responses associated with proteins are often non-ideal; in CV in particular (see Chapter 3) broadening of the voltammetric peaks, and experiment-to-experiment variation[39] are often observed.[34-38] For instance, Clark and Bowden[34], while investigating the voltammetry of electrostatically immobilized cytochrome *c* at gold electrodes, evaluated the peak broadening of the voltammetric signals as a function of the proteins surface concentration, suggesting the presence of dispersion in thermodynamic potentials due to presence of molecules experiencing different orientations and micro-environments.[34] Further investigations identified the surface roughness of the underlying gold substrate, reflected in the quality of the overlying electro-active films, as one of the main causes of thermodynamic dispersion.[40] Others ascribed the observed variations to distribution in thermodynamics or in kinetics of the proteins population across the surface.[35-38]

The non-idealities arise since the current signal measured is generated at the passage of several millions of electrons, i.e. ensemble contributions of several millions of individual protein molecules.

Variance in kinetic and thermodynamic properties across the surface can emerge as a result of a range of contributing factors, such as the lateral protein-protein interaction, variations in the strength of the electronic coupling between the redox site and the electrode, and the micro environmental variance in properties such as surface charge or molecular orientation. Also depending on their structure and chemical environment, protein molecules respond differently to the varying interfacial electric field. A graphic summary of some of the factors affecting the response of a model metalloprotein population is represented in Figure 1.2.

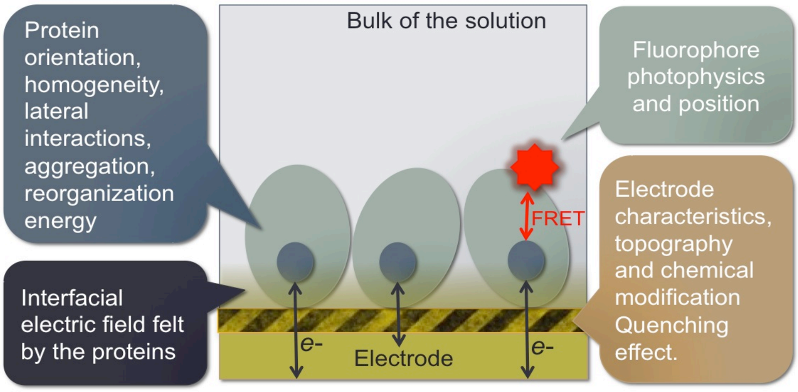

Figure 1.2: Schematic of several factors influencing the homogeneity of the response of the electroactive protein labelled with a fluoreofore on the surface of an electrode, including the dispersion in the proteines characteristics, their interaction with the chemically modified surface and the interfacial electric field and the positioning of a fluorescent molecule on the proteins surface.

One might seek to separate these effects by reducing the number of molecules electrochemically sampled, to identify groups of proteins subject to the same microenvironment and forces. Of course in this perspective single molecules resolution would be the final limit.

1.1.2 Single Molecule Bioelectrochemistry

Attempts to reduce the number of sampled proteins have been carried out in the past by reducing the electrode area where the proteins are confined, employing micro and nanoelectrodes.[41,42] For instance, Heering *et al.*[41] reported the activity of zeptomole samples (59×10^3 molecules) of nitrate reductase, co-immobilized with cytochrome *c* at gold microelectrodes. More recently Hoeben *et al.*[42] were able to isolate the catalytic currents of as few as 8-50 molecules of [Ni-Fe] hydrogenase on a $70 \times 70\ \mathrm{nm}^2$ gold electrode. However in both these examples these high sensitivities were made possible by the fast catalytic turnover of the enzymes. Each molecule of [Ni-Fe] hydrogenase, once removed the substrate diffusion limit, was able to oxidise $\sim 10^3$-10^4 hydrogen molecules per second, corresponding to twice as many electrons being transferred into the gold electrode, i.e. currents of $0.5\text{-}3.0 \times 10^{-15}$ A per molecule. In any case, detection of such small currents is possible only using specialized electrode preparations and custom-made electronic equipment.[41,42]

Recognition of the single electron transferred by single molecules of non-catalytic proteins, such as Az or cytochrome *c*, or of enzymes redox centres in the absence of substrate is currently far beyond the limit of normal electrochemical means.

An alternative way to distinguish the redox properties of simple electron transfer proteins, which are devoid of catalytic activity, at molecular size samples is to use *in situ* imaging techniques, such as Scanning Tunnelling Microscopy (STM) and contact probe Atomic Force Microscopy (AFM).[43] *In situ* tip-molecule interaction enables sub-nanometre resolution and control of the 3D organization of the contacted molecules, thus offering powerful means of investigation. However these techniques require engagement of the scanning tip with the investigated molecules that consequently need to be examined one by one. This is a large limitation when seeking to map dispersion of a number of surface-confined molecules. In this respect, the use of wide-field microscopy proposed in this thesis has the potential for monitoring many single proteins in a single image, provided that the fluorophores are adequately spaced on the surface to match the resolution of the optical system and that a sufficient number of photons can be collected from each of these.

1.1.3 Single Molecule Fluorescence Imaging

The fluorescent emission from a single fluorophore molecule at room temperature can now be routinely detected and distinguished from the background emission due to Raman and Rayleigh scattering of the surrounding environment and to the eventual presence of fluorescent artefacts. This became possible thanks to the huge developments made in fluorescence microscopy over the past decade.

Most of the optical systems able to reach Single Molecule (hereafter SM) resolution, such as confocal microscopy and TIRFM, use high dilution of fluorophore molecules and particular optical arrangements which reduce the volume where fluorophores are excited (TIRFM) or detected (confocal microscopy) to submicrometric dimensions.[44]

Commercialization of highly efficient photon detectors, such as Electron Multiplying Charge Coupled Device (EM-CCD) cameras, photomultiplier tubes and avalanche photodiodes, has made observation of SMs by TIRFM routinely available.[44]

Time traces of SM emission typically show blinking phenomena (reversible on-off times) and undergo single step photobleaching (the irreversible photoinduced degradation of the fluorophore). Statistical analysis of these processes are used to gain information about the structure, photophysics and interaction with the environment.[44] The theoretical background for these studies has been thoroughly reviewed[44-46] and examples of processes studied at SM level are very numerous, including molecular motion events,[47] DNA hybridization[48] and enzymatic catalysis dynamics[49].

The motivations to achieve to SM sensitivity are:

- the sensitivity limit: SM is the ultimate limit corresponding to 1.66×10^{-24} moles. In many medical and biochemical tests reaching detection of a single analyte molecule is the ultimate aim;
- probing the surrounding: a SM, with its small volume (typically a few nm^3), is the tiniest possible probe for chemical environment;
- removal of heterogeneity within a population: subpopulation of molecules with different structures or emission patterns would be discriminated from the average signal;
- removal of synchronization issues: kinetics of processes can be analysed independently for each molecules and possible rare intermediate can be observed;
- direct comparison with theory: the application of theoretical models and computational simulation could be directly applied.[44]

Due to the efficient exclusion of excitation of the bulk of the solution/sample (see chapter 2), has been proved particularly useful for investigation of SMs bound or close to the supporting interface (cover slide/buffer), for example in the investigation of labelled molecules or genetically engineered fluorescent protein in biological membranes of cells adhering on the cover slide.[50] Recent developments saw the combination of TIRF with other optical techniques such as two-photon excitation[51,52] and fluorescence lifetime imaging [50,53] which are going to further expand the palette of measurements and samples accessible with this type of microscopy.

To give an idea of the potential information obtained by combining of SM fluorescence imaging and bioelectrochemical control, Figure 1.3 represents a simplified schematic of the fluorescence emission intensity vs. time profile of three hypothetical physisorbed redox molecules whose emission is switched “ON” or “OFF” by an external potential applied to the surface. The potential dependence of the redox induced switching of surface confined SMs would give information about the topography of the surface potential, as well as information about the molecules population per se.

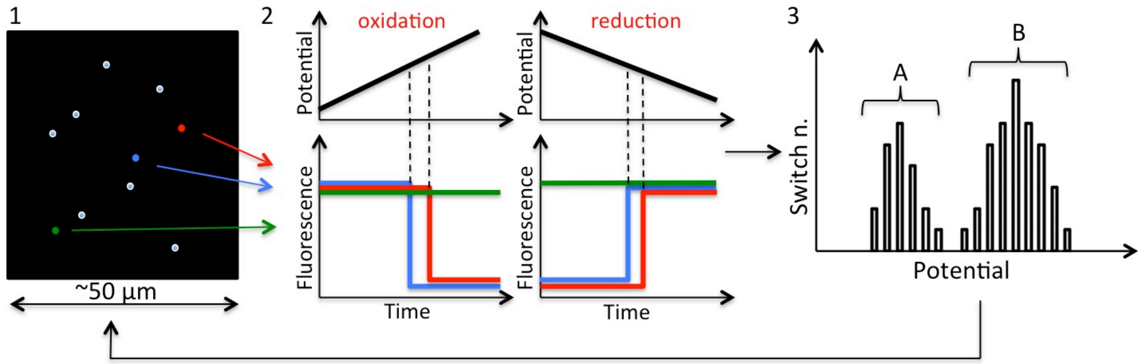

Figure 1.3: Response expected for an ideal SM experiment in which the fluorescence of the surface confined molecules is electrochemically switched on and “OFF” by oxidation and reduction (the direction of the switch is only indicative in this case). (1) represents an ideal stack of images acquired in a time-lapse during electrochemical control of the surface potential and containing many SMs. In (2) the time traces of three molecules taken as example are aligned with the potential applied, the fluorescence switch occurs at a potential corresponding to the redox reaction occurring. In (3) the distribution of the switching events over potential is used to distinguish different populations of responding molecules. The potential of the switches could be eventually reported to the imaged area to detect inhomogeneities of the response across the surface.

However as illustrated both in theory and in practice respectively in chapter 2 and 5, the confinement of fluorescent probes on conductive surfaces generally introduces a large limitation on the number of photons that can reach the detector.[54] SM observation of fluorescent electrochemically active proteins in Direct Electron Transfer (DET) contact with an electrode by means of fluorescence microscopy has not yet been reported. However several spectroscopic techniques have been successfully coupled with electrochemistry of surface confined proteins, as briefly summarized in the next section.

1.2 State of the Art

1.2.1 Spectro-Electrochemistry of Surface Confined Proteins

UV-Visible (UV-Vis.) absorption spectra of heterogeneous electron transfer from diffusing cytochrome *c* to gold mesh electrodes was first reported in the 1970s[55] and since then this spectro-electrochemical technique has been applied to many other protein solutions.[56-58] Transmission UV-Vis. spectro-electrochemistry is a bulk measurement technique generally performed in custom-built cuvettes or in Optically Transparent Thin Layer Electrode (OTTLE) cells. A thin section of the electrochemical cell is required to minimize the diffusion time of the slowly moving protein molecules to and from the surface. Typically, thin metallic meshes or transparent conductive films are used as working electrodes to increase the protein/electrode contact area, and at the same time allow transmission of the light beam. Even with these optimization the equilibration of the concentration with the bulk of the solution for spectra acquisition still requires long interval periods.[59]

Postlethwaite *et al.*[60] reported in 1995 the fast spectro-electrochemical detection of the absorption spectrum of monolayers at a concentration of $\sim 50 \times 10^{-12}$ moles cm^{-2} for metallo-porphyrins, covalently bound on gold transparent electrodes. The DET porphyrin-gold allowed simultaneous acquisition of the electrochemical and optical signal.

However, as protein monolayers typically have ~ 10 times lower surface concentrations and lower extinction coefficients, the absorption of a single (sub)-monolayer of proteins is generally too weak to be distinguished from the background noise. To increase the signal, accumulation of several layers of proteins in conductive mesoporous films[61] and in conductive polymers[62,63] has been used. Alternatively the attenuated total reflection geometries[64] have also shown to give good results.

The first spectro-electrochemical characterization of Az submonolayers and cytochrome *c* physisorbed on transparent gold electrodes has only very recently been reported by Ashur *et al.*[65] The authors attributed the unexpectedly detectable absorption of the discontinuous protein submonolayer ($\sim 5 \times 10^{-12}$ moles cm^{-2}) to signal amplification (of 1-2 orders of magnitude) mediated by the gold surface plasmons.[65] This was the first study achieving the necessary sensitivity for detection of redox linked spectral changes of surface confined proteins by UV-vis. transmission spectroscopy.

1.2.1.1 Previous Reports of CV Coupled to Fluorescence Microscopy

Previous examples combining simultaneous fluorescence microscopy imaging with electrochemical control are very infrequent. The combination of the two techniques has been used for investigation of mainly two types of processes occurring at the electrode surface:

- Motion of fluorescent molecules on a quenching gold surface.
- Heterogeneous spectro-electrochemistry of soluble fluorescent switches

1.2.1.2 Motion Induced Fluorescence Change

In the first case the electrochemically induced fluorescence variation is not due to transfer of charges from the adsorbate but rather to change of the position of the emitting fluorophore with respect to the gold surface. Bizzotto *et al.*[66-70] observed the reductive and oxidative desorption of fluorescent surfactants and fluorescent thiol monolayers from flame-annealed gold beads[66-70] and mercury drop electrodes.[71] Time resolved fluorescence imaging allowed the topology of the underlying gold beads to be mapped, as the fluorescent desorption occurred at slightly different rates on the different single crystal facets of the gold bead.[67]

Another example of electrochemically triggered motion is reported by Rant and co-workers[72-76] The authors observed the variation in fluorescence intensity due to motion of fluorescently labelled DNA strands, attached at one extremity on a gold surface. The potential applied to the electrode in this case was used to modulate the force exerted by the interfacial electric field on the negatively charged DNA backbones, thus causing attractive/repulsive forces at the gold surface.[72-76]

1.2.1.3 Heterogeneous Redox-Linked Fluorescence Switching

The second type of events is fluorescence switching triggered by redox transformation. Fluorescence microscopy was used to monitor the heterogeneous electron transfer reaction between soluble organic dyes and a metallic working electrode. Electron transfer to/from the dye resulted in switching of the fluorescent emission of the dyes. In this case the emission intensity of the dye molecules close to the surface was observed through an OTTLE cell, modified for sitting on a microscope stage[77] or by focusing on thin slots etched in a thicker non transparent electrode deposited on a glass coverslip.[78] As the fluorescent redox switches were diffusing close to the electroactive surface, the measurement performed is equivalent to a heterogeneous spectro-electrochemical test observed on a microscopic volume of solution. However detection of fluorescent signal of surface confined probes is technically more challenging due to the inherent quenching effects metallic surfaces impart and to the fluorophores photobleaching. At metallic electrodes surfaces the distance between a fluorescent probe and a metal can be controlled by chemical modification. In particular the formation of Self Assembled Monolayers (SAMs) is a well-established tool to control the distance between a probe and the electrode.

1.3 Self Assembled Monolayers (SAMs) on Gold

Interaction of proteins with surfaces, even when these are not electrified, often results in denaturation of the native structure and loss/distortion of the redox centres. Chemical control of the surface makes possible engineering of the surface properties in order to favour non-destructive physisorption of the large and often flexible structure of biomacromolecules. In particular, modification of gold surfaces by means of organosulphur compounds has been extensively explored for this purpose.[79,80]

Alkanethiol 'self-assembled monolayers' (SAMs) spontaneously assemble on noble metal surfaces due to the strong affinity of the sulphur head groups for the metal. The conditions influencing this process and the properties of the obtained films have been extensively reviewed by many authors including works from Finklea[81], Schwartz[82] and Whitesides and co-workers.[83]

Self-assembly of monolayers on gold electrodes can be obtained by simply dipping the clean surfaces in ethanolic solutions containing 0.1-5 mM thiolated molecules.[84] The process of SAM formation goes through different phases. Initially (within ~30s) a rapid reaction of the thiolated molecules with the gold surface leads to a disordered layer, with alkyl chains lying parallel to the supporting solid surface.[85] Subsequently a progressive transition to a standing up ordered phase occurs, associated to a slower increase in the molecular coverage. [81,84]

Common to all alkanethiols on Au(111) is the formation of an ordered SAM displaying a hexagonal $(\sqrt{3} \times \sqrt{3})R30°$ symmetry, corresponding to the adsorption of one thiol per three gold atoms. The alkyl chains in n-alkyl thiolate SAMs on Au(III) have been shown by FTIR studies to tilt at 28° from the surface normal, with a 53° rotation of the alkyl chain about the long axis[86], as represented in Figure 1.4. Ideal surface coverages reported for linear alkanethiolate are close to 0.77×10^{-9} moles cm^{-2}, which correspond to an hexagonal $\sqrt{3}$x$\sqrt{3}$ packing with one thiol per three gold atoms.[81]

The tilt is thought to be driven by a maximisation of the lateral van der Waals attractive forces between the alkyl chains, which stabilise the SAM.[84] Other non-covalent interactions such as dipole-dipole interactions[87] and hydrogen-bonding have been shown to affect the properties of alkanethiolate SAMs.[88]

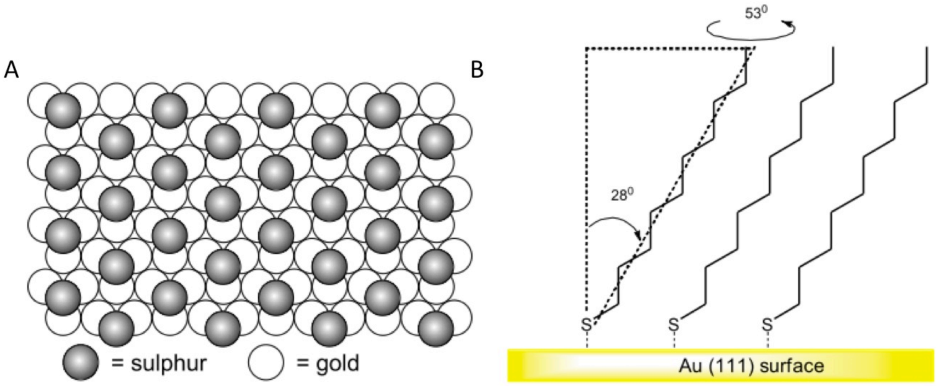

Figure 1.4: A) Representation of hexagonal ($\sqrt{3}\times\sqrt{3}$)R30° lattice of sulfur atoms on Au(111) for an alkanethiolate monolayer. B) Representation of n-alkanethiolate SAM) showing tilt angle of 28° and alkyl chain rotation of 53° about the long alkyl chain axis

The thickness of linear alkanethiol SAMs, obtained for long immersion times (12-24h), increases linearly with the number of carbon atoms in the alkane chain with a slope of 1.08 ± 0.1Å/n.[89,90] Values determined by ellipsometric thicknesses by Biebuyck *et al.*[89] and by Scanning Tunnelling Microscopy (STM) by Weiss[90] are reported in Table 1.1.

N. of carbon atoms	**Thickness (Å)**	**Number of carbon atoms**	**Thickness (Å)**
10	13.0	2	4.3±1.6
11	14.1	3	4.5±1.6
12	15.2	4	7.5±1.6
13	16.3	6	8.5±1.6
14	17.4	8	11.4±1.6
15	18.5	11	11.3±1.6
16	19.6	16	19.2±1.6
17	20.7	18	22.2±1.6
Ref. Weiss [90] (STM)		Ref. Biebuyck,[89] (ellipsometry)	

Table 1.1: SAM thicknesses measured for increasing chain langths as determined by scanning tunnelling microscopy and ellipsometry. Linear fitting with a slope of 1.08±0.1Å/C_n fits both sets of data with R^2≥0.98.

A progression in order and packing density in the SAM structure with increasing thickness has been demonstrated with various techniques, such as Fourier Transform Infrared Reflection-Absorption Spectroscopy (FT-IRRAS),[84,91] ellipsometry[89,92] and electrochemical analyses.[93] Additionally, contact mode AFM studies have suggested that longer chain SAMs are able to withstand greater tip-sample interactions, observations consistent with greater attractive chain-chain van der Waals interactions.[85,93-96]

Reflecting the higher order of the underlying surface, SAMs on Au(111) are more ordered than those obtained at Polycrystalline Gold Electrodes (PGE).[81] Defects in the SAMs at PGEs may include uncovered pinhole areas, missing single thiols and rows, and loosely packed domains.[81] Grain-like domains with ordered internal packing, but with different tilt orientation with respect to the neighbouring domains and different packing patterns on other different gold crystal facets are also expected.[84] The amount of imperfections and thus the quality of the SAM can be evaluated by several methods, including metal decoration and etching techniques, blocking studies by CV with redox active electrochemical probes and via AC impedance spectroscopy and capacitance studies.[81]

Linear alkanethiol SAMs offer a simple and effective tool to reproducibly vary the distance between the gold surface and the redox active centres of proteins physisorbed on it.[18,97,98] In chapter 6 and 8, alkanethiol-SAMs of increasing thicknesses will be used to tune the k_{ET} of Az, by varying the electronic coupling with the gold in the non-adiabatic regime. In chapter 7 a SAM terminated with negatively charged carboxylic groups will allow both covalent binding and electrostatic physisorption of proteins with distinct characteristics.

1.4 Aims of the Project

Recent work performed by our group and co-operators presented the proof of principle that protein film voltammetry can be used in combination with wide field fluorescence detection, both with normal epifluorescence illumination and in TIR,[99,100] for monitoring of surface confined redox reaction of a fluorescent bioswitch constructed on Az. The resulting method was called Fluorescent Cyclic Voltammetry (FCV).[100] The following chapters report progress made in further extending this technique to protein population analysis and to more complex bioelectrochemical systems.

In chapter 2 an introduction to the principles of optical phenomena involved is given, including theory of TIRF microscopy and the basics of dipole-dipole energy transfer theory. Likewise chapter 3 contains a brief description of the theoretical background of CV and the other electroanalytical methods used. Chapter 4 deals with the experimental instrumentation, materials and methods used to perform FCV and for complementary electrochemical, spectroscopic and topographic analysis.

Chapter 5 contains results about the construction of the fluorescent switch based on Az and the choice, preparation and characterization of the transparent electrodes. These two components will be combined in Chapter 6 to analyse the fluorescence traces of surface confined proteins under potential modulation. A simple robust method to evaluate systematically the potential at which ET is occurring in small selected areas across the surface is presented.

The extension of the FCV technique to monitoring switching emission of intrinsically fluorescent proteins, containing organic cofactors and an attempt to apply it to a multicopper oxidase enzyme is presented in chapter 7.

Finally the last results chapter is dedicated to the investigation of an electrochemical method to evaluate the kinetic dispersion of electron transfer in a distribution of surface confined electron transfer proteins.

Chapter 2

Theory: Fluorescence Microscopy

2.1 Introduction to Fluorescence

Early reports on fluorescence phenomena date back to 1840s, when Sir J. F. W. Herschel first observed a 'beautiful celestial blue colour' emitted from dilute solutions of quinine exposed to direct sunlight. The name 'fluorescence' was introduced soon after by Sir G.G. Stokes, who also described the energy loss in the light emitted from fluorescent molecules with respect to the incident beam, now called 'Stokes shift'.

It was not until the first half of 20th century, though, that a comprehensive description of the energetics of luminescence phenomena was presented, thanks to the work of Prof A. Jablonski.[54] The Polish physicist, regarded as the father of fluorescence spectroscopy and molecular photophysics, designed the diagrams (one version is shown in Figure 2.1) that are still the most common representation of the electronic transit.[54]

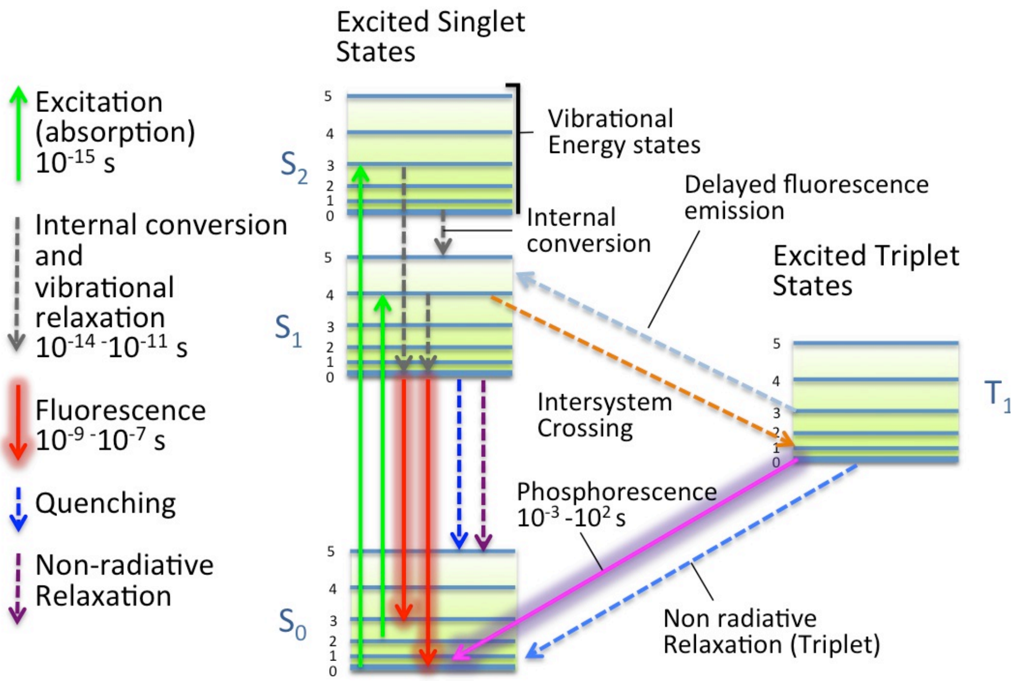

Figure 2.1: One form of the Jablonski diagram describing the most common energy transitions and the average time ranges involved in fluorescence and phosporescence emission.

When a photon of an appropriate wavelength collides with a molecule, a fast electronic transition occurs which results in one of the molecule electronic orbitals being excited to a higher quantum state. From here, return to the ground state can occur in a number of ways that can be viewed pictorially using the Jablonski plot (Figure 2.1). If the molecule has a rigid structure, rich in double bonds, then the loss of energy from vibration and rotation pathways could be slow compared to radiative relaxation, and the excited electron decays from the lower vibrational level of the excited singlet state (S_1) to the ground state (S_0) with concomitant emission of a photon.

Accordingly to Frank-Condon principle, excitation occurs in a very short time, it needs less than 10^{-15} seconds.[54] The molecule is usually excited to some higher vibrational level of either S_1 or S_2 and, within 10^{-12}s or less, relaxes to the lower vibrational state of S_1, through a process called internal conversion. From here, the electronic transition to the ground state is spin allowed, hence the cycle of excitation and decay occurs with high rates, typically with frequency values close to 10^8 s^{-1}.

In the diagram above (Figure 2.1), the process is compared to the other key type of luminescence event, phosphorescence, in which the energy absorbed from an incoming photon, through an intersystem crossing event, is moved to an excited triplet state T_1. In this case, as the electron has the same spin orientation as the one in the ground-state, the transition is spin forbidden, hence, typical phosphorescence emission rates are much slower than fluorescence decays, in the 10^{-3} to 10^2 s range and can be observed only in solids.[54]

2.1.1.1 Fluorophores

The fluorescent molecules used in biochemistry belong mainly to two categories: natural or intrinsic fluorophores and synthetic fluorescent molecules.[54]

In the first category fall a fairly limited number of natural molecules, either organic cofactors, such as the oxidized flavins (FAD and FMN, see Chapter 8), the reduced NAD(P)H, pyridoxal phosphate, and porphyrins, or the lateral chains of the aromatic amino acids (tyrosine, tryptophan and phenylalanine).

Thanks to the fairly long lifetime of the excited states that allows for interaction with the immediate environment before decay, fluorescence spectroscopy is often used to evaluate the surroundings of a fluorophore and occurrence of local changes. For example, the solvatochromic emission spectra of tryptophan residues embedded in polypeptides folds have been extensively used to monitor conformational changes, unfolding dynamics and binding of substrates to the protein structures.[54,101]

Despite being a powerful tool, proteins intrinsic fluorescence emission is often problematic to interpret, since emission spectra and lifetimes are strongly influenced by the complex photophysics of the tryptophan indole ring[102,103] and by quenching effects imparted by protonated acidic groups, such as aspartate or glutamate, and some substrates.[54]

The second category of the synthetic fluorescent molecules mainly consists of indicators and probes. Indicators are sensitive to some variable of the environment, such as the pH or the concentration of ions (calcium, magnesium and chlorides) or oxygen. These dyes are used in biology for a variety of studies, such as "calcium imaging" of neuron cell cultures in response to neurotransmitters.[104,105]

Probes include a large group of fluorescent dyes, usually functionalized with reactive groups to tag macromolecules in specific positions.[106-108] This enables an extension of the analysis by fluorescent spectroscopy and imaging to a wide variety of non-fluorescent molecules.[106-108] Their emission is ideally constant in the experimental conditions and the reactive functionalization can be tailored to target specific reactive groups or macromolecules, as in the case of immunocytochemistry or DNA microarrays.

2.1.1.2 Properties of Fluorophores

Fluorophores can be imagined as vibrating dipoles rotating freely in the three dimensions.[54] The five intrinsic properties that can be probed in a fluorescence experiment are:

- The wavelengths of excitation and emission λ_{ex} and λ_{em}, which are characteristic of the electronic structure of the emitters. The two are separated by the "Stokes shift", the loss of energy due to the IC process and to thermalization of the excess vibrational energy in the ground state.

- The quantum yield, Φ (in eq.2.1), i.e. the ratio between the number of absorbed and emitted photons, depending on the spontaneous rate of radiative emission (Γ) and on the rate of non-radiative decay (k_{nr});

$$\Phi = \frac{photons\ emitted}{photons\ absorbed} = \frac{\Gamma}{\Gamma + k_{nr}} \tag{2.1}$$

- The fluorescence lifetime τ (in eq. 2.2), the average time the molecules spend in the excited state, with most commercially available organic fluorophores having lifetimes in the nanosecond range.

$$\tau = \frac{1}{\Gamma + k_{nr}} \tag{2.2}$$

- The anisotropy, r, which describes if the light emitted by a fluorophore has unequal intensities along different axes of polarization.

After a pulse of excitation, intensity of fluorescence I decreases exponentially in time, for a fluorophore with a single decay lifetime, $I(t) = I_0\, e^{t/\tau}$.

2.1.1.3 Non Radiative Decay Pathways

Non radiative decay pathways, considered globally in k_{nr}, (eq. 2.2), can be of different types: for molecules in solutions these are mainly due to thermal relaxation and collisional quenching due to encounters with diffusing molecules (oxygen, halogens, amines and electron deficient molecules). Short-range interactions can cause decay of the excited states with mechanisms such as electron transfer or by causing intersystem crossing to T_1 state.[54]

Thus, while energy absorption involves electronic transitions that are instantaneous and influenced only by the immediate environment, fluorescence emissions are more susceptible to interaction of the excited states with the surroundings, and quenching effects become more important for longer excited lifetimes.[54]

A third important route of depopulation of the S_1 state occurs through resonant coupling of the dipole with a second molecule, as described in the next paragraph.

2.1.1.4 Dipole-Dipole Interactions

The interaction of two dipoles can be described invoking the Golden Fermi Rule in the approximation of the energy transfer, which states that the energy transfer rate k_{EnT} depends on the product of the interaction of the donor, D, and the acceptor dipole, A, involved: $k_{EnT} \approx F_D F_A$. F_i represents the interaction factor, and the geometry of the dipoles defines the extent of its decay with distance (d):

- Point dipoles, free to rotate in the three dimensions will have a contribution $F_i \approx \frac{1}{d^3}$
- Dipoles in a two dimensional array will have $F_i \approx \frac{1}{d}$
- Dipoles constrained in a three dimensional structure have $F_i \approx costant$.

The two types of resonant energy transfer processes observed in this thesis, Förester Resonance Energy Transfer (FRET) and quenching, can be both explained in these terms as dipole-dipole interactions.

The first kind, FRET, involves interaction between two dipoles and the distance dependence will consequently be proportional to $F_{FRET} \approx \frac{1}{d^3} * \frac{1}{d^3} \approx d^{-6}$.

The second, quenching, is about the interaction of a dye dipole with a metallic surface, which can be thought of, in first approximation, as a 2D dipole array, the resulting proportionality constant being $F_{quenching} \approx \frac{1}{d} * \frac{1}{d^3} = d^{-4}$. The two cases are described in the next sections.

2.2 Förster Resonance Energy Transfer (FRET)

FRET is a key process happening when molecules are in the excited state and is a radiationless dipole-dipole interaction between D and A. The two molecules do not enter in contact, but behave as two electric vibrating dipoles so that when they are close to each other interference occurs.[109] FRET coupling takes place every time there is a significant spectral overlap between the emission spectrum of D and the absorption spectrum of A.[54,109] Importantly, with respect to electron transfer prcesses, in energy transfer the medium between the energy donor and acceptor has a relatively small effect on the transfer process (n^{-4}) provided that it is transparent over the range of wavelengths at which the donor emits.[109,110]

As anticipated in 2.1.1.4, the rate of the energy transfer, k_{FRET} decays with the inverse sixth power of the distance (eq 2.3).

$$k_{FRET}(R) = \frac{1}{\tau_D} \times \frac{R_0^6}{R_0} \tag{2.3}$$

where R is the distance between D and A. Here, R_0 is the Förster distance, a parameter describing a probability of the transfer to occur (E_{FRET}) of 50%. As anticipated in 2.1.1.4, E_{FRET} decreases as the inverse sixth power of R, as in equation 2.4.

$$E_{FRET} = \frac{R_0^6}{R^6+R_0^6} \tag{2.4}$$

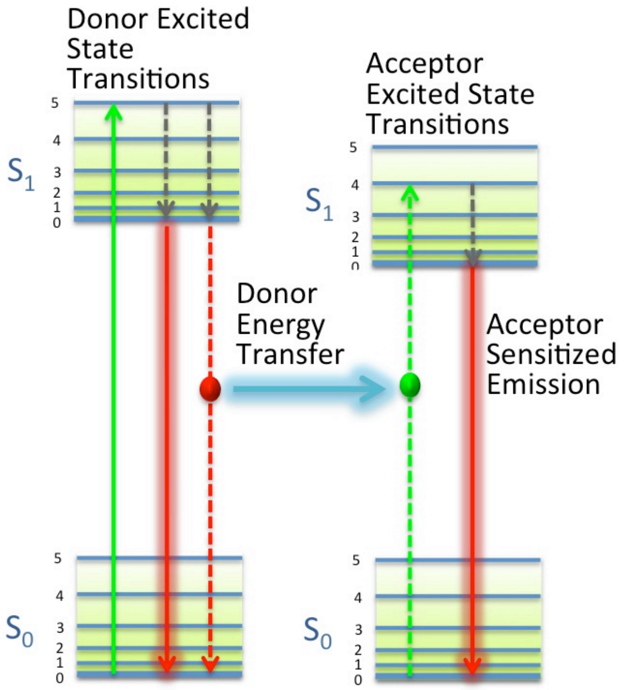

Figure 2.2: A form of the Jablonski diagram focusing on the FRET path of relaxation.

R_0 can also be calculated accordingly to Förster theory[109] as:

$$R_0 = (J\kappa^2\Phi_D n^{-4})^{1/6} \times 9.7 \times 10^3 \text{ Å} \tag{2.5}$$

where:

- n is the refractive index of the medium interposed between D and A
- κ^2 is the orientation factor for a dipole-dipole interaction, with values between 0 and 4. A κ^2 of 2/3 when both the D and A can freely rotate in the three dimensions, calculated from average of the possible reciprocal orientations of the dipoles.
- Φ_D is the quantum yield of the donor in the absence of the acceptor

- Finally the spectral overlap integral, J, is the factor quantifying the resonance, i.e. the overlay of the emission of D with the absorption of A. The higher its value, the higher is FRET efficiency E_{FRET} once the distance R has been fixed.

J is defined as in equation 2.6, where $F_D(\lambda)$ is the fluorescence intensity of the donor, $\varepsilon(\lambda)$ the extinction coefficient of the acceptor at wavelength λ in $mM^{-1}cm^{-1}$ and λ is the wavelength expressed in nanometres.

$$J = \frac{\int_{280nm}^{800nm} F_D(\lambda)\varepsilon(\lambda)\lambda^4 d\lambda}{\int_{280nm}^{800nm} F_D(\lambda) d\lambda} \tag{2.6}$$

R_0 values fall typically within 10 to 80 Å, therefore are comparable with the size of biological molecules. This allows FRET to be widely used in biology as a sensitive method for measuring inter- and intramolecularly the donor-acceptor distances, as a "spectroscopic ruler".[110]

2.2.1.1 FRET to Study the Redox State of Proteins

In most cases FRET is evaluated from the emission of the acceptor, but for it to occur the acceptor doesn't necessarily need to be fluorescent.[54] In fact the energy transfer can be experimentally quantified from the decrease of the radiative emission of the D. This can be done by comparing the fluorescent emission intensities of the excited state lifetimes of D the presence (τ_{DA}, I_{DA}) and in the absence of the "dark" acceptor (τ_A, I_A), by means of the simple relationship in equation 2.7.[54]

$$E_{FRET} = \left(1 - \frac{\tau_A}{\tau_{DA}}\right) = \left(1 - \frac{I_A}{I_{DA}}\right) \tag{2.7}$$

In most cases, especially in cell imaging, D and A are organic labels covalently anchored to proteins. However, as many intensely coloured proteins are available, the protein's prosthetic group itself can also act as an acceptor. In the past, variation in fluorescence emission from attached dye molecules or from internal emitters such as tryptophan residues have been used to monitor folding and unfolding dynamics of proteins, acting as indicators of the surrounding environment. For example FRET from an attached dye to a prosthetic heme groups has been used to measure the unfolding dynamic of yeast cytochrome *c* by FCS[111], the binding of myoglobin to antibodies[25] and the binding of nitric oxide to the heme of cytochrome *c*.[112,113]

In systems in which D and A are at a fixed, known distance, the extent of the spectral overlap J is defining the efficiency of the energy transfer. This offers an alternative to the classical use of FRET as a "spectroscopic ruler" [110] of the distance between D and A, as the fluorescence intensity can be used to onito a change in the electronic spectrum of the acceptor. This change in the absorption spectrum of the acceptor may be occurring upon reaction with a substrate or a due to a change in the redox state.[31-33] These events therefore can be coupled through FRET to a variation in emission of a donor fluorophore with appropriate emission wavelength.

2.3 Fluorescence Near Metallic Interfaces

Unlike for fluorophores in solution that are free to emit photons in all directions, surface confined emitting dipole are influenced by the presence of an interface in the nearby.[114] This modifies the "free space" condition for the vibration of the dipole, therefore the emission of light becomes anisotropic. The dielectric properties of the media constituting the interface, the position and orientation of the dye with respect to the surface determine the propagation pattern.[115-117]

Considering a fluorophore close to a metal surface, the electric field felt by the fluorophore will be affected by interactions of the incident light with the nearby metal surface and also by interaction of the fluorophore oscillating dipole with the metal. Additionally, the fluorophore-oscillating dipole induces a field in the metal.[117] These interactions can increase or decrease the field incident on the fluorophore and increase or decrease the emission.[117] Besides quenching (see section 2.3.1.1) the presence of a metallic film in the nearby can have, in the appropriate conditions, other more subtle effects, which can increase the emission of the fluorophore up to 1000 times[117,118]:

- Concentration of the electromagnetic field at the location of the fluorophore
- The increase of the intrinsic radiative decay rate of the fluorophore Γ.[32]

2.3.1.1 Quenching, or Surface Energy Transfer (SET), to the Metallic Film

Quenching is one of the main phenomena occurring in normal experimental configurations and consists in the introduction of an additional decay pathway to the ground state for the population of excited molecules.

Using a formalism similar to what seen for FRET, Chance Prock and Silbey[119] described the rate of energy transfer from a dipole to a metallic surface interband transition[119], later extended by Persson and Lang to the conduction electron of the metallic surface.[120] As anticipated in section 2.1.1.4, the quenching effect, or Surface Energy Transfer (SET) is expected to decrease as the inverse fourth power of the distance d between the dye and the gold.[121] The decay of SET with distance can be treated similarly to FRET, by substituting the sixth with the forth power of distance in eq.2.3 and substituting R_0 with the characteristic distance d_0 at which the SET efficiency is 50%, described by Persson and Lang [120] as:

$$d_0 = \left(0.525 \frac{c^3 \Phi_D}{\omega_f \omega^2 k_f}\right)^{1/4} \qquad (2.8)$$

In eq. 2.8, c is the speed of light, ω is the frequency of the donor electronic transition and ω_f and k_f are the metal's Fermi frequency and Fermi wave vector, respectively 8.4×10^{15} s^{-1} and 1.2×10^8 cm^{-1} for bulk gold.[121]

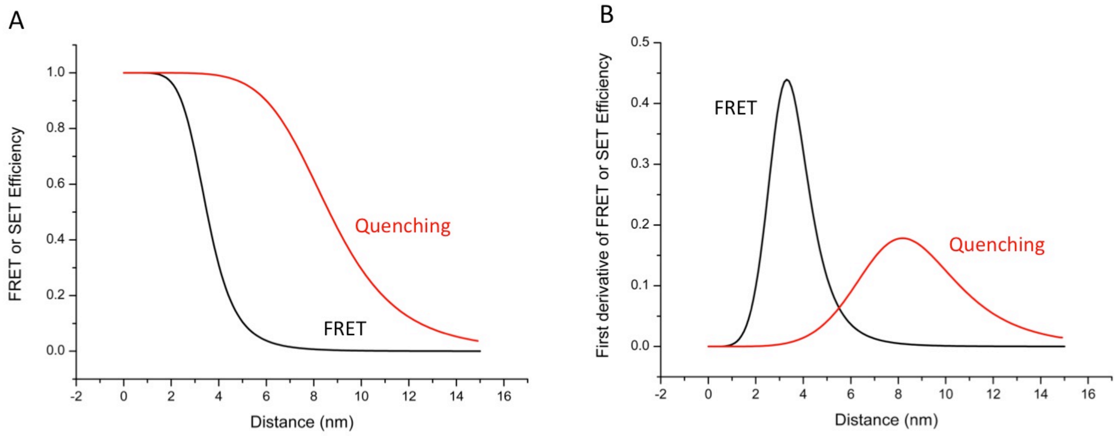

Figure 2.3: A) Simulation of the FRET and quenching decay with distance. For the FRET efficiency decay a R_0=35Å was used, for the quenching decay a of d_0= 86.5Å was calculated using eq. 2.8 for the energy transfer from dye Atto655 ($\Phi = 0.30, \omega = 2.76\times10^{-15}$) to gold. B) First derivative of the distance decay of FRET and quenching, representing the sensitivity or the fluroescence change to distance.

It is important to note that this description is valid in the range of distances comprised between 20-300Å, suitable for investigating the fluorescent systems used in this thesis. At shorter distances (1-10Å) in fact other phenomena, such as electron transfer to the metal and radiative rate enhancement take precedence.[119,121] Likewise at distances above 300Å (i.e. d~λ and above) fluorescence oscillations due to dipole-mirror effects outweigh the quenching.[119,121]

Knowing the distance dependence of the decay, the rate of emission of fluorophores can thus give an indication of the position of the dyes with respect to the metallic surface. Analogously to FRET, SET can be used as a "molecular ruler" (Figure 2.3B).[72,75,121,122] As mentioned in section 1.2.1.2, it was employed to monitor the movement of DNA strands[72,122,123] and the desorption of fluorophores from the electrode surface.[67,69]

2.4 Total Internal Reflection Fluorescence Microscopy (TIRFM)

Total Internal Reflection Fluorescence Microscopy (TIRFM) is an elegant optical technique frequently utilized to observe fluorescence of molecules in proximity of the surface of the glass/air or glass/water interface and is commonly used to investigate surface confined molecules and the membranes of cells adhering on a cover slide, an area of fundamental importance to a wide spectrum of disciplines in cell and molecular biology.[124-127]

Over conventional wide field epifluorescence and laser scanning confocal fluorescence microscopy, TIRFM offers increased spatial resolution, especially along the optical axis, simplifying the task to differentiate between individual specimen details that are overpowered by background fluorescence from outside the focal plane.[128]

The increase in signal to noise ratio is achieved by selectively exciting molecules in a thin layer of solution adjacent to the glass-water (or glass-buffer) interface of the coverslip.[128] The space-limited excitation volume is obtained using the phenomenon of total internal reflection, based on the difference in the refractive indices between the glass coverslip phase and the intervening medium (see section 2.4.1.2).

2.4.1.1 Comparison with Epifluorescence and Resolution

Wide-field epifluorescence is the oldest type of microscopy technique for detecting fluorescence and is still widely used. In wide-field microscopy the lens directly forms an image, which is then projected onto a camera or through an eyepiece. The resolution of epifluorescence microscopy is though suboptimal, because of the contribution of out of focus fluorescence, resulting in blurring of the image. A microscope for single-molecule studies needs to efficiently reject background light, which originates not only due to eventual presence of auto-fluorescence from the surroundings, but also due to Rayleigh scattering and inelastic Raman scattering of the medium around the target molecules.[44] Between the possible approaches, a common way of optically insulating the desired fluorescence signal is to restrict the number of excited molecules. Close to interfaces, this is possible by using illumination in conditions of Total Internal Reflection (TIR) of the excitation beam, thus creating a 50-100 nm thick standing wave close to the glass-solution interface and therefore excluding interrogation of fluorophores positioned further in the depth of the sample.

2.4.1.2 Total Internal Reflection (TIR)

At any interface, the Snell's law (eq. 2.9) regulates how light of an incident beam is refracted and reflected at the boundary between the two phases, depending on the incident angle θ (Figure 2.4).

$$\frac{\sin\theta_1}{\sin\theta_2} = \frac{v_1}{v_2} = \frac{n_2}{n_1} \tag{2.9}$$

In the Snell's equations above, v_1 and v_2 are the different propagation velocities of the incident (1) and transmitted (2) light waves, in the two different isotropic media, characterized respectively by the refractive indices n_1 and n_2.

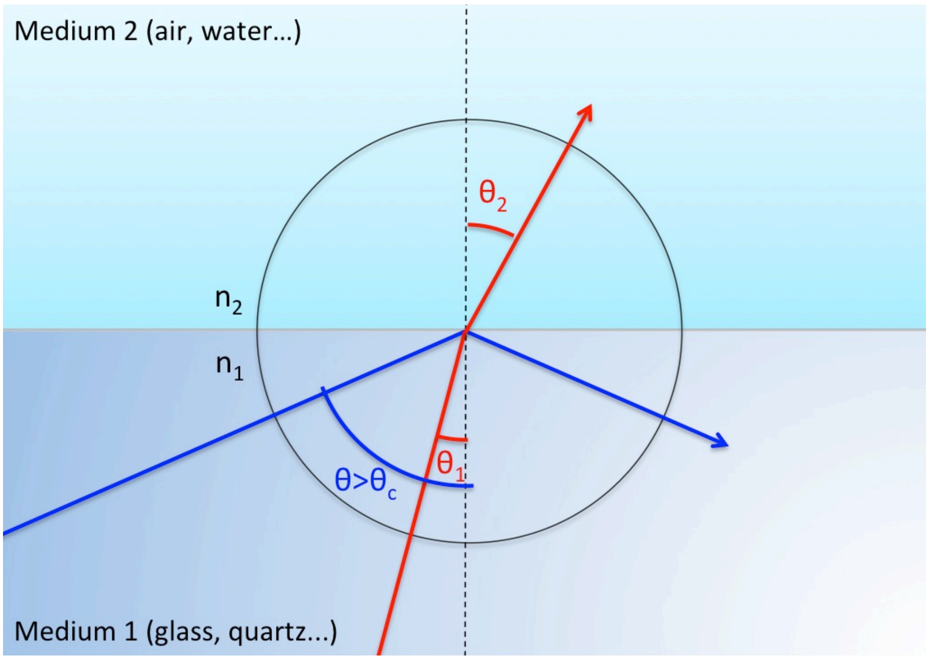

Figure 2.4: The refraction of light (red) and the totally internally reflected light (blue) at the interface between two media of different refractive indices with $n_1>n_2$.

For interfaces where $n_1 > n_2$, such as glass/water or glass/air, a specific critical angle called θ_c exists (Figure 2.4), for which θ_2 equals 90° (thus $\sin\theta_2 = 1$). At angles of incidence exceeding θ_c, the beam of light will be totally reflected from the glass/water interface, rather than pass through and refract, as in the schematic in Figure 2.5.

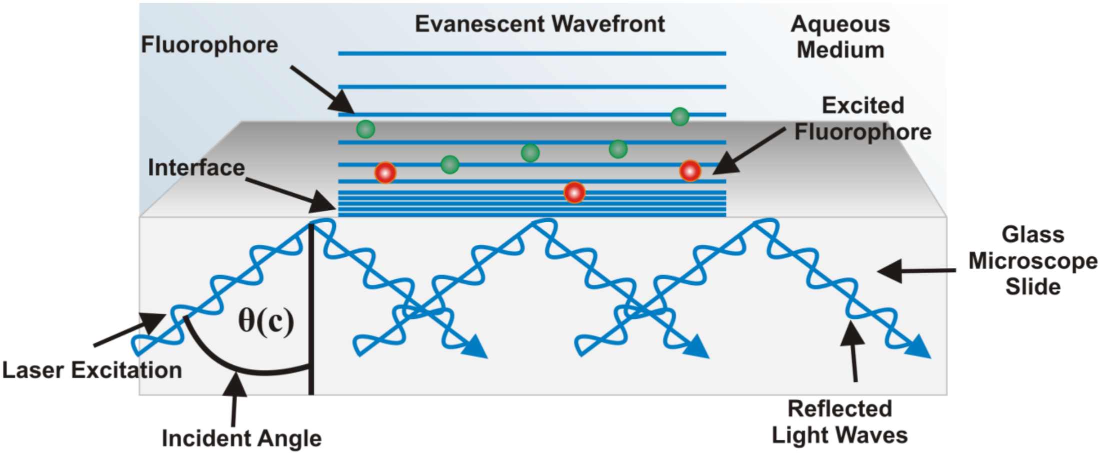

Figure 2.5: Schematic displaying the principles behind TIR mediated excitation. At angles above θ_c the incident light is reflected back into the high refractive index medium and an evanescent wave is propagated into the low refractive index medium, selectively exciting the fluorophores close to the interface.

At the glass/water and glass/air interfaces, the critical angle is respectively 41.2° and 61.2°, using the refractive indices $n_{air} = 1.00$, $n_{water} = 1.33$ and $n_{glass} = 1.518$.

$$\theta_c = \theta_1 \cdot \arcsin\left(\frac{n_2}{n_1}\right) \tag{2.10}$$

2.4.1.3 Evanescent Wave Profile

The total internal reflection of the light beam generates in the medium with lower index a very thin electromagnetic field (~100 nm), characterized by an identical frequency to that of the incident light. This excitation field, called ‘evanescent wave’, undergoes a simple exponential intensity decay with increasing distance $I(z)$ from the surface. The profile of the propagation in the lower index medium can be calculated, for any angle $\theta_i > \theta_c$ and wavelength combination, using eq. 2.10 and 2.11.

$$I(z) = I_0 e^{\left(\frac{-z}{z_0}\right)} \qquad (2.10) \qquad\qquad z_0(\theta_i) = \frac{\lambda_0}{4\pi}(n_1^2 sin^2\theta - n_2^2)^{-1/2} \qquad (2.11)$$

Typically for decay distance z_0 of the evanescent wave in the lower refractive index medium, the distance at which the intensity of the field is $1/e$ of the value at z=0, ranges between 50 and 200 nm, depending on the angle and λ of illumination.

2.4.1.4 Total Internal Reflection Fluorescence Microscope (TIRFM)

The basic components of a normal wide field epifluorescence microscope are an excitation source (a laser or a mercury lamp); a filter cube (containing excitation and emission filters and a dichroic mirror); a lens system/objective to focus the light on the focal plane; and finally a detector (an EM-CCD camera, an APD or a PMT connected to a computer for recording).

In TIRF microscopy, which was developed in the 1980s by Axelrod[116,128], a system to control the angle of incidence of the light on the surface is introduced. This enables to direct the laser towards the surface at angles exceeding θ_c so that the interface between the coverslip and the sample can be illuminated by means of an evanescent wave.

To achieve this, two main types of configuration exist: prism-based and objective-based (or through lenses) TIRFM, which are illustrated in Figure 2.6.

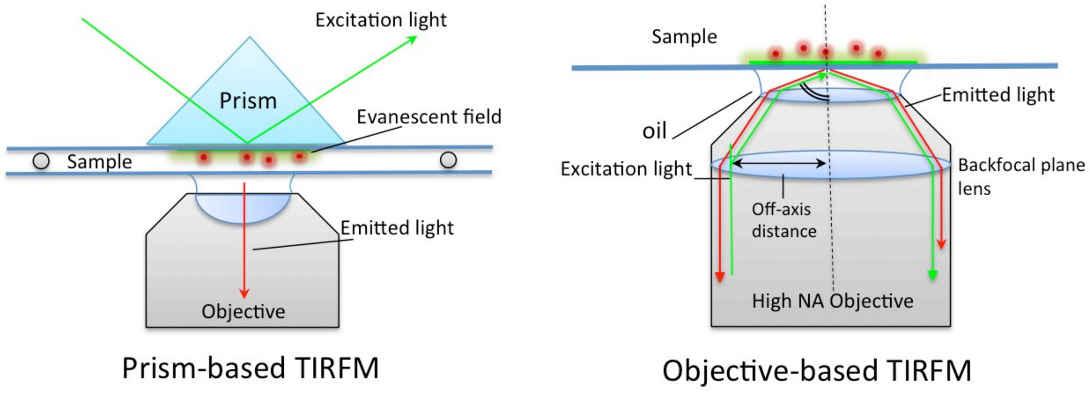

Figure 2.6: Schematic of the two types of TIRFM: prism- and objective-based configurations (drawing not to scale).

In the early TIRFM experiments, the desired illumination was achieved by directing the laser to the surface through a glass cube or a quartz prism.[128] In this configuration the prism adheres to back of the coverslip supporting the sample and the fluorescence is captured on the opposite side by approaching a microscope objective. This implementation offers advantages from the point of view of the illumination, which is more uniform, and allows collection only of the emitted light through the objective lens. However it is not very practical for experiments involving liquid samples. In particular, positioning of the objective on the surface opposite to the prism imposes restrictions on the size of the sample, which needs to be thinner than the working distance of the lenses (typically 0.1-2mm).[129]

In the 1990s, high numerical aperture objectives were developed that allowed the critical angle for TIRF microscopy to be achieved when a laser source was focused on the outer edge of the objective's back aperture. Objective-based TIRF allows increased flexibility, as the angle of illumination can be rapidly moved between epifluorescence and TIRF position and it allows switching between lasers of different wavelength connected to the microscope. Displacement of the laser on the back focal plane of the objectives, obtained through movement of a mirror in the light path, controls the angle of incidence of the laser on the surface. The maximum angle that can be reached is controlled by the objective's numerical aperture, with the simple relationship $n_{glass}(\sin\theta) = N.A.$

Objectives with N.A. up to 1.65 sapphire lenses have been designed,[50] however these required custom-made high refractive index coverslips and special matching oils to be operated.

The most commonly used TIRFM objectives have an N.A. of 1.45, which correspond to a maximum angle θ_{NA} of 72.8° on a glass lside with $n = 1.518$. Hence, since the θ_c required for TIR at the air and water interfaces are respectively 41.2° and 61.2° (see 2.4.1.1), such an objective is suitable to produce an evanescent field in both these intervening media.

2.4.1.5 Surface Plasmon Enhanced Fluorescence (SPEF)

An important additional phenomenon observed by placing fluorophores on metallic layers of thickness exceeding 10-20 nm, is the increase of the fluorescence signal occurring at specific angles of illumination.[117,130,131] This is a very counter-intuitive effect, as increasing the metal thicknesses the fluorescence collected increases, while the metallic film becomes increasingly opaque.

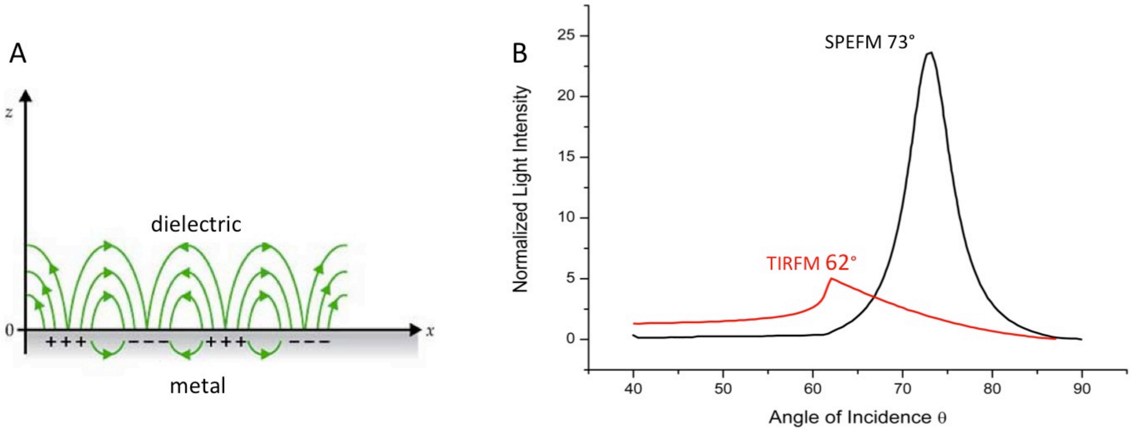

Figure 2.7: A) Schematic representing the surface plasmon waves at the interface between a thin metallic layer and a solution. B) Excitation field enhancement calculated with CPS theory for a silver film: light intensity measured at the substrate/sample surface vs. incident angle for a bare glass slide (red line) and a glass slide covered with a 40 nm silver thin film (black line). The excitation wavelength is 532 nm. The refractive indexes are for glass 1.51, for silver 0.13 + 3.25i and for water sample 1.33.

The increased emission is due to excitation of the surface plasmon of the metal with the incident laser waves at a specific angle, called θ_{SP}. When the laser reaches the surface with the angle θ_{SP}, the intensity of the electromagnetic field at the surface will be increased of several folds and with it the excitation of the fluorophores residing in the volume. The theory of Surface-Plasmon Enhanced Fluorescence (SPEF) for fluorescence spectroscopy and microscopy have been extensively reviewed by Knoll [132,133] and by Fort.[118]

In particular silver and gold films have been used to reach SPE, thanks to their optical properties. For example, a layer of silver of 40 nm deposited on the glass coverslip enhances the fluorescence signal and acts as an additional emission filter for the emitted light to reduce the background noise, improving the quality of the image.[134] The variable angle illumination installed in a TIRF microscope can be easily employed to excite plasmon waves, provided that the objective has sufficient N.A.[134,135] For silver surfaces the angle of occurrence of SPR enhancement is about 10 degrees higher than the critical angle for TIRF (Figure

2.7B) as calculated by Fort[118,135] using the theory, developed in the 70's by Chance Prock and Silbey (CPS).[119] These authors solved the Maxwell's equation for the boundary condition of a point dipole located in proximity to a semi-infinite planar surface with a certain refractive index $n(\omega)$, being able to compute the lifetime of the dipole as a function of the distance away from the metal.[119]

Chapter 3

Theory: Electrochemistry

3.1 Introduction to Electrochemical Methods

Electroanalytical techniques have been widely used in this thesis for the characterization of the fluorescent redox bioswitches immobilized on the electrode surface. In particular cyclic voltammetry (CV) was used to evaluate the number of molecules on the surface and their surface behaviour.

As any electroanalytical technique, CV can be used to address electron transfer (ET) from redox active molecules that are either diffusing in solution (heterogeneous ET) or immobilized on the surface (homogeneous ET).[136] As mentioned in the first chapter, the second case is particularly convenient for the study of proteins as sluggish kinetics due to due to diffusion and adsorption/desorption processes can be avoided and smaller quantities of biological samples can be used.[14,137,138]

3.2 Cyclic Voltammetry(CV)

CV of irreversibly adsorbed films is a powerful method for probing the chemistry of redox-active sites in metalloproteins. Immobilization of the electroactive species affords precise potential control over a tiny quantity of material that is manipulated at the interface between an electrode and an electrolyte solution, providing also information on ligand- or metal-exchange reactions coupled to electron transfer.[138]

As mentioned in the first chapter, this technique gives remarkable advantage in the study of Direct Electron Transfer (DET) for proteins, such as the removal of contributions from the solution diffusion processes and the use of smaller sample quantities. DET can occur if the protein redox cofactor is favourably connected to the electrode; in PFV, and by chemical means the adsorption of the protein on the surface can be designed to offer optimal orientation and increased electronic coupling.

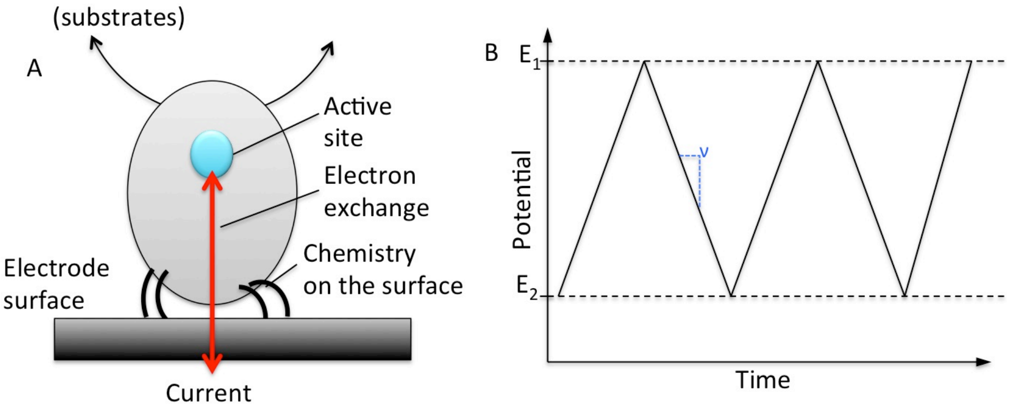

Figure 3.1: A) Schematic illustrating the positioning of a metalloprotein bound in DET on an electrode surface. B) Diagram describing the potential triangular wave applied in CV, the potential is varied linearly between E_1 and E_2 with a scan rate $dE/dt = v$.

For the general electrochemical reaction $\mathrm{O_{ads}} + ne^-_{(m)} \rightleftharpoons \mathrm{R_{ads}}$, where $\mathrm{O_{ads}}$ is the oxidized and $\mathrm{R_{ads}}$is the reduced species, the equilibrium potential, E_e, can be given by the Nernst equation.

$$E_e = E^\theta + \frac{RT}{nF}\ln\frac{a_o}{a_r} \tag{3.1}$$

Where E^θ is the standard equilibrium potential where all species have unit activity; R is the ideal gas constant, F is the Faraday constant and a_O and a_R are the activities of the oxidised and reduced species respectively.

In first instance CV can be imagined as a method in which the potential of the electrode is varied linearly at a certain scan rate ν (in $\mathrm{V\,s^{-1}}$), between two extremes values E_1 and E_2, as shown in Figure 3.1B; Nowadays, CV is often performed in digital modes the smooth voltage ramp being replaced by a series of small steps similar to a chronoamperometric step (next section). The resulting current is recorded at each potential value, after the decay of the capacitive current at half the duration of the potential step .

The total current passing is composed of two elements: the Faradaic currents due to charge transfer (i_F), and currents due to non-Faradaic or capacitive (i_C) processes.

$$i = i_c + i_F \tag{3.2}$$

Faraday's law states that the amount of chemical reaction caused by the flow of current is proportional to the amount of electricity passed, therefore the Faradaic current relates directly to the redox state of the surface confined molecules. During the potential sweep, when the electrode potential reaches the energy level for the reduction or oxidation of $\mathrm{O_{ads}}$ and $\mathrm{R_{ads}}$, the electrons start to flow to/from the protein redox centres, resulting in a current peak.

Non-Faradaic processes instead can produce external currents when the potential, electrode area or solution composition changes.

For an ideal population of strongly physisorbed molecules, reversibly exchanging one electron with the surface and investigated at a slow ν, the ratio of oxidized and reduced species will remain equal to the equilibrium value at each potential, as predicted by the Nernst equation. It is therefore said that i_F has a 'Nernstian' behaviour, as shown in Figure 3.2.

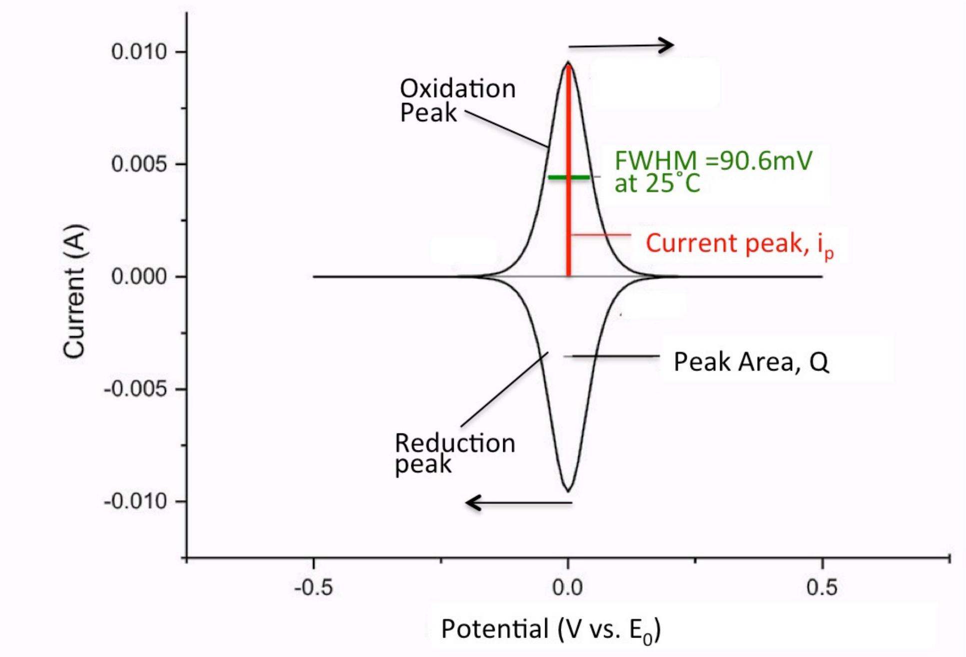

Figure 3.2: Ideal Faradaic currents for a cyclic voltammogram of a strongly adsorbed redox reversible species, obtained by simulation of the Nernst equation with n=1 and $\Gamma = 10\mathrm{x}10^{-9}$ *mol/cm*^{2}.

The main pieces of information that are provided by CV are:

- Electron transfer number:

for a species in solution $\Delta E = \mathrm{E_{pa}} - \mathrm{E_{pc}} = 58/n$, with n being the number of electron transferred per mole. For an adsorbed molecules population, in

Nernstian equilibrium, the ideal peaks width at half maximum (FWHM) is $3.53RT/nF$, i.e. 90.6 mV at 25° C for a one electron transferred and 45.3 mV for a two electron process.

- Standard redox potential:

The position of the anodic and cathodic peaks also provides the formal potential, which is calculated as $E^{0\prime} = (\mathrm{E_{pa}} + \mathrm{E_{pc}})/2$.

- Molecular adsorption:

A clear signature of surface confinement of the redox molecules is the linear variation of the peak current with the ν applied, while for diffusive voltammetry the maximum peak current varies with $\nu^{1/2}$.

- Number of absorbed molecules:

As illustrated in Figure 3.2, the Faraday charge (C/cm^2) can be extracted by integration of the Faradaic current peak at each potential after subtraction of the baseline of the capacitive currents; thus the surface coverage Γ is obtained dividing Q by the Faraday constant and A_{el}, the area of the electrode:

$$\Gamma = \frac{\mathrm{Q}}{\mathrm{nFA}_{el}} \tag{3.3}$$

- Measurements of kinetic rate constants:

as ν is increased the Nernstian conditions are not fulfilled anymore and the peaks start to separate. The rate of departure from the original position depends on the kinetic limitation of the ET between the electrode and the redox centres immobilized on it. From the Butler-Volmer equation the rate constants for the anodic and the cathodic electron transfer are:

$$k_a = k_a^0 \exp\left(\frac{\alpha_a nFE}{RT}\right) \quad (3.4) \qquad k_c = k_c^0 \exp\left(\frac{\alpha_c nFE}{RT}\right) \quad (3.5)$$

where α_c and α_a are the cathodic and anodic electron transfer coefficients, describing the symmetry of the reaction. For simple electron transfer processes $\alpha_a + \alpha_c = 1$, with their value commonly close to 0.5.

- Stability in oxidized and reduced forms and reversibility of electrochemical reaction:

The presence of coupled chemical reactions can be evaluated from the disappearance of the electrochemical peaks corresponding to the oxidation or the reduction and the reversibility can be evaluated depending on the peak-to-peak separation ΔE. In Nernstian regime ΔE should be zero, as shown in the simulation in Figure 3.2. However for protein monolayers, even at slow ν, a so-called 'Unusual Quasi Reversibility' (UQR) is often observed, consisting in a small residual peak-to-peak separation (typically 10-20mV).

3.3 Other Electro Analytical Techniques Used

3.3.1 Chronoamperometry (CA)

Other electrochemical techniques used in this thesis are chronoamperometry, (CA) and square wave voltammetry (SWV). In CA, the potential is simply instantaneously changed from E_1 to E_2, as shown in Figure 3.3. If the potential jump contains the midpoint potential of the adsorbed molecule, the measured currents will contain both fast capacitive component and a Faradaic component. For surface confined molecules, the decay constant of the exponential, measured after the initial rapid decay of the capacitive currents, is the rate of electron transfer, k_{ET}, at the applied over potential η. The k_{ET} at $\eta=0$ can be inferred using a Tafel plot, by plotting $\ln(k_{ET})$ vs. η and extrapolating to zero.

3.3.2 Square Wave Voltammetry (SWV)

SWV is a linear sweep technique in which a square wave is superimposed on the scan of the potential between E_1 and E_2 (Figure 3.3). The current is measured at the end of each square step for a forward and a backward scan and the difference of the two currents is plotted against potential. This allows minimization of the non-Faradaic capacitive background with respect to the Faradaic components, thus increasing the signal to noise ratio of the measurement. As the Faradaic signals of proteins are often weak, SWV, which is more sensitive than CV, is useful to determine the thermodynamic potential of the bioelectrochemical redox couples.

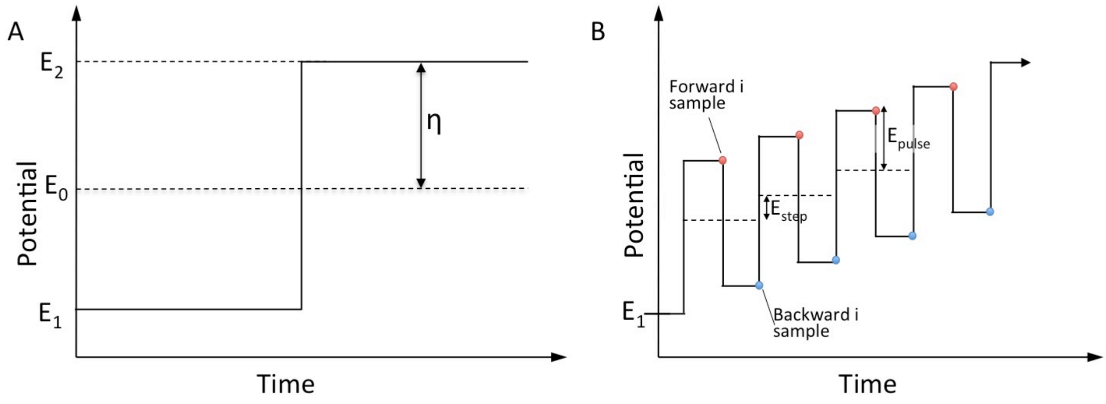

Figure 3.3: Diagrams representing the potential applied during (A) chronoamperometry and (B) asquare wave voltammetry.

3.3.3 Electrochemical Impedance Spectroscopy (EIS)

In Electrochemical Impedance Spectroscopy (EIS) a sinusoidal potential perturbation with a small (~10mV) amplitude ΔE is superimposed on a constant potential E, $E = \Delta E \sin(2\pi f t)$ and the current is monitored while varying the frequency of the modulation. The sinusoidal current response has also the same frequency of the applied potential: $i = \Delta i \, sin(2\pi f t + \phi)$, but is different in amplitude, Δi and in phase, ϕ.

The relationship between the alternating E and the resulting i is given by the impedance of the system, Z^*, a complex quantity determined by the elements in the electrochemical cell (capacitors and resistors) and their connection to each other. These elements can be extrapolated by fitting the obtained impedance plots to the appropriate Randles circuit, representing the equivalent circuit of the system.

In most cases the impedance, Z^*, which is a complex quantity ($Z^* = Z' + iZ"$) , is reported as a function of the frequency f (10^{-3} to 10^6 Hz) using the Nyquist plot, a polar diagram of the transfer function, G(s) with s = j**ω**, displaying both amplitude and phase angle on a single plot, using frequency as a parameter: Z'' vs. Z' form a semicircle as in Figure 3.4A . Other common ways to represent impedance data are the Bode plots, with frequency as the horizontal axis separate plots to display amplitude and phase of the frequency response in Figure 3.4B and C or alternatively the real and imaginary components of the impedance.

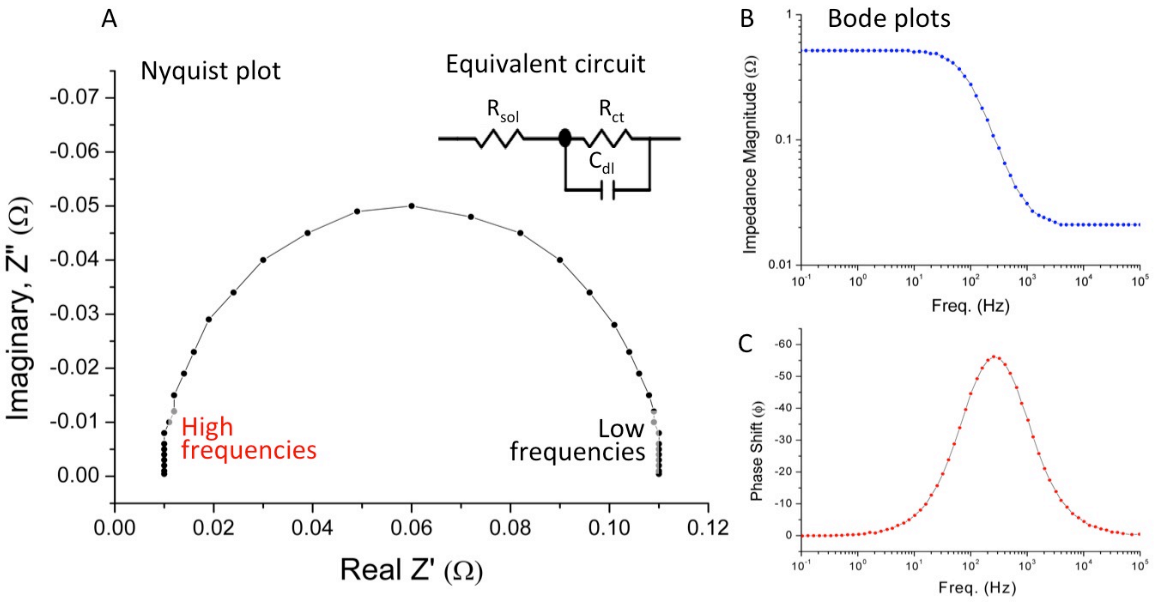

Figure 3.4: Simulation of Impedance Nyquist (A) and Bode plots (B nd C) for the indicated simple RC circuit where R_{sol} = 0.01 Ω, R_{ct} = 0.1 Ω and C_{dl}= 0.02 F, using Ecochemie FRA software.

3.4 Theory of biological electron transfer

Natural evolution selected biological electron transfer proteins that have redox centres buried in an insulating protein structure. The protein dielectric is thus shielding and tuning the electron pathways, e.g. to avoid unwanted redox reactions with the surroundings.[139] In many cases this feature of biological redox centres makes it more difficult to electrically contact them on artificial devices such as electrodes surfaces, since the cofactors are typically only weakly electronically coupled with the surface.[139] This means that the transition state for the ET reaction must be formed many times before there a successful conversion of the reactants into products can occur.[140]

According to the semi-classical approach proposed by Marcus[141], the electron transfer from a donor to an acceptor at fixed space and orientation, occurs at a rate which depends on only three parameters: [142]

- Driving force applied $-\Delta G^0$;

- Reorganization energy of the redox molecule λ, which reflects the extent of outer-sphere and inner sphere nuclear rearrangement that accompanies charge transfer;
- Electronic coupling between the redox centre and the surface H_{AB}^2

In this Marcus treatment the rate of electron transfer from a redox centre to an electrode is given by:

$$k_{ET} = \frac{2\pi}{h} H_{AB}^2 \, FC \tag{3.6}$$

where h is the Planck's constant and FC is the nuclear Franck-Condon factor, which describes the nuclear motion involved in the electron transfer process. For a given reaction, the FC factor is determined by the values of ΔG^0 and λ:

$$FC = \frac{1}{\sqrt{4\pi\lambda k_B T}} \, e^{\left[\frac{-(\Delta G^0 + \lambda)^2}{4\lambda k_B T}\right]} \tag{3.7}$$

For the electron transfer to occur the reorganization of the nuclei in the molecule, represented by λ must be compensated for by the applied driving force. Figure 3.5 describes the variation in k_{ET} as function of $-\Delta G^0$.

As is apparent from equation 3.7, under conditions where $-\Delta G^0 < \lambda$, k_{ET} increases with increasing driving force ($-\Delta G^0$). This behaviour is often referred to as the 'normal' region. Somewhat counter-intuitively though, when $-\Delta G_0$ exceeds λ , the so-called 'inverted' region, a further increase of the driving force results in a decrease of k_{ET}.[143]

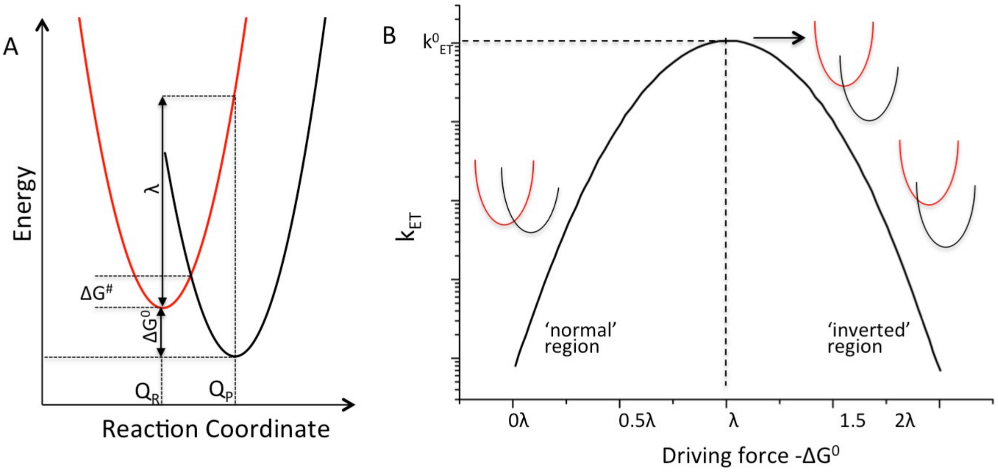

Figure 3.5: A) Diagram of the potential energy for ET between the reactants R, resulting in the formation of products P. The relationship between ET, -ΔG^0, λ and the activation energy -$\Delta G^{\#}$is indicated. B) Driving force dependence of the non adiabatic k_{ET} as predicted by Marcus semiclassical theory[143]. The maximum k_{ET} value is reached for λ=-ΔG^0, when the activation energy -$\Delta G^{\#}$ is zero. For lower -ΔG^0, k_{ET} falls in the 'normal region'. Likewise the decrease in k_{ET} for -ΔG^0>λ is referred to as the 'inverted region'.

The maximum k_{ET}, k_{ET}^0 is reached when the nuclear exponential term in eq. 3.7 is optimized, i.e. when -ΔG^0 is equal to λ (Figure 3.5). In these conditions k_{ET}^0 is limited only by the electronic coupling of the redox centre with the surface, H_{AB}, which can be controlled by tuning the distance and the intervening medium between the two-redox centres. An important tool for controlling electronic coupling in investigations of surface confined biological and inorganic redox centres is represented by use of compact layers formed by alkylthiol chains bound at gold surface, as presented in the next section.

Chapter 4

Materials and Methods

4.1 Instrumentation

4.1.1 Fluorescence Microscope

All the fluorescence microscopy experiments were carried out using a Nikon TE2000-E inverted microscope (shown in Figure 4.1), equipped with a TIRF module for the deflection of the laser in the x and y direction from the normal to the sample. A schematic of the light path internal to the microscope is presented in Figure 4.1B. In addition to the magnification of the objective a further 150x magnification internal to the microscope was used.

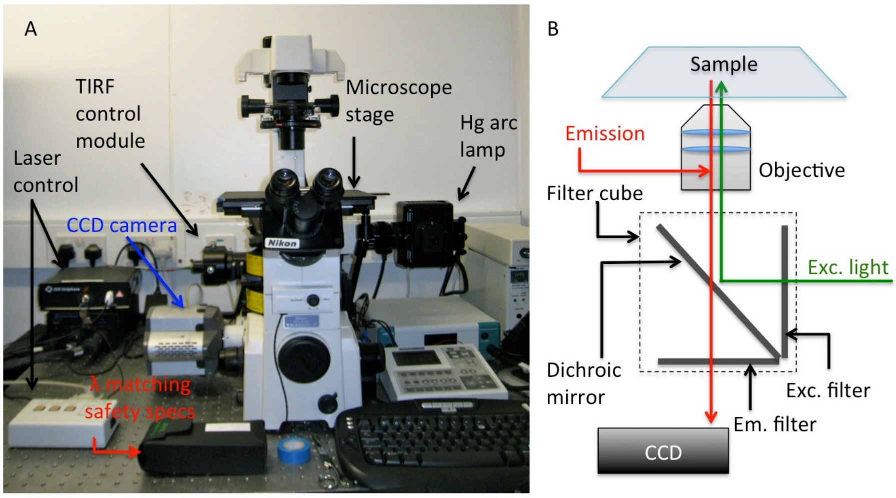

Figure 4.1: A) Nikon TE2000-E with light sources and laser lines controls labelled. B) Simple graphic of the elements in the light path of the fluorescence microscope.

4.1.1.1 Microscope Objectives

The microscope was provided with three objectives, whose magnification, working distance and numerical aperture are summarized in Table 4.1.

TIRF microscopy was performed with a 'TIRF' Plan Apo 100x 1.45 oil immersion objective. This objective can be used in the classical epifluorescence mode, or alternatively, can be employed for objective-based TIRF illumination. A manually operated micrometre allowed deflection of the laser starting from the position used for epifluorescence, in which the laser orthogonally strikes the sample surface, proceeding towards the maximum angle θ_{NA} allowed by the objective, after which only environmental noise can be detected (see chapter 5).

Magnification	N.A.	WD (mm)	Obj. type	Illumination mode
4x	0.2	15.5	Air	BF, Epi
20x	0.75	10	Air	BF, Epi
100x	1.45	0.13	Oil immersion	BF, Epi, TIRF

Table 4.1: List and parameters of the objectives used. Illumination types abbreviated as BF= bright field Epi=epifluorescence.

4.1.1.2 Illumination Sources

Besides the bright field illumination lamp used for optical transmission imaging, the microscope was connected to the following illumination sources for fluorescence excitation:

- A Super high pressure Mercury Arc lamp,
- Blue Argon Laser, 488 nm (50 mW, CW, Spectra Physics),
- Green Argon Laser, 532 nm (5 mW, CW, Melles Griot)
- Red HeNe Laser, 633 nm (20 mW, CW, JDS Uniphase)

In TIRF experiments only the lasers illumination sources were used. The light was delivered from the lasers bed to the microscope using a multimodal optical fibre.

4.1.1.3 Filters

The use of filters in the optical path allows restricting the collected light in and out to the frequencies of interest. The filters available on the microscope used for this research are listed in Table 4.2.

	excitation λ (nm)	**Dichroic λ (nm)**	**Emission λ (nm)**
FITC	450-495	>505	515-555
TRITC	530-560	>570	580-690
G1-B HYQ	540-550	>565	590 (long pass)
HQ-Cy5	590-650	>660	660-740

Table 4.2: List of available filter blocks.

4.1.1.4 Image Capture

Fluorescence images were recorded using a back illuminated, EM-CCD camera (iXon DV888x, Andor, Belfast, UK). The sensor chip was an array of 512×512 $pixels^2$, each pixel measuring $16 \times 16\ \mu m^2$. The camera was cooled with a Peltier chip to -70 °C during all the duration of the acquisitions to minimize the noise.

With the 100x TIRF oil-immersion objective, each pixel corresponded to an imaged area on the sample of $0.106 \times 0.106\ \mu\text{m}^2$, as confirmed by imaging of fluorescent microbeads. Hence for TIRF measurements with red laser illumination (633nm), the size of a diffraction limited spot, limited by $\lambda/2$, corresponds to $\sim 3 \times 3$ pixels.

Time-lapse series of images were acquired using the software Andor Solis (version 4.18.3) in the kinetic mode and recorded in the 'sif' format. For kinetic acquisitions (see chapter 6) exposure times were typically 50-200 ms, each acquisition had typically 100-500 frames and the EM-CCD gain was set at 200 unless stated otherwise. Analysis of the time-lapses acquired with Andor Solis was performed using MBF_Image J for microscopy v.1.45 (written by Waybe Rasband and freely available at http://www.macbiophotonics.ca), MatLab v. 2009b and Origin v. 8.0.

4.1.1.5 Electrochemical Equipment

All CV electrochemical experiments were performed using a three-electrode cell (Figure 4.2).

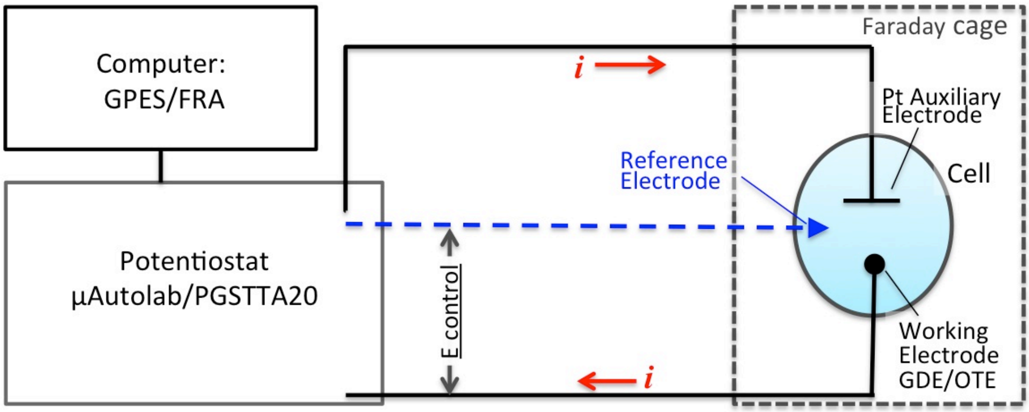

Figure 4.2: Schematic of the three electrodes cell used in all electrochemical measurements (the geometry of the cell is symbolic).

For experiments combining fluorescence microscopy and electrochemistry, a particular setup was employed (see section 4.1.1.6), controlled by a potentiostat µAutolab III (Ecochemie, NL).

Impedance measurements (EIS) were performed on an Autolab potentiostat PGSTAT20 (Ecochemie, NL) equipped with an ADC750 and a FRA (frequency response analyser) module, controlled by a computer where data were stored.

AC frequencies ranged from 1 MHz to 10 mHz, with amplitude of 10 mV. The complex Z^* (impedance) function was converted into C^* (capacitance) through the physical definition between them, i.e. $Z^* = 1/j\omega C^*$ in which ω is the angular frequency.

General Purpose Electrochemical System software (GPES v.4.9) and FRA were used for the electrochemical data acquisition and post processing.

All potentials for studies on Az, in chapter 5, 6 and 7 were measured versus a saturated calomel reference electrode (SCE, BASi); a saturated Ag/AgCl (BASi) reference was used in experiments in chapter 8 on laccase and flavoproteins.

In all cases platinum gauze was used as auxiliary electrode. All solutions were de-aerated by bubbling argon through the solution for at least 20 minutes before use and were kept under a blanket of argon throughout the experiment where this was possible.

In all "classical" electrochemical experiments a Faraday cage was used to eliminate any electrical noise. When combining the electrochemistry with the fluorescent microscopy as in the next paragraph this was not possible.

4.1.1.6 Fluorescent Cyclic Voltammetry Cell

In order to combine electrochemistry and fluorescent microscopy a three electrodes cell was built on the cover slides on the inverted microscope as illustrated in the schematic in Figure 4.3.

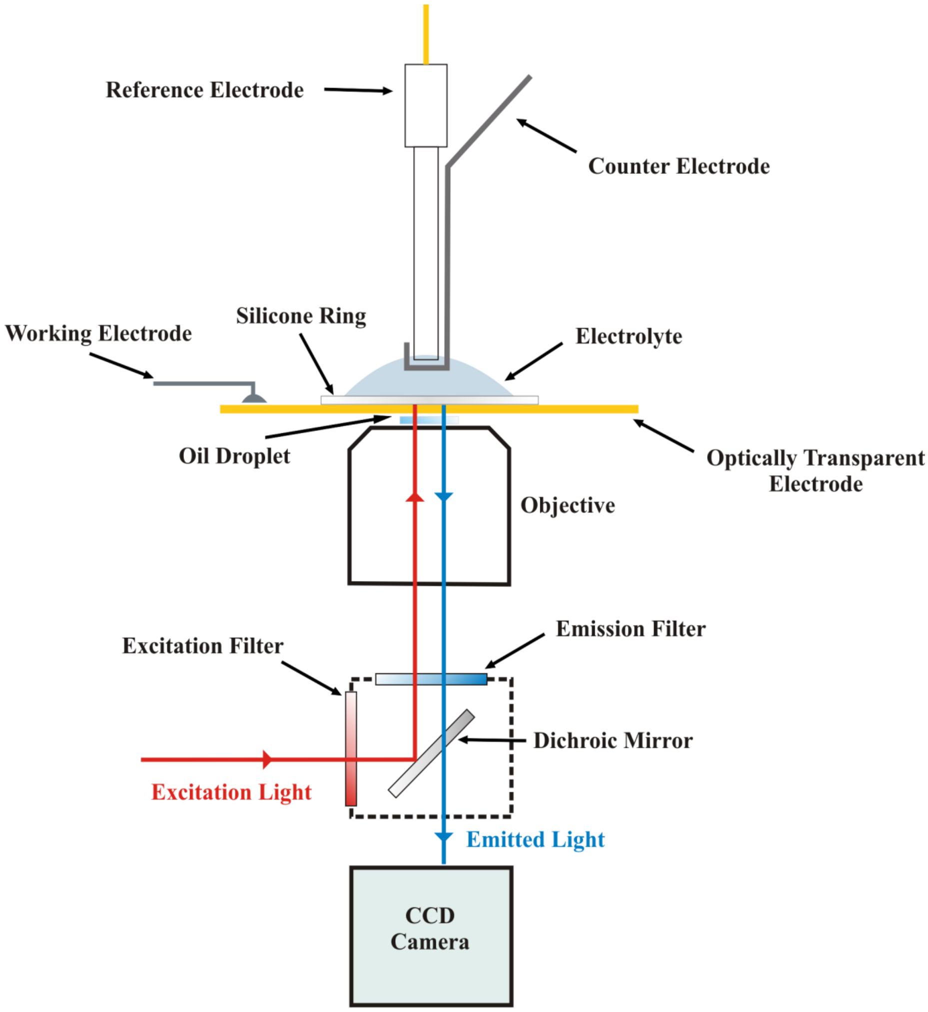

Figure 4.3: Schematic of the FCV setup and constituting parts.

- Data Synchronization

A Labview interface (N-NI Instruments, v8.6), connected to the potential output of the μAutolab potentiostat and to the computer controlling the EMCCD acquisition, was used to record the potential traces “Data Time Stamp”. These were used to synchronize the electrochemical data with the optical acquisition as discussed in Chapter 5 in post processing.

- Image Analysis Software

Post capture data analysis was carried out using Andor Solis software and Image J for Windows, equipped with MBF plugins suite (available at http://www.macbiophotonics.ca/imagej). Andor supplied additional plugins for the import and analysis of the sif files. Matlab2009 and Origin 8.0 were use in the analysis.

4.1.2 Complementary Techniques

4.1.2.1 Atomic Force Microscopy Imaging

Tapping Mode Atomic Force Microscopy (TM-AFM) was carried out using either a DI AFM (Digital Instruments, Veeco, US) with an IV controller and a 'JV' (J(AS-130)) vertical engage scanner or a JPK Nanowizard (JPK, Germany).

TM-AFM was carried out in air in intermittent contact (tapping) mode using MikroMasch (series 15 NS15/No A1) tapping tips, with an average frequency of 325 kHz.

Data analysis and post capture image processing was performed with the open software for SPM image analysis Gwyddion (v. 2.25 for Windows, available at http://gwyddion.net/).

4.1.2.2 Contact Angle

Contact angles were determined by the stationary sessile drop technique on an FTA1000B (First Ten Angstrom Inc.) goniometer at room temperature and ambient humidity. The contact angle was measured by forming a 20 μL drop at the end of a blunt-ended needle, lowering the drop to the surface, and removing the needle. The data were averaged over five readings taken at different locations on any given SAM-modified OTE.

4.1.2.3 Mass Spectrometry

LC-MS (Waters ZMD with Agilent 1050 HPLC system) of the labelled Az samples could be obtained by running for 25 minutes the 5 μM protein samples in a linear gradient of 5 mM $HClO_4$/acetonitrile from 25 to 75% on a hydrophobic HPLC column (C4, Agilent). The Waters LC-MS was equipped with an electrospray ionization unit (ESI) and a Time Of Flight (TOF) detector. Analysis of the adjacent m/z peaks was performed using the software for LC-MS, MassLynx MS v.4.1.

4.1.2.4 UV-Visible and Fluorescence Spectroscopy.

A Shimadzu UV-2401 spectrophotometer was used in the acquisition of spectra in the ultra violet and visible wavelengths range. Fluorescence spectra were recorded using a Varian Cary Eclipse fluorescence spectrophotometer, either in spectral or in the kinetic mode.

All fluorescence and UV-Vis. measurements on protein samples were acquired using a 100 μl quartz cuvette (Sub-Micro Cells, type 26, Starna, US) with a 10 mm light path.

Spectra of protein solutions were measured in aqueous buffers (typically 100 mM phosphate buffer, pH7.0) and the spectrum of the buffer alone recorded prior to each measurement was used as a baseline.

Characterization of the transparent conductive films, deposited on borosilicate glass or quartz slides as detailed in sections 4.2.1.1 and 4.2.1.2, was performed in air, by placing a freshly cleaned sample on a custom designed magnetic support, so that the light beam was normal to the active surface. A freshly cleaned slide of the corresponding supporting material (borosilicate glass or quartz) was used as the reference.

4.2 Materials

4.2.1 Substrates, Optically Transparent Electrodes OTE

4.2.1.1 Gold Optically Transparent Electrodes

In preparation to deposition of the gold film, the borosilicate cover slides were carefully cleaned, first by sonication in acetone for 15 minutes, followed by rinsing with ethanol and then water, dried under a dry nitrogen flow and finally plasma cleaned. The gold optically transparent electrodes (Au-OTE) were prepared by resistive heating evaporation of 10 nm gold on a 2 nm chromium adhesion layer, supported on the freshly cleaned glass slides (thanks to Dr Rob Jacobs, CRL, Oxford University). Until use the samples were kept between lens cleaning tissues in a sealed container in order to prevent deposition of dust on the surface.

Samples used for the experiments on surface plasmon fluorescence enhancement (presented section 9.1) were similarly produced by thermal evaporation of Ag (50 nm) and Ag (40 nm) followed by Au (10 nm) on a chromium adhesion layer of 2-3 nm, by Olivier Loison (Prof. E. Fort group, EPSCI, Paris).

4.2.1.2 Carbon Optically Transparent Electrodes

Carbon optically transparent films (C-OTE) were obtained following Donner's procedure[144] by pyrolysis of the positive photoresist AZ P4330-RS (Clarian), diluted with 1-methoxy-2-propanol acetate to 25-30% (v/v). The mixture was spin coated onto quartz cover slips (see 4.2.1.3) at 6000 rpm for 30 s in a vacuum spin coater and “soft baked” at 110 °C for 60 s on a hot plate. The films were finally pyrolyzed in a furnace at 1100 °C for 1 hour in a reducing atmosphere (N_2:H_2, 85%:15%), (the last step was kindly carried out by Michael Pitcher, in Dr Simon Clarke group, ICL, University of Oxford). Pyrolyzed photoresist films (PPF) were used after three days, to allow equilibration of the surface groups.

4.2.1.3 Glass and Quartz Cover Slides

All the cover slides used in TIRF microscopy experiments and for Au-OTE production had a #0 thickness (Menzel-Glaser, 0.085 - 0.130 mm, 25 mm ø). Quartz slides (0.090 - 0.110 mm thick, 12 mm ø) were purchased from Agar Scientific, jointly with thicker glass cover slides used in non-TIRF experiments, #1 (0.130 - 0.160 mm thick, 22×64 mm^2) and #1.5 (0.155 - 0.185 mm thick, 22×64 mm^2).

4.2.2 Protein Samples

Wild type and N42C-Az were produced during a visit to Gorlaeus Laboratories in Leiden following the procedure detailed by Van de Kamp.[145] The presence of a surface exposed thiol N42C samples was checked performing an Ellman’s titration with the reagent DTDP.

The Az holo-dimers were reduced with sodium dithionite, filtered to remove the reducing agent, and successively reacted with DTDP as described by Riener.[146] The concentration of cysteine on the surface of the reduced N42C were determined using a triple point calibration curve (Figure 4.4), obtained by monitoring the released 4-thiopyridone at 324 nm, upon reaction with cysteine standard solutions, using the extinction coefficient of ε_{324}= 21400 $M^{-1}cm^{-1}$.[146]

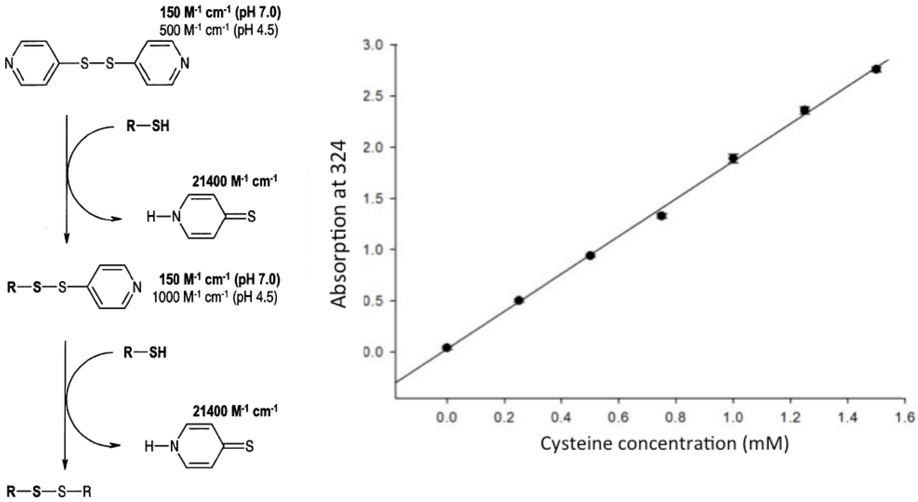

Figure 4.4: The reaction of DTDP with thiols and the cysteine calibration curve used.

Wild type and N42C-Az in their zinc and copper reconstituted forms were purified, and the concentrated stock solutions (~1 mM) were frozen in liquid nitrogen and stored in 20 mM MES buffer at pH7.0 at a temperature of -80 ˚C until use.

Native fungal laccase A, purified from cultures of the fungus *Trametes versicolor*, was kindly donated by Prof Dennison group in Newcastle Upon Tyne University.

Both Az and laccase were aliquoted and stored at -80 ˚C until needed.

Flavodoxin from *Desulfovibrio vulgaris* was kindly supplied by Prof F. Gilardi group (University of Turin). The samples of other flavoproteins tested (in section 7.3.1) were generously donated by Prof Luet Wong (University of Oxford).

4.2.3 Chemicals and Solvents

All chemicals used were of analytical grade (Sigma Aldrich or Pierce Thermo unless stated otherwise), and were subjected to no further purification. SAM forming solutions were freshly prepared prior to each experiment in HPLC-grade ethanol.

4.2.4 Water and Aqueous Solutions

De-ionized water with a final purity of 18.2 MΩcm was used throughout the experiments, obtained by filtration through an Elix 3 and Synergy 185 Millipore system (Millipore ltd, UK). Aqueous buffered solutions, mainly phosphate buffer (PB) and MES, were prepared with the appropriate chemicals, brought to the desired pH by addition of NaOH or HCl, and frozen. Thawed aliquots were stored at 4°C for not longer than a week.

4.3 Methods

4.3.1 Samples Preparation

Classical CV and where needed SWV were performed in a single compartment three electrode cell on conventional polycrystalline gold disk electrodes (GDE, Cypress system, 1 mm diameter) to test the electrochemical signature of all the labelled proteins before proceeding with the experiment combining EC and TIRFM.

4.3.1.1 Electrodes Cleaning Procedures

The GDEs surface was cleaned using a procedure well-established in the lab.[147] Briefly the GDEs were first manually polished for a few minutes using polishing cloths (Buehler, MicroCloth, in order 3, 1 and 0.3 μm) wetted with MilliQ water, until a mirror-finish was reached. Between each successive polishing step the GDEs were sonicated for periods of ~2 minutes in MilliQ water.

Mechanical treatment was followed by electrochemical polishing with ~50 CV scans between -0.5 V and ca. 1.3 V vs. SCE at 100 mVs^{-1} in 0.5 M H_2SO_4 (aq), repeated until CV currents stabilized. The surface area of bare gold can be calculated from the area of the anodic peak in the electropolishing scan using equation 4.1.[148]

$$A_{el} = \frac{Q}{482 \times 10^{-6}} \tag{4.1}$$

Following the electrochemical polishing any residual oxide was removed from the gold surface by reductive stripping with five linear sweeps from -0.5V to -1.3V vs. SCE in the same 0.5M H_2SO_4 aqueous solutions.

Au-OTE were cleaned by immersion for 30 seconds in freshly prepared hot Piranha solution, obtained by adding one part of H_2O_2 to three parts of H_2SO_4.

Caution: Piranha is extremely dangerous, reacts violently with organic materials and must be handled always under a chemical fume hood and using full protection (goggles, heavy gloves and labcoat). In the preparation take care to always add the hydrogen peroxide to the sulphuric acid and not the other way around and make sure that there is no trace of organic solvent on the glassware used for handling the solution

as this can result in explosive reactions. Dispose by diluting in abundant water in the sink.

After treatment in Piranha, the Au-OTEs were thoroughly rinsed with water and ethanol and moved to the SAM forming solution.

C-OTEs were cleaned with different procedures in order to establish the best conditions for Az physisorption. These included: treatment with UV lamp (oxidation), sonication in organic solvents and soaking in suspension of activated carbon sonicated in dry acetonitrile.

Silver OTEs cannot be treated with Piranha solution due to the presence of the easily oxidised silver layers, these surfaces were simply thoroughly rinsed in ethanol and dried under nitrogen flow before SAM formation.

4.3.1.2 SAM Formation

Surface modification with the SAM was obtained, for both the GDEs, the Au-OTEs and the Ag-OTEs, by immersion for 12 hours in 1 mM solutions in ethanol of the desired alkanethiol. 1-hexanethiol, 1-octanethiol, 1-decanethiol, and 1-dodecanethiol were used for Az physisorption, while 11-mercaptoundecanoic acid (MUA) was used to covalently link laccase and to form a negatively charged surface for the immobilization of flavodoxin.

4.3.1.3 Protein Labelling

In order to obtain an efficient FRET communication (see chapter 5), attachment of multiple labels to the same protein has to be avoided, as this may result in energy transfer between the molecules of the dye[54] or in formation of non-fluorescent dye dimers Cy5 and Atto655 between neighbouring dye molecules attached on the same target protein[149], which would affect the switching ratio.

Therefore a dye:protein ratio well below one is desired, to also increase the probability that the dye is attached at the N terminus rather than on other primary amines. In fact, normally, in amino-labelling procedures a high pH is recommended to favour deprotonation and the reactivity of the amino groups.[108] The pH of 6.0 or 7.0 was used here; in order to reduce aspecific labelling on thee exposed ε-amino groups of lysines, that have a higher pK_a (pK_a~9.5-10.5), than the N-terminus (pK_a~8).

- N-terminal labelling:

Dyes used to label wild type Az were NHS-Cy5, NHS-Atto655 and NHS-Atto647N. Laccase (Lc) was labelled with NHS-Cy5. Flavodoxin was labelled at the N terminus with NHS-Atto655.

- Cysteine labelling

Maleimide functionalized fluorophores were attached on the surface exposed cysteine (YCC and Az N42C mutant, previously reduced with TCEP).

Routinely, unreacted dye molecules were removed by gel filtration or by concentration and dilution in Microcap centrifugal filters with a cut-off of 3 kDa for Az and flavodoxin and 10 kDa for laccase. Degree of labelling was then determined from the UV-Vis. spectra as reported in chapter 5.

4.3.1.4 Protein Immobilization

After washing in ethanol and water the Au-OTE were gently dried under nitrogen flow. The quality of the SAMs was checked by contact angle, and then the Au-OTE were immobilized with adhesive tape on a clean Perspex support and a silicon mask was applied on the surface to create different electrochemical areas as in Figure 4.5. The diameter of each of the defined areas was 5 mm.

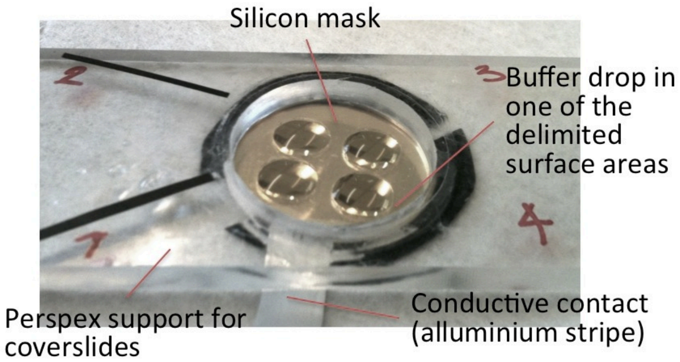

Figure 4.5: Silicon mask covering the Au-OTE electrode and delimiting different areas on the surface.

Aliquots of fluorescent proteins (50µl, ≥1 µM concentrations) were then delivered on the surface and incubated at RT for 30 min, followed by gentle rinsing with buffer.

For physisorption of flavodoxin the MUA SAM surface, negatively charged, was delivered a solution of neomycine (10 mM) for 1 minute, after gentle rinsing with buffer, a solution of flavodoxin (10 µM) was delivered on the surface and allowed to physisorb for 30 minutes. The electrode surface was then rinsed with buffer and inserted in the electrochemical cell.

4.3.1.5 Covalent Immobilization

Az physisorbs on the surface of linear alkanethiol CH_3-terminated SAMs by interaction with an hydrophobic patch on the surface. In the same way, Fld physisorbs by electrostatic interaction on negatively charged SAMs. To obtain a protein layer solutions of these two proteins were simply delivered in appropriate concentration on the surface of the SAM modified electrodes, as described in section 4.3.1.4.

When covalent immobilization was required, as for laccase, an established protocol was used to create amidic bonds between the terminal carboxylic groups of a mercaptoundeacanoic SAM and the superficial aminogroups of the enzyme. The electrode was delivered an aliquot of 75 mM EDC and 25 mM NHS for 30 minutes, rinsed with water and successively incubated for 1 hour with the protein at room temperature. After further rinsing with buffer to remove non covalently bound molecules, the electrodes were inserted in the electrochemical cell.

Chapter 5

Configuration of the Fluorescent Switch and Electrodes for Fluorescence Cyclic Voltammetry

5.1 Objectives

As discussed in the first chapter, in order to investigate the redox behaviour of a population of immobilized molecules by combination of fluorescent microscopy, a stable and well-characterized highly fluorescent switch model, supported on transparent conductive films is needed. Accordingly, the first part of this chapter (Section 5.2 and 5.3) describes the characterization of an Az based fluorescent switch, used as the case study for the development of the technique. The second part (Section 5.4), describes the electrodes used and the characterization of the optical and electrochemical response of the fluorescent switch on these electrodes. These two components will be used in the chapter 6, where the fluorescent detection will be combined with CV, in the technique named 'fluorescent cyclic voltammetry' (FCV).

5.2 Configuring the Azurin FRET Switching System

5.2.1 åBackground Information on Azurin

Together with plastocyanin, pseudoazurin and amycyanin, Az belongs to the larger family of cupredoxins, which are small blue copper proteins, involved in outer-sphere long range ET reactions.[2] In vivo their task is mediating electron transfer in a wide range of biological systems.[150] In particular Az is a soluble bacterial electron transport protein, known to interact with cytochrome *c* 551 in the electron transport chain of the bacterial membrane and involved in the response to stress situations.[150,151]

Together with cytochrome *c,* Az is also one of the most extensively studied metalloproteins in bioelectrochemistry, serving as a model system for elucidating numerous aspects of the mechanisms of biological electron transfer (ET).[140,152-155] From a more applicative point of view, great attention has been drawn by the possibility of employing redox activity of Az, whose structure is naturally tuned for fast and efficient ET, in the fields of biosensing[156] and bioelectronics.[157,158] The electrochemical and spectroscopic properties of Az have been intensely studied[155,159,160] and its β-barrel structure is stable enough to endure point mutations and surface attachments without unfolding.[160-162] Hence Az represents a very interesting system for testing new techniques, such as the one presented here.

The Az used in this study was cloned from the opportunistic human pathogen *Pseudomonas aeruginosa*. The structure of this small - 14 kDa - protein (Figure 5.1) consists of two beta sheets arranged in a sandwich configuration, offering a tight coordination, at the top of the domain, to a Type-1 (T1) copper ion, which switches between the Cu^{2+} and Cu^{1+} redox state at a potential of 270-330 mV vs. NHE.[163,164]

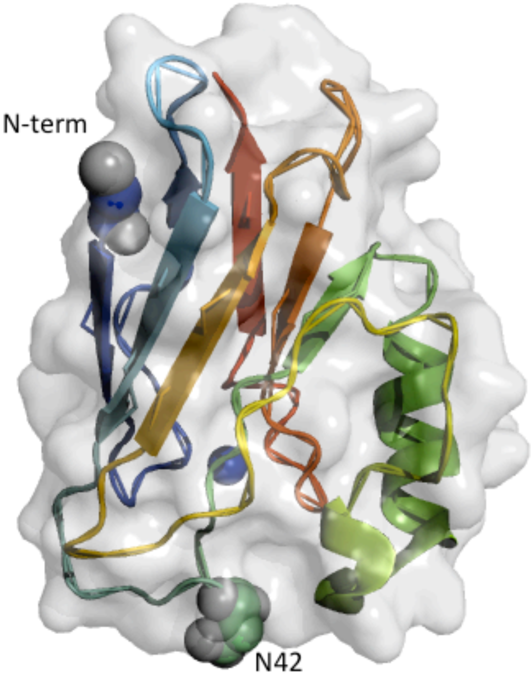

Figure 5.1: Cartoon structure of wt-Az, with the copper ion colored in blue. The N terminal residue and the residue 42 have been drawn in spheres and labelled(pdb 4AZU).

The copper ion is coordinated by three nearly in-plane ligands, the Sγ atom of Cys112 and the Nδ atoms of His46 and His117; the presence of two more distant axial donors, the Sδ atom of Met121 and a carbonyl oxygen of Gly45,[164] results in a trigonal bipyramidal coordination geometry of the copper, peculiar to Az among all other cupredoxins (Figure 5.2).[150,165]

The characteristic spectral feature of the Type-1 oxidized Cu^{2+} contained in Az is a strong absorption band ($\varepsilon = \sim 5000\ M^{-1}cm^{-1}$) at 628 nm, where normal cupric complexes usually have weak Laporte forbidden d-d transition with low absorption coefficient configuration ($<40\ M^{-1}cm^{-1}$).[164] The intense blue colour of the protein-coordinated copper originates from charge transfer transition from the ligand Cys112 Sπ to the Cu^{2+} $d(x^2-y^2)$. In the reduced protein, the full d^{10} effectively switches off this transition; consequently the reduced protein is colourless. Due to these spectral changes (see below), the copper T1 site can be employed to construct a fluorescent switch based on Forster Resonance Energy Transfer (FRET) with a fluorescent dye (section 5.2.2).

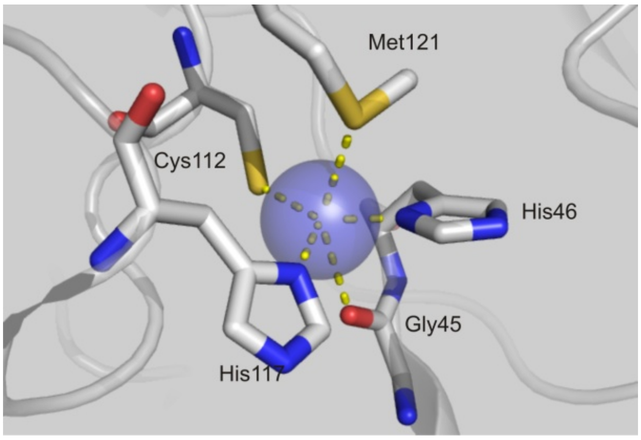

Figure 5.2: Wt Az T1 copper coordination environment with coordinating residues (Met112, His46, Gly45,His117 and Cys112) labelled. Sulphur, nitrogens and oxygen atoms are respectively rendered in yellow, blue and red. . The picture was rendered using PyMOL and the .pdb file 4AZU.

5.1.1.1 FRET-Based Redox Switches

Fluorescence detection of protein redox states was developed in the last few years in Prof G.W. Canters and Dr J.J Davis groups and has been applied to a variety of systems.[31-33,166] The method allows detection of the redox state of proteins at SM levels, a gain of several orders of magnitude over the classical absorption spectroscopy.[32] The technique involves attachment of a fluorescent dye molecule to a reactive group on the protein surface, at a fixed distance (typically below 5nm) from the protein coloured redox center. This results in energy transfer (by FRET) from the dye to the redox center, with the extent of the effect of the chromophore on the dye emission being proportional to the overlap between the fluorescent emission and the redox center absorption spectra as described by classical Förster theory (section 2.2).[54] The several fold amplification in the readout of the redox state is due to translation of the change in absorption into a modulation in the fluorescence emission frequency of the dye.

Numerous fluorophores with high quantum yields and short lifetimes (typically few nanoseconds) are commercially available and many biological redox centres undergo considerable spectral changes upon reduction/oxidation or binding of substrates,[2] therefore the FRET-based approach can be extended to a variety of systems, among these, cupredoxins, cytochromes, flavoproteins, type 3 copper proteins and nitrite reductase.[167]

5.2.2 Azurin as a FRET Switch

As FRET phenomena are strongly dependent on the distance of the donor-acceptor couple,[110] it is desirable to have the ability to reliably control site specific labelling on the protein surface. To allow site specific labelling a mutant of Az was produced in which a surface-exposed asparagine residue, N42, is substituted with a cysteine. The N42C mutation causes the formation of cysteine-cysteine homo-dimers.[168] These however display the same spectral features (UV/Vis, EPR and NMR) as the wild type Az (wt-Az), indicating that no structural changes occurs at the copper site.[168] Wt-Az and the N42C-Az mutant used in this study were produced during a visit at Gorlaeus laboratories in Leiden University (section 4.2.2), expressed in *E. coli* and purified by several passages of FPLC, using a procedure adapted from Van de Kamp *et al.*[145,169] with yield of 3.3mg/l of wt-Az and 0.3mg/l of N42C-Az mutant. After purification the proteins, reconstituted with either copper or zinc ions, were stored at -80C° in 20 mM MES buffer pH7.0 until use. The N42C-Az mutants were titrated with an analogue of Ellman's reagent (DTDP),[146] in order to check the reactivity of the exposed thiol groups (section 4.2.2). Under native conditions no free cysteines were detected in the N42C-Az holo-dimers; correspondingly after chemical reduction of the S-S bridges, 0.8±0.1 equivalents of DTDP per monomer of N42C-Az reacted, confirming the presence of no more than one free thiol per monomer, in agreement with previous reports.[169]

5.2.2.1 Labelling with Fluorophores

Both the types of proteins produced, the wt and N42C Az, were modified by anchoring a fluorescent molecule on their surface. As described in section 4.3, wt Az was labelled at the N-terminal, and the N42C mutant on the surface-exposed thiol (Figure 5.3).

Initial studies were conducted on the wt-Az labelled with the cyanine dye Cy5.[99] However the photochemical instability of this label and the blinking emission[170] proved to be problematic when the labelled molecules were immobilized on surfaces. Cy5 dye is also reported to undergo photo isomerization between cis and trans isomers, with different fluorescent emissions in the two states, which can interfere with the fluorescence measurements.[170,171] Hence for all the later experiments Atto655 and Atto647N were used. These dyes allowed for longer illumination periods through reduction of the photobleaching effects (see chapter 6).

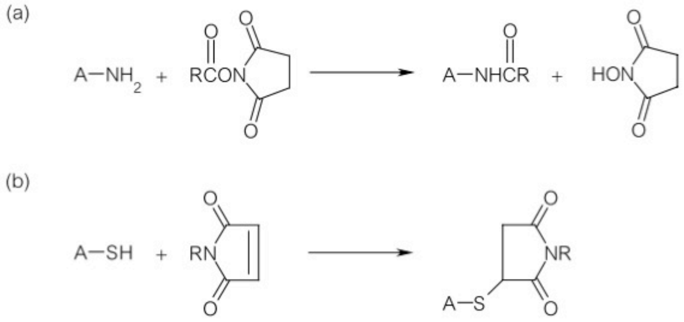

Figure 5.3: Reaction summary for the primary amine of a protein (A) with an NHS ester (a) and a sulphydryl group of a protein with a maleimide (b). In both cases (R) denotes the fluorophore (cy5, Atto655 or Atto647N) and a variable length carbon linker

After dye removal, labelling efficiencies (DOL) were calculated from the UV-Vis. absorption spectra (Figure 5.4), using equation 5.1

$$DOL = \frac{A_{\max} - \varepsilon_{prot}}{\left(A_{prot} - A_{\max} \cdot CF_{280nm}\right) \cdot \varepsilon_{\max}} \tag{5.1}$$

where A_{max} is the maximum absorption of the dye at the appropriate wavelength and CF_{280nm} is the necessary correction factor for the dye absorption at λ=280nm, at which the protein absorption A_{prot} is measured. With these conditions, dye to Az ratios typically below 30% were obtained and the labelling was repeated, on freshly thawed Az aliquots every two weeks.

The fluorescence excitation and emission spectra of the bound fluorophores matched those of the free dye (Figure 5.4), suggesting the vicinity to the protein structure does not alter their photophysics. Additionally, in order to confirm the labelling with only one dye molecule per protein, liquid chromatography followed by electrospray ionization mass spectrometry was employed (as outlined in 4.1.2.4). The molecular weights obtained for the wt-Az labelled at the N-terminus and the cysteine labelling are reported in Table 5.3 (the corresponding elution profiles and chromatograms are reported in the Appendices).

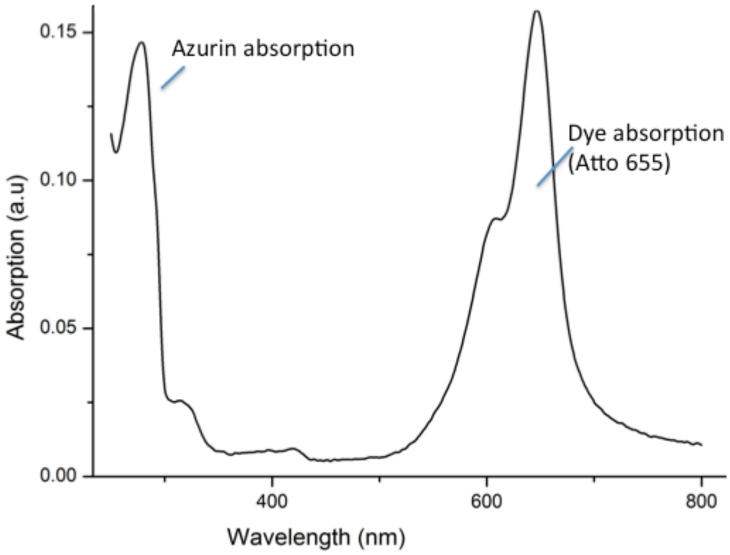

Figure 5.4: Absorption spectrum of wt-Az labelled with Atto655, with a degree of labelling of 7%. At 280 nm the absorption peak of the protein backbone is visible, and the absorption peak of the dye at 660nm. The remaining absorption peak in the region 300-500 nm are due to the absorption at shorter wavelengths of the dye.

Briefly, for all the unlabelled molecules, the weights were consistent with the expected ~13900Da calculated from the amino acids sequence. The N42C mutants both reconstituted with copper and zinc were forming dimers of ~28KDa, which after reduction and labelling of the exposed thiols, were separated into monomers. After labelling both at the N terminal and on the cysteine the molecules showed an increase in MW of 600-800Da consistent with the weight of the appended dye.

Importantly for both the wt-Az and the cysteine mutant, the determined MWs were consistent with the values expected for singly labelled protein molecules and in all the labelled samples analysed, it wasn't detected the presence of multiply labelled Az molecules. This is coherent with the results obtained from the chemical switching in solution, presented further on. However a further purification of the labelled samples of wt-Az by means of ionic chromatography on a MonoQ column (not shown), suggested the presence of minor contributions from several labelling sites on the surface of the wt-Az other than the amino terminus. After the same treatment N42C-Az was eluted in only two peaks (the protein partially reoxidised during the separation), further confirming the site specificity in the labelling of the surface exposed cysteine.

Sample	Label position	Dye MW (Da)	Apo protein MW (Da)	Observed MW (Da)
Wt Cu Az	-	-	13945	13934, 13991
Wt Zn Az	-	-	13945	13934
N42C Cu Az	-	-	27890	27895, 27954
N42C Zn Az	-	-	27890	13922, 27967 13986, 28646
Wt Cu Az +Atto647N	N-term	628.9	14574	14589
Wt Cu Az +Atto655	N-term	509.6	14455	14434
N42C Cu Atto647N-Az	Cys42	769.0	14714	14685, 14739
N42C Cu Atto655-Az	Cys42	694.8	14640	14573

Table 5.3: List of MW determined by LC-MS of labelled and unlabelled samples of Az wild type and N42C mutant.

5.2.2.2 Expected Switching Efficiency

In the case of Az, the energy transfer occurs due to the overlap between the emission spectrum of the red absorbing dyes used (Cy5, Atto655 and Atto647N), and the absorption peak at 628 nm of the oxidized Cu^{2+} T1 site embedded in the protein. When the latter switches to the reduced state, the overlap, and thus the energy transfer, drops to nearly zero (Figure 5.5).

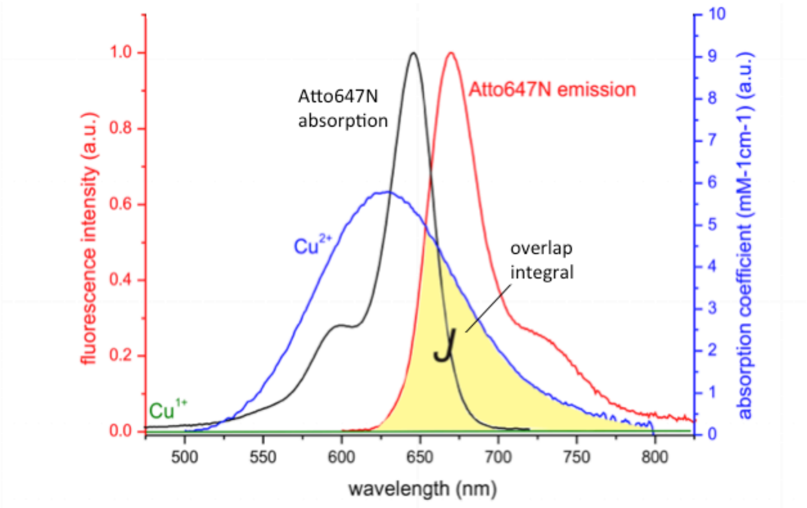

Figure 5.5: The absorption spectra of wt-Az in the reduced (green line) and in the oxidized state (blue line) The area shaded in yellow is the overlap integral, J, between the oxidized Az absorption spectrum and the emission of the dye Atto647N.

An important aspect of the process is that the FRET dye → Cu^{2+} interaction is a dipole coupling. Therefore, accordingly to the Frank-Condon principle, it is insensitive to the intervening medium (unlike electron transfer processes).[139] This provides a sensitive read out of the redox state of Az, and the change in emission virtually immediately reports for transfer of one charge to/from the T1 copper. In Figure 5.6 a simplified schematic of the fluorescent switch based on Az is reported.

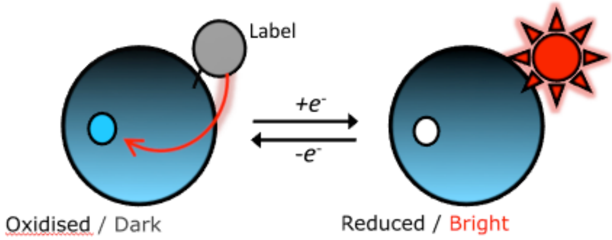

Figure 5.6: Schematic representation of the FRET based communication between the redox centre and the dye molecule. In the oxidized state the energy needed for photon emission is transferred through dipole resonant coupling to the copper, therefore the fluorescence is quenched. In the reduced (Cu^{1+}) state, the protein has negligible absorption at 628 nm, resulting in maximu emission from the dye.

From Förster theory,[110] the probability for the resonant energy transfer between donor and acceptor, decays exponentially with the sixth power of the distance:

$$E = \frac{R_0^6}{R^6 + R_0^6} \tag{5.2}$$

where R is the total A-D distance and R_0 is the Förster radius, calculated from the overlap integral J of the donor and acceptor spectra. R_0 represents the distance at which the FRET efficiency equals 50%. The distances (d) for the attachment point of the dye were measured from the crystallographic structure and were 2.4 nm at N-terminal and 1.0 nm at the C_α of the cysteine on C42. The total distance (R) from the dye to the accepting prosthetic group was then estimated as R = (d+1) ± 0.5 nm to account for the approximate length of the linker chain.

Fluorophore	**R_0 (nm)**
Cy5	**3.9**
Atto655	**3.5**
Atto647N	**3.6**

Table 5.4 List of the Forster Radius calculated for the FRET couple Az-Cu^{2+}-dye. As both the crystallographic distances are within such a distance efficiencies above 50% are expected

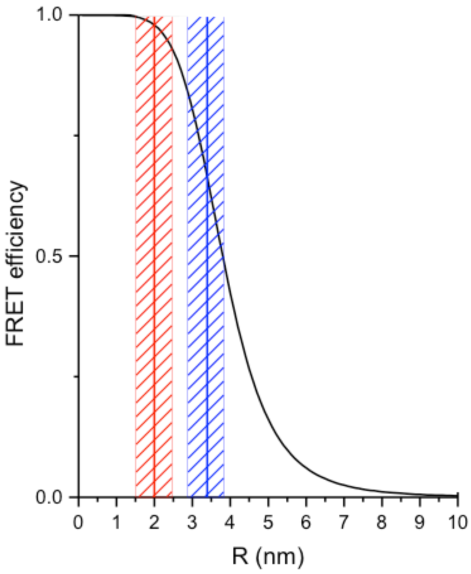

Figure 5.7: The calculated FRET efficiency plot over distance for a fluorophore with a 37 Å Förster radius. The position of the labels at residue C42 and at the N terminus are respectively represented by the red and blue vertical lines and are reported with a ±0.5 nm shaded area.

The theoretical Förster radii distances were calculated from the integral of the overlapping area between the dye emission spectrum and the emission of the oxidized Az, resulting in the distances reported in Table 5.4. On the basis of the reported R_0 the decay of expected FRET efficiency versus distance is reported in Figure 5.7.

5.2.2.3 Observed Switching Ratio in Solution

Once the labelling was confirmed by UV-Vis. and LC-MS, the FRET communication between the dye and the copper centre was checked by chemically oxidizing and reducing diluted solutions of labelled Az, and monitoring the dye emission by fluorescent spectroscopy in a 100μL quartz cuvette. Typical fluorescent traces are reported for the wt-Az labelled at the N terminus (Figure 5.8) and the cysteine labelled N42C-Az mutant (Figure 5.9).

For the experiments in cuvette, diluted solutions, ~100 nm, of labelled protein were used, in order to minimize inter-protein interactions. Typically only two to three oxidation-reduction cycles were applied, as the effects are progressively decreasing due to the formation of a redox buffer in the solution with the increasing concentrations of added chemicals. Figure 5.8 shows wt-Az in the oxidized state at the beginning of the measurement. Conversely due to the necessary reduction step in the labelling protocol, the N42C-Az mutant is completely reduced, and the initial emission is at the maximum (Figure 5.9).

Fluorescence switching was quantified as in Table 5.5, by comparing the expected switching efficiency, E, with the observed switching efficiency, Q. The latter was defined as:

$$Q = 1 - \frac{F_{min}}{F_{max}} \tag{5.3}$$

where F_{min} and F_{max} are the minimum and maximum value of the fluorescence intensity corresponding to the completely oxidized and reduced states, respectively.

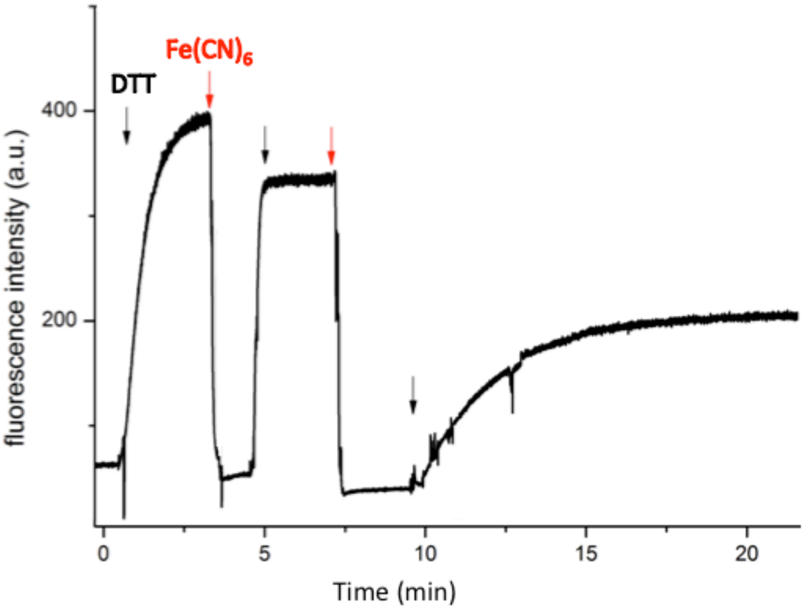

Figure 5.8: N-terminally labelled wt-Az (with Atto655) ~100 nm in phospahte buffer 100 mM pH7.0, switching in solution by addition of dithiothreitol 10 mM (DTT, black arrow) and ferricyanide 100 mM as reducing (red arrow) oxidizing agents which react reversiby with Az.[172] *The protein sample was initially in the oxidised state, corresponding to a minimum emission.* λ_{exc}*=659 nm,* λ_{em} *=670 nm.*

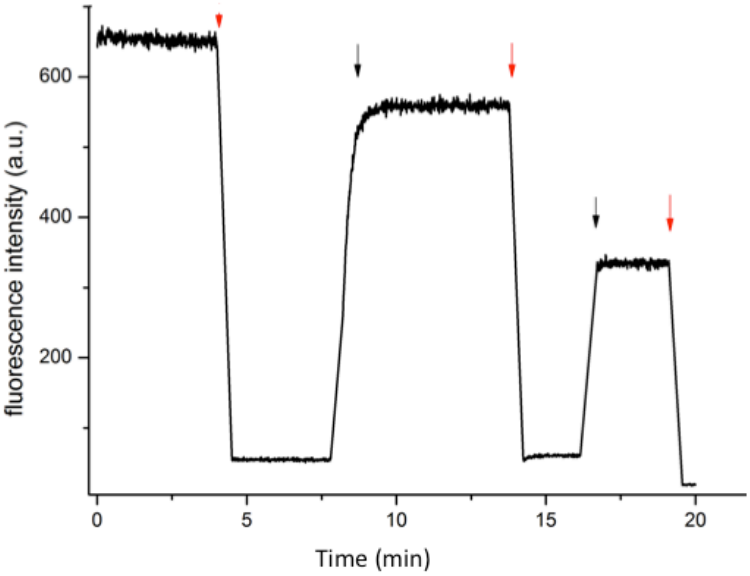

Figure 5.9 : 100 nm solution of N42C-Az labelled with Atto655, time trace acquired during the addition of dithiothreitol 10 mM (black marker) and ferricyanide 100 mM (red) as reducing and oxidizing agents. In this case the protein in solution is initally in the reduced state, corresponding to the maximum emission at the beginning of the acquisition, λ_{exc}*=659 nm,* λ_{em} *=670 nm.*

From Figure 5.8 and Table 5.5, it is concluded that the wt-Az labelled on the N-terminus with Cy5 are about 70% less fluorescent in the oxidized than in the reduced state. In the same way, when labelled with Atto647N and Atto655 dyes, a switching of about 75% was observed, in good agreement with the expected values calculated accordingly to Förster's theory (Figure 5.7).

Az Sample	Label	Label Position	R (Å)	R_0 (Å)	E_{FRET}	Q
Wt copper	**Cy5**	**N-term**	**34±5**	**39**	**0.69±0.20**	**0.70±0.26**
N42C copper	**Cy5**	**Cys 42**	**20±5**	**39**	**0.97±0.05**	**0.80±0.13**
N42C copper	**Atto655**	**Cys 42**	**20±5**	**37**	**0.97±0.05**	**0.93± 0.05**
N42C copper	**Atto647N**	**Cys 42**	**20±5**	**35**	**0.98±0.05**	**0.92± 0.06**
Wt copper	**Atto655**	**N-term**	**34±5**	**37**	**0.66±0.20**	**0.76± 0.14**
Wt copper	**Atto647N**	**N-term**	**34±5**	**35**	**0.66±0.20**	**0.75± 0.10**
Wt zinc	**Atto655**	**N-term**	**34±5**	**0**	**0**	**0±0.05**
Wt zinc	**Atto647N**	**N-term**	**34±5**	**0**	**0**	**0±0.05**
N42C zinc	**Atto655**	**Cys 42**	**20±5**	**0**	**0**	**0±0.04**
N42C zinc	**Atto647N**	**Cys 42**	**20±5**	**0**	**0**	**0±0.04**
	Cy5	**-**	**0**	**0**	**0**	**0±0.05**
	Atto655	**-**	**0**	**0**	**0**	**0±0.05**
	Atto647N	**-**	**0**	**0**	**0**	**0±0.04**

Table 5.5 : Switching efficiencies calculated from the theory, and the observed Q, calculated on the first cycle of chemical reduction and oxidation. S.d. were calculated from the average of at least three different switching experiments. The interval on the calculated efficiencies corresponds to the values calculated for the distance ± 0.5 nm.

The N42C-Az mutant solutions had Q as high as 93%, in line with the correlation between the distance dye-copper, R, and the expected FRET efficiency, E. For all the three dyes considered, the fluorescence of the free dye in solution was tested with the same redox agents, as listed in the table.

A further control was performed by labelling a redox-inactive form of Az with the Atto dyes and adding the same amounts of reducing and oxidizing agents. In this protein the copper ion had been replaced by Zn^{2+}; this substitution causes the protein to lose any absorption above 300 nm. Furthermore, in Zn-Az, electron transfer reactions are prevented, as the potential for the reduction of zinc is not outside of the range of investigation. As a result the addition of DTT and ferricyanide doesn't cause any change in the absorption spectrum of zinc-Az. Hence, after labelling, this behaves as an "always reduced" Cu-Az and the fluorescence emission doesn't change significantly upon addition of chemicals.

These two controls indicate that the fluorescence quenching and enhancement upon variation of the redox state in Cu-Az is not caused by chemically induced changes in the microenvironment surrounding the dye on the surface of the protein or by chemical changes in the dye molecule itself.

Larger standard deviations are observed in the response of the wt samples labelled at the N-terminus with respect to the N42C. The differences could be due to several contributing factors: firstly in these samples, the estimated distance between the dye and the protein copper centre is 34 ± 5 Å, ain contrast with the ~20 Å of N42C. So R is close to the calculated Förster radius R_0 of 36-39 Å, where, according to Figure 5.7, a higher sensitivity of E to small variations in R is expected. To a lesser extent, an additional contribution to deviation in the FRET efficiency observed in the N-terminally labelled wt-Az molecules could arise from heterogeneity in the labels position with respect to the N-terminal: the whole amino acid sequence of Az contains eleven exposed lysine residues, five of these are grouped on the extremity of the beta barrel opposed to the copper center, at about 35-40 Å; the remaining six lysines are positioned around the hydrophobic patch between 11 and 20 Å from the T1. Therefore assuming an equal reactivity of these amino groups, the different contributions should compensate each other. To be able to do more precise inferences on distances, however, the value of the orientation factor κ^2 should be also known. The used value, 2/3, is based on the assumption that both the donor and the acceptor dipoles are freely able to rotate in 3D with respect to each other. However, interaction with the protein surface might limit the dye rotation, introducing an uncertainty of up to 30% in the expected value.[54]

In any case the observed Q were (within experimental error) in agreement with the calculated values, hence confirming that the molecules of Az were in every case mono-labelled and with high switching efficiencies. The labelled proteins were stable and could be stored for a week at 4° C without loss in Q. Experiments therefore proceeded with tests to probe the optical TIRF setup and the electrochemical response of the labelled wt-Az as presented in the next sections.

5.3 Imaging of Labelled Azurin by TIRF Microscopy on Glass

5.3.1 Increase in the SNR and spatial resolution

As introduced in the theory chapters, TIRF microscopy offers the advantage of increased SNR ratio with respect to widefield microscopy thanks to exclusion of the background light from the bulk of the solution.[54] In this section nanoparticles labelled with Atto655 were observed on a glass/buffer interface and the emission in normal epifluorescence illumination and TIRF mode were compared. The possibility of seeing single labelled Az molecules and observing switching from surface confined labelled wt-Az was also explored.

5.3.1.1 TIRF Imaging of Surface-Confined Nanoparticles

The effect of the variation of the incidence angle of the laser on the resulting fluorescent images was tested on a suspension of silica nanoparticles (NPs) labelled with Atto655 (100 µM, 2 nM, ø 50 nm) on a clean glass coverslip.

After a 30 minutes incubation with the suspension and rinsing for several times with fresh buffer, the fluorescent NPs immobilized on the surface could be clearly distinguished in the epifluorescent mode (with the laser directed vertical to the sample surface, so that the angle of incidence, measured from the normal to the surface is zero), as shown in Figure 5.10.

From this position, the angle of the laser was slowly increased using a micromanipulator to vary the position of a mirror inserted in the light path, which displaces the focused light from the central position on the backfocal plane of the objective lens. To test the effect of the passage to the TIRF mode of illumination a time lapse of the resulting images was acquired while performing this operation, a typical time trace is shown in Figure 5.10. On the reaching of the critical angle an increase in the emission with respect to the epifluorescent illumination was observed. For NPs and for zinc Atto655-Az molecuels (in the next section) immobilised on glass surfaces, the fluorescence intensity increased of about 3.1 times when reaching the critical angle of TIR, in agreement with what expected.[44]

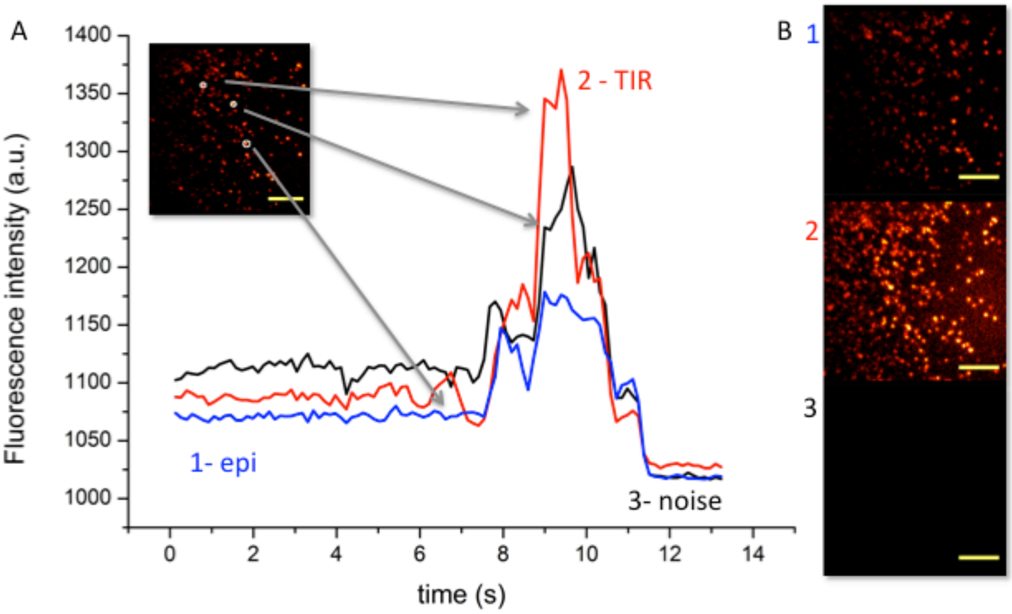

Figure 5.10: Images of silica nanoparticles (50 nm Ø) labelled with Atto655 and physisorbed on a glass coverslip. A) Intensity traces of three nanoparticles (white circles in the insert) acquired as the laser was displaced from the direction normal to the surface. At the beginning of the acquisition, in classical epifluorescence (1), the angle between the normal to the surface and the direction of the laser beam is $\theta=0$. The beam is then rotated slowly until the critical angle θ_c is reached (2) where TIRF excitation occurs. Continuing the rotation, the angle with the normal exceeds the maximum NA of the objective lenses (3), only residual light is collected at angles above the NA ($\theta>\theta_{NA}$). B) Frames of the acquired stack, corresponding to position 1, 2 and 3. A red filter has been used to aid visualizing the nanoparticles. Exposure time: 10ms, EMDAC: 100, in phosphate buffer 20 mM; scale bar = 3μm.

5.3.1.2 Single Molecule Imaging

After spin coating of a diluted (10nM) zinc Az-Atto655 solution, molecules of the labelled protein could be clearly observed as well-isolated, bright features on the glass coverslip (Figure 5.11) in TIRF mode. These were recognizable as SMs due to the distinctive single step photobleaching in their emission profile. In Figure 5.11 the background corrected fluorescence emission of the three molecules is illustrated. As can be observed this has initially a steady constant value and drops in one single step to a lower steady value after photobleaching, thus confirming the possibility of seeing fluorescence of the labelled single Az molecules on glass by TIRF.

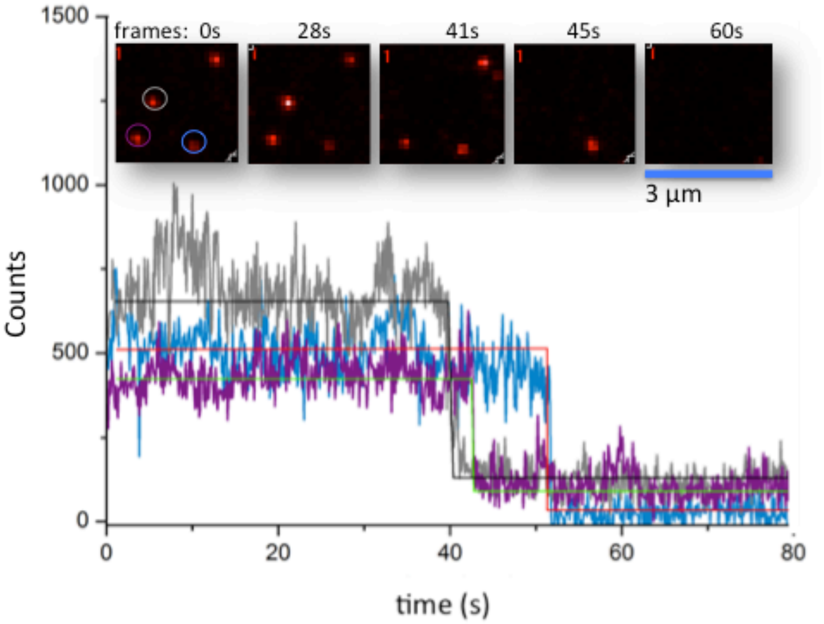

Figure 5.11: Photobleaching traces of three SMs of Atto655 wt-Az molecules (10 nm solution) physisorbed on a glass coverslip (100 ms exposure time, 200x EMDAC) and imaged in TIRF. In the Insert: 3µm side images of the fluorescent spots at different acquisition times.

5.3.2 Chemical FRET Switching on Glass Surfaces

As seen in section 5.2.2, the fluorescence switching was clearly and repeatedly observed in dilute solutions of labelled protein. Hence an experiment to track the redox-linked switch in the fluorescence intensity of surface confined molecules by fluorescence microscopy was undertaken. Labelled wt-Az was drop cast on a glass slide and, after extensive rinsing, was imaged in a drop of buffer containing 40 µM DTT (Figure 5.12).

The FRET-linked change is clearly visible in Figure 5.12, where two frames of the same kinetic acquisition are displayed. The one on the left contains wt-Az SMs in the reduced state, at initial stages of the acquisition, while the frame on the right was acquired after the oxidation had occurred.

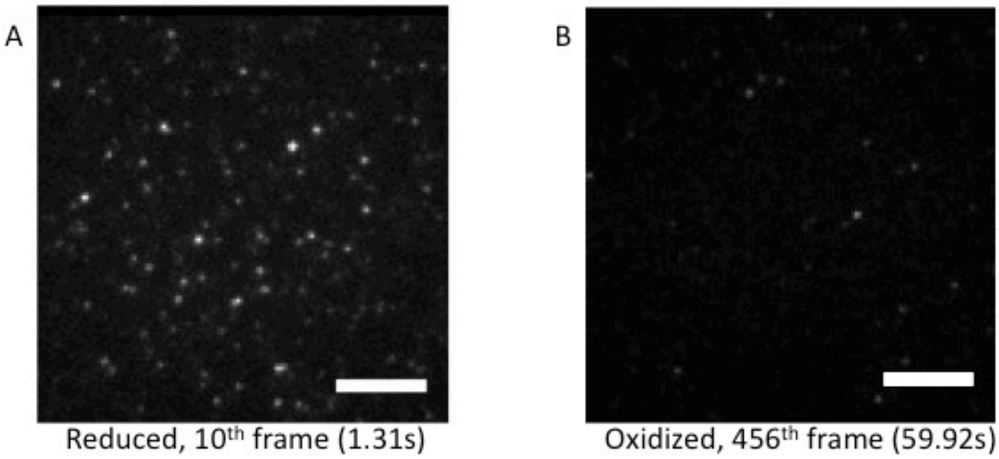

Figure 5.12: Two frames from a stack of images acquired before and after chemical oxidation of Atto655 labelled wt-Az molecules drop-cast on a glass coverslip, displayed with the same intensity scale. Each frame was acquired with a 100 ms excitation time, with a 633 nm laser illumination in the TIRF mode. The images are reported on the same intensity scale and correspond to 128 × 128 pixel area each, the white bar is 3μm.

The Atto655-Az molecules, at their brightest state, were chemically oxidized after a few minutes, by carefully releasing a 2μL aliquot of ferricyanide (10 mM) on a side of the buffer droplet, taking care not to disturb the focus of the image. As illustrated in the emission profile of the acquisition stack (Figure 5.13), the addition of oxidizing agent took place after ~30 seconds from the beginning of the kinetic acquisition (red arrow). As the ferricyanide slowly diffused into the solution and reached the volume illuminated by the evanescent wave, the number and size of fluorescent features suddenly dropped. This decrease in fluorescence emission occurred within ~10 seconds from ferricyanide addition and was repeatedly observed for the both the Atto655 and the Atto647N wt-Az samples and the cysteine mutants.

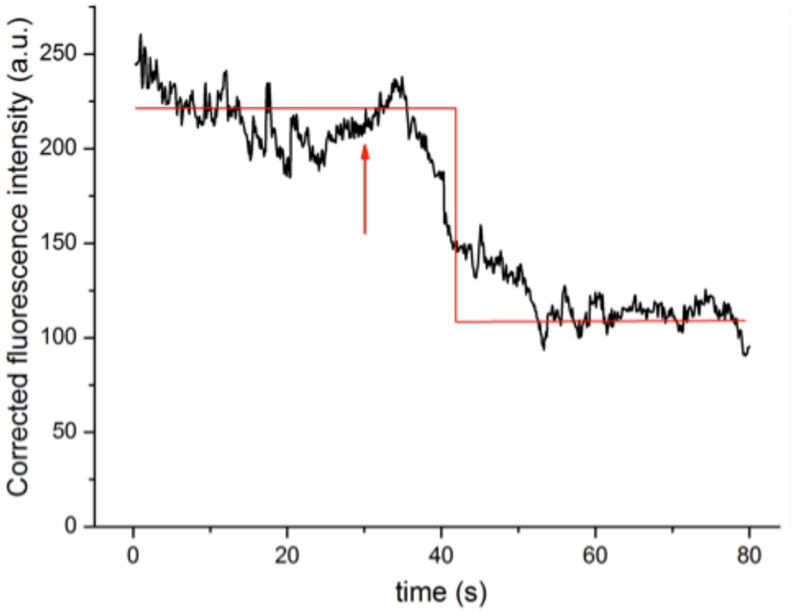

Figure 5.13: Time trace acquired over the full image area shown in Figure 5.12. The red arrow indicates the time of addition of 2µl of oxidizing agent to the solution. The red line is a guide for the eye, indicating the maximum and minimum fluorescence intensity on which the switching (0.55) has been calculated.

The switching ratio for wt-Az-Atto655 oxidation averaged over the whole area of three different images was found to be 55±12% of the initial fluorescence value. Similar values of 50-65% switching were observed when Atto647N and the cysteine mutant N42C-Az were employed. It was also possible to partially recover the initial fluorescence intensity by replacing the droplet with fresh buffer containing DTT, although the substitution of the buffer changed the focus of the image. On the contrary, when the same experiment was repeated with the only dye or with the labelled zinc Atto655-Az on the surface, the decrease recorded was only 1-5%, compared to the 50-65% switching obtained for the FRET process, and was mainly attributed to the collisional quenching of the diffusing ferricyanide molecules.

The switching values reported in the previous section for the freely diffusive Atto655-Az in solutions are higher, especially for the N42C-Az mutants whose switching was ~95%. The lower Q (~55%) encountered when Atto655-Az was physisorbed on the surface could be due to several factors linked to surface confinement with random orientation: firstly it is possible, although unlikely due to the stable fold of Az[162,173], that partial denaturation of some labelled Atto655-Az molecules occurs during drop casting; secondly the immobilization on glass might lead to hindering of the interaction of the ferricyanide molecules with the T1 center, hence reducing the rate and number of responsive FRET switches. A third additional source of difference with the solution Q values may originate from the reduction of the dye dipoles freedom by interaction with the glass. However, despite the decrease in FRET efficiency upon immobilization on glass, the experiments clearly indicated the change was large enough to detect the change in the oxidation state of the surface confined proteins. Therefore we proceeded to the analysis of the labelled Atto655-Az by electrochemical means.

5.4 Establishing voltammetry

5.4.1 Labelled Azurin Voltammetry

The electrochemical signature of Az is known since a long time.[36,152] It is not until recent however that the importance of specific surface residues in interaction with anions and protonation and deprotonation of histidines in determining the redox potential has been fully established.[159] Jeuken et al. also a recently reported that an appended fluorophore can dramatically affect the CV response of redox proteins by causing reorientation of the surface confined molecules.[174] Notably, Az is known to physisorb on alkanethiol SAMs thanks to the hydrophobic interactions between a surface patch, close to the T1, and the terminal methyl groups on the SAM.[174] This confers a preferential orientation of the proteins, as shown in Figure 5.14,[175,176] enabling the fast electron transfer dynamics reported in the literature.[177] The ability of the labelled Atto655-Az to establish a good electric contact with the gold despite the chemical modification with the dye (as in Figure 5.14) was therefore evaluated, separately, by CV before proceeding to the combination of the electrochemical and optical measurements.

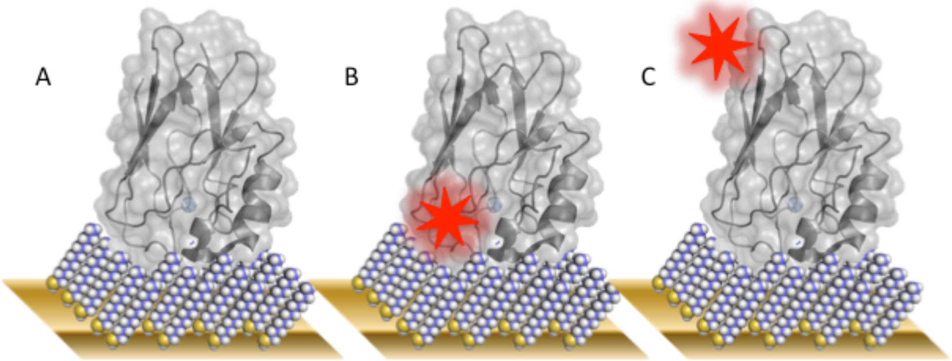

Figure 5.14: Schematic of Az immobilized on a linear alkanethiol SAM with the hydrophobic patch in contact with the surface: A) wt unlabelled Az, B) N42C-Az mutant labelled at the residue 42 and C) N-terminally labelled wt-Az.

The CVs, acquired in a conventional electrochemical cell on gold polycrystalline disk electrodes (GDEs) at pH6.5 in PB buffer 100 mM for the Atto655 N-terminally labelled Az, are shown in Figure 5.15. In these conditions the CV of the labelled Atto655-Az (in Figure 5.15) shows a couple of peaks at the potential of 45 mV vs. SCE corresponding to the one electron process:

$$\text{Azurin-Cu}^{2+} \underset{-e^-}{\overset{+e^-}{\rightleftarrows}} \text{Azurin-Cu}^{1+}$$

It is possible to see in Figure 5.15 that the height of the peaks scaled linearly with the ν, as expected for immobilized electroactive molecules. The ET rate is measured by observing the peak-to-peak distance in the CV and plotting this against the logarithm of ν in the so-called 'trumpet plot', shown in Figure 5.15 (further examples of trumpet plots of Az at lower pH and on different electrodes are reported in chapter 8). The broadening of the trumpet plot seen between $0.5\ \mathrm{V\,s^{-1}}$ and $20\ \mathrm{V\,s^{-1}}$ is due to an intervening gating reaction, specifically protonation of histidines on the surface of the protein. As reported by Jeuken *et. al.*[155,178] and by Monari *et al.* [159], protonation of these superficial groups affects Az ET in solutions with pH 6-8, where the $\mathrm{pK_a}$ of the superficial histidines lies. For ν applied exceeding $20\ \mathrm{V\,s^{-1}}$ gating can no longer affect the ET, due to its different timescale and the k_{ET} of the process can be calculated by fitting to the Butler-Volmer equations (fit represented by red lines in Figure 5.15B). The thermodynamic and kinetic parameters and the values obtained for the modified Atto655-Az monolayers were close to those obtained for the unlabelled wt-Az samples although a slightly lower ET rate was observed on the labelled samples (Table 5.1).

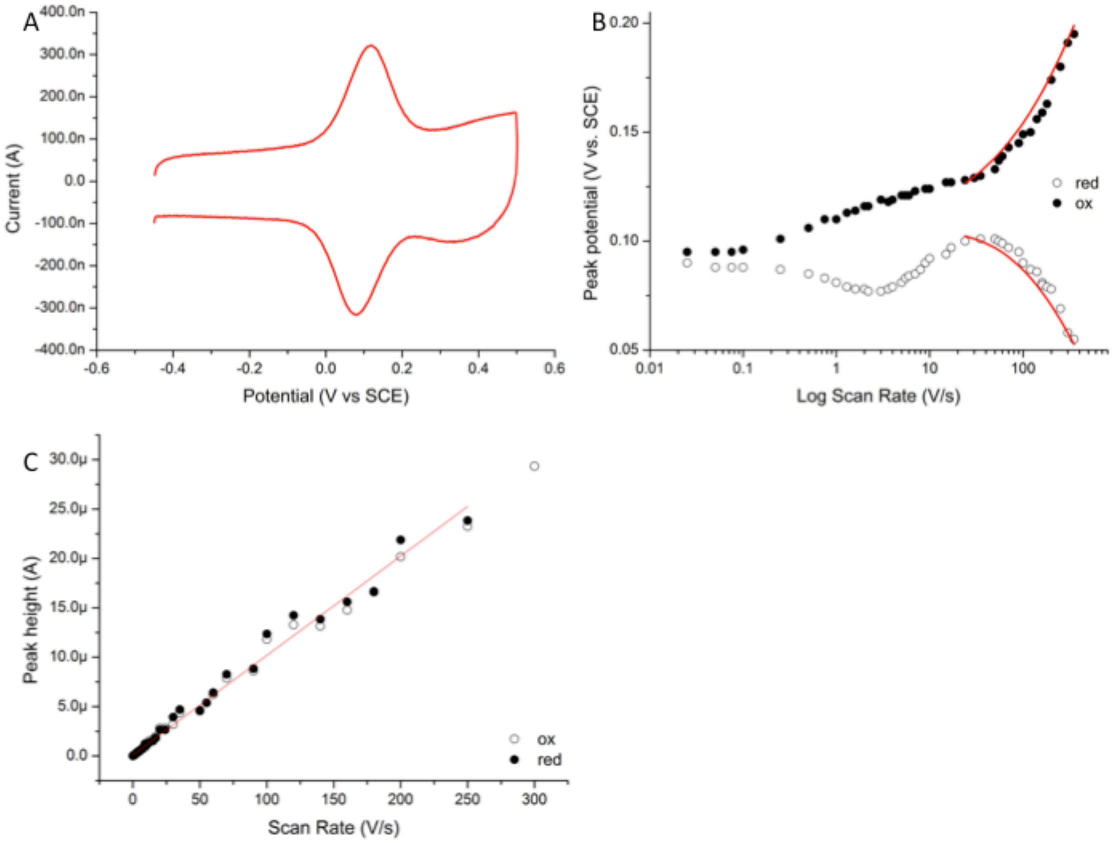

Figure 5.15: A) CV of wt-Az labelled with Atto655 on octanethiol at 1 $V\ s^{-1}$. B) Trumpet plots showing the peaks displacement determined at different ν. The red lines correspond to the BV fitting above 20 $V\ s^{-1}$. C) Linear correlation between the peak height and the ν (R^2=0.98). Data acquired in PB 100 mM pH7.0.

Label position	Dye	E_0 (mV vs. SCE)	ΔE_p at1 $V\ s^{-1}$	i_{pa}/i_{pc}	k_{et} (s^{-1})
N-term.	**Atto655**	**45-57mV**	**31mV**	**0.91-1.13**	**1860±168**
Cys 42	**Atto655**	**50-63mV**	**38mV**	**0.89-1.15**	**1480±120**
Wt Az	**-**	**46-54mV**	**17mV**	**0.92-1.10**	**2810±230**

Table 5.1: Electrochemical parameters determined for labelled Atto655-Az/octanethiol SAM-modified GDEs. SD from the average of three measurements.

From comparison of the values reported in the Table 5.1, and taking into account previous published values[155], it appears that the binding of the dyes on the protein surface didn't drastically compromise the electron transfer process with regards to rate and to the electrochemical potential, as reported for NIR.[174] This is reasonable, in the wild type, where the dye is mostly located far from the hydrophobic patch of adhesion between the Az and the SAM. In case of the N42C-Az mutant, however, a higher influence of the dye would be expected, as the residue 42 is positioned in close proximity to the T1, at the edge of the hydrophobic patch, as shown in the schematic in Figure 5.14. We could however speculate that the dye could be oriented towards the buffer solution rather than inserted between the T1 and the SAM, and therefore is not disturbing significantly the electronic coupling T1 copper-gold. As a slight decrease in the k_{ET} and increase in the redox potential were observed, it would not be surprising if, upon labelling at such a close distance from the T1, subtler changes in the enthalpic and entropic contribution to the electron transfer were generated, which would require more in-depth voltammetric analysis. Due to the slightly different voltammetric behaviour of N42C-Az, in the next chapter the application of the combined CV and fluorescent microscopy will be demonstrated mainly on wt-Az labelled with Atto655, which behaved more similarly to the unlabelled molecule.

5.5 Optically Transparent Electrodes

5.5.1 Background on OTEs

The coupling of imaging and electrochemical techniques, using objective based TIRF microscopy, necessitates an optically transparent, conductive surface on which the fluorescent molecules can be supported. In addition, the conductive surface should allow for thorough chemical modification, in order to attain convenient surface confinement of the studied redox probes in direct electric contact with it.

Optically transparent electrodes (OTEs hereafter) are traditionally manufactured by spin coating, evaporating or depositing thin layers of conductive materials on suitably transparent surfaces. With regard to the conductive film, examples of electrodes obtained by depositing indium and tin oxide, gold, platinum, silver and to lesser extents, mercury, carbon, and boron doped diamond have been reported.[179-182] The electrodes used here were mainly made of glassy carbon and gold and were prepared as described in chapter 4. Both materials have been extensively used as substrates for bioelectrochemistry and can be variously chemically modified to favour oriented immobilization of the protein.[183]

Importantly, for TIRF imaging, besides transparency and conductivity, an extra constraint has to be considered in the choice of the supporting substrate. Due to the limited working distance of the TIRF objective, substrates for the production of electrodes must be thinner than 0.13 mm. Quartz and glass slides are available in such thin format. The first ones are resistant to elevated temperatures and can be used for fabrication of the Carbon-based OTEs (C-OTEs) by pyrolysis of a photoresist film (PPF). Glass coverslips, which are considerably cheaper and more readily available on the market, were used for the production of gold thin-films (Au-OTE).

5.5.1.1 Au-OTE and C-OTE

Gold thin films on glass have been used in the last 50 years for a variety of measurements, including electrochemical,[184,185] ellipsometric, XRD, FTIR, AFM[185] and spectro-electrochemical investigations[60,184,186] of both soluble and immobilized reactants. Typically these films are obtained by vapour deposition of gold on glass slides previously primed with chromium, titanium or with silanes.[184,185] On these surfaces the growth of gold films begins with formation of islands (Volmer Weber mechanism), which then coalesce once reached the percolation threshold thickness of 5-6 nm. Below ~20 nm the films are semi-transparent in the visible window and reflective in the IR spectrum.[187] Di Milla *et al.*[184] established a procedure for deposition of 10 nm thick gold films on glass substrates, and the resulting electrodes, freshly immersed in thiols forming solution, were found to be substrates as good as, if not superior to, thicker gold layers, due to their increased optical transparency and flatness.[184] Following Di Milla's procedure, the Au-OTE used in the present work were10 nm thick gold layers, thermally evaporated on a 2 nm chromium adhesion layer on a plasma-cleaned glass slide.

It has been reported that PPF films reproduce many of the surface characteristics of the common glassy carbon electrodes,[188] and at low thicknesses display high transparency and flatness (see section 5.5.2.1).[144,188] Unlike the metallic thin films, which form by coalescence of neighbouring island, the PPF electrodes form continuous smooth films even at exceedingly low (>10 nm) thicknesses.[144] A picture of the two types of electrodes described, Au-OTE and C-OTE, is shown in Figure 5.16; the grey-blue colour of the Au-OTE electrode is characteristic of 5-20 nm thick gold layers.[185] The colour gradually turns into the typical yellow reflective aspect of polycrystalline gold layers at increasing gold thicknesses.[184] The optical and topological properties of the two OTEs are briefly presented in the next paragraph.

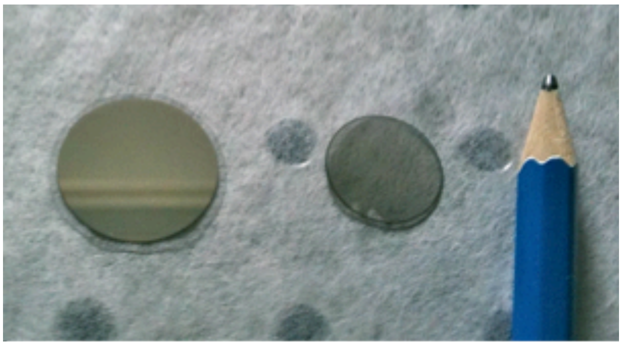

Figure 5.16: Two electrodes used in the work: on the right Au-OTE on a 0.1 mm thick glass slide (25 mm ø), modified with 2 nm chromium and 10 nm gold. On the left a C-OTE, ~15 nm thick PPF on quartz slide, (12 mm ø).

5.5.2 OTEs characterization

Both the types of electrodes were found to be mechanically and chemically stable, surviving the tape adhesion test without delamination, but also harsh treatments, such as immersion in Piranha solution (diluted 1:3 in water) for up to 30 minutes and periods of up to 60 minutes in UV light - ozone generating cleaning chamber, without peeling off from the substrate. After the two last treatments, though, an increase in the surface wettability of both the OTEs was observed, due to oxidation of superficial layer of gold and carbon atoms. Contact angles for Au-OTE varied from 69.5±4.3 (untreated electrode) to 62.3±1.3 after Piranha cleaning, for C-OTE from 37.5±5.2 to 24.2±7.1.

5.5.2.1 Surface Roughness

The surface topography of the electrodes was evaluated by TM-AFM. The roughness of the surface is very important especially for gold electrodes as scattering phenomena and plasmon effects are closely linked to the surface structure and might be involved in the imaging process.[118] Also, for the simple purpose of topographically determining the molecules concentration, a flat surface is desirable. The Au-OTE TM-AFM analysis resulted in a RMS below 0.5

nm over areas of $1 \times 1\ \mu m^2$ for bare Au-OTE (Figure 5.17). Accordingly to previous reports[189], the topography of the thin gold layer followed the underlying glass surface (which had a mean surface roughness of 0.3 nm over $1 \times 1 \mu m^2$).

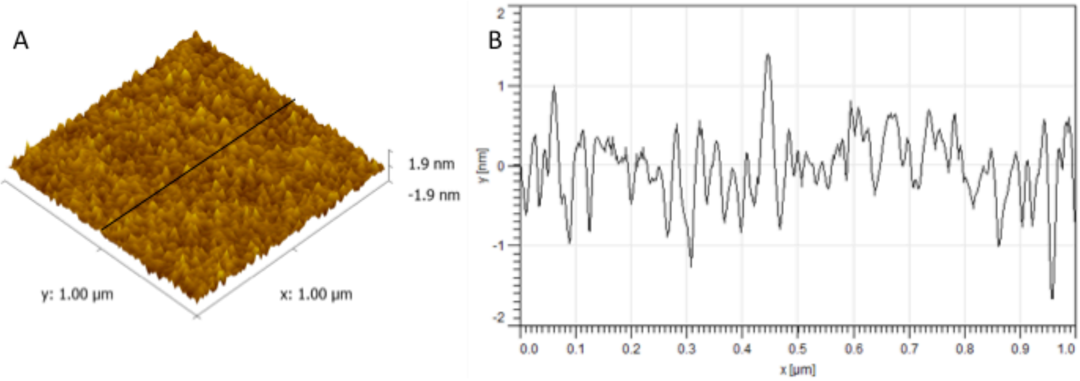

Figure 5.17: A)TM AFM image form the 10 nm thick Au-OTE surface, B) the corresponding height profile, as measured on the black line.

Occasionally batches of Au-OTE electrodes presented discontinuous surfaces, presenting island formations, most likely due to problems in the evaporation process. Batches of electrodes with these characteristics (~10% of the total) were easily recognized as clearly damaged by the Piranha treatment and promptly discarded. For gold increased flatness can be achieved by using template stripping gold[189,190] or post production annealing of the gold film.[185] A few attempts in this direction were done, by acquiring AFM images after overnight incubation of the Au-OTEs at 200˚C. These did not show any successful smoothing of the surface. However on a RMS of 0.5 nm, the Az molecules (2.5 × 3 × 4 nm) can be already clearly recognized (see section 5.5.5); in fact features of 2.7-5 nm in Z-direction and 4 nm in diameter (without considering eventual tips convolution issues) are expected.[191,192]

The mean surface roughness of a pyrolyzed carbon film was found to be 0.82 ± 0.03 nm, in good agreement with the measurement done by Donner et al.[144], who reported a surface roughness of 0.8 nm for a 18 nm thick PPF.

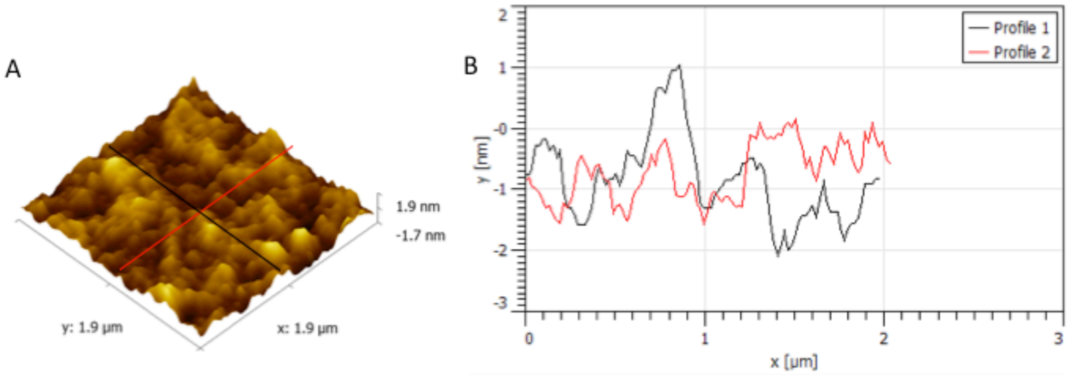

Figure 5.18: A) AFM image of C-OTE, the white line displays where the cross sections were taken. B) Height profiles associated with the two cross sections indicated in A.

5.5.2.2 Absorption Spectra of the Conductive Films

As reported by Donner et al.[144], the optical properties of the electrodes depend on their thickness and structure. For PPFs an analysis of the electronic spectrum can give an indication on the thickness of the sample; the film thickness is dependent on the initial photoresist concentration and the number of applied layers.[144] Figure 5.19 reports the absorption spectra of an Au-OTE in the visible range, together with the spectra of two C-OTEs obtained from spin coating of the quartz with a 25% and 30% dilution of the photoresist.

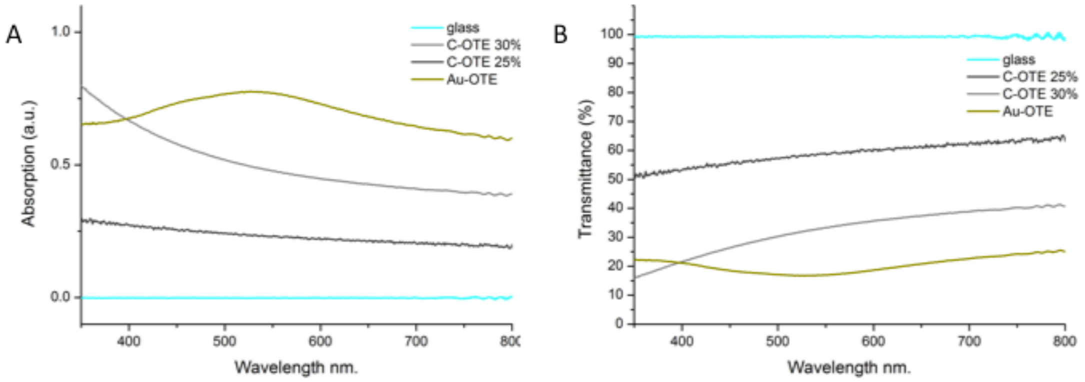

Figure 5.19: A) Absorption and B) transmission spectra between 350-800 nm of the two types of electrodes (Au-OTE, C-OTE 25% and C-OTE 30% in yellow, dark and light grey respectively) and the supporting glass slide (light blue).

As expected the Au-OTE are semi-transparent in the visible range accordingly to previous reports, with the maximum absorption over this range of about 0.75 a.u. (at 550 nm).[184] C-OTEs showed even higher transparency than the metallic films and their spectra were matching a 10-25 nm thickness when compared with the absorption intensities reported by Donner et al.[144] Topographic investigation by TM-AFM at the edges of the PPF coating was employed to unequivocally measure the thickness of the films resulting in steps of 10 – 20 nm.

At the wavelength of 630-690 nm, at which the excitation and emission of the Atto dyes takes place, the light transmitted is 25% for the Au-OTE and 30 to 60% for the C-OTE. Hence, from an optical point of view, both the substrates can be employed for optical imaging.

5.5.2.3 Electrical Resistance

In conductive films, the sheet resistance varies inversely to the thickness of the layer: for example, for the 10 nm thick Au-OTE values of 1-35 Ω\square have been reported.[185,186] In our experiments Au-OTEs with resistances below 50 Ω/square were used, the suitability for electrochemistry of the gold electrodes was further investigated by electrochemical means (see Section 5.6). For the C-OTE much higher resistances were found, in the order of 10^3 Ω/square for PPFs below 35 nm, in agreement with the literature.[144] In fact such a high sheet resistance hindered their use as a convenient support for microscopy and quite variable responses were obtained when using them as electrodes in CV.

To conclude, despite C-OTEs represented an attractive electrode material because of chemical and electrochemical stability, high transparency and flatness. However these electrodes also presented significant drawbacks, the most important being the high sheet resistance, high cost for the quartz slide and the small size (ø 12 mm), which made them difficult to use in an electrochemical cell.[188] The problem with the small slides size in particular was that, once the C-OTE was enclosed in a O-ring sealing cell or microscope support containing the buffer, there was not adequate space left for the x-y movement of the objective on the quartz side of the electrode. An added disadvantage was the high wettability of the surface, which increased the chance of buffer leakage from the electrochemical cell onto the microscope oil-immersion objective.

As a consequence, for the combination of the electrochemistry with TIRF microscopy, further work focused mainly on the gold substrates, which fully encountered the need for transparency, conductivity and flatness. In the next section the chemical treatment of the surface is described.

5.5.3 Chemical modification on Au-OTEs

As reported above the required characteristics of transparency and conductivity were satisfied by the 10 nm thick gold films evaporated on a supportive layer of

2 nm-thick chromium on glass, after which the possibility of readily and reproducibly chemically vary the surface by SAM formation was investigated.

Different cleaning procedures were tested, such as sonication in solvents, cleaning with UV-ozone generating lamp and a treatment with Fenton reagent[193]; effects were compared using AFM imaging and contact angle. Between the discarded procedures, in particular the electropolishing of gold, typically applied on polycrystalline disk electrodes in 0.1M sulphuric acid, resulted in macroscopic alteration of the gold films, that were attributed to oxidation and migration of the chromium adhesion layer to the gold surface at oxidising potentials.[194] The treatment with hydroxyl radicals (Fenton reagent) was successful in reducing the islands formations in those electrodes that presented a discontinuous gold film; nonetheless, as the "flattening" was associated with increased resistance, these samples were discarded. Of the examined alternatives, immersion in diluted (1:3) Piranha solution for 5 minutes followed by thorough rinsing in water and ethanol was chosen as a standard method for both reproducibility and suitability for our practical needs.

5.5.3.1 SAM formation

In OTE used for investigation of optical properties the chemical modification with SAMs can be used both as a promoter for the protein electron transfer and to control the distance between the dye and the gold, as explained in section 5.5.3.2.

The process of SAM formation is well known and proceeds through two structural phase transitions[81]; a quick initial binding of the thiolates groups to the surface forms a disordered structure in which aliphatic alkane chains may be lying on the surface of the metal or may be bent within the SAM. In a second moment, a slower reorganization of the chains takes place for several hours, accompanied by a slower increase of the number of attached molecules and rearrangement in a crystalline ordered structure. As described in section 1.4, on monocrystalline gold in the final structure the alkanethiol chains are tilted of an angle of 28° from the surface normal, reaching an upper surface coverage of 0.77×10^{-9} moles cm^{-2}.[81]

As described in chapter 4, SAMs were formed by overnight incubation of the cleaned gold electrodes in 1 mM thiol solutions in ethanol. UV-vis. spectroscopy showed that modification with the linear alkanethiol SAMs didn't alter the absorption spectra of the OTEs. On the contrary, a predictable large increase of the hydrophobicity of the surface was observed. This was quantified by measuring the contact angles value of droplets of water deposited on the surface, the angles determined for several different SAMs are reported in the Figure 5.20. Consistently, the contact angles decreased of 10-15 degrees after protein immobilization; the decrease in hydrophobicity of the surface is due to coverage of the CH_3 groups and to the exposure of the hydrophilic Az surface at the surface/water interface.

Attempts to observe changes in the electronic spectrum of the SAM/OTE after absorption of the Atto655-Az by means of UV-Vis. spectroscopy were unsuccessful, possibly due to the condition of protein deposition, which were tailored to achieve monolayer to sub-monolayer coverages, as detailed in the next section and in the next chapters.

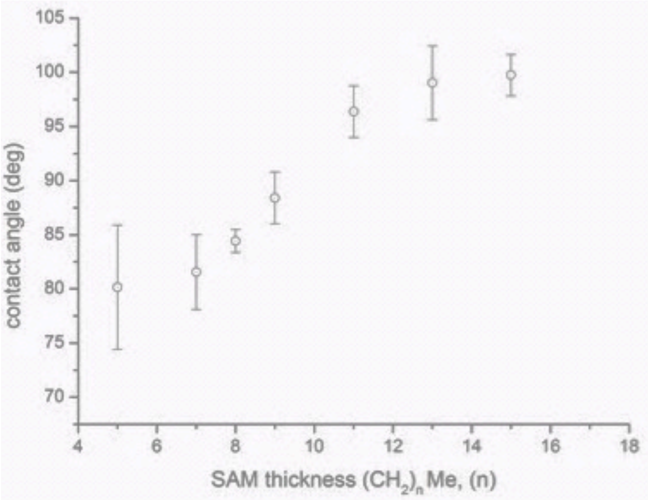

Figure 5.20: Contact angles measured on the surface of SAM-modified Au-OTE after overnight SAM formation in 1 mM $SH(CH_2)_nCH_3$ solutions in ethanol. The SD were determined from a minimum of five different CA measurements.

SAM	**$(CH_2)_n$**	**CA (deg)**
Bare gold	**0**	**62.3±1.3°**
Hexanethiol	**5**	**80.2±5.7°**
Octanethiol	**7**	**81.6±6.2°**
Nonanethiol	**8**	**84.4±1.1°**
Decanethiol	**9**	**88.4±2.4°**
Dodecanethiol	**11**	**96.4±2.4°**
Tetradecanethiol	**13**	**99.0±3.4°**
Hexadecanethiol	**15**	**99.8±1.9°**

Table 5.2: Contact angle values measured on SAM modified gold OTEs at increasing SAM thicknesses.

Further investigation of the SAM formation by ellipsometry resulted in ambiguous values, possibly due to experimental details, such as the excessively low thickness of the glass substrate and the limited reflectivity of the gold layer. However, further confirmation of the positive formation of the SAM monolayers was obtained by observing a reproducible decrease in the capacitive currents at the metallic surface in the CV experiments after insulation of the metal with the alkylthiol layer.

5.5.3.2 Quenching of the Dye Emission

The presence of the metallic layer introduces several factors affecting the amount of emitted photons that are able to reach the EM-CCD sensor: first of all, the incoming excitation beam and the emitted light are both reduced by the absorption of the semi-transparent chromium/gold layer of approximately 75% as measured in section 5.5.2.2. Secondly, the presence of the metallic layer in the nearby of the fluorophore has important effects on the dye emission, as reviewed by several authors[116,118,195-197] and resumed in the theory chapters.

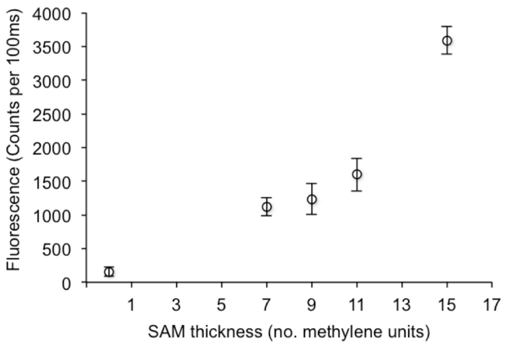

32

Figure 5.21: Fluorescence intensity of a layer of Atto655 molecules (100µL, 1µM) was drop cast at different distances from the metal in TIRF configuration. All the measurements were taken in air, EMDAC=100, excitation time is 100ms, the error bar reports the SD across the surface of 128 × 128 pixel^2 for each SAM.

The most important of these effects is quenching of the fluorescence, which is a type of energy transfer from the excited states of the fluorophore to the metallic surface, as described in the theory chapter. Similarly to FRET coupling, quenching is strongly dependent upon distance, as described in section 2.3.[54,121] Hence the use of a long chain alkane layer as a physical barrier to separate the gold and the dye can decrease the dipole coupling between the two and increase the photon emission and hence improve the optical signal. With the aim of measuring the effect of the intervening SAM layer, a solution of Atto655 in water (100 µL, 1 µM solution) was drop cast on the surface of Au-OTEs, and the resulting fluorescence intensities collected by the EM-CCD camera were measured before and after surface modification with thiols of different lengths, as reported in the plot in Figure 5.21.

At the four increasing SAM thicknesses the collected light was 7 to 22 times the light collected on the bare gold surface, thus showing that the SAM layer introduced a consistent decrease in the quenching effect of the gold film. Nevertheless the correspondent signal collected from the same solution on glass coverslips was over 100 times higher, indicating that, although reduced, the gold quenching is still very effective even on the thicker thiols. Of course assembly of even thicker spacers is possible, but the length of the alkanethiol chain for the electrochemical response of a redox switch is limited by the maximum distance over which electrons are able to tunnel to/from the gold surface, as it will be described in the next chapters. For a more careful quantification of the effect of the gold on the emission rate of the fluorophores further studies including evaluation of the emission lifetimes variation would be needed. This simple experiment however demonstrated the feasibility of increasing the photon collection at the CCD chip of the TIRFM by introducing a SAM spacer between the dye and the gold.

In consideration of the balance between electronic coupling and quenching distances, the studies presented in this thesis were performed mainly on linear SAMs of the type $SH\text{-}(CH_2)_n\text{-}X$ with a number of methylene units (n) between 5 and 11, with X corresponding to CH_3 in case of Az (chapter 6) and to COOH in case of laccase and flavodoxin (chapter 7).

5.5.4 Azurin surface confined on OTE

5.5.4.1 Cell design

Routinely the electrodes were modified with the SAM before being assembled on the microscope stage. Efforts to directly form the SAM on the Au-OTE, when already assembled on the microscope, failed due to the leakage of the ethanol-based solution from the electrochemical cell.

After SAM formation, the Au-OTEs were rinsed with ethanol and water and dried under nitrogen, then turned into working electrodes by electrically contacting the surface with a drop of silver paint and a conductive wire. The electrodes were supported on a Plexiglas holder on the microscope stage and a geometrical area of 0.196 cm^2 was delimited by adhesion of a silicon ring (5 mm internal diameter) on the SAM surface.

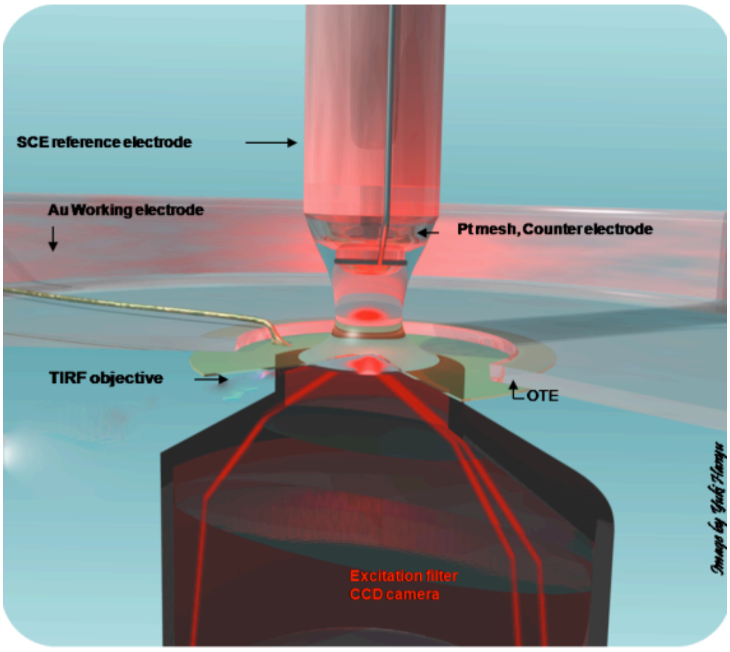

Figure 5.22: Pictorial of the cell arrangement on the stage of the TIRF microscope.

Several experimental designs were tested to craft a flow cell, in which gas and eventually analytes concentrations could be controlled. In particular one of the most promising cells was obtained using a rubber O-ring, pressed on the surface with an external screw-loaded frame made of Teflon, in which the reference and the counter could be inserted. However, during the experiments, the use of the sealed cell resulted problematic, due to the fragility of the glass coverslips that were often broken under the combined pressure of the ring on one side and of the objective on the lower side of the glass.

Contamination of the electrochemical signal with undesired peaks, possibly due to redox active chemicals from the rubber ring, was often observed in these conditions. Therefore, when working with Az, which is relatively insensitive to oxygen, the buffer solution was left in contact with air as in the picture in Figure 5.22.

5.5.4.2 Electrochemistry of Azurin at OTEs

Typical current signals obtained at ν of 100 to 200 mV s^{-1} are shown in Figure 5.23, here the protein was deposited as described in section 4.3.1.4 and CV scans were acquired in the cell shown in Figure 5.22. Although Argon was bubbled through the solution prior to use and buffers were frequently changed during the experiment, an increase in currents at the extremes of the potential window was observed, which was not occurring in conventional CV cells (Figure 5.15a). This was attributed to the experimental limitation in maintaining the solution deoxygenated throughout the experiment on the microscope stage.

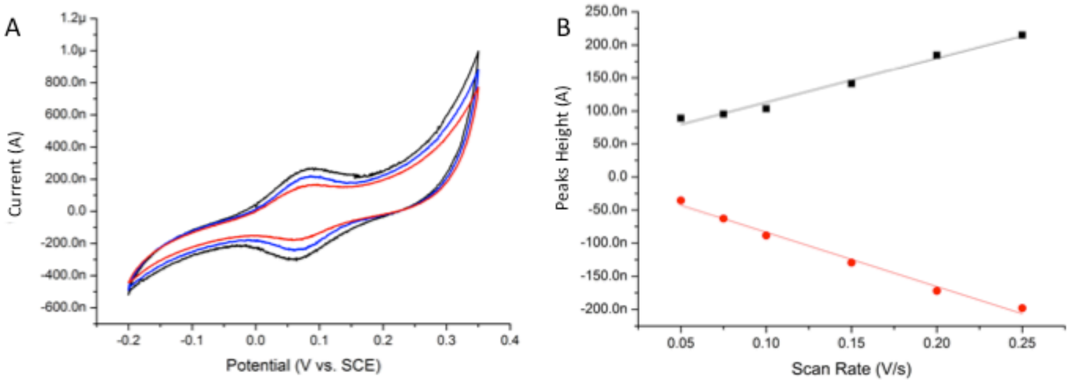

Figure 5.23: A) Cyclic voltammograms of Atto655-wt-Az, physisorbed at an octanethiol-modified Au-OTE in 200 mM MES buffer pH5.0 at ν of 0.1 V s^{-1} (red),0.15(blue) and 02 V s^{-1} (black). B) The linearity of the peaks height with the applied ν confirms the redox-active molecules are irreversibly physisorbed on the surface.

In the reported voltammogram, the midpoint potential is 67 mV vs. SCE, in agreement with literature values for pH 5.0. [159] Once again the peak heights scaled linearly with the ν, indicating an irreversibly surface confined redox centres. In this experiment, the peaks area corresponded to a charge transferred of 8.5×10^{-8} C, or 5.3×10^{11} electrons, which are exchanged by as many proteins. With the geometrical size of 0.196 cm^2 for the electrode area enclosed in the silicon ring, the number of electroactive proteins could be estimated as 2.71×10^{12} molecules ($\sim 4.5 \times 10^{-12}$ moles) per cm^2. Similar coverages were found by others in more conventional setups,[98,198] and previously for Cy5 labelled wt-Az.[99,100] At the theoretical monolayer coverage, for closely packed molecules oriented with the hydrophobic patch to the surface, Az would have a surface concentration of $\sim 25 \times 10^{-12}$ moles cm^{-2} (assuming that one molecules occupies a circular area with a radius of 1.5 nm), therefore the electroactive layer occupies about 18% of the Au-OTE area. The peaks FWHM is about 10 mV larger than the ideal value of 90.6 mV suggesting a small dispersion in the thermodynamic or kinetics of the protein layer.[19,34,199] At low ν a constant non-zero peak-to-peak separation was observed of 10-15 mV. This phenomenon, frequently referred to as "unusual quasi-reversibility" (UQR, following Feldberg and Rubinstein denomination[200]) is often observed in protein electrochemistry[19,41] and was present for the labelled Az on GDEs presented earlier in section 5.4.1.

5.5.4.3 Surface Concentrations of Azurin

The surface concentration of Az molecules was further verified by height analysis of topographic images acquired by TM-AFM in air (Figure 5.24). The topography of the octanethiol-modified Au-OTE (Figure 5.24A) showed only a slightly higher roughness than the bare gold layer (Figure 5.17), instead after Az immobilization features of 2-7 nm in height were observed as shown Figure 5.24B, these had a surface concentration of about 11×10^{-12} moles cm^{-2}.

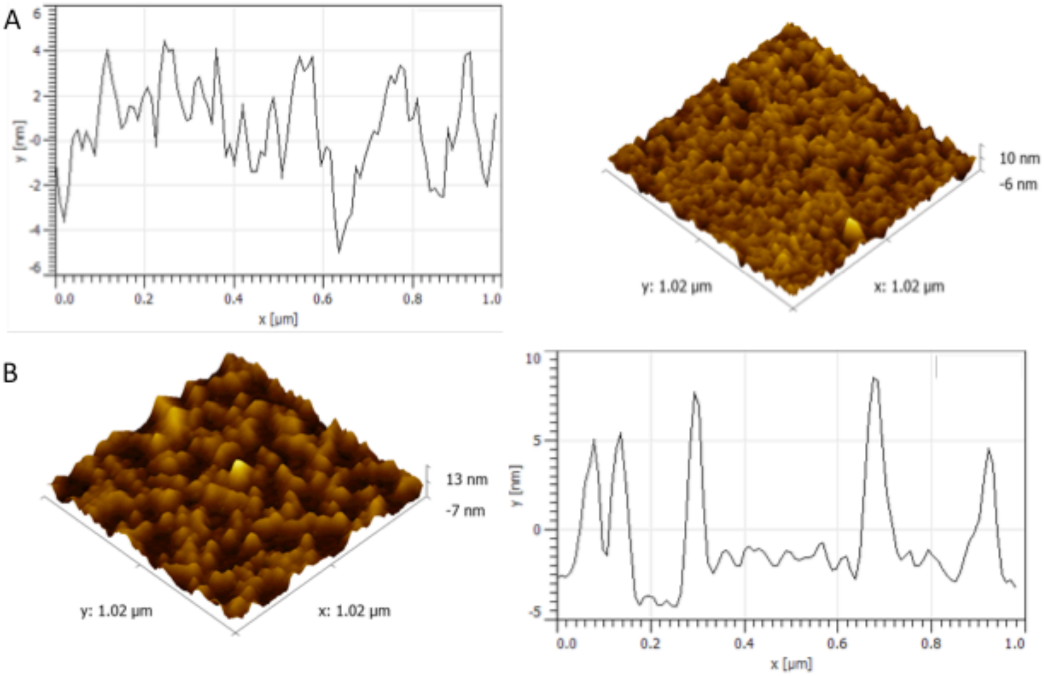

Figure 5.24: Atomic Force Microscopy images of a Au-OTE electrode modified with A) an octanethiol SAM and B) with a octanethiol layer and Atto655-Az.

The higher amount of molecules detected by AFM with respect to CV is consistent with previous reports that suggest that only part of the surface confined Az molecules are electroactive.[20]

According to the literature, the height analysis (Figure 5.25) shows a prevalence of features of 3-5 nm indicating binding of single Az molecules.[201] However a smaller amount of features exceeding this height was observed. These were distributed around 6.5 nm, which could be due to formation of aggregates of 2-3 molecules. Wild-type Az forms small oligomers in concentrated solutions, as recently observed by LC-MS[202] and the amount and size of clusters can be diminished using higher ionic strengths. It was also noted that when higher protein concentrations and lower ionic strengths were used, even bigger aggregates of 15-20 nm in height were present. Therefore great care was taken in keeping constant conditions during physisorption in order to reduce formation of protein aggregates on the SAM surface.

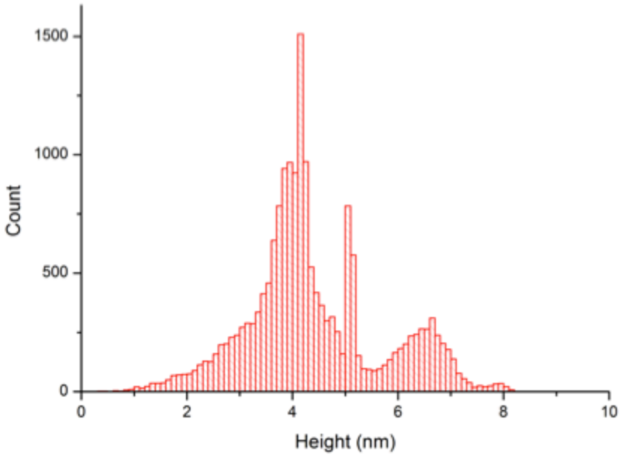

Figure 5.25: Height distribution of the AFM images acquired in non-contact mode AFM..Wt- Az 200 nm on an octanethiol-modified electrode, Grains analysis has been carried out with Gwiddion version 2.20.

5.5.5 Imaging Labelled Azurin physisorbed Au-OTE/SAM

A typical fluorescence image of a wt Az, labelled with Atto655, at sub-monolayer concentration (taken from a stack of acquisitions measured at 100 mV s^{-1} with 4.5×10^{-12} moles cm^{-2} surface coverage) is shown in Figure 5.26. The fluorescent monolayer is observed as uniform across the surface, despite interruption by presence of a few brighter spots, possibly due to aggregates.

As only the 28% of the electroactive Az molecules are labelled, the image corresponds to a concentration of fluorophore molecules of 1.26×10^{-12} moles cm^{-2}. Based on this concentration, Table 5.3 gives an indication of the average amount of labelled Az upon selection of different geometrical areas on the surface.

Remarkably, as reported in the table, by reducing the imaged area to the diffraction limited spot it is possible to sample Az populations down to ~750 molecules, or 1.2×10^{-21}moles, at this relatively high surface coverage. A further reduction of the sampled population can be achieved by using more dilute solutions or shorter times of incubation. However as the amount of collected light is already very low, further dilution of the Az layer increases the difficulty to focus on the fluorescent molecules layer and contributions from the background become more important.

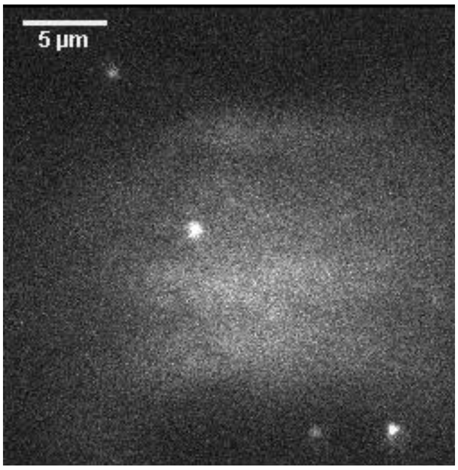

Figure 5.26: A frame of the acquisition in an area of 256 × 256 pixels², that corresponds to an imaged area of 27.1 × 27.1 µm², modified with a sub-monolayer concentration (1.28 × 10^{-12}moles cm^{-2}) of wt copper Az-Atto655.

Pixel	**Area**	**Labeled molecules**	**Moles of Az seen by**
3	0.	$7.5\ \times10^{2}$	1.2×10^{-21}
10	1	$8.36\times1\ ^{3}$	1.4×10^{-20}
47		1.85×10^{4}	3.4×10^{-19}
128	269	1.36×10^{6}	2.3×10^{-18}
256	729	5.48×10^{6}	1.0×10^{-17}

Table 5.3: Number of molecules under investigation at different ROI sizes, referring to the surface concentration reported in Figure 5.26.

Additionally in images acquired on Az sub-monolayers, obtained after deposition of 100 nM Atto655-Az solutions (10 times more diluted with respect to Figure 5.26), the lower fluorescence intensity was accompanied by increased inhomogeneity and presence of aggregates across the surface, as displayed in Figure 5.27.

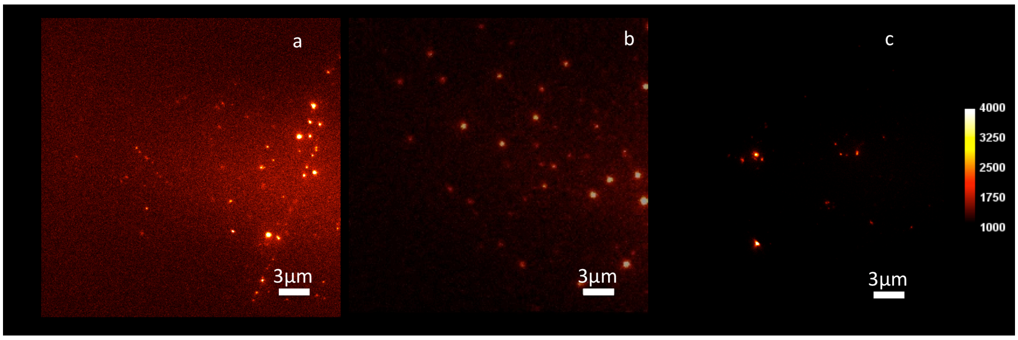

Figure 5.27: Images of Az monolayers taken after physisorption of 1µM (a) and 10 nM concentrations (b) and 100 nM (c) of Atto655 wt-Az for 30 min at room temperature. In c an example of the aggregations/artefacts observed in some of the lower dilution of Az used. The same intensity scale is used for a, b and c. All images were acquired in NaPB with 100ms excitation.

Due to the inhomogeneity in the Az distribution, the detection of fluorescence at lower surface concentrations is thought to be more heavily biased towards the detection of aggregates or clusters[203] due to higher local concentration of fluorescent molecules and to their location at larger distances from the gold film, which reduces their exposure to quenching. To avoid these complications data presented in the next chapter were acquired with the conditions described previously (1 µM protein concentration) and surface concentrations similar to those reported in Table 5.3 on selected areas of 1µm^2 containing about 8360 molecules, corresponding to 13.8×10^{-21} moles of Az, which is still several orders of magnitude lower than the smallest sample (in the femtomolar range) monitored in conventional CV.[204]

5.6 Conclusions

In this chapter the components necessary to achieve the combined electrochemical and TIRFM measurement of surface confined redox switches were presented and characterized separately. The switching efficiency of singly labelled Az molecules was observed both in dilute solutions and when surface confined on glass coverslips on the TIRF microscope. A 10 nm thick gold film deposited on a chromium adhesion layer presents enough conductivity, transparency and flatness to allow formation of SAMs and subsequent physisorption of Az monolayers at sub-monolayer concentrations. Both electrochemical signal and fluorescent emission of the labelled Az molecules could be observed from Az monolayers formed at Au-OTEs assembled in a open cell sitting on the microscope stage.

The presence of the linear alkanethiols SAMs aids both orientation of the Az switches in a direction favourable to ET and prevents the nearly complete quenching of the fluorescent labels, Atto655 or Atto647N, by the gold. However while it is relatively straightforward to obtain images of SMs on the surface of glass coverslips, the same concentrations applied on SAM-Au-OTE result in very poor images. Therefore for viable observation of the fluorescent signal in time a compromise has to be reached with regard to number of molecules sampled versus surface concentration and time of excitation. The next chapter will present the combined acquisition of the time-resolved fluorescence traces while modulating the potential of the gold electrode with CV.

Chapter 6

Fluorescent Cyclic Voltammetry on Atto655-Azurin films

In the previous chapter the construction of a highly fluorescent bioelectrochemical switch (section 5.2) and characterization of a transparent conductive surface (section 5.5) to confine the switching molecules has been presented. The two elements are here coupled using FCV, which allows monitoring of ET transfer events occurring at the electrode surface with the spatial resolution allowed by fluorescence wide field microscopy.[99] This approach may be extrapolated to several purposes, for example, offering tools to investigate the interaction of the fluorescent switches with the local surrounding environment and study of micro-patterned surfaces, with sensitivity approaching the molecular scale.[100,203] In this chapter the application of FCV to the constructed Atto655-Az switch in various conditions is reported and limits and advantages are discussed.

6.1 Data acquisition and analysis

The labelled proteins were physisorbed on the surface of the OTE in order to temporally monitor the change in fluorescence in the images in combination to the applied potential. To do so, as described in the Chapter 5, the potentiostat was connected to the 'cell' by inserting the reference and counter electrodes into the droplet of buffer in contact with the Az/octanethiol SAM/Au-OTE surface. After focusing on the fluorescent Az monolayer immobilized at the interface SAM/solution, the angle of the laser was adjusted to reach the highest fluorescence intensity in TIR position. Kinetic series of images, typically containing 100-200 frames, could then be acquired, while varying the potential across the E_0 of Az.

For each stack of images the frequency of frames acquisition, f, is equal to $f = 1/(t_{exc} + t_{off})$, where t_{exc} is the time of excitation (typically 100ms), and t_{off} is the time required by the EM-CCD chip to transfer the image to the processor, which depends on the size of the acquisition.

The detector of the Andor EM-CCD camera can record images of up to 512 × 512 pixel^2 (Table 6.1). However stacks were normally acquired on smaller areas of 128 × 128 pixel^2, corresponding to a 13 × 13 µm^2 imaged surface, in order to reduce the t_{off} and to avoid areas of uneven illumination, due to curvature of the lens of TIRF objective.

Image Size		t_{off}	t_{tot}	f_{im}
Pixel2	**µm^2**	**ms**	**ms**	**Hz**
512 × 512	**54.3 × 54.3**	**77.74**	**177.74**	**5.62**
256 × 256	**27.1 × 27.1**	**47.75**	**147.75**	**6.77**
128 × 128	**13.6 × 13.6**	**32.76**	**132.76**	**7.53**
64 × 64	**6.8 × 6.8**	**25.27**	**125.27**	**7.98**

Table 6.1: List of the transfer times and frequencies of acquisition corresponding to each image size in pixel^2 for a 100ms excitation time.

6.1.1 Potential Modulation of Surface Confined Molecules

For the synchronization of voltammetric and optical signal, a Labview card was installed on the terminal controlling both the EM-CCD camera and the potentiostat. The Labview interface, on the computer controlling both the camera and the potentiostat, enabled recording of the time stamps of potential trace recorded (Figure 6.1) and of the images with respect to the internal clock of the computer, so that the alignment of the fluorescent intensity traces and the potential could be accomplished in post processing using a MatLab routine.

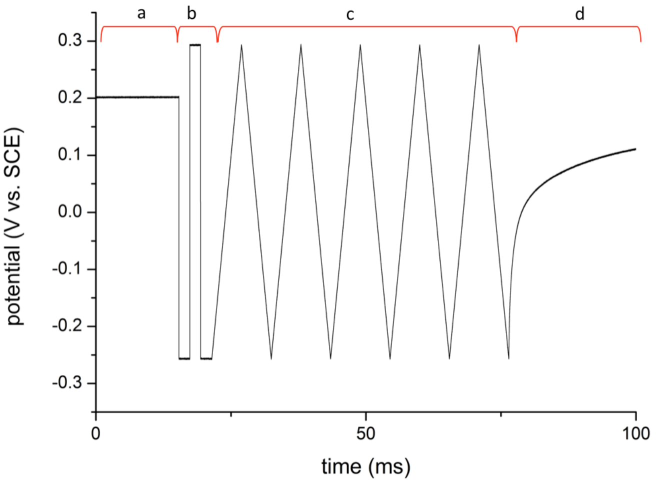

Figure 6.1: Time trace of the potential applied to the Au-OTE modified with the fluorescent switches: a, open circuit potential, b, start of the potential modulation with three chronoamperometric steps, c, five cycles of CV, d, open circuit potential.

Further validation of the correspondence between the potential trace and the fluorescence intensity was obtained with a few diagnostic checks. Firstly, the CV was preceded by a series of three chronoamperometric steps, (for 2 seconds each) between the two extremes of the potential window investigated (Figure 6.1). As it will be illustrated in section 6.1.2, the vertical potential jump produces a characteristic response in the fluorescent traces that can be used to double-check the alignment procedure. Secondly, the potential window was purpose fully kept asymmetric with respect to the zero potential of the reference electrode and stacks were acquired using two different potential windows, typically (-0.25 V, +0.30 V vs. SCE) and (-0.30 V, +0.25 V vs. SCE), to reduce possible computational errors/bias towards zero in the following image analysis.

6.1.2 Fluorescent Traces and Photobleaching

The time traces of images, shown in Figure 6.2 show a periodic variation of the fluorescence intensity overlaid on a negative slope, which is due to the progressive photobleaching of the dye under the laser illumination. As it can be easily observed in Figure6.2 the photobleaching was largely limited passing from the Cy5 labelled samples to the Atto655 dye with comparable labelled Az surface concentration.

This allowed for a prolonged illumination with lower need for correction. A precise quantification of the photobleaching rate is challenging due to the numerous contributing factors, such as the length of the illumination time, the applied ν, the dye molecules intrinsic characteristics and position with respect to the metal. As a result the switching ratio, Q, and extent of photobleaching varied from area to area. Hence, prior to further analysis, subtraction of an exponential baseline, determined by fitting the segments of the intensity/time profile before and after the electrochemical control, and normalization of the resulting signals were carried out for each individual trace.

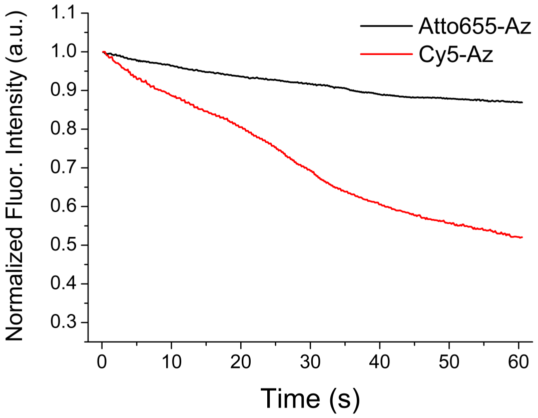

Figure 6.2: Comparison of intensity:time traces setup for two (128 × 128 pixels^2) images acquired in the FCV setup on a layer of Cy5 and Atto655-labelled Az at octanethiol-modified OTE, During the 60 seconds acquisition (at a frequency of 0.143s/frame) showing the increased photobleaching occurring in the Cy5-labelled film with respect to the Atto655. During the acquisition the potential of the electrode was hld constant at -200mV vs. SCE.

6.1.3 Image Segmentation

In post-processing each stack of images with several regions of interest, or “ROIs” (up to 100 per image) was manually selected using the ‘time profile’ macro in MacBiophotonics ImageJ (developed by Wayne Rasband, NIH, Bathesda, MD) so that the switching behaviour of the contained proteins could be studied. Observation of the signal fluctuation in areas as small as the diffraction limited spot (at 670 nm corresponding to ~ 4 × 4 pixel^2), containing ~800 molecules (1.2 zmol), was possible. However optical noise on smaller areas is more of a concern, as the SNR increases proportionally to the square root of the number of detected photons. Therefore to avoid problems in the fitting procedure, the intensity traces were evaluated on ROIs of 10 × 10 pixel^2, corresponding to an estimated sample of about 8360 molecules (~15 zmol).

These were selected from uniformly fluorescent areas across the surface and brighter emitting spots were avoided as these are thought to originate from clusters of aggregated proteins, where both the electronic coupling and the fluorescent signal are likely to be affected by intermolecular interaction and inhomogeneous distance from the gold surface.

6.2 Correlation between Fluorescence Intensity and Potential

As anticipated, the fluorescent traces of the ROIs selected in each image acquisition were aligned to the corresponding potentials using a MatLab routine (Figure 6.3).

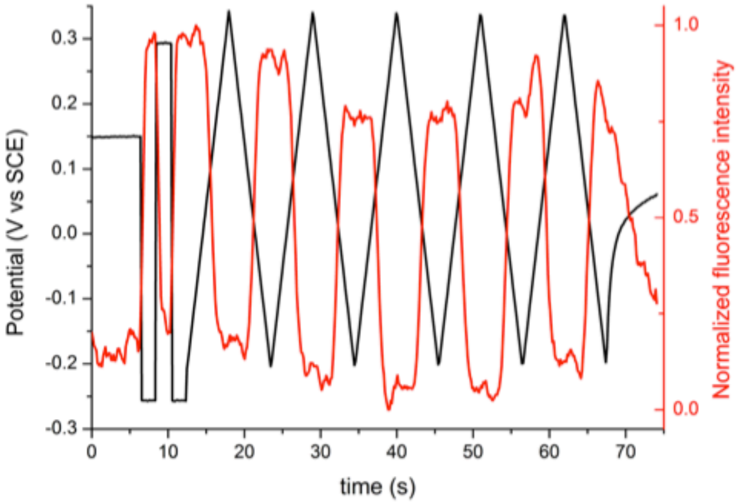

Figure 6.3: Alignment in time of the potential trace and the fluorescence intensity, acquired at v*=100* $m\ V\ s^{-1}$ *and* t_{exc} *=100 ms in MES 200 mM pH5.0.*

As illustrated in Figure 6.3, the beginning of the acquisition, prior to potential application, corresponds to a minimum fluorescence emission, indicating that, at open circuit potential, the Az molecules are in their “off” oxidized state. Application of the initial CA steps corresponds to a rapid and complete switch between the minimum and the maximum intensity levels, occurring in 1-3 frames. These were followed by the triangular wave of the CV, during which, as expected, the fluorescent emission varies with the same frequency and with direction opposite to the applied potential value.

The maximum fluorescence intensity occurs when all the redox-active Az molecules are in the reduced form, corresponding to the cathodic limit of the applied potential, vice versa the fluorescence shows a minimum value at the anodic potential limit. The extremes of the potential window correspond to a plateau level in photon emission, as all the responsive fluorescent switches are reduced/oxidized, indicating that the number of surface confined switches is constant.

Switching efficiencies were observed to vary across the surface between 25% and 50%, in good agreement with the changes seen for surface confined labelled molecules upon chemical switching in section 5.2.2.3 and previously on Cy5 labelled Az films.[100] The diminished Q with respect to solution values is thought to originate from the contribution of electronically uncoupled or inactive redox centres, from scattering by the metallic film[116] and from quenching effect of the gold surface in the nearby of the fluorophore[120] (at about 4 nm of distance) on the "ON" state of the switch.

6.2.1 The Fluorescent Cyclic Voltammogram (FCV)

For each ROI selected the normalized fluorescence intensity traces of the anodic and cathodic potential scans, reported versus the corresponding applied potential values result in a sigmoidal trace, as shown in Figure 6.4, which from here on will be referred to as Fluorescent Cyclic Voltammogram or FCV.

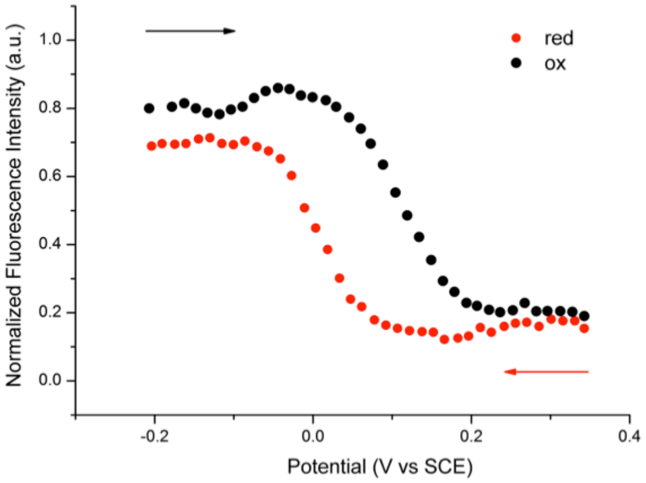

Figure 6.4: FCV determined for an area of $1 \times 1\ \mu m^2$ *containing ~ 8360 labelled Az molecules at 100 mV* s^{-1} *with an acquisition time of 100 mV* s^{-1}*.*

Each of the FCV scans obtained from subsections of several imaged areas could be similarly analysed to obtain an optical determination of the thermodynamic parameters of the contained samples of labelled Az. Acquisition parameters were adjusted to obtain a minimum of 15 frames per scan. At ν = 100 mV s^{-1} typically ~35 points were recorded so that fitting of the fluorescent traces could be accurately performed, as illustrated in the next section.

Optical FCVE$_0$ Determination

For each of the ROIs, the FCV plots (backward and forward) were fitted to a Boltzmann sigmoid (eq.6.1), adapted to describe the variation of fluorescence intensity. Boltzmann fitting is commonly used in electrophysiology to describe the potential-dependent opening of membrane ion channels as a function of the membrane depolarization.[205] The parallel with the ionic currents well suits our system, as the chromatic change of the copper ion in the Az molecules can be thought of as a potential dependent spectral gate for the emission of photons.

$$I = I_{min} + \frac{I_{min} - I_{max}}{1 + \exp\left(\frac{E - E_p}{dE}\right)} \tag{6.1}$$

In eq. 6.1, I_{min} and I_{max} are the right and left horizontal asymptotic values corresponding to minimum and maximum fluorescence intensity. The inflection point, E_p, corresponds to the potential of maximum rate of oxidation or reduction, respectively in the forward and backward scans of the FCV. The two E_0 will be hereafter referred to as $FCVE_a$ and $FCVE_c$ in correlation to the anodic (E_a) and cathodic (E_c) peak poentials of the conventional CV analysis.

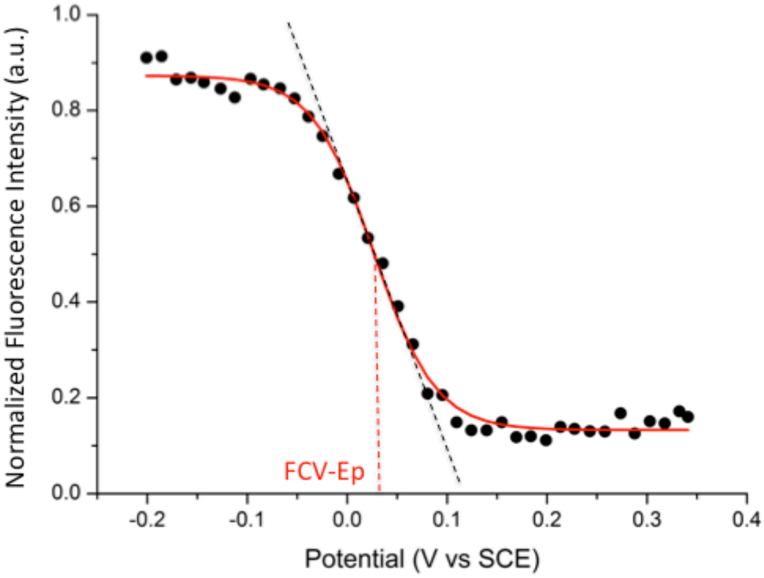

Figure 6.5: An example of sigmoidal fitting to a forward FCV scan, taken from the 3 × 3 pixel² time trace illustrated in Figure 6.3. Dotted lines indicate the potential $FCVE_p$ *(red) and the slope of the curve (black) at the inflection point.*

In Figure 6.5 the sigmoidal curve corresponds to the fraction of reduced Az molecules (in the “on” state) at each potential, therefore differentiation of the fitted traces, reported in Figure 6.6, results in peaks shaped similarly to a conventional CV plot. The fist derivative of the intensity traces can be easily fitted with a Gaussian model (eq 6.2), to extrapolate the FCV peaks positions and full width at half maximum (FWHM). The width of the peaks, for the ~14 zmoles samples contained in each of the analysed ROIs, as the one in Figure 6.5, fell within 15 mV from the theoretical value of 89.6 mV predicted for a monolayer of non interacting redox active molecules at 22°C.[206,207]

$$y(E) = y(E_p) + \frac{A}{FWHM\sqrt{\frac{\pi}{2}}} \exp\left[-2\frac{(E-E_p)^2}{FWHM^2}\right] \tag{6.2}$$

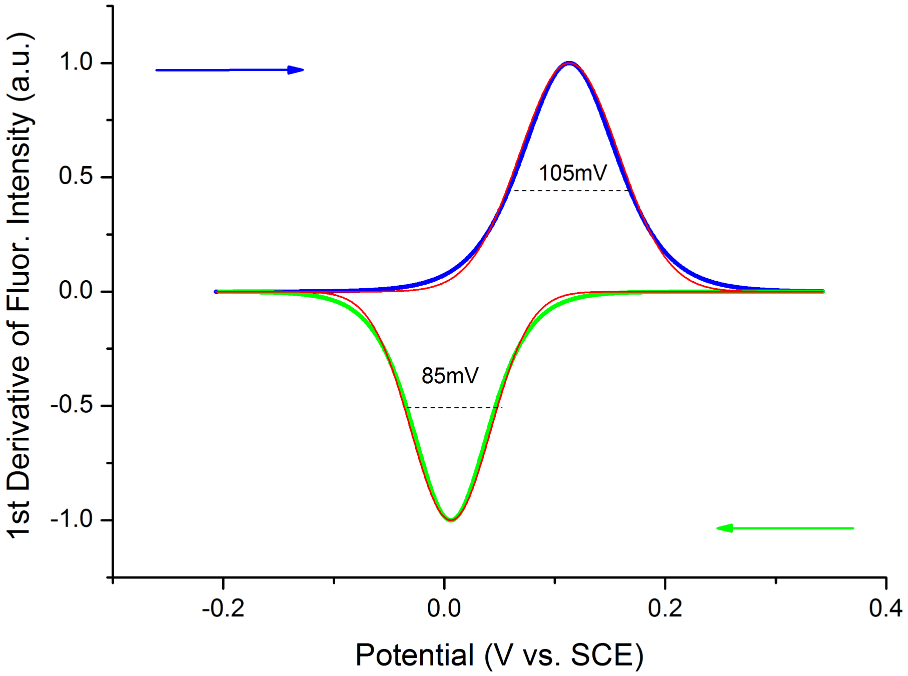

Figure 6.6: First derivative of the fluorescence intensity vs. potential trace (reported in the insert) results in an optical equivalent of the classical cyclic voltammogram. The derivatives of the oxidative and reductive process (in light and dark blue) were fitted with a Gaussian model (red dotted trace) to find the peak position and the FWHM values as reported in the plot.

After performing the fitting on each of the ROIs selected, the so-determined $FCVE_a$ and $FCVE_c$ positions were plotted in histograms, as the one reported in Figure 6.7, representing the analysis of ROIs from four stacks acquired at 100 mV s^{-1} on an octanethiol SAM in MES 200 mM pH 5.0. The optically determined midpoint potential, $FCVE_0$, was calculated for each couple of scans as in eq. 6.3:

$$FCVE_0 = \frac{FCVE_a + FCVE_c}{2} \tag{6.3}$$

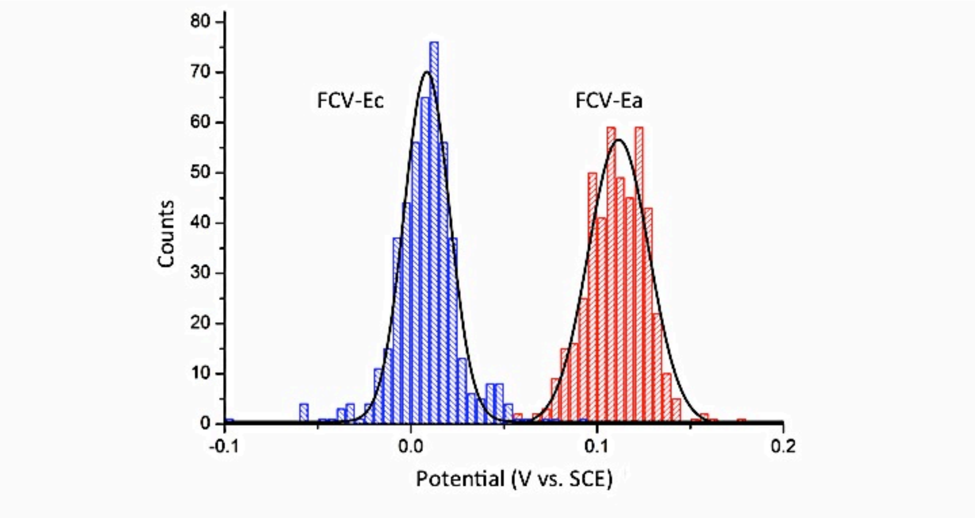

Figure 6.7: Distribution of $FCVE_c$ *and* $FCVE_a$ *obtained from the analysis of ROIs selected from four images of Atto655 Wt-Az immobilized at octanethiol-modified Au-OTE, at* ν *of 100m* $V\ s^{-1}$, *in pH 5.0 MES buffer 200 mM.*

At this relatively high surface coverage of electroactive molecules (in this example $4.5\ \times 10^{-12}$ moles cm^{-2} of which 28% were labelled) the electrochemical peaks positions correlated closely with the optically determined equivalents. Furthermore for the samples with lower coverage, where Faradaic peaks were undistinguishable from the capacitive currents, (therefore a coverage >1×10^{-12} moles cm^{-2} was assumed) the fluorescence signals could still be detected (see section 6.4).

The resulting distributions of midpoint potentials from ROIs, selected in four successive kinetic acquisitions taken at different locations are compared in Figure 6.8A and B (associated descriptive statistics listed in Table 6.2).

As mentioned earlier the four stacks of images were acquired while sweeping the electrode potential in two ranges across E_0 of Az, specifically -0.25V to +03V vs. SCE (sets of ROIs 1 and 2) and -0.3V to +0.25V vs. SCE (for sets 3 and 4).

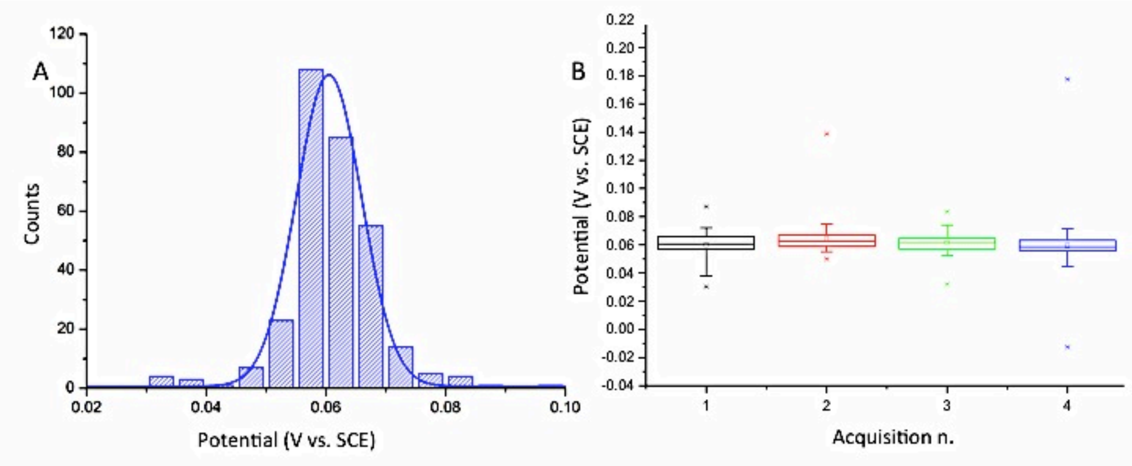

Figure 6.8: A) Cumulative distribution of FCVE$_0$ measured for four images acquired at different positions across a Au-OTE modified with octanethiol and a 1.28 pmol/cm^2 wt-Atto655-Az monolayer, acquired in pH5.0 in MES buffer. B) The FCV E$_0$ determined for the four different areas of an octanethiol-modified Au-OTE in pH5.0 MES buffer. Each of the boxes represents the midpoints of ROIs of 1×1 μm^2 *each, or ~8360 molecules; sets of ROIs 1-2 were selected from FCVs images taken in the potential range, (0.25V and -0.30 V vs.SCE) while sets 3-4 were acquired at (0.30 V and -0.25 V vs.SCE).*

	N total	FCVE$_0$ (mV vs. SCE)	SD (mV)	FWHM (mV)
1	**53**	**59.8**	**11.1**	**26.2**
2	**83**	**64.2**	**10.2**	**24.0**
3	**93**	**61.3**	**7.1**	**16.6**
4	**96**	**59.6**	**16.7**	**39.4**

Table 6.2: Optically determined midpoint potentials for Az monolayers on octanethiol, corresponding to the data in Figure 6.8. Data 1 and 2 were two acquisitions carried out in the potential window (0.25 V to -0.30 V vs. SCE) data in line 3 and 4 were acquired at (0.30 V to -0.25 V vs. SCE).

In Table 6.2 the potential distribution obtained for four different acquisitions. Despite the variation of the investigated potential window, the resulting FCVE$_0$ fell within one standard deviation from one another (Figure 6.8B). The comparison reinforces the validity of FCV in determining the redox potential of the zeptomole samples monitored. In the next sections, the technique will be used to explore the response of surface confined Az population while varying the buffer pH and the applied ν, for which shift in the peaks position is expected.

6.3 Microheterogeneity effects on the surface confined switches

6.3.1 Origins of the pH effect on the Az electrochemistry

It has been shown in the previous section that FCV allows determination of the $FCVE_0$ of molecules with close correspondence to the electrochemical analogous; in this section, effects of the variation of the experimental conditions are explored, in particular the effect of variation in the pH of the electrolyte solution.

The electron transfer characteristics of surface confined metallo proteins are strongly affected by changes in the chemical groups in the first and second coordination sphere of the active site.[208] It is known that many cupredoxins, at low pH, undergo an important structural reorganization of the T1 site, with dissociation of the Nδ of the C-terminal histidine ligand, which is the electrical connection between the T1 centre and the surface of the protein, from the reduced copper.[208,209] Such an important change causes a great increase in the reduction potential, substantially causing a 'redox inactive' state.[150,208]

In contrast with all other blue copper proteins, Az retains a stable coordination of the homologous His117 residue, with much smaller change of the first coordination sphere.[210] Insights into Az peculiar behaviour were gained especially by studying the cavity mutant H117G[208,210] and by genetically engineering the surface exposed loop in which the His 117 and two other copper ligands (Cys 112 and Met 121) are located.[211,212] Despite the smaller structural change, the E_0 and ET rate of Az vary considerably as a function of pH. Both soluble and surface confined Az molecules, in the high pH form, are faster in transferring electrons to enzymatic partners[213] or to the electrode.[159] At the same time the transition to low pH form is accompanied by a nearly 100 mV anodic shift in E_0.[97,154,159] In this section of the thesis FCV was used to investigate the shift in E_0 induced by change in pH of the solution. The described pH dependence, which is scarcely sensitive to ionic strength variation due to compensative contributions from the enthalpic and entropic factors[159], could be useful to either finely control the potential at which the optical switch takes place or for construction of pH responsive surfaces.

6.3.1.1 Shift in the FCVE$_0$ Position

FCV acquisitions were performed as presented in the previous section, on an Atto655-Az monolayer at octanethiol SAM in the following buffers:

- MES 200 mM buffer pH5.0 and pH6.0,
- Sodium Phosphate Buffer 200 mM at pH7.0
- TRIS 200 mM buffer at pH10.5.

In agreement with what expected, a cathodic shift in the position of the FCV sigmoidal curves was observed (as exemplified in Figure 6.9) upon increasing the buffer pH from 5.0 to 10.5.

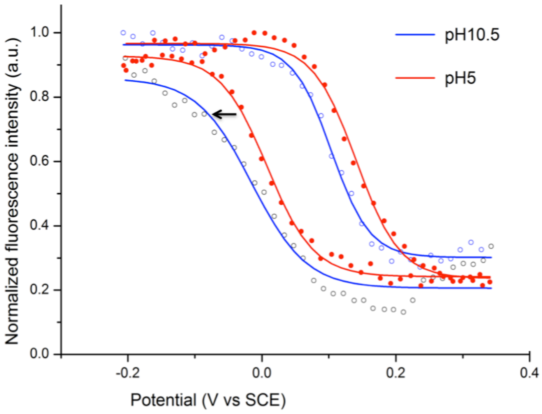

Figure 6.9: Two typical FCV curves determined for wt Atto655-Az confined on Au-OTE at ~5 $\times 10^{-12}$ mol cm^{-2} at the two pH extremes showing the shift of the optical signal to lower potentials for higher pH.

As in the previous section the distribution of $FCVE_0$ was constructed from four images acquired at each pH and the resulting $FCVE_0$ histograms are illustrated in Figure 6.10 for pH 10.5, 7.0, 6.0 and 5.0.

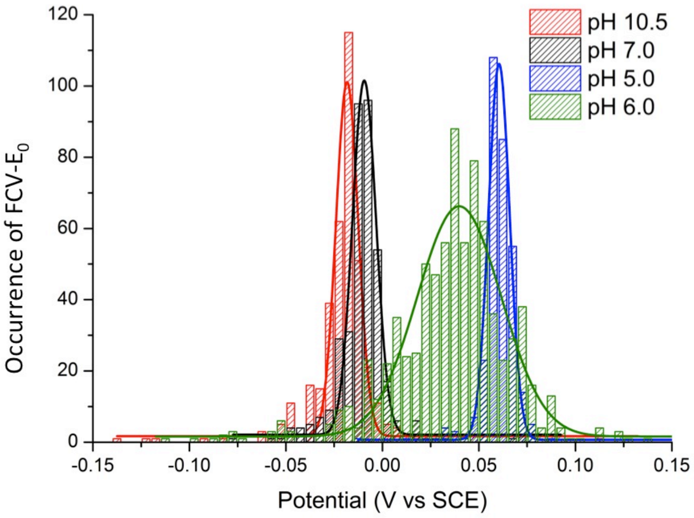

Figure 6.10: Histograms of midpoint potential distribution for the FCVs measured at four different pH values, the data were acquired at 100 mV s^{-1} in the potential window (-0.25V to +0.30V vs. SCE).

Once again the analysis confirmed that the $FCVE_0$ closely corresponded to the CV equivalents. Varying the pH from 5.0 to 10.5 resulted in a change of nearly 80 mV in the $FCVE_0$ and of 90 mV for the correspondent E_0 in agreement with previous reports based on CV and spectroelectrochemistry. The close relationship of the CV and FCV sets of values is clearly visible in Figure 6.11 and Table 6.3.

Previous work has shown, the ΔE_0 changing with pH was attributed to the influence of acid/base equilibria of residues in the second sphere of coordination.[154,159] Protonation of His35 located in a crevice close to the T1 and (to a lesser extent) of His83 accompanied by a conformational change due to a peptide bond flip,[214] are thought to be responsible for most part of the pH-dependency observed between pH 5 and 7.[159,213]

The pH dependence of the reduction potential is described by two dissociation constants, one for the reduced ($pK_{a,red}$) and one for the oxidized ($pK_{a,ox}$) form of the protein.

$$E_{0,(pH)} = E_{0,low\ pH} + \frac{RT}{nF} ln\left(\frac{(K_{a,red}+[H^+])}{(K_{a,ox}+[H^+])}\right) \tag{6.4}$$

Non-linear least square fit of the redox potentials to equation 6.4 allows to calculate the two values[215]: $pK_{a,red}$ of 7.0 and 6.9 and $pK_{a,ox}$ of 5.5 and 5.7 were found respectively for the CV and FCV acquisitions. These constants broadly fall within the range of values reported for Az wild type ($pK_{a,red}$=7.1; $pK_{a,ox}$=6.2) and its mutants[215], although a higher discrepancy (~0.5pH) in the oxidized state is observed.[159,215] This is possibly due to the different buffers used, which strongly influence the transition. The CV and FCV pK_a values within our measurement are in better agreement, with only a minor decrease in pK_a (~0.1-0.2pH) determined by FCV.

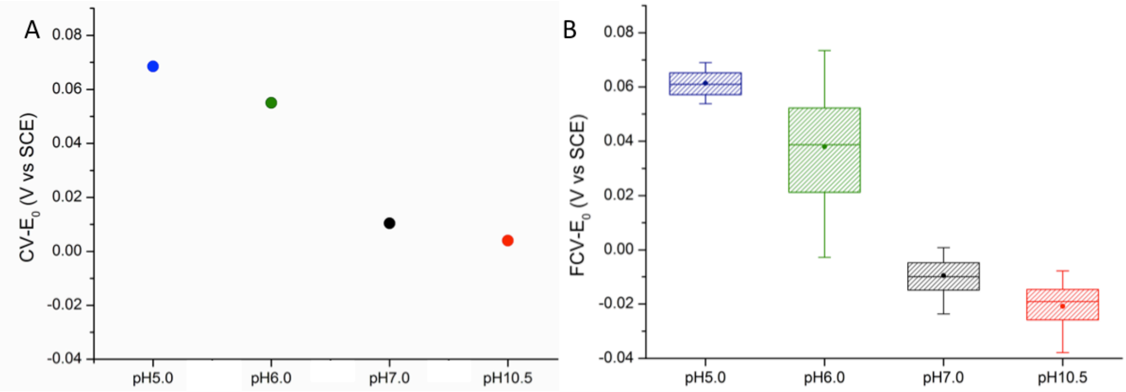

Figure 6.11: A) Plot of the conventional CV-E$_0$ potentials at different buffer pH values, compared, in B) with the corresponding optically determined FCV E$_0$. Values are reported for comparison in Table 6.3.

In Figure 6.11 it is possible to note that a larger distribution is observed at pH 6 with respect to the other measurements. The origin of this spread is unclear. One plausible cause might be the higher sensitivity, in proximity of the pK$_a$ of the histidine residues, to small variations in the pH, which may occur during the time of the measurement. It is also interesting to note that, while in acidic environment the CV and FCV redox potential closely corresponded, at increasing pH, $FCVE_0$ is about 10 mV higher than the electrochemical one. The ~10 mV potential shift might be linked to small superficial changes occurring in the labelled Az molecules in transition to the high pH form.

		CV (mV vs. SCE)			FCV (mV vs. SCE)		
pH	**Buffer**	**Ec**	**Ea**	**E0**	**$FCVE_c$**	**$FCVE_a$**	**$FCVE_0$**
5.0	**MES**	**63.4**	**73.5**	**68.45**	**16**	**119.1**	**68.0**
6.0	**MES**	**48.9**	**61.5**	**55.2**	**-113.3**	**199.6**	**43.5**
7.0	**PB**	**-4.6**	**25.4**	**10.4**	**-56.4**	**52.5**	**21.9**
10.5	**Tris**	**-12.1**	**20.2**	**4.05**	**-62.8**	**42.6**	**21.0**

Table 6.3: Thermodynamic parameters determined at different pH values for Atto655 labelled wt-Az immobilized at octanethiol monolayers, compared with the electrochemically determined potentials.

Small changes in the photophysics of the Atto655 dye with variation in pH have been reported in lifetime imaging SM studies and are mainly consistent in a increased duration of redox-linked "OFF" times in acidic conditions.[216,217] However, as variation in fluorescence intensity studied here is normalized, such variations, which affect only the fluorescence intensity are expected to be secondary.

It can be concluded that the FCV analysis can be used to obtain detailed thermodynamic information about subtle variation in the electrochemistry of the surface confined molecules localized within diffraction limited spots, with sensitivity in the potential dimension[218], close to the thin film voltammetry determined values.

6.3.2 Determination of Electron Transfer Rate by FCV

Determination of the k_{ET} of redox SAMs by CV is commonly accomplished by fitting the Faradaic peak-to-peak separation at increasing ν to Butler-Volmer equations (see section 3.2). An analogous procedure can be applied to FCV enabling the mapping of the kinetic components.[100]

Az molecules immobilized on short alkanethiols SAMs (less than 8 methylene units) exchange electrons with the gold as fast as ~$10^3 s^{-1}$, with variations depending on the pH of the buffer. In these conditions the process is too fast to be investigated by FCV as the peaks start to separate only at ν above 1-10 V s^{-1}. However on thicker SAMs the k_{ET} decays, as described by the relationship in eq, 6.5.

$$k_{ET} = k_0 \exp\left(-\beta d\right) \qquad (6.5)$$

Where d is the distance between the redox active centre and the electrode, k_0 is the extrapolated value of the rate constant at zero distance and β is a decay constant specific to the SAM considered (see Chapter 7).

The test presented here was performed on labelled Az physisorbed on a dodecanethiol SAM, where the k_{ET} is expected to be ~$100 s^{-1}$ and therefore separation between the FCV-E_p potentials should vary in a range accessible by FCV. Traces obtained by analysis of a full image (13 × 13μm^2) acquired at ν of 50, 200 and 300m V s^{-1} are displayed in Figure 6.12.

As expected the traces of the FCVs started to separate at increasing ν and fitting of the resulting “trumpet plot” (Figure 6.12D), performed using Jellyfit software (written by Dr Lars Jeuken), allows extrapolating an k_{ET} of ~1.5 s^{-1}. The value is lower than the $80s^{-1}$ found for the wild type Az on the same buffer and SAM by normal CV on a gold disk electrode (see Chapter 7).

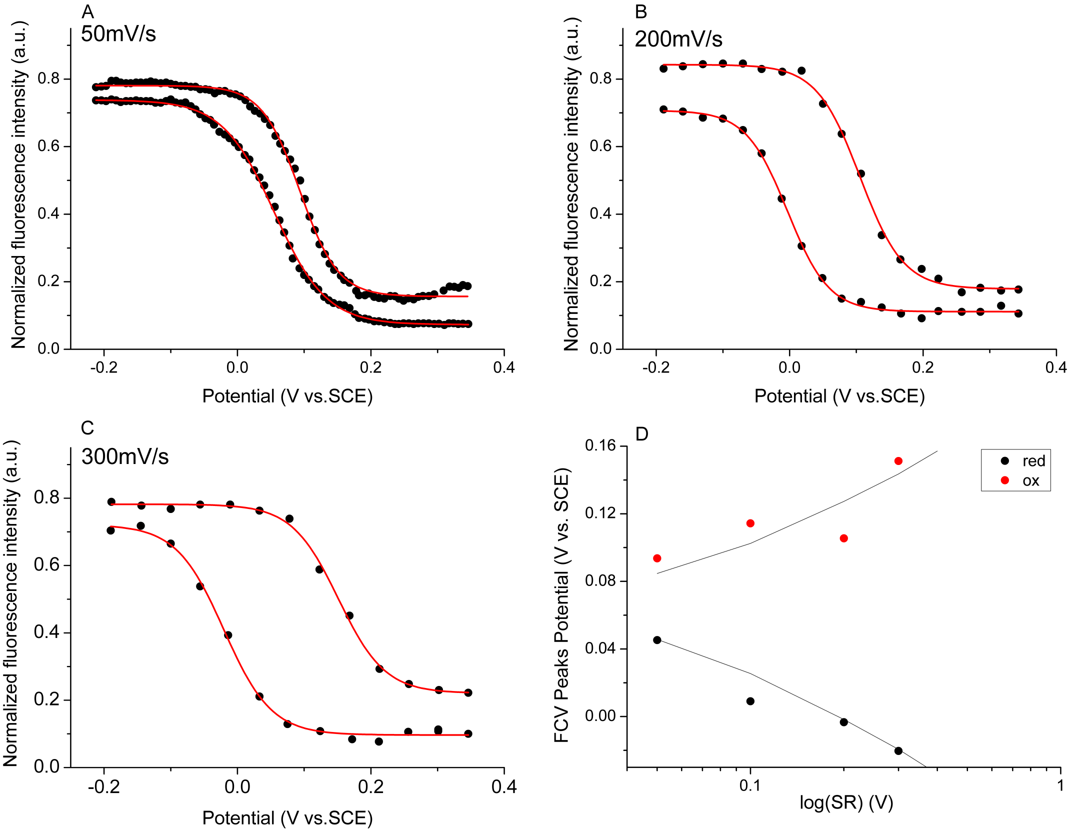

Figure 6.12: Kinetic FCV acquisitions on a dodecanethiol monolayer display increasing peak-to-peak separation at increasing v. Traces were acquired from analysis of 13×13 μm^2 *areas (containing* 3×10^6 *molecules) in 200 mM MES buffer at pH 5.0: A)*v = *50* $mV\ s^{-1}$*, B)* v = *200* $mV\ s^{-1}$ *C)* v = *300* $mV\ s^{-1}$ *D) Trumpet plot showing the position of the FCV-*E_0*, the grey traces represent the simulation of the peak separation with a* k_{ET} *value of 1.5* s^{-1}*.*

Therefore, the diminished ET rate determined by FCV, also observed previously with Cy5 labelling[100], hints at a bias of the FCV towards molecules that are located at a higher distance from the gold surface and are thus less sensitive to the metal quenching effect. The observation correlates with the AFM reports (Chapter 5) of some level of aggregation of the surface confined molecules. It can be deduced that the kinetic analysis obtained by FCV can give insights into the distance of the investigated molecules from the surface.

6.3.2.1 Aggregation in Azurin Monolayers

Using a dodecanethiol SAM thickness of 1.6 nm, taken from the literature [81], and assuming that Az molecules are oriented with the hydrophobic patch on the surface and the label on the N terminus towards the solution (at 3.8 ± 0.5 nm from the hydrophobic patch), it is possible to estimate a distance $d_1$of 5.4 ± 0.5 nm between the dye and the surface of the gold (Figure 6.13A). The copper in this configuration is close to the SAM surface and, accordingly to what was determined for the unlabelled wild type Az (see Chapter 7), a k_{ET} constant of 80s^{-1} is expected.

From eq. 6.5 and using a β decay of 1.02 Å^{-1}, a crude estimate of the average shift in position of the T1 centres of the responding Az can be given, with respect to those in the ideal layer of the model, which have their T1 close to the 1.6 nm thick SAM.

The average increase in the tunnelling distance for the ET to occur with the optically estimated frequency of 1.5 s^{-1} is about Δd = 0.4 ± 0.1 nm. This distance is relatively small when compared to the size of Az, which is 2.5 × 3.5 × 4.0 nm.

It is also possible to imagine the presence of a second layer of molecules (Figure 6.13C) with their label located at a further 3.5 nm from the gold, at a $d_2$of about 8.9 nm. Following Yun's model the quenching efficiency on the dyes at d_1 is >95%, and it decreases to ~65% at d_2, therefore a seven fold increased emission from a second layer would be expected. Note, however that molecules in the second layer will have their T1 sites at ~4 nm from the metal, distance at which the k_{ET} tends to zero. Therefore two possible conclusions are suggested:

- the optically responding molecules may be located in intermediate positions between the first and the second layer with non optimal orientation for the ET, but in an optically privileged position with respect to the first layer;
- other electronic pathways might be involved, such as intermolecular ET between the first and second protein layer.

To better test the electronic coupling of the Az switches with the gold, however, technical solutions allowing collection of a higher number of optical points for each scan would be beneficial, so that a comparison with kinetic determination via other techniques (such as chronoamperometry) and CV scanning in a wider range of ν may become possible.

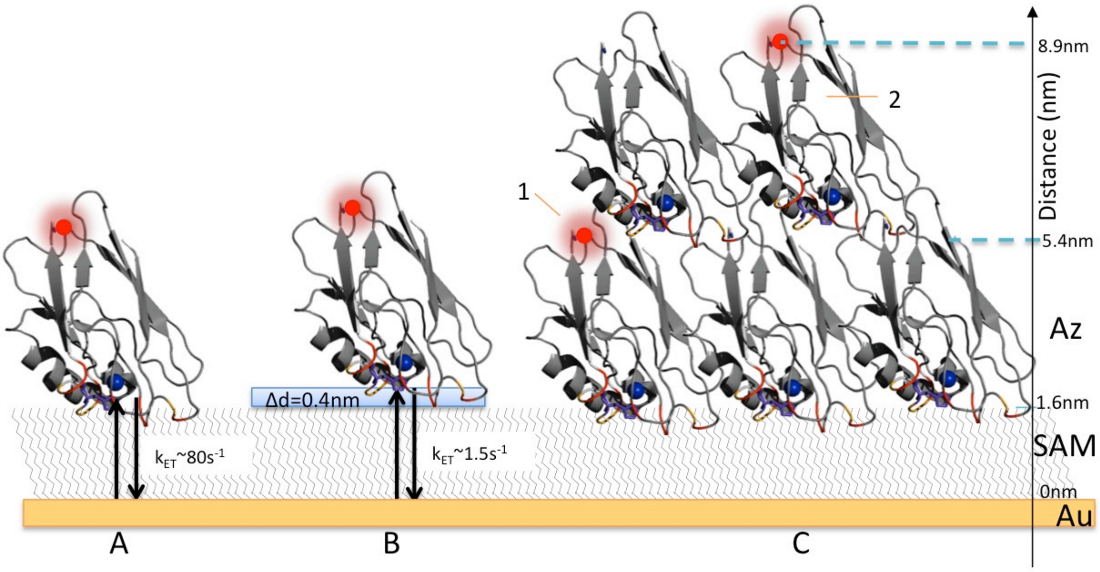

Figure 6.13: Schematic of the possible positions of labelled Az molecules with respect to the surface of the dodecanethiol SAM. A) The expected ideal position of Az with the hydrophobic patch (residues highlighted in red) close to the interface SAM/solution. B) At the position expected for a k_{ET} *of* $1.5\ s^{-1}$*. C) Possible model of aggregation of Az with two layers (1 and 2) r of Az molecules with homogeneous orientation. An attempt to evaluate the increase in fluorescence emission with distance can be made using the model for the decay of quenching efficiency proposed by Yun.*[121]

6.4 Variation in FCVE_0 dispersion

Variance in the orientation and in the microenvironment surrounding the surface confined electro-active molecules, in addition to irregularities in the self assembled crystalline monolayer and in the underlying gold surface, can result in spread in the redox behaviour of the surface confined molecules. One of the main consequences of such heterogeneity, both in the redox potentials and in the electronic coupling with the surface, is broadening of the voltammetric peaks.

The resulting dispersion/distribution of kinetic and thermodynamic properties within the population has been studied in the past by mathematically manipulating the non-idealities of electrochemical responses of signals arising from typically pico to nanomoles samples.[34,199,219] Therefore these measurements result from the average of the contributions of a large number of molecules, respectively 10^{12} to 10^{15}electron transfer proteins assuming a one-electron reaction, as in the case of cytochrome *c* and azurin.

FCV offers a step towards filling this gap by both spatially resolving the electrochemical reactions, with potential for translating the acquired image into a map of "optical currents", and by reducing the number of sampled molecules of several orders of magnitude with respect to typical electrochemical measurements, ideally aiming to SM resolution.

As seen so far in the chapter, the detection of the emitted photons is limited (mainly) by the absorption and quenching effect of the conductive layer, making necessary the use of a crystalline self assembled alkanethiol monolayer to allow sufficient photon counts by controlling the distance between the quenching surface and the dye. Interestingly the variation of the SAM thickness also offers a convenient way to control the electronic coupling of the surface confined electroactive protein layers with the electrode.[18,153,177,220]

As mentioned in the introductory chapter (section 1.4), the driving force for formation of the two dimensional arrangement of the linear thiol molecules at the interface originates both from the sulphur binding to the gold and from lateral interactions between the aliphatic chains. Therefore in thicker SAMs the crystallinity of the monolayer increases, as indirectly suggested by the contact angles measurements (Chapter 5).[81]

In this section the FCV of Az monolayers at two different SAMs thicknesses is compared. The aim of the experiment is to investigate the effect of the distance and of the increased order of the SAM film on the optical response of Az.

The effect of such a variation on the FCV output has been analysed on more diluted submonolayers, obtained after immobilization of a 100 nM wt Az-Atto655 solution (200 mM Phosphate Buffer, pH7.0) on two different SAMs, octanethiol and dodecanethiol. The decrease in the number of electro-active molecules on the surface well matched with the decrease of the CV peaks, which became indistinguishable from the capacitive currents, with an estimated surface concentration > 1×10^{-12} moles cm^{-2}. As reported in Chapter 5, at these lower concentrations the fluorescence intensity becomes discontinuous with presence of brighter spots on the surface, which are estimated to contain less than 500 molecules each.

After manual selection of these brighter spots in 5 × 5 pixel^2 ROIs (50-100 per image), sigmoidal fitting and plotting of resulting distribution of the FCVE$_0$ resulted in the histograms in Figure 6.14.

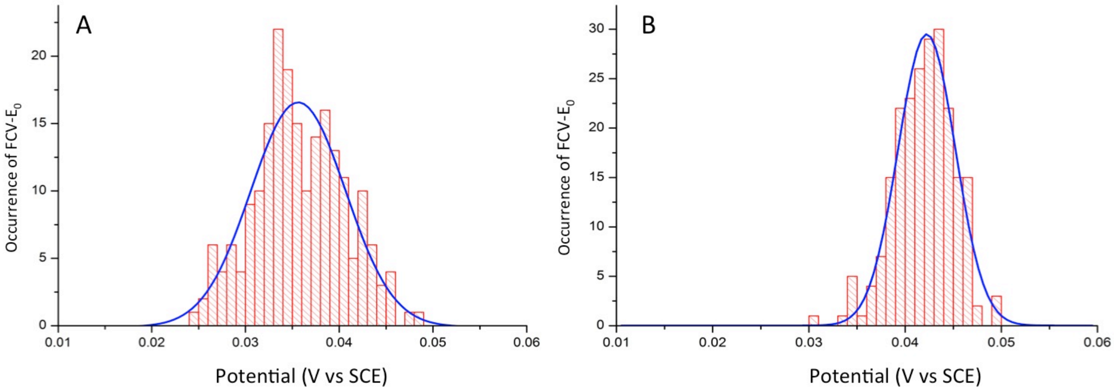

Figure 6.14: A- Distribution of $FCV\,E_0$ *at octanethiol-modified Au-OTEs and B- on dodecanethiol SAMs.*

On octanethiol, these diluted protein layers were found to present a larger spread of midpoint potential than on dodecanethiol. Gaussian fitting of the histograms reported a FWHM of 13 mV, matching with the one observed on more concentrated SAMs in Figure 6.8 and Figure 6.10. The FWHM decreased to 8 mV on dodecanethiol, suggesting a role of the SAM thickness in controlling the distribution of the thermodynamic properties of the protein population. Further work by Dr. Amol Patil, applying a similar analysis to a range of SAMs varying between 5 and 11 methylene units, indeed confirmed that increase in the SAM thickness is associated with a 30% decrease in the spread of the FCV potentials, with a maximum change between octanethiol and decanethiol.[203]

It is therefore possible to conclude that the increased order in the SAM/protein monolayer is reflected in a lower thermodynamic dispersion in the redox response of the labelled Az molecules as monitored by FCV.[203] However, as the increasing distance is also affecting other parameters of the measurement (such as the fluorescence quenching by the gold and the force of electric interfacial field) it is likely the observed decrease in the Gaussians width might have contributions from other, less easily segmentable, elements. In the attempt to gain further insight on this issue, in the next section the effect of the voltage scan on layers of non electro-active, labelled zinc Az molecules were analysed, after physisorption on SAMs of different length.

6.5 Field modulated protein motion

The electro inactive, zinc substituted form of Az, already used as a control in fluorescence spectroscopy experiments in Chapter 5, is completely devoid of any optical absorption band above 300 nm. As a consequence, after labelling, zinc Az does not undergo any FRET dependent phenomenon correlated to redox change. Physisorption of labelled zinc Az on a SAM modified Au-OTE therefore offers in an equivalent of the system investigated in the previous sections, in which all the molecular switches are locked in their “on” state. This configuration allows further segmentation of the components affecting the interfacial electron transfer, through comparison between the behaviour of the redox active and the redox inactive films.

The resemblance of the molecular layers is warranted by the high similarity of the Zn^{2+} and Cu^{2+} protein surface. In fact crystal structure alignment (PDB entry codes 4AZU and 1E67) shows that substitution of the copper ion with zinc has negligible effects on the overall protein folding[221,222], thus protein surface and physisorption dynamics, in the same experimental conditions, are expected to be similar.

6.5.1 Non-FRET potential modulation

As for any insulating film, a complete absence of Faradaic peaks in the CV and of potential modulation in the FCV traces is expected. However, while this is indeed the case for the CV signal (between -0.3V and 0.3V vs. SCE), analysis of the FCV traces revealed a small potential dependence of the fluorescence intensity, with a typical fluctuation of 5-15% of the initial intensity value (Figure 6.15).

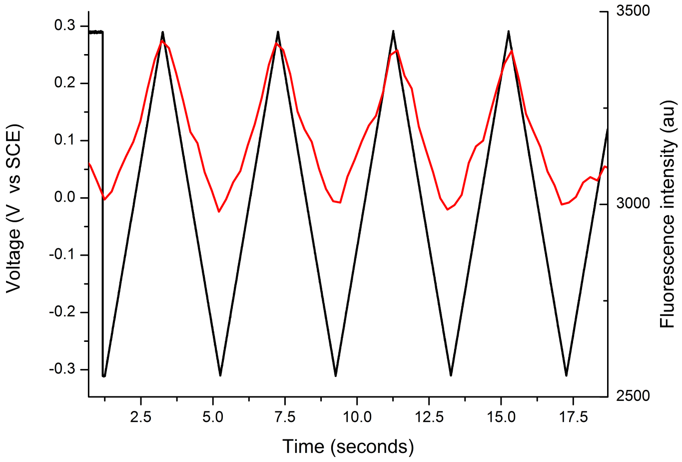

Figure 6.15: The fluorescence potential modulation observed at zinc Az films in buffer at pH 7 (1 μ M, 1hr deposition time) at decanethiol electrodes, the periodical signal is linear with the applied potential, therefore in opposite direction to the profile of Figure 6.3, and the size of switching is smaller (5-15% of the maximum fluorescence intensity) of the switch observed at copper Az monolayers.

The most likely reasons for the observed intensity fluctuation are:

- Sensitivity of the fluorescent probe to the varying interfacial electric field
- Changes in the optical properties of the gold film induced by variation of the Fermi energy level under electrochemical control: this in particular might affect the excitation of surface plasmons in the TIRF configuration and/or modulate the quenching properties of the metallic film.

- A motion/deformation of the molecule in the z axis due to the force imparted by the electric field, generated at the electrode/electrolyte interface by the applied potential, on the net charge on the protein.[123] This might result either in a deformation (in a compression/release model) or, as the charges are confined on the surface of Az, in a rotational oscillation of the protein on the surface. In both cases the motion of the label closer to the gold would result in a reduction of the emitted fluorescence due to increased energy transfer to the metallic film.

Of these three hypotheses, the first was readily discarded after observing that a film of Atto655 dye molecules, physisorbed on an octanethiol SAM didn't show any sensitivity to variation of the electric field between -0.3 to +0.3 V vs. SCE. Although the extent of surface-plasmon related effects on the detected fluorescence intensity in these conditions is unknown, as well as the correlation between quenching efficiency and Fermi energy level, observation of a stable signal from the octanethiol+Atto655 film is also indicative of little perturbation of the fluorescence due to the potential applied to the metal between the considered extremes. The third hypothesis can be more finely investigated by varying the intensity of the electric field exerted on the protein structure, and the model for the interpretation of the results can be derived from existing work on DNA-SAMs motion in variable electric fields[122] and referring to the Gouy-Chapman-Stern (GCS) model of electrical double layer at the electrode/electrolyte interface.[136]

6.5.1.1 Effects of the Interfacial Electric Field

According to Gouy-Chapman-Stern theory, the interfacial potential (ϕ) decays in the solution with an exponential profile: $\phi = \phi_0 e^{-\kappa d}$, where ϕ_0 is the potential at the electrode surface, κ is the inverse of the Debye length and d is the distance from the surface.[136] Knowing the potential and the ionic strength of the solutions it is therefore possible to determine the electric field E at every position by means of eq. 6.5[136]:

$$E = -\left(\frac{8kTn^0}{\varepsilon\varepsilon_0}\right)^{\frac{1}{2}} \sinh\left(\frac{ze\phi}{2kT}\right) \tag{6.5}$$

Where n^0 is the number concentration of ions in solution, ε is the dielectric constant of the electrolyte, z is the charge on the ions and all other symbols have their usual meanings.

The dependence of the E on the buffer concentration and on the potential means that the depth of the profile decay in the solution and the electrical force exerted on the protein film can be finely tuned by varying these two parameters.

6.5.1.2 Variation in Buffer Concentration and ν

Results of acquisitions performed in 10, 50, 100 and 200 mM phosphate buffer for zinc Az films on octanethiol and heptanethiol are reported in Figure 6.16A.

Despite the large variation from area to area in the obtained Q, which is reflected in the large error bars, it is possible to observe that the extent of the potential modulation decays both with the increasing buffer concentration and with the increasing d. Higher Q values were obtained in particular on the heptanethiol and octanethiol SAMs, whereas zinc Az layers immobilized on decanethiol and dodecanethiol SAM did not show any distinguishable fluorescence modulation (data were therefore not plotted in Figure 6.16).

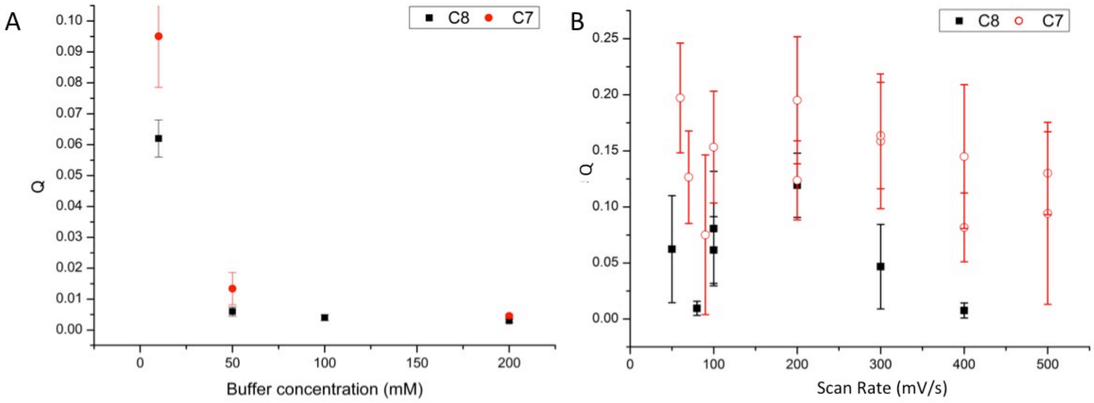

Figure 6.16: Investigation in non-redox potential modulation effects on monolayers of labelled zinc Az at SAM-coated Au-OTEs. A) Dependence of the switching efficiency Q on the buffer concentration for a octanethiol SAM, at $\nu = 100 m V s^{-1}$ *(ROIs from 3 images analysed per each buffer concentration) B) Q obtained from the analysis of heptanethiol and octanethiol SAMs compared in 10 mM buffer, for the thicker decanethiol and dodecanethiol Q of 1-0% were recorded, therefore the relative points are not displayed on the chart.*

The decay of Q with the concentration of the buffer suggests that in the previously presented results on redox active layers (in section 6.3), effects of the molecular motion were minimized due to the relatively high ionic strengths used during the acquisitions (200 mM buffers). The trend is explained with the shielding effect that both thicker insulating SAMs and more concentrated ionic atmospheres surrounding the proteins have on the decay of the interfacial electric field in the solution.

A similar dependence of Q on the buffer concentration was also found in FCV studies performed on non-FRET switching Atto550-cytochrome *c* probes (data not shown) and was observed in monolayers of covalently bound laccase (Chapter 8).

6.6 Reductive Desorption of the Atto655-Az SAM film

At anodic potentials the Reductive Desorption (RD) of the thiolate self-assembled monolayer occurs, with the following reaction:

$$RSAu + e^{-} \rightarrow RS^{-} + Au \qquad (6.5)$$

The reaction in 6.5 provides a simple and effective tool to measure the number of thiols on the surface, which can be quantified by applying a linear potential sweep in basic solution. This produces a single cathodic wave for the reduction of the thiolate layer typically between -0.5 and -1.5V vs. SCE, with the exact potential of the current peak depending both on the lateral interactions between adjacent molecules in the film and on the strength of the gold-sulphur bond.[81] The integral of the of the RD peak reports on the surface coverage, Γ, by way of the simple relationship $Q = nFA\,\Gamma$, where Q is the total charge passed, n is the number of electrons involved in reaction 6.5 and A and F are the electrode area and the Faraday constant. Surface coverages reported for the reductive desorption of linear alkanethiolate SAMs from gold are typically close to 75 μC cm^{-2}, i.e. 0.77×10^{-9} moles cm^{-2}, which corresponds to $\sqrt{3} \times \sqrt{3}$ packing on the surface of Au (111). Similarly to the optical FCV determination it is possible to evaluate the surface distribution of the reductive desorption by analysing the time traces for several areas of the electrode.

In the past a combination of epifluorescence microscopy and RD has been used, by Bizzotto and co-workers,[67-70] to map the stripping of fluorescent SAMs from different terraces of single crystals on flame annealed gold beads. As the fluorescent molecules were desorbed from the surface and diffused away in the solution, a peak in fluorescence intensity was observed, due to the unquenched emission of the dyes as the distance between the emitters and the metallic surface increased, followed by a decay when the molecules diffused away from the surface in the bulk of the solutions.[70]

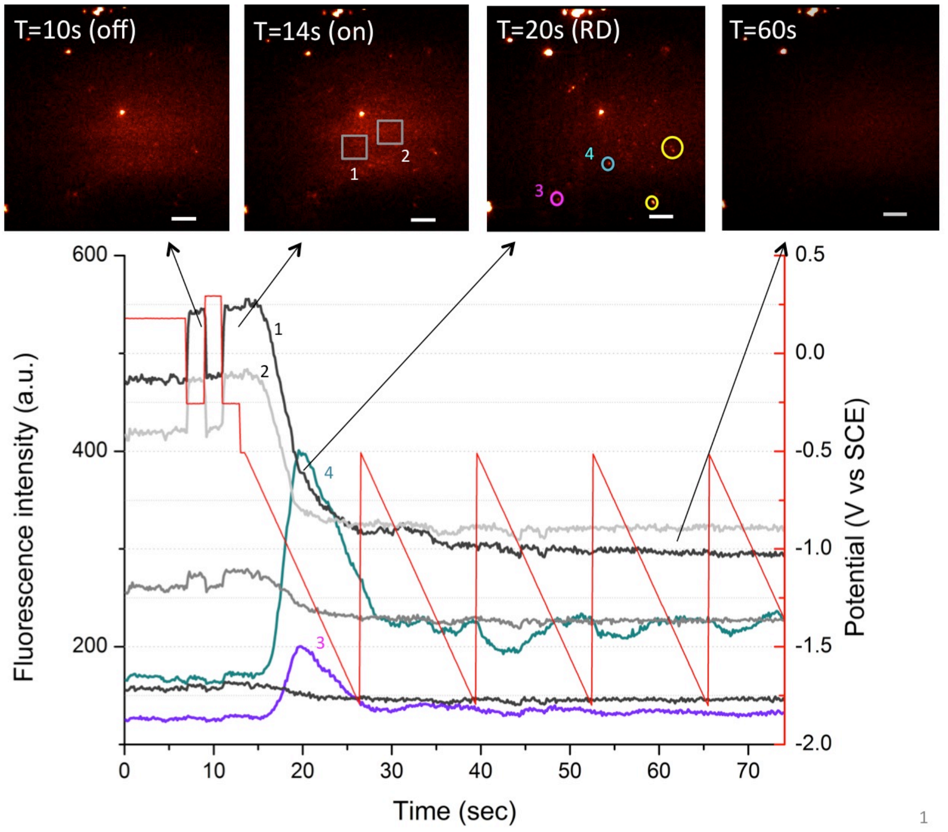

Figure 6.17: Time traces of the linear sweep of the reductive desorption of wt-Az labelled withAtto655 on a octanethiol SAM, the electrolyte was 0.5 M NaOH, deoxygenated with Argon prior to use, showing heterogeneity of response in different ROIs within the imaged area: the homogeneous emission in ROIs 1 and 2 desorbed un synchronous with the electrochemical current peak, while areas reported in the circles 3 and 4 present atypical desorption, with formation of aggregates.

The anodic stripping by FCV of Az on octanethiol is illustrated for ROIs in Figure 6.17. The simultaneously collected electrochemical current (Figure 6.18A) presented a well-defined cathodic peak at -759 mV vs. SCE. The integration of the peak, reported a charge of 1.46 × 10^{-5} C, equivalent to the desorption of 1.21 × 10^{-9} moles of thiols per cm^2. Such a coverage is higher than what usually found on gold (111) and for polycrystalline GDEs (typically 0.6-0.9 ×10^{-9} moles cm^{-2}), however it has to be considered that on Au-OTE the coverage was calculated on the geometrical and not on the electroactive area, thus the increase is expected due to the surface roughness.

The position of the electrochemical peak corresponds to a steep decrease in the fluorescence intensity, as represented by the gray traces in Figure 6.18.

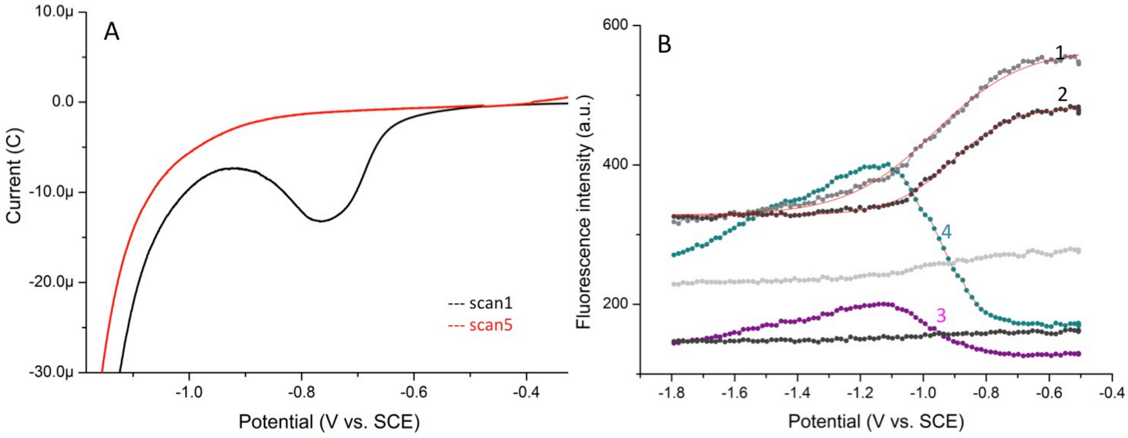

Figure 6.18: Reductive desorption peak for an Au-OTE and Atto655-Az. A) Electrochemical peak of the RD, B) associated fluorescent traces (colours corresponding to the areas selected in Figure 6.17). The optical reductive desorption line correspond to the ROIs highlighted in Figure 6.17.

In most of the traces the fluorescence intensity simply decayed from its maximum value, starting at the potential of approximately -650 mV vs. SCE and with a flex at -800 mV, close to the RD peak potential. After desorption, the fluorescent signal quickly decayed as the probes were travelling outside of the excitation volume of the TIRF and were not influenced by the following potential sweeps.

In this case the behaviour of the grey traces (1 and 2 in figure 6.18) is different from what reported by Bizzotto *et al.* [69,70,223] This could be due to the much lower surface concentration (of about three orders of magnitude) of fluorescently labelled Az with respect to the continuous layer of fluorescent thiols used in Bizzotto's work and in the different diffusion. However it can be noticed in Figure 6.17 that a few areas responded in a different way (for example areas 3 and 4 in Figure 6.17), showing an emission maximum when the electrode reached the potential of -1.12 V vs. SCE. At the corresponding potential a series of brighter spots could be clearly observed (in circles 3 and 4 in Figure 6.17), suggesting the formation of aggregates during the desorption process, which abandon the surface at a higher potential than the rest of the monolayer and without immediate dilution in the solution. The presence of distinguishable optical signals in the FCV-RD is interesting as in the future it might be used for discrimination of micropatterned areas and help in the interpretation of stripping currents.

From the aligned intensity-potential traces it is also clear that the layer of labelled protein was completely desorbed during the first linear sweep, after which the collected light stabilized on a minimum constant value, insensitive to further potential sweeps, as the thiol molecules diffused far in the solution.

6.7 Summary and Conclusions on Azurin FCV

FCV, applied to redox switching FRET labelled Az and to electro-inactive films of zinc Az, allows collection of several pieces of information about the processes occurring at the interface electrode/electrolyte.

Observing the change in the fluorescent emission of copper Az, allows to employ the microscope resolution for the localization of “optical currents”. The fluorescence emitted while the potential is swept across the E_0 of the protein, is proportional to the integral of the transferred electrical charges. The resulting FCV plot can be thought of as a translation of electrical current into a flow of photons, as the transfer of each single electron in the CV is amplified by means of the fast excitation/emission cycle of the fluorophore.

With illumination times of 100ms, a maximum resolution of 10^3 -10^2 molecules, contained in many spatially resolved ROIs selected all across the imaged area, can be reached, with an increase in sensitivity of up to ten orders of magnitude with respect to the conventional electrochemistry (considering 10^{12} -10^{15} molecules usually sampled in CV).

Importantly, for the data analysis, a reliable method to determine the distribution of midpoint potentials from different areas of interest, selected across the acquired images was developed and used to routinely analyse the redox potentials in ROIs selected across the surface of several samples.

In comparing analysis of FCVs at different SAM layers it was noted a decrease in the potential distribution towards thicker SAMs. The more uniform response, in first instance, was believed to originate from an increased order in the supporting thiol monolayer.

The distribution of optically determined midpoint potentials showed a good correspondence with the average E_0 values obtained by CV, while attempts of determining the k_{ET} of the protein monolayer resulted in a value almost two orders of magnitude smaller than expected. This was interpreted as an effect of bias of the FCV signal towards emission of molecules positioned at a larger distance from the surface, where the quenching of the gold is less effective. In this model Az molecules in the first layer in contact with the SAM would have a larger electronic coupling but lower emission rates, while the contrary would occur for Az in a second layer, which would have preferential optical coupling and lower (~ 0) k_{ET}.

Investigation on the electro-inactive monolayers of the zinc-substituted protein, where the occurrence of FRET (and thus a FRET based modulation) is not possible, reveals a smaller linear fluorescence fluctuation, which is opposed in direction to the switching of the redox process. The extent of this modulation is strongly attenuated by increasing SAM thickness and increased ionic strength, indicating that electrostatic forces are involved. The potential modulation was therefore attributed to the influence of the interfacial electric field on the protein charges, inducing conformational movement of the labelled protein with respect to the quenching gold surface. In consideration of the possibility of fluorescence modulation due to field-induced motion of the fluorophore, the fact that the dye molecule possesses only a small dipole moment and is neutral once coupled to the protein means that a contribution here is unlikely.

Sensitivity of the FCV technique to the position of the proteins in the z direction has been further confirmed by investigating the reductive desorption of the fluorescent molecules. Good correspondence of the stripping current with a concomitant decay of the fluorescence intensity is observed. Importantly the optical signal also allows discrimination of inhomogeneous desorption areas which respond out of synchronous with respect to the rest of the surface. Thus the possibility of mapping optically, with sub-micrometre precision, the potential and the distribution of the redox reactions occurring at the surface opens interesting possibilities to the use of this technique for the analysis of mixed systems and patterned surfaces.

Chapter 7

The Optical Monitoring of Laccase and Flavodoxin Redox

7.1 Introduction

In the previous chapters, examples of FCV applied to a fluorescently labelled cupredoxin, Az, has been given. In the present chapter two further examples of biological systems that were investigated by FCV. The first example is the multicopper oxidase, laccase (referred to as Lc hereafter), from the fungus *Trametes versicolor*, and the second is the two-electron shuttle, flavodoxin (Fld), from the bacterium *Desulfovibrio vulgaris.* While Az has a well-behaved and well-characterized electrochemistry, analogous studies on Lc and Fld are notably more complicated and under explored. It is noteworthy that these two proteins can both transfer more than one electron and also contain redox centres that represent the most oxidizing and the most reducing agents known in bioelectrochemistry.

7.2 Laccase as a FRET Switch

Though the first Lcs were isolated at the end of the XIX century,[224] these enzymes are still of great interest to researchers thanks to a number of theoretical and practical reasons. In particular, in fundamental research both the origins of the exceptionally high redox potential of some Lcs and the mechanisms of intramolecular electron transfer are intensely studied.[164,225-228] On the other side, Lcs ability to catalyse a remarkable four-electron transfer directly to oxygen molecules[225,229], while oxidizing a broad range of aromatic (particularly phenolic) and even some inorganic compounds (Figure7.1) drives an intense interest for application in a number of industrial processes and analytic devices.[230-237] For example, these enzymes are employed as biocatalysts for challenging biotechnological and industrial reactions, such as in bioremediation[237,238] and in green biodegradation of xenobiotics[233] and lignin polymers.[231,239] Other reported applications include immobilization in films as reducing agents on the surface of enzymatic fuel cells cathodes[240-246] or as biosensing elements for amperometric detection of environmental pollutants, particularly phenols.[247-252]

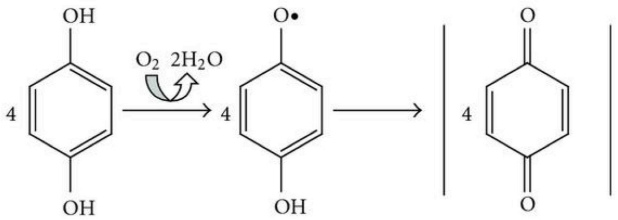

Figure 7.1: Schematic of the 4-electron reduction of oxygen to water typically catalysed by laccase, where a diphenol (hydroquinone shown here) undergoes a one-electron oxidation to form an oxygen-centred free radical. This species can be converted to the quinone in a second enzyme-catalysed step or by spontaneous disproportionation. Quinone and free radical products undergo polymerization.

In this context the newly gained ability to simultaneously monitor the electrochemical signal and the fluorescence emission from redox centres applied to localized Lc enzymes through FCV is not only relevant to developing alternatives to amperometric detection for biosensoristic applications, but has potential to provide further insight into the intra molecular electron transfer mechanisms. In fact, as will be illustrated in the following section, the redox centres embedded in the protein matrix have distinct spectral characteristics and only one of these is well suited for FRET-based coupling. As a consequence its electrochemical signal can be optically resolved from the other redox processes.

7.2.1 Laccase as a Redox Switch

Laccases (Lcs hereafter, E.C. 1.10.3.2) are an ancient group of enzymes widely distributed in nature,[253] as monomers, dimers or tetramers. Together with ascorbate oxidase, bilirubin oxidase and ceruloplasmin, Lcs belong to the enzymatic family of blue multicopper oxidases (MCOs) and their monomers structure is constituted by three repeated cupredoxin-like modules, similar to the Az β-barrel fold.[236,254]

As indicated by the family name, each Lcs monomer contains four copper ions, which are classified accordingly to their spectroscopic signature as T1, T2 and T3.[255] The first sphere of coordination of the coppers is highly conserved between species[236], while the surface may differ, (fungal and plant Lcs are variously glycosylated on their surface, with carbohydrates typically constituting 10-15% of their molecular mass).[256]

7.2.1.1 T1 Redox potential and Laccase Classification

Perhaps the most remarkable characteristic of Lcs is the redox potential of the T1 copper sites. Potentiometric titrations with redox mediators revealed T1 redox potentials for a great number of different Lcs[236]; as presented in Table 7.1, the values range from 430 to 790 mV vs. NHE.[229,257-259]

As T1 is the catalytic site for the oxidation of the aromatic substrates, its redox potential influences the catalytic efficiency for some reducing substrates and the range of molecules that can be oxidized.[229,260,261] According to T1 potential, Lcs have been classified into three groups: low, middle and high potential,[236] as shown in Table 7.1. Because of the wider range of substrates oxidized, the latter group is of particular interest for practical applications, but it is also worth noting that bacterial Lcs, relatively recently discovered, are rapidly attracting interest because of their increased stability, ease of production and absence of glycosylation.

Group	T1 potential range	Sources	T1 Axial ligand
Low $\boldsymbol{E_{T1}^{0'}}$	340–490 mV	Mostly plant Lcs	Methionine
Middle $\boldsymbol{E_{T1}^{0'}}$	470–710 mV	Plant and fungal, bacterial Lcs	Leucine
High $\boldsymbol{E_{T1}^{0'}}$	730–780 mV	*T. hirsuta* and *T.versicolor*	Phenylalanine

Table 7.1: Classification of Lcs based on the redox potential of T1.

7.2.1.2 Laccase A from *Trametes versicolor*

In the present work, a high potential Lc has been used: Lc A from *Trametes versicolor,* kindly donated by Prof C. Dennison (Newcastle University). A cartoon representation of its crystal structure, as reported by Bertrand *et al.* and Piontek *et al.*[262,263], is shown in Figure 8.2. This fungal enzyme is a glycosylated monomer consisting of 499 amino acids, with dimensions of 65 × 55 × 45 Å and a remarkable T1 potential of 780 mV vs. NHE. In nature Lc A, is secreted by the white root fungus *T. versicolor* as mandatory component of a pool of oxidative enzymes that carry out the complex degradation of the lignin polymer.[263]

Figure 8.2 shows the position of the copper centres in the Lc A structure and a schematic of their function in the catalysis. It can be clearly seen that the T1 copper is located close to the surface (at about 6 Å), in a pocket where the substrate (in pink in Figure 8.2) can be accommodated. The other three ions, one type 2 (T2) and two type 3 (T3) copper centres, are buried more deeply in the protein structure, at about 14 Å from the T1 Cu.[262-264]

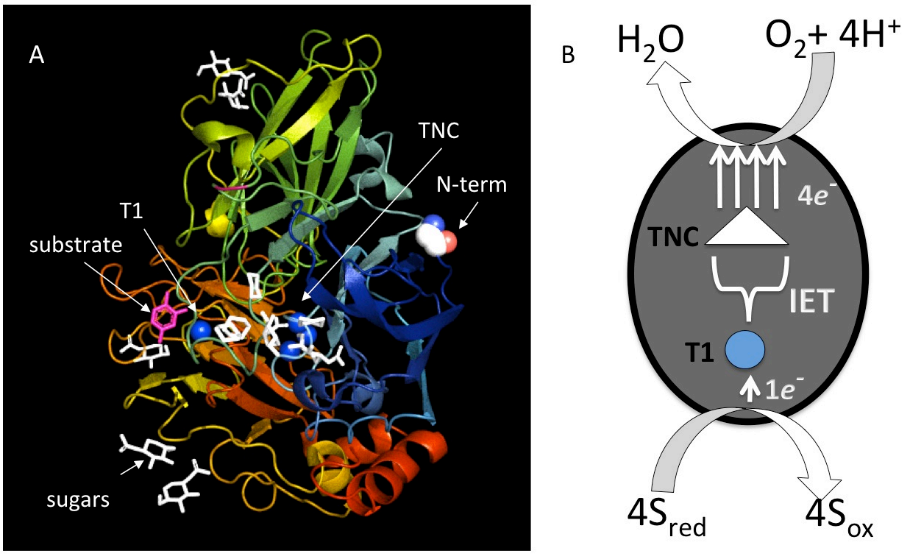

Figure 7.2: A: Cartoon representation of T. versicolor Lc with the four copper ions indicated as blue spheres, sugar residues are pictured as white sticks and a molecule of xilidine substrate at the T1 copper centre is coloured in pink (pdb file 1KYA). B: schematic illustrates the pathway of the electrons (white arrows), from the reduced substrates to T1 and subsequently transferred through internal electron transfer (IET) to the trinuclear copper centre (TNC) and finally to a dioxygen molecule.

The catalysis (schematic in Figure 7.1, right) involves the binding of a reducing substrate at the T1 and subsequent reduction of the $Cu^{2+}$to Cu^{1+} at the T1 site, followed by Internal Electron Transfers (IET) from T1 to the T2/T3 cluster or Tri-Nuclear copper Center (TNC). In the reaction mechanism proposed by

Solomon *et al.*[227], the enzyme, initially in the fully reduced state containing four Cu^{1+} ions, reacts with oxygen to give a semi-reduced peroxide intermediate. Two subsequent 2-electron transfer events between the coppers and the peroxide lead to rupture of the O-O bond, with formation of a 'native intermediate' in which all the coppers are oxidized. The final step is either a release of a water molecule with formation of an oxidized resting form of Lc, or a rapid (proton coupled) reduction of the native intermediate to the initial fully reduced state.[227,265] Despite significant recent insights offered by a combination of techniques, among which circular dichroism and X-ray absorption spectroscopy, the dynamics of IET between the copper ions in catalytic and non catalytic conditions are not yet completely understood. It is therefore attractive the idea of using FRET coupled emission to separate the signal of the T1 with respect to the other ions; this is possible because, unlike T2 and T3, the T1 site is suitable for FRET coupling, having a spectral signature in the visible range similar to the copper center of Az.

In Lac the T1 $Cu^{2+/+}$ has trigonal coordination (see Figure 7.3) with two histidines and a cysteine as conserved equatorial ligands. The fourth axial position instead varies from species to species (Table 7.1). Incidentally, the identity of this axial ligand strongly influences the oxidation potential of the enzyme, providing one of the mechanisms for regulating its activity.[236] Other factors determining the redox potential, have been studied by Piontek *et al.* who identified the role of H-bonds in the second coordination sphere in modulating the electronic density of the T1 of *T. versicolor* Lac.[263]

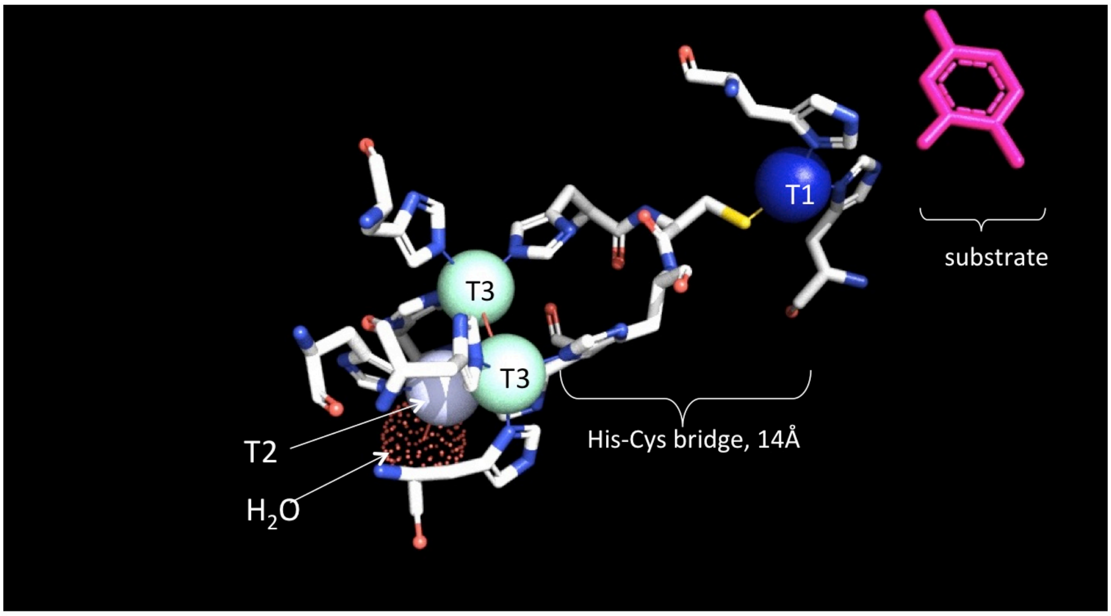

Figure 7.3: Detail of the first sphere of coordination of the coppers contained in T. versicolor laccase. The red line between the two T3 coppers is an hydroxyl bridge and the dotted red sphere attached to the T2 is oxygen from water molecules coordinating to the T2 copper. As indicated in the figure, the length of the Cys-his bridge is 14Å.

In Lac from all sources, the Cys ligand at the T1 copper, responsible for the blue colour analogously to Az, is flanked on either side in the polypeptide sequence by histidines, which in turn are ligands to the pair of T3 Cu atoms. This tripeptide, the “histidine-cysteine bridge”, is thought to be the pathway for the Internal Electron Transfers (IET). Besides the His of the His-Cys bridge, the coordination sphere of each T3 copper ion is completed by the other two-histidine ligands and by a hydroxyl bridge between them. The T2 copper is 3-coordinate by two histidine ligands and a water molecule. Both the T2 and the T3 are silent in UV-Vis. absorption spectroscopy and should therefore not interfere with the FRET communication between the T1 and the dye.

7.2.1.3 Background on the Electrochemistry on Laccase

Prerequisites for most of the uses mentioned previously and for the establishment of FCV include immobilization of the enzyme molecules and establishment of an effective electronic communication between the electrode surface and the substrate-redox center. Fungal Lcs have been characterized electrochemically, with quite different results[254]. Electrode surfaces employed for Lc protein film voltammetry are mainly graphite and gold, although in applied research a variety of other immobilization materials have been tested for biocathodes and biosensors construction.[240] On these, ET can happen directly (DET) or through a redox mediator. In general for enzymes, DET is desirable, as it allows for the use of the full thermodynamic potential of the enzyme, thus circumventing activation barrier needed for the electron transfer from the enzyme to the mediator. However DET requires positioning of the enzyme active site within electron tunnelling distance from the electrode [266,267] Unlike for the simple physisorption of Az, achieving DET for Lc is more challenging due to the relatively large size of the protein and the lack of easily achievable oriented immobilization.

Some advances in this direction have been recently reached on graphite electrodes, for which methods to favour the surface bound orientation with the T1 acceptor close to the surface have been reported.[240,245] This was achieved by chemically modifying the graphite with substrate-like aromatic moieties, which connect with a “plug-in-socket” non-covalent interaction with the hydrophobic pocket of the T1 site. This strategy offers enhanced electronic communication and bioelectrocatalytic currents densities when compared to films composed of randomly oriented Lc molecules.[240,241,246] On a bare gold surface, physical adsorption of various fungal Lcs was found to induce alteration of the reaction mechanism, resulting in partial reduction of O_2 to H_2O_2.[268]

The use of thiol layers (aminothiophenol in particular) allowed observation the full four electron reduction of dioxygen to water, starting at potentials of ~250-350 mV vs. SCE (depending on the type of SAM).[268,269] Pita *et al.* succeeded in partially controlling Lc orientation on gold, reaching higher catalytic current densities.[241] Even for these partially oriented Lc layers, however, the non-turnover electrochemical signatures of the copper centres are not clearly detected. On both graphite and gold electrodes, in fact, most of anaerobic voltammetric investigations of Lc show broad and poorly defined peaks barely distinguishable from the background capacitive currents.[268]

Heterogeneous spectro-electrochemical studies of Lc produced from different Basiodiomycota in capillary gold electrodes were in some instances used to integrate the CV studies. Differential spectra, acquired under anaerobic conditions, distinctly revealed reversible change in the T1 absorption band, even in association with very faint CV peaks.[254,268,270] Hence, the possibility of monitoring in time the variation in redox state of the T1 site, via tagging Lc with a label appropriate for coupling the absorption change to the fluorescent emission was explored in this part of the thesis, hoping that FCV might be a way to increase the signal to noise ratio of the spectro-electrochemical measurement enough to allow following the T1 redox from a single layer of surface-confined labelled Lc molecules in non-catalytic conditions.

7.2.2 Fluorescent Switching of Laccase A

7.2.2.1 UV-Visible Absorption Spectra

The electronic spectrum of oxidized Lc, as shown in Figure 7.4, is characterized by the absorption band of the T1 copper, positioned between 550-650 nm (Figure 7.4, green line). As for Az, this blue absorption originates from a charge-transfer transition between the cysteine ligand and the T1 copper and disappears upon chemical reduction (Figure 7.4, red line). Therefore labelling with a dye emitting at these frequencies should result in a redox-sensitive fluorescent emission with an Förster radius close to 35 Å calculated as detailed in section 2.2.

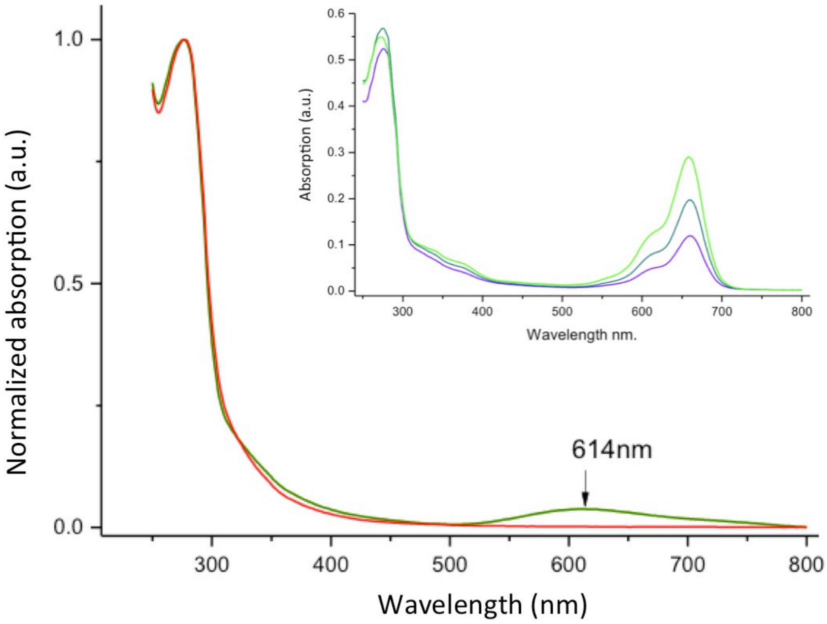

Figure 7.4: Normalized absorption spectra of T. versicolor Lc, before (green) and after (red) reduction with DTT in deareated PB solution, 20 mM pH7.0. Inset: absorption spectrum of Lc A after labelling with 0.5, 1 and 2 equivalents of Atto655, resulting degree of labelling with one equivalent was 24±6%.

Lc A was labelled at the N-terminal, located at about 33 Å from T1, with NHS functionalized Cy5, using the procedure outlined in chapter 4. The resulting degree of labelling obtained from reaction with one equivalent of dye was determined by the UV-Vis. absorption spectra, shown in the insert of Figure 7.4.

7.2.2.2 Fluorescence Switching in Solution

Upon chemical reduction with excess DTT, the fluorescent emission of Lc-tethered Cy5 dye increased by 48 ± 20%. An example of the switch is given in Figure 7.5 (left), in which the emission at 673 nm is monitored while chemically oxidizing and reducing the solution (1μM) of labelled enzyme.

The observed switching efficiency is lower than Q of ~70% found for Az, but this can be expected considering the increased distance between the dye and T1 and the slightly lower spectral overlap (not shown).

Although the labelled protein solutions were stored at -20˚C, it was found that Q decreased after repeated storage and thawing, possibly due to protein damage during change of temperature. In the same conditions labelled Az was perfectly stable, even at 4˚C, for prolonged periods. Variations in the catalytic activity and auto-reduction phenomena of Lcs after prolonged storage in solution have been previously noted.[271]

For example both fungal Lcs and another multicopper oxidase, bilirubin oxidase, are known to aggregate during storage; for the latter enzyme aggregation proceeds through interaction of the catalytic site with superficial aromatic residues of other molecules, which are recognized as substrates. The same mechanism has been proposed to explain auto-reduction and formation of Lc aggregates in solution.[271]

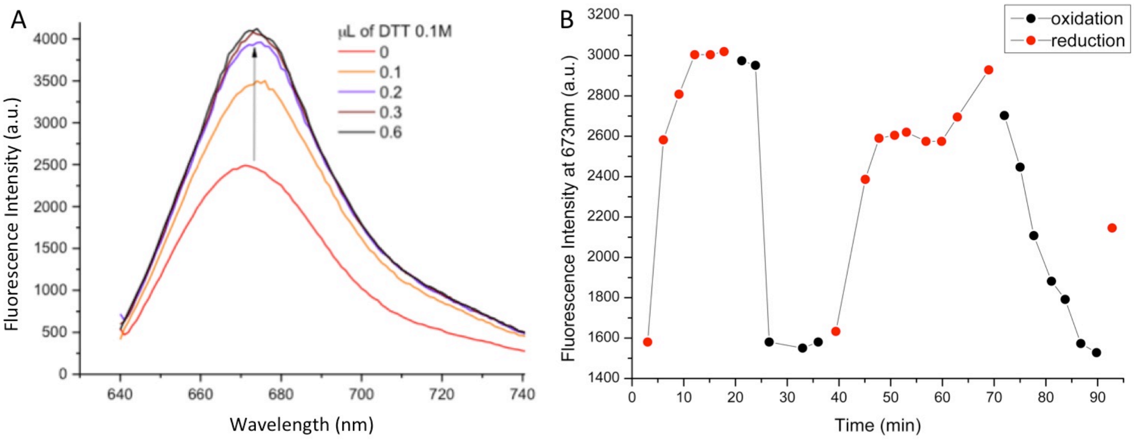

Figure 7.5: A) Increase in the fluorescence emission in response to addition of reducing agent to a 100μl of Lc (1-10μM). B) Fluorescence intensity values determined for Cy5-labelled laccase upon chemical oxidation and reduction. All measurement performed in PB buffer pH6.0 100 mM in a 100μl quartz cuvette, solution in equilibrium with air. The reducing agent was 100 mM DTT and oxidizing agent was 10 mM hydrogen peroxide, with additions progressively increasing from 0.1 to 2μl.

It is therefore tempting to speculate that the decreased switching efficiency after storage could be due to enzymatic attack on the aromatic rings of the exposed dye molecules. However, current understanding of the factors regulating the activity of Lc is not complete; the formation of "resting" and inactive forms has also been suggested to describe the variation in enzymatic activity and electrochemical response to temperature, concentration and level of oxygenation of the solution.[227,271]

To avoid further complications, the FCV and fluorescence spectroscopy experiments were performed with freshly labelled solutions. In these conditions the redox linked switching was repeatedly observed, therefore the research progressed to immobilization and electrochemical investigation of the labelled enzymes.

7.2.3 Covalent Immobilisation of Laccase A

Initially several strategies were explored to physisorb or covalently attach Lc A in an electroactive configuration on SAM modified gold electrodes. In particular, these included:

- Hydrophobic physisorption on methyl terminated SAMs;
- Electrostatic physisorption on positively charged SAMs (4-aminothiophenol and 11-amino-1-undecanethiol) exploiting the dominant negative charges on the protein surface close to the T1;[42]
- Covalent binding on amino-terminated SAMs after oxidation of Lac superficial sugars moieties by $NaIO_4$ and activation of the obtained carboxylic groups by EDC/NHS, as in Shleev and Pita's procedure.[156,268]

As none of these strategies resulted in a clear and reproducible Faradaic electrochemical signal, a consolidated protocol for covalent immobilization was employed.[153,272] Gold surfaces were modified with a carboxy-terminated SAM of 1-mercapto-11-undecanoic acid (MUA) and EDC-NHS chemistry was used for activation as shown in Figure 7.6. The protein solution (1μM) was left to react at 4C° for 4 hours or overnight and the surface concentration was evaluated by Surface Plasmon Resonance (SPR).

7.2.3.1 Surface Concentration of Covalently Bound Laccase by SPR

The amount of immobilized proteins on the surface of the SAM-modified gold electrodes could be accurately measured by means of SPR spectroscopy. In SPR instruments, p-polarized light is directed at the glass surface with varying angles, causing direct excitation of the surface plasmons at the metal-solution interface.

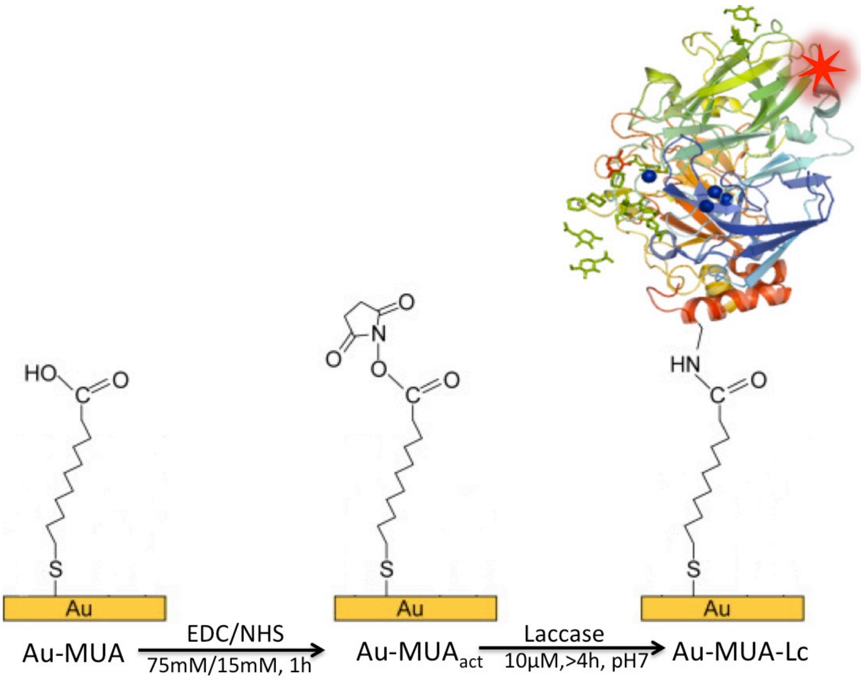

Figure 7.6: Schematic representing the covalent immobilization of labelled Lc on the surface with a EDC/NHS protocol (drawing not to scale).

The angle of excitation of the SPR, $\theta_{m,}$ depends on the dielectric constant of the interfacial region that is in contact with the gold and varies (*inter alia*) with the thickness of the adsorbed protein layer. Thus absorption/desorption process causes a shift in the angle. For DNA and proteins, this can be quantified using the conversion factor of 122×10^{-9} g mm^{-2} of deposited material per millidegree of shift.[273]

An SPR gold chip, cleaned and modified with a MUA SAM, was inserted in the flow cell of the SPR machine; after several washing cycles with PB, the EDC/NHS protocol was applied and the resulting trace after protein addition is displayed in Figure 7.7.

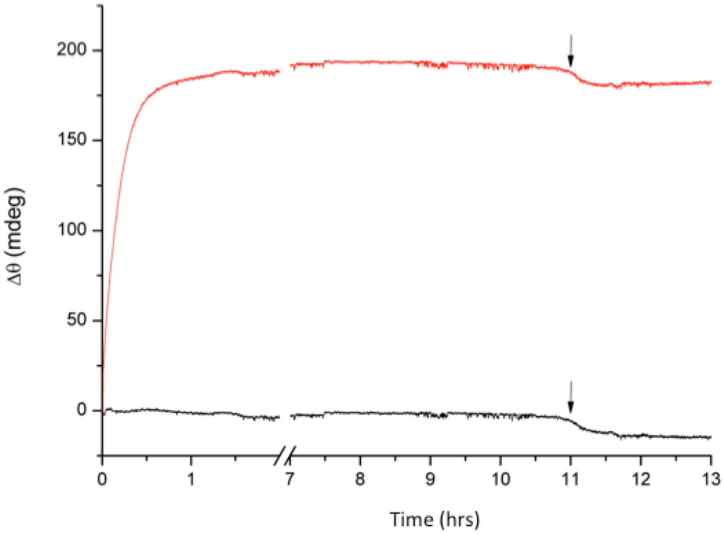

Figure 7.7: The covalent immobilization of Lc onto carboxy-terminated SAM of MUA monitored through SPR during overnight reaction. The resulting change in the resonance angle (θm) is plotted versus time. At the time 0 a 1μM Lc solution (red line) in 100 mM PB pH7.0 is delivered on the MUA, previously activated by EDC/NHS chemistry; a control containing only buffer was simultaneously measured in a second channel (black line). The two black arrows indicate the beginning of washing cycles with buffer to remove any unbound protein, the distance between the two lines after the signal has stabilized was used to determine the amount of protein covalently bound.

The resulting Lc A surface coverage was $2.3 \pm 0.12 \times 10^{-12}$ moles cm^{-2} at pH 7.0 and $2.2 \pm 0.15 \times 10^{-12}$ moles cm^{-2} at pH6.0, which is 41-45% of the maximum theoretical surface coverage, calculated with a close sphere packing model on an average molecular diameter of 5.4 nm (as estimated from $(4.5 \times 5.5 \times 6.5)^{1/3}$).[262,263]

The reported coverage is in good agreement with STM images of similarly immobilized fungal Lcs.[274] The presence of the protein on the surface was also checked by TM-AFM imaging on the functionalized Au-OTE, revealing single isolated features of ~6 nm in height (data not shown) and close to the size of Lc molecules determined by crystallography.[262,263]

The Cy5-labelled enzyme covalently bound was also catalytically active, being able to oxidize solutions of the chromogenic substrate ABTS at open circuit potential, while the MUA-OTEs did not show any trace of the green coloured radical product (detected via UV-Vis. absorption using $\varepsilon_{420nm} = 3.6 \times 10^4$ $M^{-1}cm^{-1}$) even after overnight immersion in the solution.[274] An approximation of the rate of the reaction was obtained measuring the absorption spectrum of the solutions 10 minutes after the electrodes were immersed in it (1 mM ABTS, 100 mM PB buffer pH6.0, 22°C, stirred and in contact with air); this was broadly consistent with a 0.5-3 $\times 10^{-9}$ moles cm^{-2} of ABTS being oxidized per minute. It was established, therefore, that the protein was both bound on the surface at acceptable and reproducible coverage and able to oxidize the substrate. The next phase of the work involved an attempt to follow substrate turnover and T1 oxidation state optically by FCV.

7.2.4 Conventional CV and Fluorescent CV of Cy5-laccase A

For acquisition of CVs and FCVs of Lc A on the TIRF microscope, a sealed Teflon flow-cell was built, in order to control diffusion of oxygen into the electrochemical volume. In the FCV cell, for geometrical requirements, it was necessary to substitute the bulky SCE reference electrode with a thin flexible no-leak electrode (DriREF, WD, ø 2mm). This choice was also practical in preventing the leakage of Cl^- ions into the buffer solution, as these are known to inhibit the electrochemistry of Lcs.[242] The potentials measured aainst DriRefWere then converted to SCE values.

7.2.4.1 Electrochemical Signal of Labelled Laccase on Au-OTE/MUA

A CV obtained upon the electrochemical interrogation of a typical Lc A monolayers presented in Figure 7.8. The voltammogram was acquired on an OTE in the FCV setup on the microscope, after application of the protocol in 7.2.3, in 100 mM phosphate buffer pH6.0.

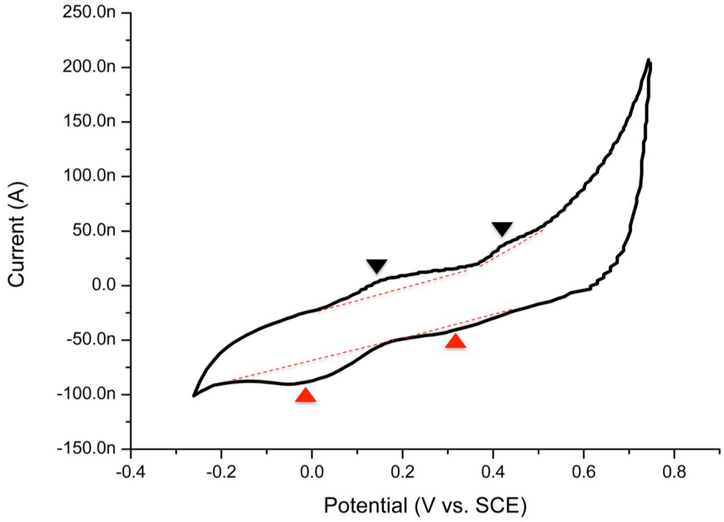

Figure 7.8: CV plot obtained with ν of 20 mV s^{-1} after EDC/NHS immobilization of Lc A in 100 mM PB buffer pH6.0. The peaks a1 and c1 correspond to the lower potential couple (~100 mV vs NHE) and a2 and c2 to the higher potential one (~400 mV vs. SCE).

In deareated conditions the electrochemical non-catalytic signal resulted in two broad, barely distinguishable couples of peaks in the potential range of 100 mV and 400 mV vs. SCE (as in Figure 7.8). Frustratingly, the current signals detected varied considerably from experiment to experiment, and in some cases in areated solutions only one of the two couples (the lower potential one) was visible. These differences were possibly due to poor control of the gas concentrations in the FCV cell and to variations in the temperature at the monolayer after prolonged illumination with the red laser. The DriREF is less stable than the SCE electrodes, showing variations of up to 5 mV between the beginning and the end of the experiments (to reduce variability the DriREF was calibrated/checked separately by chronopotentiometry before and after experiments against a calomel electrode).

In the more conventional electrochemical experiments on polycrystalline gold disk electrodes (GDEs) results were more reproducible, however the area underlying the Faradaic peaks was always corresponding to sub-monolayer coverages, suggesting that only a part of the molecules observed by SPR is responsive to the CV investigation. This is not surprising considering that *T. versicolor* Lc A has eight reactive superficial lysine residues that can be used for EDC-NHS coupling on SAM surfaces. All of these are exposed on the surface, but none is close to the T1 (which is surrounded by a negatively charged patch) or to the TNC. Thus, a low electric coupling is to be expected due to dominance of non-optimal orientations of the molecules on the surface.

Secondly, the area of the peaks was observed to decrease rapidly after the first scan. As the protein is firmly covalently bound on the SAM, decrease in the peaks area might suggest formation of inactivated states following the potential scan, which is in agreement with Shleev and Pita's remarks[268,275] and consistent with Solomon's model involving an all oxidized resting form of Lc.[227]

It was also noted that after reductive desorption of the SAM, it was very difficult to clean again the gold surface of the GDEs, possibly due to contamination by copper ions. In fact to retrieve the 'standard' bare gold electropolishing curve, it was necessary to introduce both a potentiometric step tailored at obtaining the oxidative stripping of Cu^{2+} from the surface, followed by chelation with concentrated EDTA in solution, and a prolonged procedure of manual mechanical polishing, as suggested by Pita *et al.*[268] It is not clear, though whether the leakage of the copper ions was occurring during the reductive desorption of the SAM, due to the highly reductive potential applied, or during the normal CV scans acquisition.

The obtained potentials and the observation of metallic contamination of the gold surface were consistent with reports published on other fungal Lcs bound on gold and are in line with the literature.[268] It was therefore considered reasonable to proceed with the investigation of the FCV signal through analysis of the fluorescence/time traces.

7.2.4.2 Fluorescence Fluctuation Under Potential Control

The Lc monolayers showed generally a lower fluorescence intensity than that detected from Az monolayers. This is predictable as the Lc A molecules are larger, more diluted on the surface (about half the concentration of labelled Az) and labelled with a more photosensitive dye (see section 6.1.2). However, during the same acquisition, the behaviour of the fluorescence emission can be evaluated in correlation to the potential trace as displayed for two different ν in Figure 7.9A and B. These two plots are typical time traces of the FCVs obtained from the laccase monolayers, acquired while sweeping the potential between -0.4 and 0.6 V vs. SCE at 2 V s^{-1} (Figure 7.9A) and 1 V s^{-1} (Figure 7.9B). The traces shown correspond to ROIs of 3×3 pixels^2 selected across the acquired image. Using the SPR results to estimate the surface concentration, each of these should contain 1.34×10^3 molecules. As only one fourth of these are labelled (see section 7.2.2.1), it is possible to estimate an optically monitored sample of ~350 Lc molecules per trace.

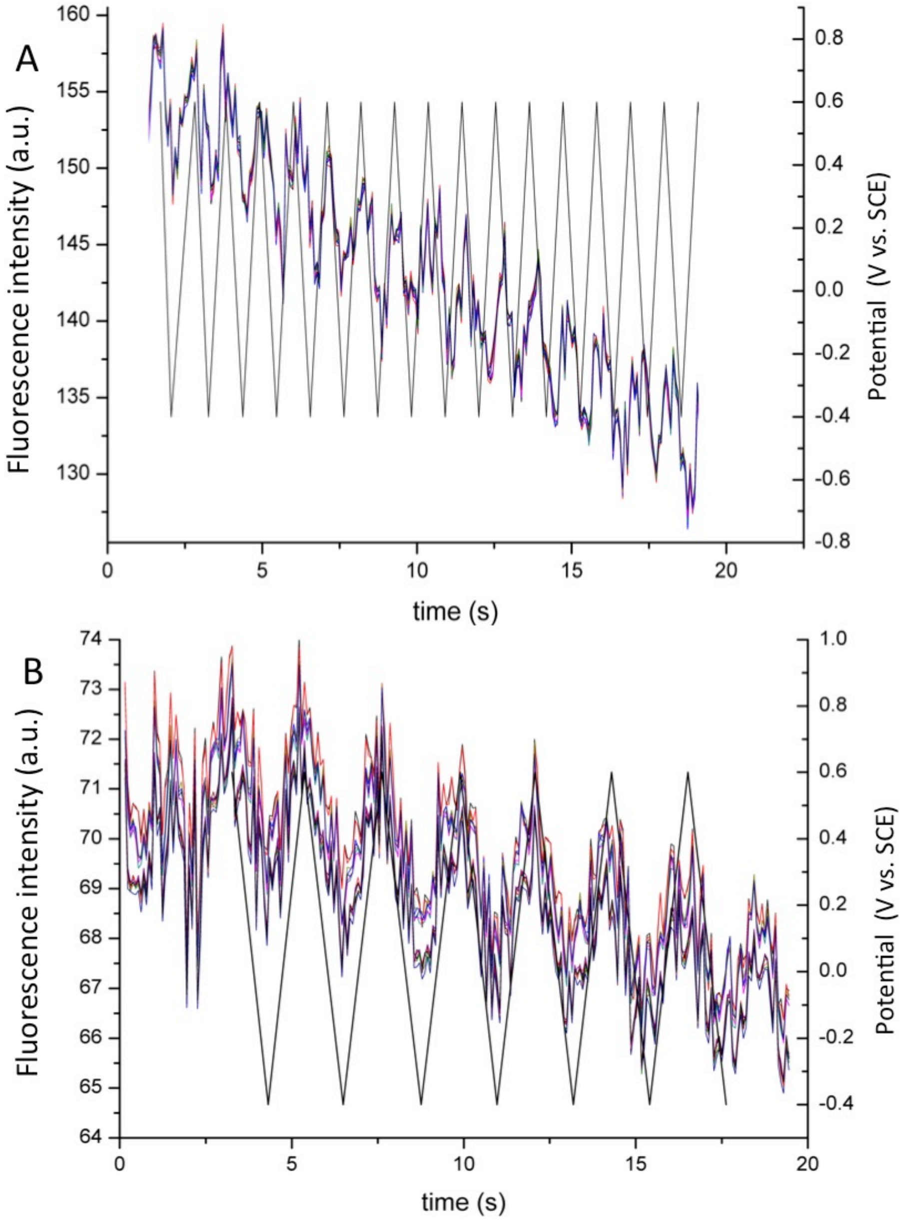

Figure 7.9: FCV traces of 3 × 3 pixel ROIs in two different acquisitions on an Lc modified OTE. The two traces show respectively the response at 1 and 2 V s^{-1}. The black line indicates the potential waveform applied.

As clearly visible in Figure 7.9, a decay of the fluorescence intensity is observed, superimposed to a triangular wave whose period and amplitude is controlled by the applied ν. The gradual baseline decay in the fluorescence intensity is due to irreversible photobleaching of the Lc-coupled Cy5 dyes, bound on the surface. The amplitude of the superimposed potential modulation of the fluorescence, clearly in phase with the applied potential, is lower than the normal switching values (~0.5) observed for the Az monolayers. In fact, the Q observed at various ν was always comprised between 0.08 and 0.2, calculated over the whole area of the image (256 × 256 pixel^2) for different ν. This is consistent with a dominant optical signal being acquired from weakly coupled Lc. However, the fluorescence modulation of the surface confined labelled proteins goes in opposite direction to the expected redox-linked switching that had been clearly established by chemical oxidation/reduction in solution (see schematic in Figure 7.10). The application of a reducing potential in fact causes a decrease of the fluorescence and vice versa the oxidative potentials causes increase.

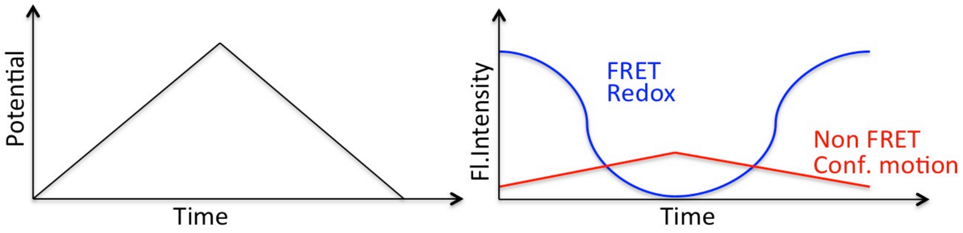

Figure 7.10: Schematic showing the opposite behaviour of FRET and non-FRET fluorescence intensity potential modulation.

The variation in the fluorescence intensity in phase with the applied potential was consistent in size and direction with what observed for the non-FRET coupled labelled proteins, such as labelled zinc substituted Az molecules and cytochrome *c* (see section 6.5). In these non-FRET systems, the distance between the dye and the gold controls the emission by determining the extent of metallic quenching on the probe. Motion of the molecules with respect to the surface, induced by the force exerted by the varying interfacial electric field on the protein charges (resulting in variation in the metal-dye distance), is thought to be the main component of the observed modulation as reported in Chapter 6. Rant *et al.* [75,122] reported a similar behaviour for negatively charged DNA strands SAMs immersed in varying interfacial electric fields.

7.2.5 Conclusion on Laccase Studies

To summarise, the FRET switching has been clearly observed in solution upon addition of chemicals and is consistent with the expected efficiency in terms of distance between the T1 and the Cy5 dye. The enzyme Lc can be also robustly and reliably immobilized on gold electrodes at $\sim 10^{-12}$ moles cm^{-2} coverages and subsequently exhibited voltammetric and SPR features both self consistent (see point above) and in broad agreement with prior reports for other fungal Lcs.[268,270,274,276] The mechanism of mediatorless electron transfer of *Trametes hirsuta* and *Cerrena unicolor* Lcs, two similar high potential fungal Lcs, covalently bound on MUA was described by Shleev [268,270,276] and Klis.[274] Both sets of authors saw two peaks couples at 150 mV and 500-600 mV vs. SCE and suggested the anodic one was due to the T1 copper and the cathodic to the TNC's connections with the electrode.

On the other hand, the FCV investigation indicated that in the same potential window we were not able to detect the expected FRET-coupled switching of the T1 but only a much smaller electric field modulation.

This could be due to different causes; the most plausible reason is a failure in achieving an efficient electronic communication between the protein T1 centre and the gold surface, such that dominant optical signal was acquired from labelled molecules moving in the interfacial electric field. From the potentiometric titration and voltammetry on graphite electrodes it is known that the potential of the T1 should be close to 540 mV vs. SCE, therefore about 150 mV higher than the potential of the detected peaks. In the observed voltammetry, the anodic couple is instead quite close to the potential expected for the TNC.

Attempts to extend the investigated window over 600 mV vs. SCE to more positive potentials, where the oxidation of the T1 might occur, were ineffective, resulting in very high oxidative currents and in the irreversible modification of the sample, possibly due to oxidative damage to the SAMs or to the gold film surface.[194] The same investigation on more robust GDEs revealed instability of the MUA SAM above 600-650 mV vs. SCE, with irreversible changes to the baseline currents.

On the other side, if the 400 mV vs. SCE signal was due to the T1 we should have observed a FRET based fluorescence potential modulation similar to Az, as already clearly seen in solution. Possible reasons for the lack of FRET might be either

- Denaturation occurring upon immobilization of Lc (disrupting the FRET based coupling),
- Interference of a coupled reaction, such as an IET to the TNC, which might reoxidised the copper
- Progressive deactivation of the surface bound Lc molecules.

The first possibility can be at least partially discarded, as the catalytic activity of the Lc versus ABTS (which is oxidized at the T1 center) was repeatedly observed after the electrochemical measurements.

The second possibility, i.e. the occurrence of a coupled reaction re-oxidising the copper, might take place due to small amounts of oxygen in the electrolyte solution. In the experiments in cuvette, where FRET coupled switching was obtained by addition of chemicals, continuous reduction of the diffusing DTT molecules of the T1 centres can take place, keeping the Lc in the reduced state. On the contrary, for the randomly oriented surface confined population, the electronic communication with the gold is not very efficient and a fast reoxidation of the T1 copper, would be beyond the time limits of the optical detection. In fact the FCV sampling frequency is limited by the exposure time of the image acquisition (~100-150 ms), thus fluorescence changes occurring on a much shorter timescale would result averaged out in time. Further attempts to overcome these temporal and potential limitations using a more transparent substrate (see work on the C-OTE presented in chapter 5) were unsuccessful due to technical problems.[245]

From a practical perspective, the FCV experiments with Lc were particularly demanding, not least because the glass/gold substrate easily cracked under the pressure of the sealing ring, but also because buffer frequently leaked out of the confined area during the potential scan, due to the high wettability of the COOH-SAM (contrasting strongly with the highly hydrophobic interfaces utilized in the Az work). When the buffer reaches the silver-paint contacts outside the ring, the CVs are heavily compromised due to the excess of current passing through the film and to contamination with strong metallic peaks of the silver nanoparticles at approximately 150-200 mV vs. SCE, it is thus essential to prevent the contact between the buffer and the contacts.

7.2.6 Conclusion on Lc FCV

To conclude, Lc was successfully labelled and chemically oxidized and reduced. When chemically immobilized on the MUA modified OTEs and GDEs was able to oxidize substrate, and electrochemical peaks could be observed in line with previous reports. However, when interrogated by FCV this enzyme resulted to be a much more complex and challenging system with respect to both Az and Fld (in chapter 6 and section 8.3 of this chapter respectively). Despite working with deareated solutions and a sealed FCV cell, the presence of small amounts of oxygen or formation of redox inactive states might be responsible for failure in observing the FRET-switching caused by redox of the T1 copper. The resulting fluorescence potential modulation observed is comparable to the response of redox inactive zinc Az (section 6.4).

Despite these issues, Lc presents further interesting features that might be addressed by FCV. In particular the oxidized T3 centres, present in Lc and other multicopper enzymes, are fluorescent at shorter wavelengths (λ_{exc}= 330 nm; λ_{em}= 420 nm), and their emission is sensitive to binding of O_2 to the TNC site.[254,277,278] In the future, monitoring of changes at different wavelengths may allow spectral isolation and potential resolution of T1 and TNC redox sites.

FCV experiments in the blue region of the spectrum have been carried out successfully on another interesting group of proteins, presented in the following part of the chapter.

7.3 Fluorescent Cyclic Voltammetry of Flavodoxin

7.3.1 Flavoproteins

Flavoproteins are proteins that have a derivative of riboflavin as a co-factor. In nature these derivatives are almost exclusively flavin adenine dinucleotide (FAD) or flavin mononucleotide (FMN) (Figure 7.11), they are found in over 150 different proteins that either directly interact with substrate or that are involved in respiratory pathways.[279] Most of the work described in this part of the thesis was carried out on Flavodoxin (Fld) from *Desulfovibrio vulgaris* (described in section 7.3.2), however a brief comparison with other possible FCV target molecules of the flavoproteins family is included in section 7.3.5.

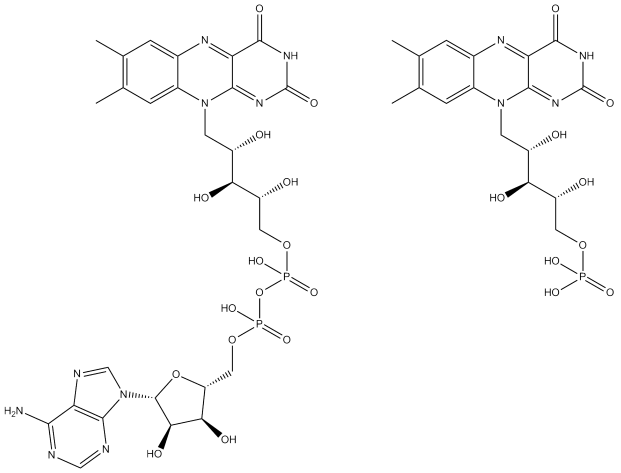

Figure 7.11: Structures of FAD (left) and FMN (right) in the completely oxidized form.

Flavoproteins can be separated into two main classes: proteins that are metal free and those that contain iron. Both groups interact with their substrates in a two-electron process; these electrons can then be passed on either simultaneously or sequentially. In the latter case the half-reduced state of the flavin requires stabilization by the protein matrix. Flavins are often non-covalently bound to dehydrogenases and oxidases, which can easily react with molecular oxygen to form H_2O_2, re-oxidising the flavin in the process.[280]

7.3.1.1 Flavins Cofactors

FAD and FMN can exist in three different redox states: quinone, semiquinone and hydroquinone, as illustrated in Figure 7.12.

Being amphoteric the solution pH sensibly affects any redox reaction.[281,282] At neutral pH the free FAD and FMN undergo a simultaneous two-electrons and one-proton reduction.[282] Both the free flavins are readily active at carbon electrode surfaces, with reported E_0 values of approximately -0.21 V vs. NHE for $FMN_{ox} + 2e^- \rightleftharpoons FMN_{red}$ at mercury and carbon electrodes.[282,283]

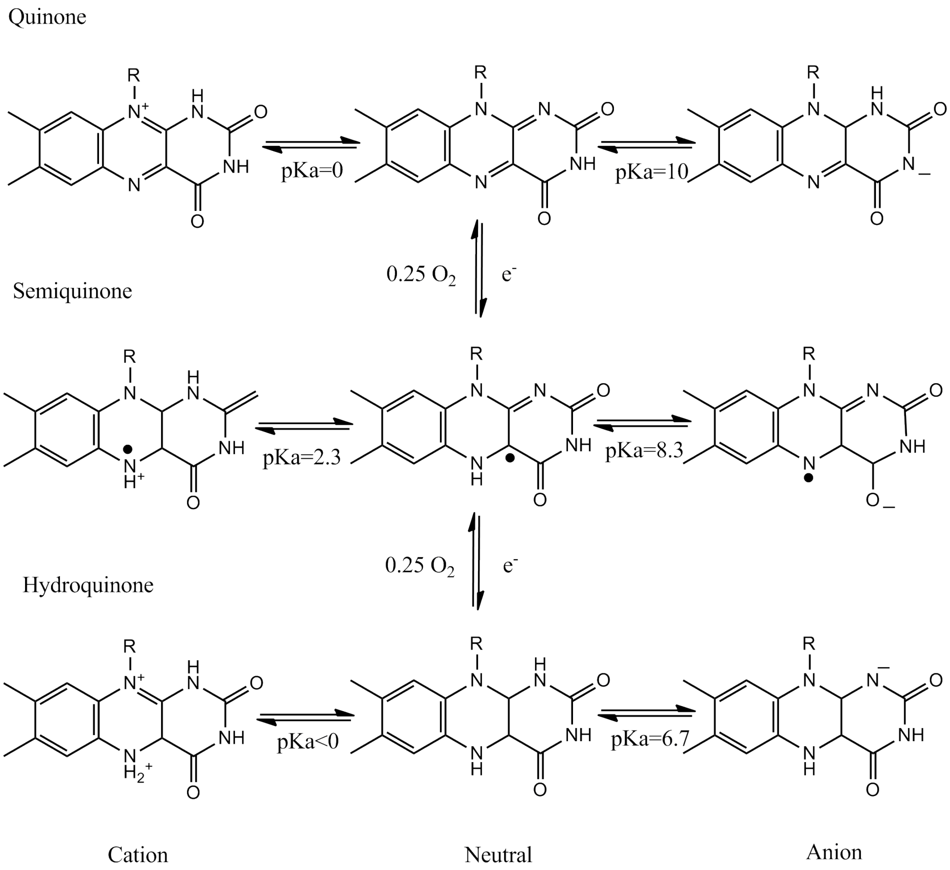

Figure 7.12: Diagram showing the structure of flavins in the three different redox states and the relative equilibria of protonation and deprotonation in acqueous solutions.

7.3.2 Structural Features of Flavodoxin

Flavodoxin (Fld) from *Desulfovibrio vulgaris* is a small flavoprotein, consisting of 148 amino acids, with a molecular mass of 15.7 KDa. Flds from different sources have little sequence homology (20-40%), but interestingly present a common tertiary structure[282], illustrated in Figure 7.13. They are produced only in bacteria, often as an alternative to ferredoxin in iron-poor media, and are involved in several pathways such as reduction of sulphite and nitrogen fixation, acting as a partner to several proteins and as an electron donor to bisulphite reductase.[284,285] Unlike Lc, Fld is stable, even in highly concentrated solutions, thanks to the solid fold and the high concentration of charges on its surface, typically ranging from -10 to -20, with a pI of ~ 4.[285]

One non-covalently bound molecule of FMN acts as redox cofactor in Fld.[282] The FMN is accommodated between three loops at the top of the protein in proximity of the surface and is in contact with the solvent. The complex FMN-Fld is more stable than the apoprotein alone, being stabilized by H bonds on the FMN ribityl chain and phosphate group and by sandwiching of the isoalloxazine ring between two aromatic residues.[285] In *D. vulgaris* these are tyrosine 98 and tryptophan 60.[286]

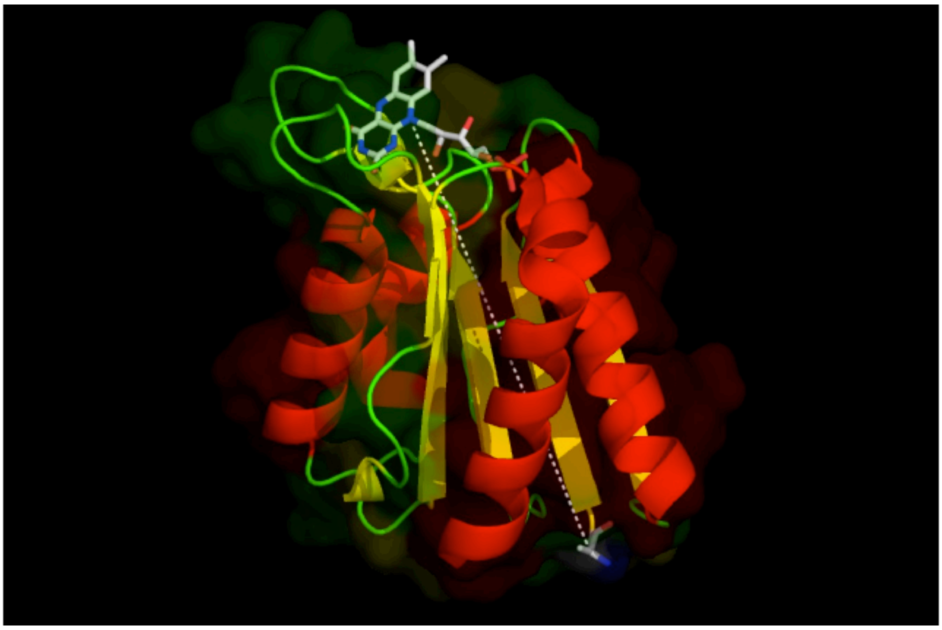

Figure 7.13: Cartoon representation of the crystal structure of D. vinelandii Fld (PDB: 1J8Q). The FMN cofactor and the N terminal amino acid, exposed respectively on the top and on the bottom sides on the protein surface, are represented by coloured sticks. Its overall fold is similar to that of other Flds, with a central five-stranded parallel β-sheet (colored in yellow) flanked on either side by α-helices (in red). The loops are displayed in green and the distance of 32 Å between the FMN and the N-terminus is represented by the white dotted line.

The binding of FMN in Fld affects both its emission and its electrochemistry. Indeed, researchers attention for Flds has been directed in particular to elucidation of the dynamic contribution of the protein structure and solvent in controlling the redox potential and optical properties of the FMN[287-289] and the connected biological functions.[285] Part of the interest on Flds electrochemistry is also driven by the possibility that, due to the multiple enzymatic partners, Flds might be used for construction of a range of biosensors and bio catalytic surfaces.[283] For example, Fld has been used by Gilardi and coworkers in the so–called “molecular Lego” approach for construction of a catalytically active chimera, in which the heme domain BM3 of cytochrome P450 was fused to the Fld module.[290]

7.3.2.1 Redox Potential of Flavodoxin

In contrast to the tight coordination imposed by Az on the T1 copper center, in most flavoproteins the FMN is bound to the protein structure by non-covalent interaction. In *D. vulgaris* Fld this is very tight, with dissociation constants of 10^{10} M for the FMN-apoprotein complex at neutral pH.[282,291] Stabilization of the interaction between the apoprotein and the redox group is decreased at pH values below 5 and is also dependent on the ionic strength and the type of ions present in the solution.[282]

Upon incorporation in proteins, the potential of the FMN is shifted to more negative values, mainly as a result from stacking interactions between the flavin ring and the sandwiching aromatic residues which disfavour reduction to the hydro-quinone form of the cofactor.[6] Other residues present at the binding site further tweak the protein redox potential; the presence of basic residues and H-bonds for example increases the potential by electrostatically stabilizing the anionic hydroquinone[292] and conformational changes associated with the redox state of the protein have been reported for *D. vulgaris* and Flds from other sources.

When FMN is bound in Fld, the two electron transfer steps can be observed separately at the two different potentials E_1 and E_2 due to stabilization of the semiquinone state by the protein fold.[283]

The lower potential couple of peaks, with $E_0 = E_1$, is due to the semiquinone/ hydroquinone forms and is one of the most reducing couples in bioelectrochemistry: previous CVs of Flds at various surfaces revealed E_1 values between -640 and -760 mV vs. NHE.[283,293-297] The higher potential couple E_2, instead, corresponds to the quinone/semiquinone reduction, occurring between -340 and -400 mV vs. NHE at neutral pH.[283,298] This second peak is not always visible and can be confused with the free FMN signal due to the similar redox potential (E_{FMN}~ -220 mV vs. NHE).[283,293] E_1 is pH independent above 6, while the E_2 potential varies with a slope of -59 mV/pH unit, as binding of a proton is involved in the reduction.[283,295]

Several groups have reported bioelectrochemistry of Fld, and a short list of published works is summarized in Table 7.2. The concentration of Fld required in these heterogeneous voltammetry studies in order to observe any electrochemical signal is typically 50-100 μM and Square Wave Voltammetry (SWV) was often necessary to disambiguate the Faradaic currents.

Van Dijk *et al.*[293] were successful at observing the two separate electron transfer events from Fld by homogeneous voltammetry at mercury electrodes.[293] Later, Vervoort[282] and Heering[283] *et al.* studied the complex behaviour of heterogeneous ET from Fld on oxidized glassy carbon electrodes (GCE). On these negatively charged surfaces only the E_1 was visible. Both groups concluded that FMN is progressively detached from the protein scaffold during the electrochemical investigation and physisorbs on the surface. In some reports the immobilized FMN was used on purpose as a promoter to catalyse the ET from Flds and other flavoproteins.[56,283]

Heering and Hagen[283] addressed the reasons of the absence of the E_2 couple in most of the heterogeneous CV (and SWV) tests on GCEs. They suggested that the complex behaviour of Fld can be explained by a combination of electron transfer mediated by the physisorbed FMN, comproportionation of the hydroquinone and quinone Fld forms and direct electron transfer of holo-Fld to the electrode.

Reference		**Fld Source**	**Electrode**	Modifier	pH	Redox couple(s)	
						(mV vs. NHE)	(mV vs. Ag/AgCl)
Van Dijk	293	*Megasphaera elsdenii*	Hg	Polylysine	7.4	E_1=-114 E_2=-392	-311 -595
Armstrong	294	*Megasphaera elsdenii*	PGE	$MgCl_2$ $Cr(NH_3)_6$	5.0	E_1=-318	-515
Bianco	295	*Desulfovibrio vulgariis*	PGE	Polylysine	6-7.6	E_1=-430	-627
Bagby	297	*Azotobacter croococcum*	PGE	Neomycin	7.0	E_{1a}=-305 E_{1b}=-520	-502 -717
Heering	283	*Desulfovibrio vulgariis*	GCE	Neomycin	7.0	E_{FMN}=-218 E_1=-413	-415 -610
Steensma	296	*Azotobacter vinelandii*	GCE	Neomycin	7.84	E_2=-459	-656
Nöll	56	Wrba of *Escherichia coli*	Au	Surface tethered flavin	7.0	$E_{1,2}$=-465	-662

Table 7.2: Examples of Fld CV investigations reported in the literature. PGE= pyrolitic graphite electrode, GCE = glassy carbon electrodes. Potential values are reported against NHE and Ag/AgCl (sat) which is the reference electrode employed in these experiments.

7.3.3 Immobilisation of Flavodoxin

In the previous chapters it was reported that Lcs was covalently bound to the SAM modified electrode using EDC-NHS chemistry. This is likely to give a random orientation of the protein molecules that doesn't necessarily facilitate homogeneous or efficient electron transfer (as possible, for example, through the hydrophobic immobilisation of Az on modified gold). Fld was instead immobilised by physisorption.

As all Flds are strongly negatively charged at neutral pH (Figure 7.14), electrostatic interactions between the charged surface of Fld and electrodes are commonly used to obtain the immobilisation of these proteins. The presence of a cationic promoter is necessary to prevent the repulsion between the negatively charged protein and the negatively charged surface. Frequently used “bridges” are poly-L-lysine and neomycin[283,293-296], but also other antibiotics such as kanamycin, gentamycin, ions (Ca^{2+}), organic amines (spermine) and cationic surfactants (dimethyl-didodecyl ammonium chloride) effectively “screen” repulsion with the surface and adjacent molecules.[283,294] Coadsorption on polycathionic polymers[293] is also understood to decrease comproportionation and increase the rate of the E$_1$ reduction, making it possible the observation of the E$_2$.[282,283]

In this part of the thesis, work carried out on gold electrodes (GDEs and OTEs) is presented. In order to control the surface charges for the electrostatic physisorption, the metallic surface was modified with a SAM of linear alkanethiol molecules terminated with carboxylic acid groups, specifically 11-mercaptoundecanoic acid (MUA). A layer of neomycin was subsequently used as a polycathion to neutralize repulsion SAM-protein and to favour the electronic coupling.

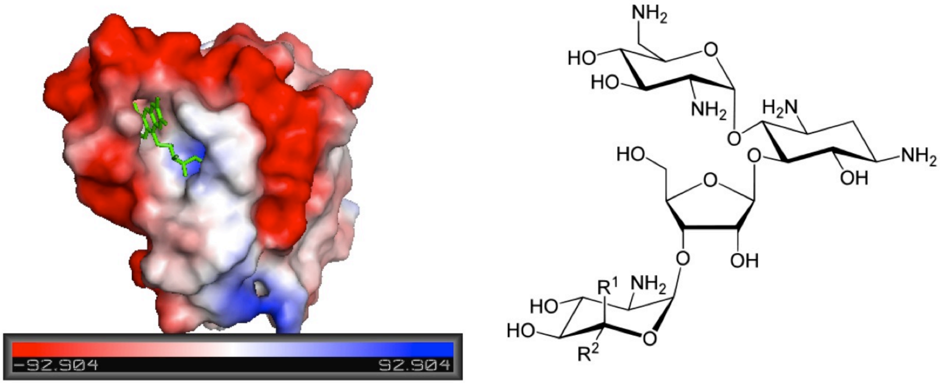

Figure 7.14: A) Schematic indicating the distribution of charge on the surface of Fld. Negatively charged areas are depicted as red, positive as blue and neutral white. FMN is shown in green (PDB: 1J8Q). The charge distribution was obtained using MacPyMOL. B) A molecule of neomycin, the aminoglycoside used for the immobilization of Fld on the negatively charged MUA SAM.

The SAM was also useful in preventing the adhesion of FMN on the bare electrode surface and, as for Az and Lcs, in introducing a physical barrier to reduce the quenching of the fluorescent emission. To our knowledge this would also represent the first report of electrochemical investigation of Fld on MUA modified gold electrode surfaces.

7.3.4 Flavodoxin as a Two Colour Switch

The aim of this section was to screen the emission and the emission switching characteristics of a range of available flavoproteins, in order to compare them with Fld and possibly select new systems suitable for investigation by FCV. It was specifically noted that it may be possible to either directly follow the flavin redox processes without the need for any additional labelling (using blue laser 454 nm excitation) or that the spectral changes associated with the site (Figure 7.13) could be followed by FRET at longer wavelengths.

7.3.4.1 Intrinsic Fluorescence Switching

It was mentioned in the initial chapters that FAD and FMN are amongst the most studied naturally occurring fluorescent molecules. The cause for the radiative emission of light is evident when observing the structure of the two molecules: due to the high aromaticity of the flavin's structure, vibrational and rotational motion of the molecule is restricted and radiative decay is the main pathway for depopulation of the S_1. Oxidized flavins are thus intrinsically fluorescent, absorbing around 450 nm and emitting at 525 nm.[54] The photon emission originates from the lowest π-π^* transition of the isoalloxazine moiety that excites the flavin electron into a singlet state with a lifetime of approximately 5 ns, with a quantum yield in water of 0.26.[54] Inclusion of FMN in the protein induces partial quenching of the cofactor emission by the surrounding aromatic amino acids side chains.[6,292]

As the molecule is reduced the structure of the FMN is altered: double bonds become unsaturated and disruption is caused to the conjugation and planarity of the molecule (Figure 7.12).[299] Alternative mechanisms of relaxation back down to the ground state become more favourable compared to fluorescence and the fluorescent yield is therefore decreased upon reduction.[54]

7.3.5 Fluorescence Spectroscopy of Flavoproteins

In order to quantify the magnitude of the fluorescence quenching upon complete reduction of the Fld, the fluorescent spectra was recorded in solution in the fully oxidised and fully reduced states. This was compared to the switch observed from other flavoproteins, which were kindly donated by Dr Luet Wong (University of Oxford) and to the emission of the free FMN cofactor in solution (Figure 7.15).

Additional analysis was carried out with glucose oxidase (GOx), putidaredoxin reductase (PdR), palustrisredoxin reductase (PuR), and ferredoxin reductase (ArR), all four proteins containing a FAD cofactor.[300-304] The fluorescence spectra were recorded before and after the addition of reducing agent.

Despite the very negative reduction potential of Fld and some of the other proteins, it is reported that dilute solutions can be completely reduced to the hydroquinone form by adding excess sodium dithionite (DT) in neutral pH buffer.[282]

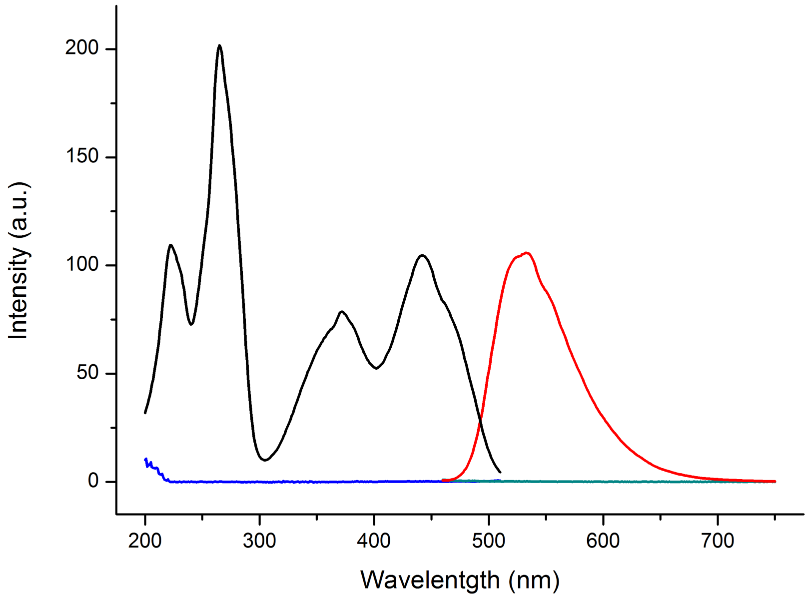

Figure 7.15: Fluorescence excitation (λ_{em}*=525 nm) and emission (* λ_{ex}*=454 nm) spectra of free FMN in oxidized (black and red) and reduced (blue and green) states, showing almost complete loss of the fluorescence emission. After reduction the fluorescence could be slowly recovered by flushing the stirred solution with air, causing the reoxidation by oxygen of the* $FMNH_2$ *molecules.*

Using excitation and emission slit widths of 10 nm and a medium (600 V) photomultiplier tube (PMT) voltage, only the emission from PdR could be observed. The emissions from the remaining proteins were too weak and had to be measured with a higher (800 V) PMT voltage.

The large differences in the fluorescence emission intensity observed from the different protein solutions can be attributed to the different redox cofactor (FAD instead of FMN), to the conformation taken by the flavin in the protein structure and to the effect of the neighbouring residues on it. The FAD flavin co-factor, in particular, both in solution and when bound to a protein binding site, can exist in different conformations: the two extremes are the closed conformation, where the isoalloxazine and adenine rings are stacked, and the open, un-stacked conformation. In the stacked conformation the fluorescence is considerably quenched due to reductive photo-induced electron transfer from the adenine moiety to the isoalloxazine ring.[54] FAD exists in a more open conformation in PdR than the other flavoproteins; in fact a more intense fluorescence is observed in the oxidized state of PdR with respect to other protein solutions with the same concentration.

On the other end, Fld contains an FMN as a cofactor and therefore there is no quenching effect by the adenine moiety. However the close proximity of the indole ring of Trp60 to the FMN reduces the emission of the oxidized cofactor by ~99%.[292]

The spectral features determined by interaction of flavins and binding sites and the conformational constraints imposed by the protein on the three redox states of the flavin are a complex issue that is being actively investigated.[288,289] It is not surprising that, despite comparing protein solutions at the same concentration (determined from the absorption spectra), both the initial fluorescence emission and the observed variation after chemical reduction of the different flavoproteins varied considerably (Figure 7.16). Qualitatively however it can be noted how, for almost all of the tested flavoproteins, chemical reduction caused a diminution of the fluorescent emission, consistently with the previous description of flavins redox-linked emission. GOx emission was not decreased by DT, however a small reduction was observed upon addition of the substrate glucose (not shown), suggesting catalytic turnover of the contained flavin between oxidised emissive and reduced “OFF” state.

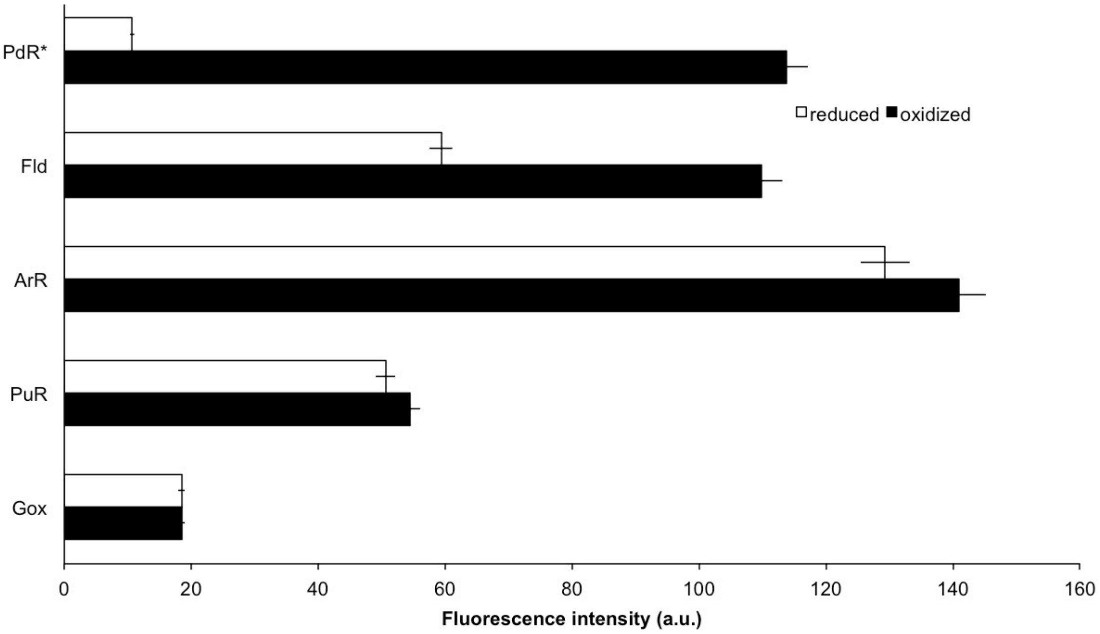

*Figure 7.16: Bar chart showing the fluorescence intensities at 525 nm (with λ_{exc} =450 nm) of the flavoproteins in the oxidised and reduced states (*PdR with a PMT voltage of 600 V, all the others 800V). All the flavoprotein solutions compared had a concentration of 1.6μM (180μL of 100 mM PB pH7.0), and were reduced by addition of sodium dithionite (final conc ~3mM).*

In summary, the largest difference of intensity between oxidised and reduced states was observed for PdR followed by Fld, with 90% and 45% quenching of the fluorescence signal respectively upon reduction. As a result, PdR and Fld were chosen as the most likely candidates to show "ON"/"OFF" switching on an optically transparent electrode.

7.3.6 Epifluorescence Switch of Fld Physisorbed on Glass

Having observed fluorescent switching from bulk solutions of Fld and PdR, the possibility of detecting a switch on the microscope was explored. As an excitation source a 454 nm blue laser was used and a TRITCH filter set was inserted in the microscope light path. Due to complications in reaching the TIRF angle at wavelengths below 550 nm, during the experiments with the blue laser the microscope was used in an epifluorescence mode. A dilute solution containing 0.5 μM concentration of Fld was subsequently let to dry on the surface of the glass coverslip, previously modified with neomycin (by depositing on the glass for 30 s a 10 mM solution and rinsing twice with MilliQ water), to favour protein physisorption on the negatively charged glass. The surface was rinsed with water prior to imaging, to remove non-physisorbed molecules and covered with a drop of buffer at pH 7.0.

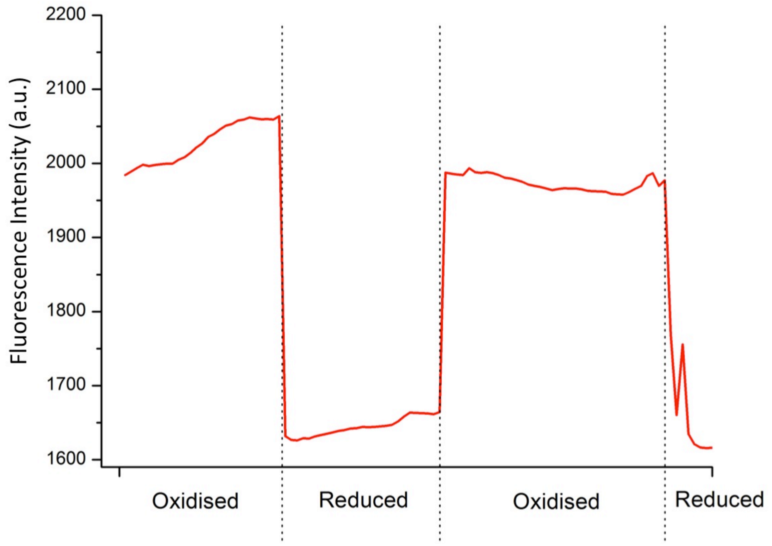

Figure 7.17: Fluorescence intensity of a Fld layer deposited on a glass coverslip, recorded on TIRF microscope as 5μl oxidising and reducing reagents (5 mM dithionite and 10mM ferricyanide) are added to the buffer solution. A similar response was observed with PdR. Excitation time of 100ms.

As with Az (see 5.2), a parallel control was carried out where reducing (dithionite) and oxidizing (ferricyanide) reagents were added to a droplet of buffer only positioned on the SAM-neomycine modified electrode and no fluorescent switching was observed. Therefore any changes in fluorescence observed can be attributed to the protein itself. As consecutive 5 μL volumes of reducing and oxidizing reagent were added to the proteins physisorbed on the neomycine modified glass, the fluorescence intensity, from the average of the whole area recorded by the EM-CCD camera, cycled reversibly and faithfully, with a quenching of 40 ± 5% of the initial fluorescence for Fld (as shown in figure 4.4). A similar test showed a switching of 60 ± 6% for PdR. As both Fld and PdR showed a commutation of fluorescence that is observable on the microscope through glass, both flavoproteins progressed to the electrochemical and immobilisation studies.

7.3.7 Electrochemistry of Fld and PdR

In the previous section, the switching of fluorescence has been observed in solutions of Fld and PdR. The proteins were then subjected to electrochemical analysis to determine whether the electrochemical and fluorescent responses could be correlated. Preliminary PdR studies on GDEs produced promising results, with a current response detectable by CV, in agreement with a published report.[305] Due to shortage of the PdR solution, further experiments proceeded on Fld.

7.3.7.1 Flavodoxin CV and SWV

All the experiments on Fld voltammetry were recorded using an Ag/AgCl electrode, with a potential of -43.4 ± 1.2 mV vs. SCE at 20°C (measured by chronopotentiometry). Initial attempts of heterogeneous voltammetry revealed two Faradaic couples of peaks associated to quick protein denaturation on the bare metallic surface. However to ascertain if the electrochemical and fluorescence measurements of Fld could be recorded simultaneously, the electrochemical signal must be evaluated on surface confined protein populations. Gold OTEs and GDEs were therefore modified with MUA overnight and the negatively charged SAM was further tailored for interaction with Fld by delivery of a neomycin solution for 30 seconds. Finally a 10μM droplet of Fld in low ionic strength buffer was left to interact on the surface, as described in the experimental chapter (in section 4.3.1.4).

Unfortunately, in conventional CV on GDEs, the Faradaic signal of Fld resulted to be undistinguishable from background capacitive currents when ν of 50-200 mV s^{-1} were applied. However two couples of Faradaic peaks could be observed by SWV (Figure 7.18). This may suggest that only a small amount of the Fld proteins is in close proximity of the electrode and oriented favourably enough for the electron transfer to take place.[294] From the average of the positions of the anodic and the cathodic peaks, the SWVs indicated two E_0 values at -689 ± 4 mV vs. Ag/AgCl and -451 ± 4 mV vs. Ag/AgCl.

These values are in good agreement with the range of reduction potentials reported in the literature respectively for E_1 and for E_{FMN} (see Table 7.2) and also with previously observed Faradaic peaks in heterogeneous voltammetry at platinum electrodes (not shown). It is therefore reasonable to attribute the lower potential peaks to the signal of the protein bound cofactor, while the other redox couple at anodic potentials could be either free FMN or the E_2 couple.

In order to clarify the identity of the second peak, the SWV data were compared with the response of free FMN in solution at a MUA modified gold electrode. In these conditions FMN gave a peak at -456 ± 4 mV vs. Ag/AgCl, thus suggesting that the second peak in the SWV is free FMN.

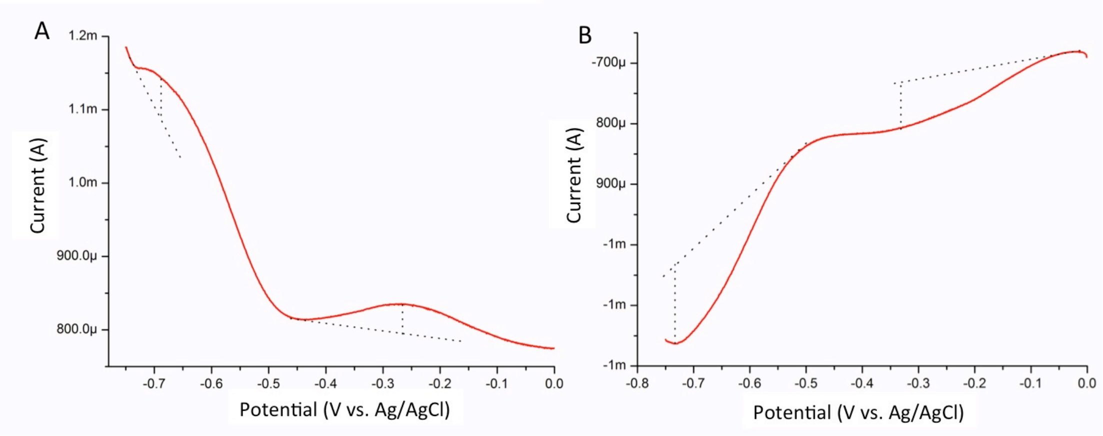

Figure 7.18: Anodic (left) and cathodic (right) square wave voltammetry of the flavodoxin immobilized to a gold OTE modified with MUA and Neomycin, data acquired at a frequency of 100 Hz with 10 mV potential step in 0.1 M sodium phosphate buffer (pH7.0). Each scan shows two broad, weak peaks corresponding to electron transfer processes occurring at -689 ± 4 mV and -451 ± 4 mV vs. Ag/AgCl. during the reduction of FMN and the oxidation of $FMNH_2$ *bound to the protein and free in solution.*

The lack of CV response though impeded the evaluation of the peaks shapes and the assessment of Fld surface concentration. Therefore, before proceeding to the FCV experiments, a quantification of the number of surface confined molecules was carried out on Au-OTE modified with MUA, neomycin and Fld. Tapping mode AFM (carried out by Dr Amol Patil) and analysis of the heights of the features based on the protein crystallographic dimension[299] were used to map the topography of the Fld immobilised to the surface of the modified OTEs. The surface concentration was found to be 4.40×10^{11} molecules/cm^2, corresponding to submonolayer coverage.

It was concluded that, at this concentration, the Fld molecules could be addressed electrochemically in an immobilized state by only SWV. As already observed for laccase, the measurements were therefore suffering from poor levels of electronic coupling of the protein to the supporting electrode, resulting in weak electrochemical signals being observed. The intensity profiles obtained under potential control during FCV investigation are presented in the next section.

7.3.8 Fluorescence Cyclic Voltammogram of Flavodoxin.

7.3.8.1 Flavodoxin Intrinsic Switching

In FCV, under blue laser illumination, the Fld layer showed a clear response to the applied potential as it was swept back and forth its standard redox potential in the potential window -0.85V to -0.25V vs Ag/AgCl. 30 ± 3% of the original fluorescence intensity emitted at 525 nm was decreased on the application of a reducing potential (Figure 7.19). As in the case of Az, the switching observed was lower (of about 70-30%) of what observed in solution and was reproducible over multiple cycles, repeated over several experiments with relative ease. When positive over potentials were applied to the modified OTE, the fluorescence intensity increased up to -400 ± 10 mV and then plateaued, which indicates that the sample was fully switched at this potential.

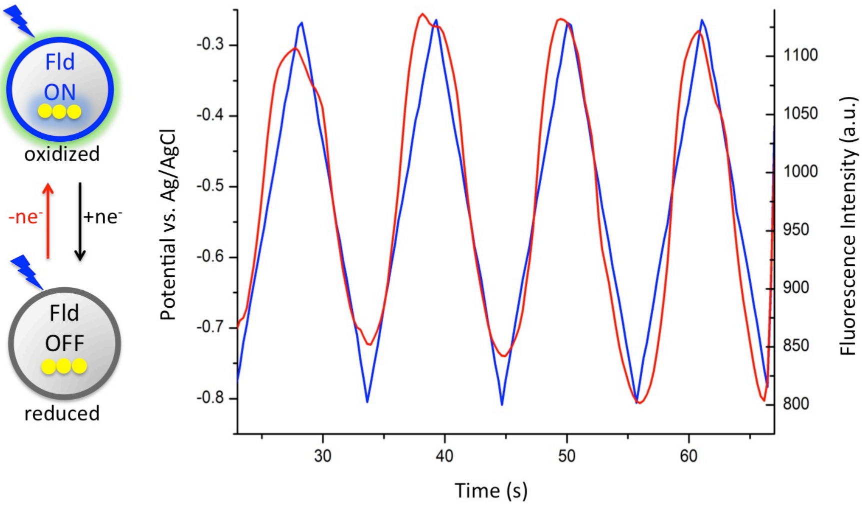

Figure 7.19: Fluorescence intensity of Fld plotted against time (red line); overlaid is the change in potential against time (blue line). On the right a schematic of the fluorescent switch suggested as responsible for the fluorescence variation. The fluorescence intensity is

As a control, images were acquired both when no potential was applied and when the potentials were cycled outside of the potential window where the redox process occurs, namely between 0 to 0.5V vs. Ag/AgCl. At these potentials, the protein should be completely oxidized and no change in emission, beside photobleaching or quenching due to molecular motion, is expected.

As predicted, FCV traces acquired in the control experiments reported no intensity fluctuation, apart from a photobleaching slope, indicating that the protein is stably bound on the surface of the SAM.

At this point, however, it is still not clear whether the reaction corresponds to a single or double electron transfer event. In theory the highly emitting form of the FMN is the completely oxidized quinone. Switching “on” of the fluorescence with more positive potential seems therefore to suggest that at least a part of the protein population undergoes a double ET between the quinone/hydroquinone forms. Determination of the FCV potential can help addressing this point.

7.3.8.2 FCV Potential

The alignment of the fluorescent traces with the potential, as reported in chapter 5, confirmed that the switching was confined clearly to the redox window of the protein, and occurred, specifically, at or very close to the E_1 half wave potential of Fld. Indeed, a derivative of the fluorescent graphs from the averaged signal of 30 ROIs (shown in Figure 7.20) indicated an $FCVE_0$ of -630 mV vs. Ag/AgCl, which is in reasonable agreement with the E_1 obtained from the SWV of -689 mV and with the potentials reported in literature for the E_1 peak on glassy carbon of -610 mV.[282,283]

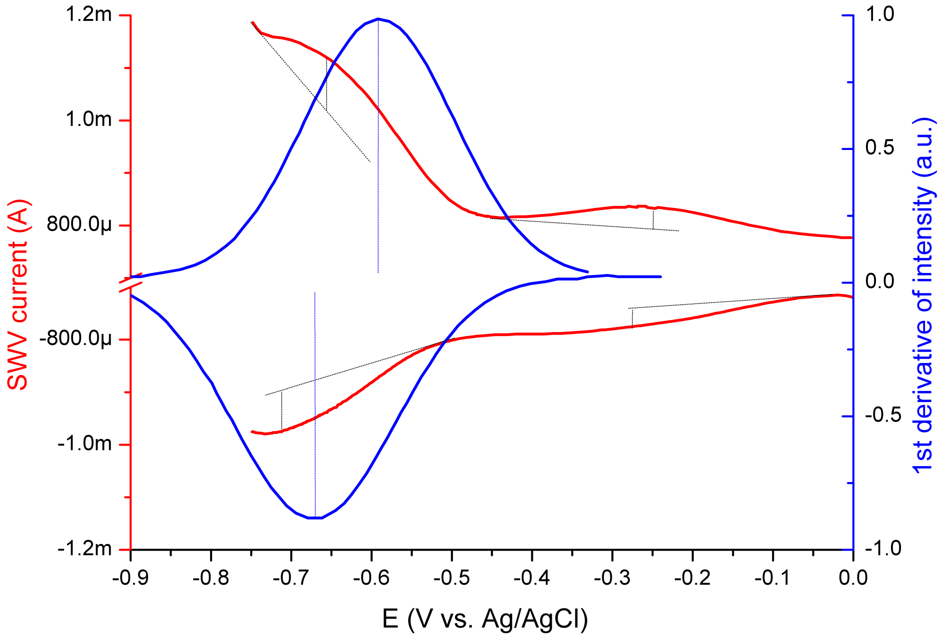

Figure 7.20: The first derivative of the direct fluorescence resolved electrochemistry at 530 nm (λ_{exc} =454 nm) for a monolayer of immobilised Fld. The optical signal (blue line) was calculated from averaging 30 traces of 3 × 3 pixel² and compared with the SWV currents (red trace) presented earlier (section 7.3.7.1).

It can therefore be concluded that the oxidation of the fully reduced hydroquinone to either semiquinone or quinone states although too weak to be detected by CV, can be observed by FCV, using the fluctuation in the emission of the FMN cofactor. The AFM analysis of the surface confined population suggested a surface concentration of about 0.7×10^{-12} moles cm^{-2}, it can therefore be estimated that the switch observed was recorded from as little as a few hundred molecules (~450) per 3 × 3 pixel² ROI.

Having confirmed the switching of unlabelled Fld at the electrode surface, a series of experiments were undertaken to explore the possibility of extending the measurement to longer wavelengths by means of FRET-coupling of the changes in the absorption spectra to the emission of an appended fluorophore, which can give complementary information about the redox process.

Furthermore labelling with an extrinsic organic dye, which has higher quantum yield and extinction coefficient might improve the imaging quality.

7.3.9 FRET Based Switching

In contrast with the quinone and hydroquinone state of Fld, the neutral semiquinone state of the protein absorbs in the blue[91,92] and the difference in the absorption spectra at these frequencies is suitable for construction of a FRET based switch.[33]

The electronic spectra of the three states of Fld at pH7.0, obtained after reduction of the air-oxidized Fld solution with solid sodium dithionite, are reported in Figure 7.21, overlaid to the normalized emission of the Atto655 dye.

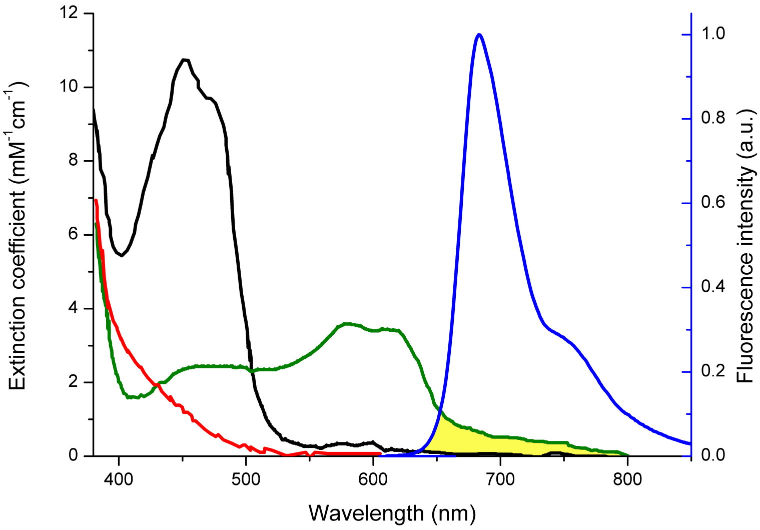

Figure 7.21: Spectral overlap between the absorption spectra of D. vulgaris Fld in the three redox states. Black line: Fld completely oxidized, in equilibrium with air in phosphate buffer pH7.0; red line: Fld-semiquinone, after reduction with solid sodium dithionite; green line: further reduction to the hydroquinone state, obtained in deareated conditions. The blue line represents the normalized fluorescence emission of Atto655 (λ_{exc}= 658 nm) and the differential spectral overlap (J) at ~650-700 nm is indicated in yellow.

The yellow area illustrates the extent of the spectral overlap (J) between the semiquinone state of the protein and the emission of the fluorophore, from J a Förster radius of 32.5Å can be estimated as detailed in section 2.2.[33]In Figure 7.21 it can be easily seen that the Fld semiquinone has a much larger overlap with the emission spectrum of the dye (blue line) with respect to both quinone and hydroquinone, therefore the FRET communication of FMN with the Atto655 will determine an ON-off-ON switching mechanism, as presented in the schematic of Figure 7.22.

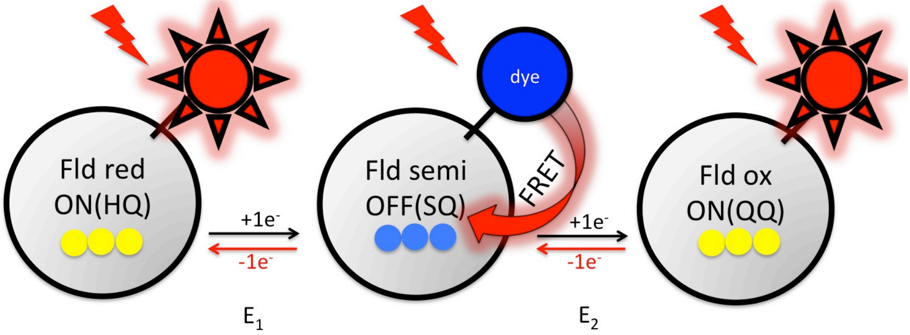

Figure 7.22: Schematic representing a model of the (redox dependent) double switching expected at 670 nm based on FRET N-terminally labelled Fld. Form the completely reduced state, the oxidation occurs in two steps, referred to as E_1, from the hydroquinone to the semiquinone, and E_2 from the semiquinone to the quinone state. The intensity change associated with E_1 is an on→off and viceversa "OFF" → "ON" is expected across E_2. Research illustrated in the remaining part of the chapter focused on the E_1 redox process, by selecting a suitable potential window.

Fld was therefore labelled with a NHS-ester Atto655 dye on the N-terminus. The procedure was analogous to the one used for Az and Lc A and resulted in a ~30% labelled Fld solution. As in the previous case the degree of labelling was kept well >1 on purpose to avoid nonspecific multiple labelling of the same protein.

As indicated in the 3D structure in Figure 7.13, the N terminus is positioned at the opposite side of the protein structure with respect to the FMN, at a distance of 32.5Å from the FMN molecule (measuring from N10 to the Cα of the N-terminal amino acid). Accounting for the linker length, the distance R between the dye and the FMN can be estimated as 4.25 ± 0.5 nm and the expected FRET efficiency over this interval of distances is expected to be 10-30%.

7.3.9.1 FRET Based Switching of Flavodoxin

After tagging and removal of unreacted dye by filtration, the protein was immobilized on the MUA-neomycin layer and subjected to electrochemical scanning to observe the fluorescence response, while exciting the Atto655 dye at 633 nm. The potential window investigated was limited to the region of the E_1 potential, scanning from -0.7V to -0.2V vs. Ag/AgCl; the obtained fluorescence fluctuation response is shown in Figure 7.23.

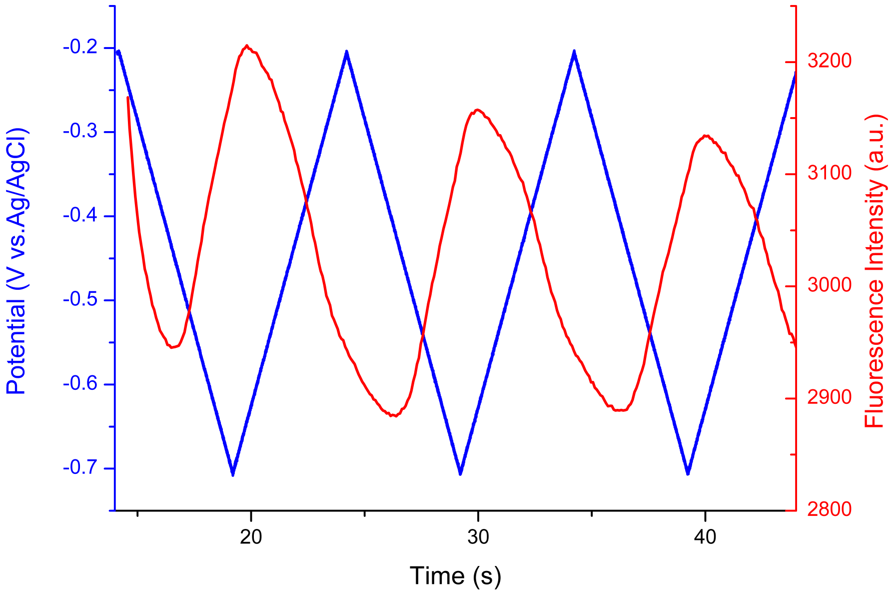

Figure 7.23: Fluorescence intensity (red line) of Fld tagged with Atto655 immobilised on a gold OTE plotted over time. The blue line is the potential time trace, swept between -0.2 and -0.7 V vs Ag/AgCl. The oxidized form of the protein is "OFF" while the reduced is "ON" as expected for oxidation and reduction across the E_1 potential.

The time trace clearly displays a decrease of the fluorescence at higher potentials consistent with quenching of the emission by the semiquinone Fld. After subtraction of the environmental noise, the switching efficiency determined from the surface confined protein layer was 10-15%, in good agreement with the expected values based on Förster theory.

Since the same conditions used to immobilize the unlabelled Fld were retained in this test, the surface concentration is assumed to be close to what measured previously by TM-AFM, about 0.7pmol/cm. Thus, accounting for the fraction of labelled molecules (30%), it is possible to estimate that the optical signal is obtained by as little as 150 molecules contained in each diffraction-limited spot.

The observed switching efficiency of surface confined Atto655-Fld (Q=10-15%) is in line with the calculated E value (section 7.3.8.1). Notably, in the only previous report of FRET labelling on a flavoprotein (a cysteine mutant of Fld from *A. vinelandii),* a large discrepancy was observed between the expected and observed value, respectively Q=25% vs. E=80-100%.[33] In this specific case, however, the dye (Cy5) was positioned at only 2 ± 0.5 nm from the FMN site, where short range interactions (Dexter type), direct interaction (e.g. stacking) and photoinduced ET from the quinone to the Cy5 dye, may occur, thus quenching the "ON " state of the fluorescent switch.[33] The present study thus may benefit from the increased distance (~4 nm) between the fluorescent Atto655 and the flavin, resulting in Q close to the calculated value (E=10-30%).

As already observed for the unlabelled Fld molecules, the FCVE$_0$ is close to -650 mV vs. Ag/AgCl, close to what expected for a E$_1$ "ON"→"OFF" switch, and no significant modulation was observed outside of the redox potential window. Since the chromophore is not electroactive in the explored potential window and the red laser (λ = 633 nm) used does not directly excite FMN, the change in fluorescence of Atto655 confirms that the detected fluctuation is originating from FRET to the Fld semiquinone state.

7.3.10 Interpretation of the Intrinsic and FRET Coupled Switching

A direct comparison between the image acquisition upon illumination at 450 nm and 633 nm is difficult due to the different light pathways used. However qualitatively it can be observed that acquisition at longer wavelengths was easier, resulting in higher photon counts and more defined images, as visible in the fluorescence intensity scale in Figure 7.20 and Figure 7.23. This is due firstly to the higher absorption coefficient and quantum yields and extinction coefficient of the Atto655 dye with respect to protein bound FMN. Secondly a higher signal is generally obtained in the red region, where the OTE, has lower absorption (section 5.5.2) and TIRF illumination can be used to increase the signal to noise ratio.

The two opposite fluorescence switching behaviours observed are summarized in the schematic in Figure 7.24.

Interpretation of the two different switching is not completely straightforward. On one side, the clear modulation observed for the FRET system (Figure 7.23) suggests that at least part of the population of surface confined molecules is undergoing a one-electron reaction at potentials close to -650 mV. This is consistent with previously reported E_1 potential of oxidation. The change in fluorescence emission originates from passage from the colourless hydroquinone to the blue semiquinone state, in which FRET quenches the fluorescence of the appended dye (section 7.3.9.1). Accordingly, at *increasing potential* the fluorescence displays an "ON"→"OFF" switch centred at E_1.

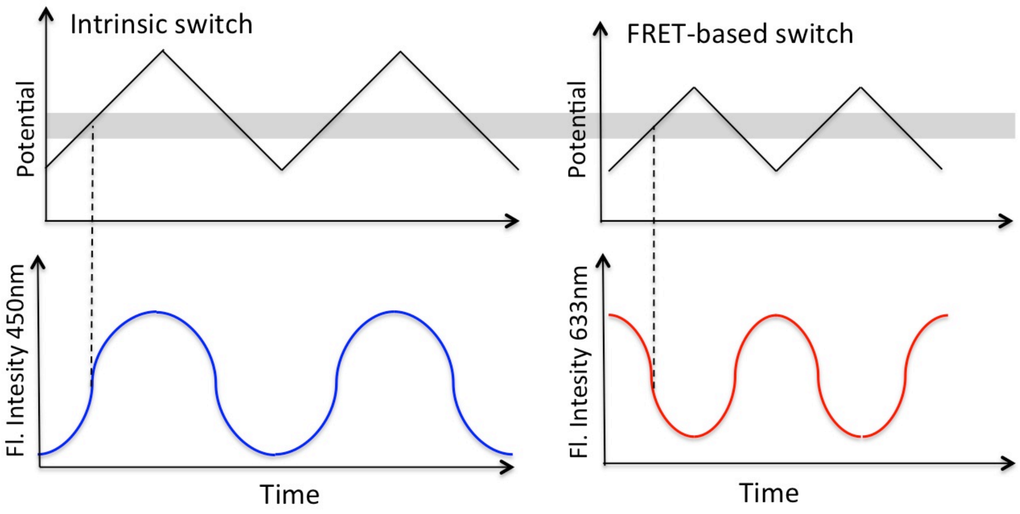

Figure 7.24: Schematic of the observed fluorescence switching respectively for the intrinsic switching observed for the unlabelled protein at λ_{exc} =450 nm and FRET based system upon illumination at λ_{exc} =633 nm. The potential band shadowed represents the FCV E_0 range.

Correspondingly, FCV interrogation of the unlabelled Fld intrinsic fluorescence (section 7.3.8.1), showed an opposite "OFF"→"ON" response (Figure 7.24). This was also consistent with oxidation of the Fld molecules. The determined FCVE_0 was occurring at potentials 20 mV positive of the FRET coupled switch, thus 630 mV vs. Ag/AgCl. The potential of such event is too negative to belong to free FMN in solution, which in separate control experiments was observed to respond at higher potentials.

However the intrinsic switch, where the completely oxidized form of FMN is thought to be the brightly emitting species, hints at a two-electron transfer event, which is apparently conflicting with the one-electron transfer process highlighted by the FRET-coupled response occurring at only 50 mV lower potential.

The observations might be explained hypothesizing the presence of different forms of Fld on the surface, which react in a one or two electrons reaction, as already suggested for electrochemical investigations on glassy carbon electrodes by Heering.[283] Further tests, also taking into account the kinetics of the two ET events, would be required to extend the FCV investigation to the potential region of the semiquinone/quinone couple, where a second "OFF" →"ON" switch is expected (see schematic in Figure 7.22).

7.3.11 Conclusion on Flavodoxin Fluorescent Cyclic Voltammetry

The possibility of extrapolating the use of FCV to a physisorbed monolayer of Fdl has been reported. Potential modulation of the fluorescence intensity was repeatedly observed where purely electrochemical analysis failed in resolving any Faradaic CV peak and only weak currents were observed by employing a more sensitive SWV technique. TM-AFM imaging confirmed the surface coverage was 0.7×10^{-12} moles cm^{-2}, corresponding to about 450 molecules for the intrinsic switching and 150 molecules for the FRET coupled one. The work thus confirms that FCV is a highly sensitive technique able to detect changes in redox states of a few hundred molecules, whose electronic coupling is too weak to be detected by macroscopic electrochemical methods, which typically require 10^{10} molecules in order to detect electron transfer.[204] The spectral resolution obtained by using two different laser/filters combinations can be extended to analysis of other flavoproteins and can provide a way to resolve transient intermediates and multiple species within the surface confined populations. Beside Fld, among the screened flavoproteins, PdR showed promising characteristics for investigation by FCV.

7.4 Summary and Future Perspectives

This part of the work sought to extend application of FCV to bioelectrochemical switches alternative to Az. Two diverse and interesting proteins, such as Lc A from *T. versicolor* and Fld from *D. vulgaris,* were successfully confined on the carboxylic terminated MUA SAM at Au-OTEs, using covalent binding and electrostatic physisorption.

The emission of an appended dye (and intrinsic emission of the flavin redox centre itself in the case of Fld) exhibited significant optical responses to potential modulation. As already observed for Az, fluorescence fluctuation could be clearly seen where current responses were weak or impossible to detect.

In the case of Lc the presence of the electrochemical signal in absence of redox-linked optical response suggests that the T1 copper centre is either not responsible for the observed faint peaks in the CVs or that a further reaction is occurring, preventing the detection of switching. The small potential modulation observed is therefore thought to arise from the motion of the protein with respect to the gold as already observed for zinc Az (in section 6.5.1) and previously for labelled cytochrome *c*.

In the second case, surface confined Fld has shown to respond optically to changes in redox state, producing a highly reversible on/off switching of emission. Not only it was possible to monitor the variation in the intrinsic emission of the flavin cofactor by exciting with a blue laser and collecting light in the green, but also the protein showed sufficient spectral changes in the hydroquinone/semiquinone transition for the electron transfer to be observed at >670 nm, after FRET coupling with an Atto655 dye.

One of the central concepts of this work was the inherently higher signal to noise ratio available in fluorescence as opposed to voltammetry. It is therefore important to note the low concentration of the surface confined molecules studied, approaching the limit of 1-2×10^{-12} moles cm^{-2} usually accepted for detection of non turnover peaks by conventional CV.[204] The optical detection of areas of few µm^{2} down to diffraction-limited areas, allows a further restriction of the number to sample sizes of few hundred molecules, respectively 350 and 150 for labelled Lc and Fld.

Furthermore the present chapter importantly explores systems in which FCV reading at multiple wavelengths is possible, opening a perspective to spectral isolation of different redox processes occurring on the surface.

Chapter 8

A study of Azurin DET Kinetics by Electroactive Monolayers Capacitance Spectroscopy

8.1 Introduction

As described in chapter 3, the rate of non-adiabatic electron tunnelling from the fluorescently tagged metalloproteins, as from any other redox probe, to the surface depends critically on the driving energy applied, on the reorganization energy of the redox centres and on the electronic coupling between electrode and redox center.[142] The coupling is controlled by the intervening medium dielectric properties and by the distance between the protein redox-active center and the electrode surface.[306]

Clearly retaining DET while increasing the dye-metal distance is highly relevant to FCV, in that it allows a positioning of the fluorescent switching proteins further from the surface. Increased surface fluorophore distance is not only beneficial in reducing the SET effect due to the metallic substrate[70,74,121,307] (as detailed in section 2.3 and 5.5), but can also result in maximization of the fluorescence Surface Plasmon Enhancement (SPE) for certain types of metallic layers.[117,118,131,133] SPE has a maximum at ~20 nm from the surface, while metallic quenching/SET is expected to fall sharply between 5 to 10 nm from the surface (see section 2.3) therefore any nanometre of distance gained in this region is expected to greatly increase the number of detected photons.[117,118,121] On the other side electronic coupling requires the redox centres to be positioned close to the surface, as the limit for long-range ET in proteins is of 1.4 nm.[142,177] Thus, ideally, in a single layer of FRET-based bioswitches, the label should be positioned on the side of the molecule directed towards the solution to maximize the optical signal, while the redox centre should be directed towards the electrode surface to improve the electronic coupling.

In this perspective, the development of a method to evaluate quickly the position of the two elements with respect to the surface is relevant to the development of the FCV models. One way of measuring the distance between the redox centre and the surface is, once known the intervening medium, to use the rate of electron transfer.

The aim of this chapter is to illustrate preliminary analyses done by Electrochemical Impedance Spectroscopy (EIS) as novel method to characterise the kinetic properties of metalloproteins films, using an Az layer, physisorbed at SAMs of increasing thickness as a model.

The aim here is not to investigate the electrochemical properties of the Az molecules, but rather to evaluate the response of the proposed approach in the analysis of DET kinetics. Therefore, determination of the k_{ET} of Az is used to make a comparison between the commonly employed CV procedure based on the time-domain measurements and, the proposed method, based on frequency resolved measurements of the complex capacitance of the film, C^*, which will be here referred to as Electroactive Monolayer Capacitance Spectroscopy (EMCS).

8.2 Electron Transfer Rate Determination by CV

Several electrochemical methods are available to determine ET kinetics of immobilized redox active centres, such as CA, SWV and the most popular CV.[136,308] It is commonly accepted that each of these methods has advantages and drawbacks and is more or less suitable for different systems. For example, chronomethods, such as CA afford the advantage of not requiring an *a priori* model for the potential dependence of the electron transfer rate. This is in fact simply measured from the decay of the i following a potential stimulus. However, especially for a system that has fast kinetics, such as Az on short alkanethiol SAMs, the distinction of the i_f from the i_c contribution in CA can be difficult as the two components may overlap significantly. On the other side, SWV methods have the benefit of minimizing capacitive contributions to signal and are particularly convenient in bioelectrochemistry for detection of i_f of diluted proteins sub-monolayers.[136,178,219,309] However kinetics extrapolation by SWV require complicated analysis and extensive computation.[136,219]

As a consequence, CV, which unites simplicity of analysis and reasonably easy separation of capacitive and Faradaic currents, is the most commonly used method in bioelectrochemistry.

A simple example of the use of CV for the determination of Az (unlabelled) kinetics on a series of SAM-modified polycrystalline GDEs is shown in this section, and will be compared with the EMCS analysis, performed on the same electrodes, in section 8.3.

8.2.1 Voltammograms of Azurin at Octanethiol-Modified GDEs

Az molecules were physisorbed on SAM functionalized GDEs as outlined the experimental details in section 4.3. In the examples of CV reported in this chapter, the Az film had a submonolayer surface concentration of 2-10 $\times 10^{-12}$ moles cm^{-2}, determined from integration of the Faradaic currents (eq. 3.3), and a E_0 potential (section 3.2) of 89 ± 3 mV vs. SCE, in agreement with literature reports for this pH.[153,159]

A sequence of CVs obtained at the Az-octanethiol-GDE is reported in Figure 8.1A. In the CVs shown the voltammetric ν was progressively varied from $0.5\ \mathrm{V\ s^{-1}}$ (red line) to $12\ \mathrm{V\ s^{-1}}$ (black line). Accordingly the current response increased with the ν applied.

The peaks characteristics: area, FWHM, height and position were determined using the peaks fitting function in GPES software. From this analysis, the oxidation and reduction peaks resulted to be symmetric (ratio of oxidative and reductive peaks area ~0.9-1.1) and displayed a FWHM of 95-100 mV. The peak-to-peak separation, ΔE, at $\nu < 1\ \mathrm{V\ s^{-1}}$ ranged between 10-20 mV. Notably, the reported values diverge only slightly from the FWHM of 89.6 mV at 22°C and ΔE=0 mV predicted by Nernst equation for a one-electron reversible process.[206,207]

The linear change of the height of the peak currents (i_p) with the applied ν (Figure 8.1B) was commensurate with DET from an adsorbed redox probe, as opposed to heterogeneous electron transfer from diffusing redox centres, for which a variation of i_p linear to $\sqrt{\nu}$ is expected.[19,41,136,200]

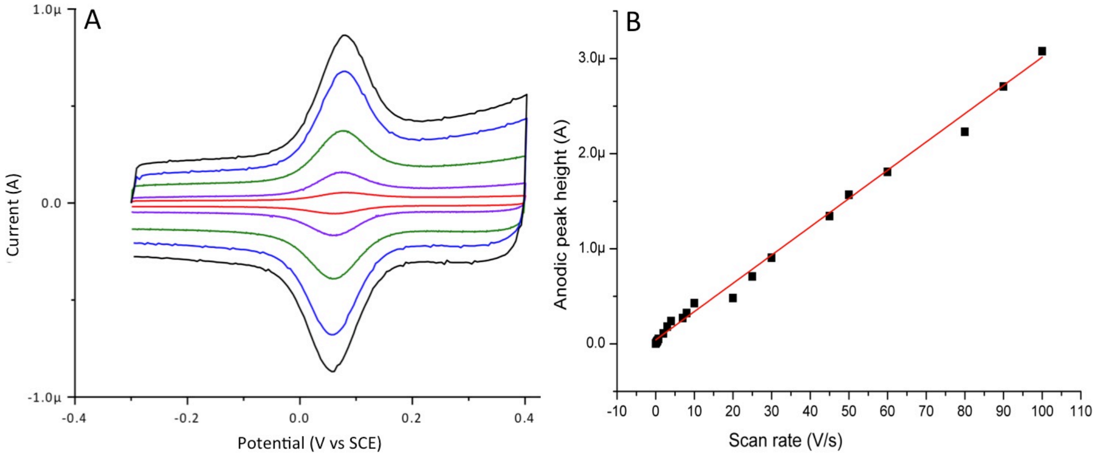

Figure 8.1: A) Voltammograms at variable ν measured for Az immobilized on octanethiol SAM in pH5.0 MES buffer with 200 mM NaClO₄ supporting electrolyte. Starting from the central line red line, data were acquired at a ν of 0.5 $V\ s^{-1}$*, 3* $V\ s^{-1}$*, 5* $V\ s^{-1}$*, 10* $V\ s^{-1}$ *and 12* $V\ s^{-1}$*. B) The height of the current peaks increases linearly with the applied ν for a film of Az at octanethiol-modified electrode, indicating that the number of the redox centres is finite and that these are confined at the surface; in red is a linear fitting with* R^2*=0.98.*

The CVs shown in Figure 8.1 were acquired on an octanethiol layer. The same procedure was repeated for Az on SAMs of different thicknesses (data not shown), namely hexanethiol, decanethiol and dodecanethiol, which were used to control the distance and thus the electronic coupling of Az with the electrode.

8.2.2 Fitting to the Trumpet Plot

The position of the cathodic and anodic peaks depends on the scan rate applied and on the distance between the protein and the surface. As illustrated earlier in Figure 8.1, at slow ν (<1 V s^{-1}), the current peaks of Az on octanethiol are close together, and the Az i_f develop similarly to the Nernstian model (reported in figure 3.2). When the voltammetric ν is increased, the peaks start to move apart from the redox potential of the couple, and this displacement can be fitted to a theoretical model (section 3.2) to determine the k_{ET}.

The positions of the experimentally determined anodic and cathodic peaks (E_{pa} and E_{pc}), reported versus the logarithm of the applied ν, result in the 'trumpet plots', so called because of their characteristic shape. These plots contain information on many aspects of the electron transfer process, such as the thermodynamics, kinetics, and on the time scale of coupled reactions eventually occurring.[19,36,308,310]

In this pH range, the absence of coupled reactions gating Az electron transfer (as opposed to trumpet plot of Figure 5.15, taken at pH 7.0) is revealed by the symmetric and monotonic shift of the anodic and cathodic arms of the trumpet plot with ν.[19]

When trumpet plots acquired at different SAM thicknesses are compared, it can be noticed that the abscissa where the anodic and cathodic peaks positions separate from E_0 scales inversely to the thickness of the SAM. For instance Figure 8.2 shows a comparison of trumpet plots of Az immobilized on four thiols of increasing thickness: hexanethiol, octanethiol, decanethiol and dodecanethiol.

As the thickness of the SAM increases, the peaks start to separate at smaller applied ν, indicating a decrease in the electronic coupling between Az and the electrode.

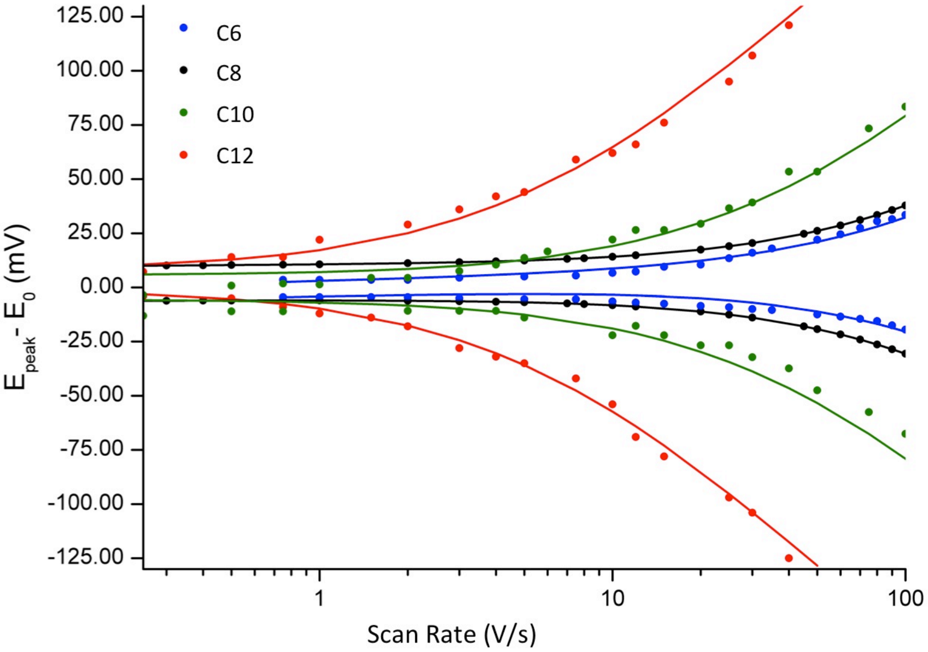

Figure 8.2: Trumpet plots of Az immobilized on hexanethiol (C6), octanethiol (C8), decanethiol (C10) and dodecanethiol (C12). The point correspond to the peaks positions evaluated at each ν applied ad the continuous lines represent the best fit to the data and the corresponding electron transfer rates, $k_{ET,}$ were 3050 s^{-1} , 3390 s^{-1} , 520 s^{-1} and 80 s^{-1} respectively for hexanethiol,octanethiol, decanethiol and dodecanethiol.

A least square fitting procedure[178], carried out with the software Jellyfit (written by Dr Lars Jeuken, University of Leeds), is used to fit the displacement of the peaks to the Butler-Volmer equations (eq. 3.4 and 3.5), after subtracting contributions from a constant peak splitting observed at low scan-rates (UQR, see section 3.2).

The continuous lines in Figure 8.2 represent the best fit to the data obtained with this procedure, corresponding to k_{ET} values spanning two orders of magnitude, from the fast kinetics of ~3000s^{-1} observed at hexanethiol and octanethiol SAMs, to the minimum of 80s^{-1} on dodecanethiol. Specifically the determined values for the set of electrodes displayed in Figure 8.2 are listed in Table 8.1, in section 8.3, compared with those obtained with the frequency-resolved method described in the remainder of the chapter.

8.2.2.1 Remarks on Electron Transfer Rate Determination by CV

The CV approach practically involves measuring numerous voltammograms at different ν (here between 0.1 and $100\ \mathrm{V\ s^{-1}}$), followed by subtraction of the capacitive current background and manual fitting of the peaks position for each of the acquired scans. This can be done either manually or by means of peak fitting functions, commonly provided in the potentiostat software. Finally the k_{ET} value can be determined from the shift in the peaks potential either with Laviron plots or by fitting the $\Delta E_p(\nu)$ traces to Butler-Volmer equations, as exemplified in the previous section.

The method has many advantages as it is very versatile and consolidated,[206,207] and there is a large body of literature using it.[311] Additionally both the procedure and the analysis are simple and free software packages for analysis are available.[312]

Although methods to resolve the kinetic heterogeneity in the population of redox centres from the CV plots have been reported[34,38,39,199,313], these require further complex mathematical analysis of the peaks shapes and their variation with ν.

Additionally, acquisition of the large series of voltammograms requires time. Instrumentally, construction of programmed acquisition routines is not always possible, due to changing current ranges at increasing ν and to biases that can occur when analysing fast responding molecules (such as Az) on potentiostats not equipped with fast scan modules. Also interpretation of the peaks position can be subject to evaluation error, especially, when the Faradaic currents are small. As a consequence the whole procedure is generally time consuming and prone to error with respect to the method based on EMCS.

8.3 Electroactive Monolayers Capacitance Spectroscopy

By using EIS, the electron transfer of surface confined proteins can be explored in the frequency domain by continuously varying the frequency of the potential modulation. In its most common operation mode, an EIS potentiostat enabled the superimposition of a monochromatic sinusoidal wave, with a small amplitude (10 mV), to an applied constant potential or to a linear variation of potential between two extreme values (AC voltammetry).

The superimposed modulation is small enough to correspond to an approximately linear current response, so that the system at constant potential is in steady state.[136]

In the form of AC voltammetry, the frequency and amplitude of the superimposed modulation is kept constant, while the potential is swept linearly between two values, as in SWV.[136] The k_{ET} of redox active monolayers can be evaluated from the resulting current/potential AC voltammograms using the 'current-ratio' protocol proposed by Creager and co-workers.[314] This method requires the acquisition of many AC scans at different frequencies, plotting of the ratio $\frac{i_{peak}}{i_{background}}$ vs. the ω of acquisition, followed by fitting with two adjustable parameters, the k_{ET} value and a ratio of the C_{dl} to the pseudo-capacitance C_{ad} of the redox active adsorbate.[314] This approach also allows a relatively simple evaluation of the kinetic heterogeneity for subpopulations of molecules with different k_{ET} and same E_0.[315] However, like in in normal CV, several acquisitions and manual evaluation are required to extrapolate the $\frac{i_{peak}}{i_{background}}$ vs. the ω, making the analysis laborious.

In the approach proposed here, EIS measurements were performed in the simple steady-state mode, where the amplitude and potential of the sinusoidal potential variation are kept constant and in the range of frequencies varying between 10^{-2} to 10^{6}Hz.

The electrochemical impedance, $Z^{*}(\omega)$ is the measure of the opposition of the whole electrochemical cell to the small sinusoidal stimulus applied at each frequency. In fact the whole cell itself can be considered as an impedance to the small sinusoidal excitation.[136] From the complex impedance the contribution of each element of the cell to the impedance plots in the complex plane, in terms of resistive and capacitive elements and distribution of these, can be extrapolated either by defining a mathematical model, or by using an empirical fitting approach, based on a electrical equivalent circuit.[136]

Figure 8.3 shows a proposed circuit equivalent to the system under study, composed of capacitive contributions from the double layer of ions in solution, from the SAM dielectric, the ionic species permeating the film, the inherent solution resistance (R_{sol}) and from the Faradaic component due to the (charging of) protein redox centres.

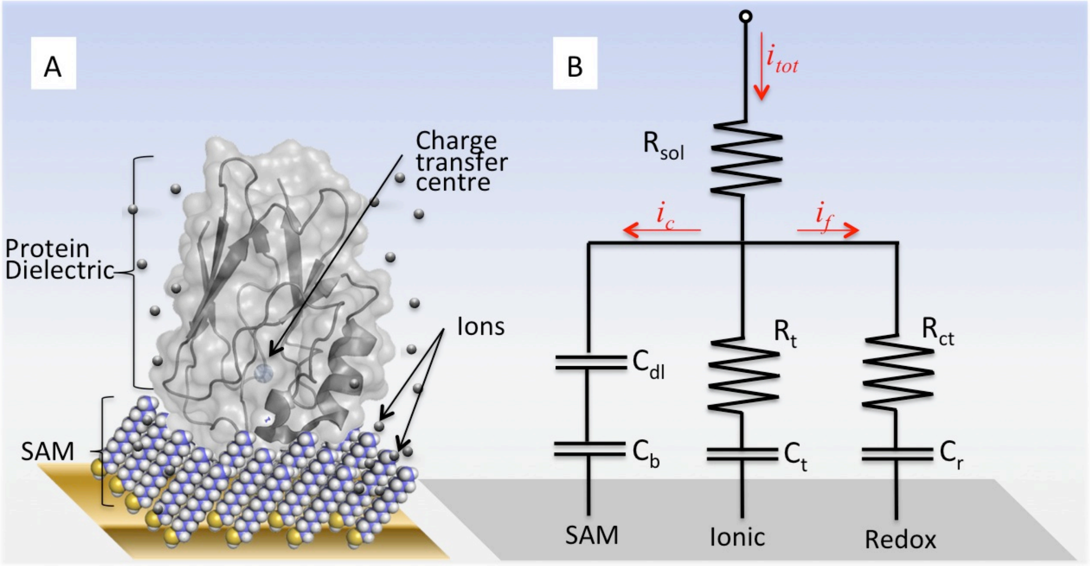

Figure 8.3: A) Schematic representation of Az coupled to an underlying metallic gold electrode through an alkylthiol SAM. Variation of the alkanethiol chain length was used to modulate the electronic coupling and therefore the electron transfer rates. B) Equivalent circuit modelling the capacitances and the resistive components of the electroactive monolayer and solution. Specifically R_{sol} is the solution resistance; the elements positioned in the three parallel branches describe the capacitve component of the double layer of ions in solution C_{dl} and of the electronic relaxation of the dipoles in the SAM C_b in the first branch, the resistance R_t and capacitance C_t due to movement of ionic charges entrapped in the SAM on the central branch and the protein's charge transfer resistance R_{ct} and redox capacitance C_r

8.3.1 Conversion of Impedance into Capacitance

The method presented here is based on acquisition of two frequency scans at constant potential and followed by conversion of the complex impedance curves to complex capacitance.

Before this could be done the solution resistance (R_{sol}) had to be eliminated from the spectrum by means of $Z^{'}(\omega) - R_{sol}$. This is equivalent to the iR drop correction in transient techniques.[136] Even though this process normally requires a determination of R_{sol},[136,314] this was not required here since this contribution was clearly visualized from the beginning of the real part of $Z^{'}$ at high frequency as a separate hemicircle in the Nyquist plot and could be, thereafter, simply subtracted. R_{sol} was found to be constant value of 60-70 Ω over the several measurements acquired, as the geometry of the cell and the buffer ionic strength were kept unvaried.

At the end of this procedure, then, the $C^*(\omega)$ function could be obtained from $Z^*(\omega)$ without unwanted iR drop contributions. The acquired $Z^*(\omega)$ was then converted phasorially into complex capacitance, $C^*(\omega)$, with its real and imaginary components, using the following relationship:

$$C^*(\omega) = \frac{1}{j\omega Z^*(\omega)} \tag{8.1}$$

In Bode plots, the magnitude of C^* or of the real (C') and imaginary (C'') components can be plotted separately as a function of the frequency (usually logarithmic), so that the occurrence of different processes at the interface can be resolved. This is displayed for instance, in section 8.3.2.1 for the C" component of the SAM-modified GDE, poised at a potential of -200 mV.

In the following sections the redox components of the capacitance of the electroactive monolayer of Az physisorbed on alkanethiols of different lengths are presented. These experiments were part of a broader project for the development of capacitance-based studies of redox-active monolayers and the theoretical framework is currently under development in collaboration with Prof Paulo Bueno group at San Paulo University, BR.

In particular in this work the complex capacitance trend is followed as a function of the distance between the protein and the gold and compared with the CV-determined values of electron transfer rate.

8.3.2 Components of the Interfacial Capacitance

The total interfacial capacitance at the electrode/SAM/electrolyte interface is composed, in the first instance, by two series capacitances, that of the insulating monolayer and that of the ionic double-layer in the solution[136], shown in Figure 8.3 as C_{dl} and C_b. The dielectric properties of the SAM are associated with a polarization term composed of resistive and capacitive contributions (in the Debye formulism),[316,317] these however relax too quickly to be observed in the frequency range of the spectroscopic scan.

The R_t and C_t elements in the diagram in Figure 8.3, are the resistive and capacitive components associated with the movement of ionic charges through the pinholes and defects of the SAM monolayer. As the movement of the ions is slowed down by the SAM chains, the generated charge accumulation can be directly and separately resolved in the spectroscopic capacitance measurement, specifically in the steady-state frequency domain regime of complex capacitance (in section 8.3.2.1).

The additional protein layer will behave as dielectric or redox active depending on the potential of interrogation. Once the spectroscopic features of the SAM and of the additional protein layer at a potential where no Faradaic process occurs are known, spectral comparison can be performed with the data examined at the E_0 potential of the Az layer, which therefore include the contribution of the redox process C_r and R_{ct}.

The experimental procedure therefore consisted in acquisition of EIS spectra on the SAM- modified GDEs before and after deposition of the electro-active protein layer. Two frequency scans, from 10^{-2} Hz to 10^{6} Hz, with an amplitude of 10 mV, were acquired at two fixed potentials as mentioned before:

- at a 'non-redox' potential of -200 mV vs. SCE, where all the Az molecules on the surface are reduced,
- at the E_0 of Az of 90 mV vs. SCE, previously determined by a simple CV scan.

The acquisitions were extended to the same four different thiol SAMs used in the previous section 8.2. After conversion of the measured $Z^*(\omega)$ curves to $C^*(\omega)$ it was possible to observe distinct responses between the two stages of the GDEs preparation: the SAM modified gold (GDE/SAM) and the SAM with Az physisorbed (GDE/SAM/Az). The responses of the modified electrodes were recorded at the non redox potential of -200mV and at Az redox potential of 90mV and compared.

8.3.2.1 Complex Capacitance of the Ionic Component

The imaginary capacitance (C") response of a GDE modified with a dodecanethiol SAM and poised at -200 mV vs. SCE is shown in Figure 8.4. The response of the $C_t$and R_t components to the modulating field determines a peak in the imaginary component of the capacitance at a frequency of ~10 kHz corresponding to a relaxation time τ_1. This is due to the second branch component of the circuit pictured in Figure 8.3 (although C_{dl} contributes this contribution is small as this the magnitude of this is large; the relaxation process is thus dominated by R_t , C_t and C_b – these are all dielectric/nonfaradaic contributions).

Investigation at this potential, after addition of the protein monolayer on the surface is represented by the black circles in Figure 8.4. It can be observed that the frequency of the observed signal was not shifted due to physisorption of the protein sub-monolayer on the SAM surface. Only the peak height and area was slightly reduced, consistently with partial blocking of the sites for ion permeation by the proteins molecules.

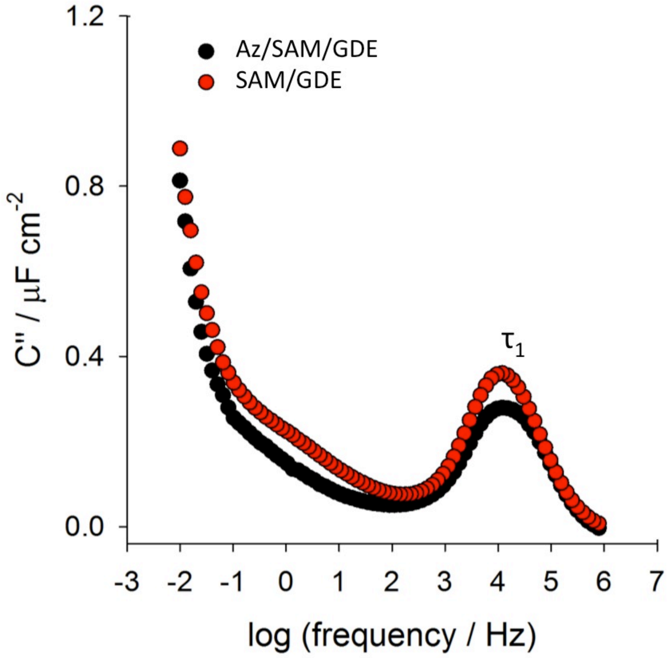

Figure 8.4: The imaginary part of complex capacitance of a non-redox active dodecanethiol SAM reported vs. log(ω) presents a τ_1 peak at 10kHz, due to the the dielectric charging and resistance contributions. Immobilization of the protein layer, investigated at the non redox potential of -200 mV vs. SCE, resulted in a peak at the same frequency but with diminished C". Similar relaxation frequencies were observed for the four different SAMs analyzed with and without the additional protein dielectric. The frequency is reported on a $\log_{10}$ scale for clarity.

The τ_1 occurring at about 10 kHz and the similar trend after immobilization of the protein that are shown in Figure 8.4 for the dodecanethiol, were consistently reproduced at the same frequency for the other three SAMs tested and before and after Az physisorption (at the non-redox potential).

8.3.2.2 Complex Redox Capacitance at Az Reduction Potential

C"(ω) for the four SAM-modified GDEs, with Az physisorbed, was subsequently evaluated at the E_0 potential of the protein, applying the same 10 mV potential modulation and frequency scan. Remarkably, when the GDE/SAM/Az system was poised inside the redox window at 90 mV *vs.* SCE an additional charging process was activated. At the redox potential, the imaginary component C" plotted against the sampling frequency allowed distinction of two partially overlapping peaks, as reported in Figure 8.5. The first peak matched the previously described ionic component $\tau_1$at 10kHz. For all the Az/SAM systems analysed, a second peak, designated as τ_{ct}, appeared at lower frequencies and was attributed to interfacial charging through redox (not only is it absent in the absence of a redox addressable moiety, but its frequency correlates with expectations – see below).

Specifically, the frequency associated to the τ_{ct} component varied depending on the SAM thickness as would be expected for a variation in electronic coupling. For instance, in Figure 8.5A and B two examples of the spectra resolved respectively for the hexanethiol and the dodecanethiol measurements are shown.

As easily observed in Figure 8.5A, the τ_{ct} on hexanethiol occurs at higher frequencies than on dodecanethiol due to the comparatively small spatial separation between the copper centre and the underlying gold. Due to the fast rate of charge exchange the Faradaic signal partially overlaps with the dielectric $\tau_1$component at 10KHz, in Figure 8.5A.

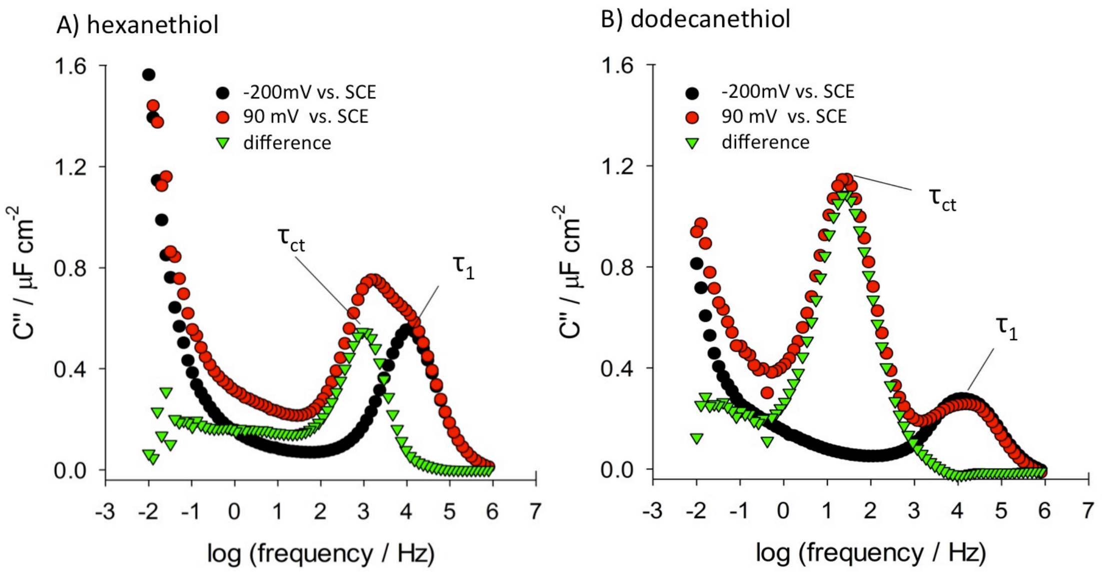

Figure 8.5: The imaginary part of complex capacitance of an Az redox active film. The working electrode was moved into a region of optimum Faradaic activity (90 mV vs. SCE), where the redox process was resolved (red spectrum). Subtraction of the ionic response, previously isolated in Figure 8.4, generates the purely redox response (green spectrum). Data shown for A) Az-on-hexanethiol SAM B) Az-on-dodecanethiol film, where the kinetics are slow compared to the hexanethiol analogue. The frequency is reported on a log$_{10}$ scale for clarity.

Higher separation between the two components τ_1 and τ_{ct} can be observed for the thicker SAM when the electron transfer reaction is slowed down, due to a larger tunnelling distance, as shown with the dodecanethiol sample in Figure 8.5B.

Larger separation between the two components τ_1 and τ_{ct} has been observed when the electron transfer reaction is slowed down, due to a increased tunnelling distance, as shown with the dodecanethiol analogue in Figure 8.5B.

To isolate the Faradaic contribution of the Az layer from the overall detected signal, the constant τ_1 term was subtracted, as reported for instance for the green spectra in Figure 8.5A and B. The Faradaic signal was here resolved at 740Hz and 30Hz respectively for hexanethiol and dodecanethiol SAM.

8.3.3 Redox Kinetics from EMCS at increasing SAM thickness

The spectroscopic subtraction of the dielectric contribution from the C" spectra collected on the different thiol lengths enables comparison of the purely Faradaic components for the SAMs. Figure 8.6 shows the resultant spectra that resolve the timescales as $\sim 30\ s^{-1}$, $\sim 140\ s^{-1}$ and $\sim 740\ s^{-1}$ for τ_{ct} of Az on hexanethiol, decanethiol and dodecanethiol supported films, respectively. Therefore τ_{ct} frequencies will be compared with the k_{ET} from CV on the corresponding SAMs thickness in the next section.

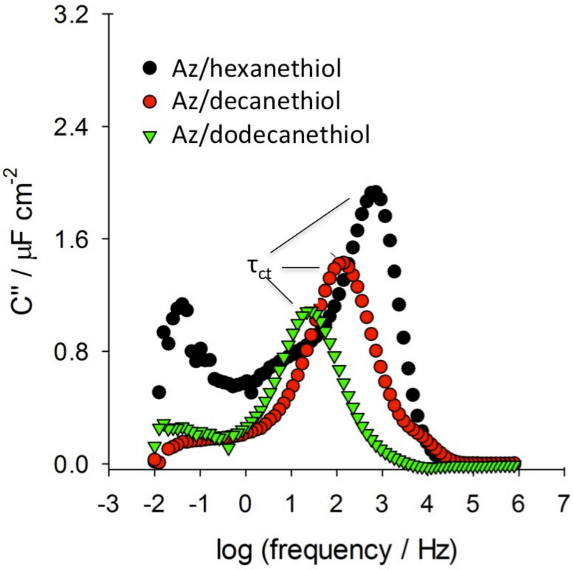

Figure 8.6: Plot of the redox C"(ω) peaks determined for monolayers of Az, obtained after subtraction of the dielectric contribution from the scan outside the redox potential. For the three different SAMs τ_{ct} was determined at frequencies of 30 s^{-1}, 140 s^{-1} and 740 s^{-1} respectively for hexanethiol, decanethiol and dodecanethiol. The frequency is reported on a $\log_{10}$ scale for clarity.

In summary, the redox capacitive analysis of the protein modified interface resolved in frequency dependent manner, both the electronic response of the film dielectric to the modulating applied field and, separately, the interfacial charging through redox. The latter is thought to directly and simply report the electron transfer kinetics.

8.3.3.1 Relationship Between Distance and Electron Transfer Rate

Electrochemical studies of the immobilized redox-active proteins film offer many practical advantages, since the spatial and electronic coupling of the redox sites with the electrode can be tightly controlled through choice of the underlying SAM layer.

Several groups have investigated the k_{ET} between transfer proteins and SAM-coated gold electrodes as a function of the SAM thickness. [18,220,318,319] It was shown that at large distances, a 'non-adiabatic' regime applies with an exponential -(βd) distance dependence for the k_{ET}. At shorter distances instead, the rate becomes independent of SAM thickness, reaching a plateau value.[18,220,318,319] This upper limit in the k_{ET} has been attributed either to an adiabatic limiting regime in which the electron transfer becomes friction controlled[175] or to proteins dynamics, i.e. the need for the proteins to reorient to reach an alignment with respect to the Au–SAM surface favourable for DET.[177,320]

In the non-adiabatic regime the properties of the insulating thiol monolayer contribute to control the tunnelling decay constant β. For linear alkanethiols, a β of 1.0-1.2 per methylene unit has been reported by several authors for both physisorbed cytochrome *c* and Az.[27,98,153,154,220,321,322]

It is clearly visualized in Figure 8.7 that the series of values obtained by EMCS have the same trend as the parallel voltammetric analyses on the same films. For both sets of data the trend of k_{ET} on distance is divided in the two regions formerly described.

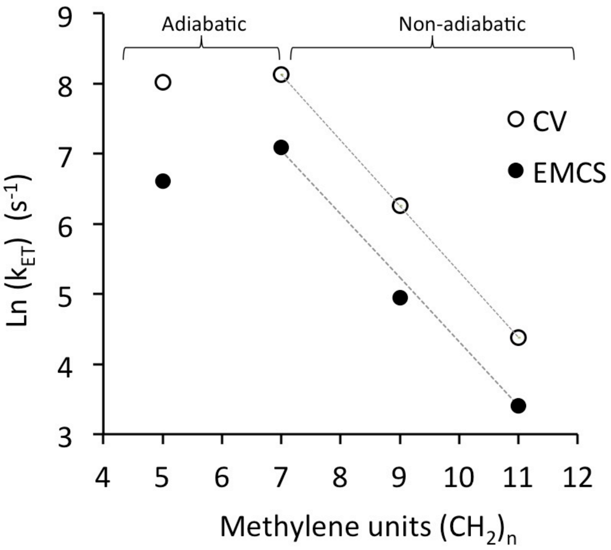

Figure 8.7: The variation in k_{ET} at the four investigated thiols, determined with the EMCS method (black dots) is compared with values obtained with Butler-Volmer fitting of the CV peaks positions (white dots). The gray lines are representative of a decay constant β of 0.93 and 0.91 respectively, in good agreement with previous determinations.[177] Also the typical biphasic kinetic behaviour of Az is respected, as at shorter thiols a maximum plateau value is reached, due to the passage from the non adiabatic tunnelling regime to the adiabatic, intrinsic mechanism.[323]

SAM molecule	**hexanethiol**	**octanethiol**	**decanethiol**	**dodecanethiol**
$\boldsymbol{k_{ET}}$ *determined by CV*	3050 s^{-1}	3390 s^{-1}	520 s^{-1}	80 s^{-1}
$\boldsymbol{\tau_{ct}}$ *determined by EMCS*	740 Hz	1195 Hz	141 Hz	30 Hz

Table 8.1: Electron transfer rates determined by fitting the Trumpet plot at different SAMs and the correspondent peak frequencies observed by EMCS.

An apparent β_{app} value was derived for Az sampled at the three thicker alkanethiol films, resulting in a value of 0.91 per methylene unit for EMCS. The equivalent β_{app} as determined by Butler-Volmer CV method was remarkably close, being equal to 0.93 per methylene unit. The exponential decays determined here, represented by the gray lines in Figure 8.7, were about 0.1-0.2 lower than previous literature reports, probably due to inclusion in the fitting of the octanethiol value, which is at the limit between the non-adiabatic and adiabatic regime.

Interestingly, a systematic difference was observed in the kinetic determinations by EMCS and traditional voltammetric methods for the same films. in fact The latter method yields a k_{ET} about 2.6-4 times larger for all the SAMs considered. The difference may originate from a bias of one of the two techniques towards slower or faster components of the responding redox centres. However it is worth noting that differences in the comparison of k_{ET} determined with different techniques have also been reported.[324]

The method presented here allows comparison the redox and the dipolar relaxation contributions, thus allowing a quick screening test for the identification of the frequency at which electron transfer occurs.

8.4 Conclusions and Future Perspectives

As reported in the introduction to this chapter, the close relationship between distance and k_{ET} is highly relevant for studies of protein films and to FCV. The study of kinetics of surface confined redox centres gives information on the distance of redox centres from the electrode surface[318,325] or the orientation and the tunnelling pathway of electrons through proteins.[154,322] CV is the most common techniques for the k_{ET} determination, however, as for AC voltammetry, it requires numerous acquisition scans and lengthy fitting procedures.

On the contrary the EMCS approach for the determination of the ET rates of Az films proposed here entails the benefit of requiring only two scans:

- One scan at the redox potential (determined by a simple CV)
- One scans at a potential where only the capacitive currents are observed.

Subtraction of the solution resistance first and of the dielectric component later allows determination of the frequencies of the charge transfer free of the iR_{sol} distortion. The analysis of the imaginary components of the complex capacitance, C”(ω), enables to directly localize the redox process on the ω axis.

The novel method may offer a fast and facile tool for probing the distribution of standard rate constants for populations of molecules with same redox potential but distribution of kinetics, by looking at the frequency dispersion of the resulting redox peaks. The kinetic distribution in the response is directly reported in the C” vs. frequency plot, without need for further analysis. Therefore EMCS may be used in the future to discriminate between different sub-populations of molecules within the investigated film, to evaluate the homogeneity in orientation of redox proteins or to determine the distance of redox probes from the surface as in the example reported.

One of the reasons for investigation of k_{ET} by means of frequency-resolved capacitance measurements was the need to investigate systems in which surface confinement is dependent on the redox state of the redox centre. Specifically it is hoped that this method will allow in the future investigation of ‘cavity’ mutant of azurin, Az H117G (Figure 8.8).

This protein can be anchored on the gold surface by “wiring” on conductive pyridine-terminated linker protruding from the SAM,[326] by coordination of the pyridine nitrogen to the T1 copper.[327] The T1 is made accessible through the cavity created by substitution of the histidine 117 ligand with a smaller, non coordinating, glycine residue.[176,328] The coordination by an external ligand results in recovery of the typical blue absorption of the T1 sites[329], thus making the protein a possible candidate for FRET coupling.

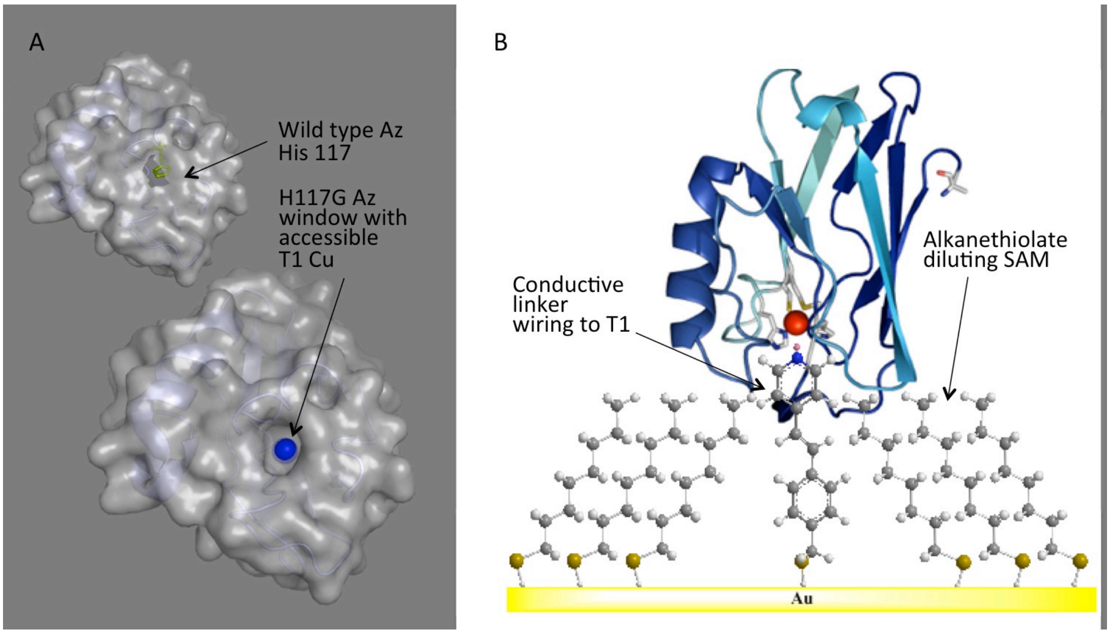

Figure 8.8: A) Top view of wild type and H117G azurin crystal structures, obtained with PyMol. The residue in green sticks in the wild type molecule corresponds to the histidine 117 protruding from the surface. The blue area in the cavity mutant corresponds to the solvent accessible T1 copper ion. B) Schematic representing the cavity mutant of azurin, H117G, immobilized on a mixed self assembled monolayer of octanethiol and conductive linker. The pyridine of the linker coordinates directly to the Cu(II) in the protein copper site.

However spectroscopic and electrochemical characterization have shown that the described coordination is stable only in the oxidized Cu^{2+} state while the external ligand is repelled from the binding site in the reduced Cu^{+} state.[330] Crio-voltammetry and fast scan voltammetric investigation revealed that efficient electron exchange, comparable to that of the native Az, can be obtained when the electrochemical interrogation is fast enough to “entrap” the ligand wire in the cavity of the mutant.[176]

Notably SAMs with a different chemical structure than linear alkanethiols, such as the π-conjugated systems oligo(phenylenevinylene) (OPV) used for the linker and oligo(phenyleneethynylene) (OPE), have lower β values, ranging between 0.2 to 0.7 Å^{-1}.[331,332] As a consequence, on these SAMs electronic coupling can be preserved over longer distances.[331,333-335] An exciting perspective is thus that in the future, immobilization of fluorescent switches on these SAMs may facilitate retention of electronic coupling, while improving the optical detection.

It is hoped that the possibility of the measuring the redox capacitance at high frequencies of modulation using the EMCS method proposed here might be useful in the future for investigation of similar unstable supramolecular complexes at room temperature.

Chapter 9

Conclusions

The aim of this work was to achieve progress toward the study of bio-electrochemical reactions of surface confined redox proteins at a molecular scale level, in order to explore the microheterogenity of the electro-active protein population. Efforts were channelled into three main areas: the consolidation and application of FCV to mapping the reaction of fluorescently labelled Az films on Au-OTE, the extension of FCV analysis to more complex systems, in particular Fld and Lcs, and finally an application of EIS to determine the kinetics of electron transfer of the surface confined Az molecules.

The first two tasks were achieved via the use of fluorescent switching proteins samples suitable for coupling fluorescence detection and electrochemical control. These were selected to have either direct (Fld) or indirect (Fld, Az and Lcs) redox controlled fluorescence emission. Indirect fluorescence modulation was obtained through labelling of the protein molecules with a fluorophore, whose emission was FRET coupled to the redox-dependent variations in the absorption spectra. Singly labelled Az molecules had a switching efficiency upon chemical reduction and oxidation in solution in line with what expected from theory calculations; the same labelling conditions were used for the other two proteins, with yields similar to Az (≥30% dye per protein).

Immobilization of the fluorescent switches for a combination of TIRFM and electrochemistry required the use of a conductive transparent surface. Two types of OTEs were tested, consisting respectively of gold and carbon thin films (~10 nm) on a transparent support and were successfully characterized by UV-Vis. spectrophotometry, AFM and contact angle.

C-OTE films, prepared by pyrolysis of a diluted photoresist, provided promising results in terms of high transparency and flatness. However, due to the inconvenient size of the quartz supports required for TIRFM, the high cost and higher film resistance with respect to gold electrodes, they were found to be impractical for TIRFM use (although better results may be possible in epifluorescence, using objectives with longer working distances).

The Au-OTE surface was reproducibly modified with alkanethiol SAMs of increasing thicknesses and successively with labelled-Az films. The homogeneous electron transfer of the physisorbed protein molecules on the OTEs could be observed by cyclic voltammetry using a cell geometry that allowed simultaneous optical and electrochemical investigation.

Potential controlled fluorescent emission of copper Az-Atto655 was repeatedly observed on SAM-modified Au-OTE. A procedure that enables careful alignment of the image frames to the corresponding applied potentials was employed. This allowed investigation of the optical signal from selected regions of interest, whose dimensions could be as small as the diffraction-limited spot. The number of fluorescent switches per ROI was in the range of few hundred molecules, with our results demonstrating an increase in sensitivity of several (~10) orders of magnitude with respect to the amount of molecules typically responding in CV.

For each of these localized intensity:time traces, by fitting with a Boltzmann sigmoid, it was possible to determinate an optical $FCVE_0$, thus allowing mapping of the distribution of redox potentials across the surface.

It was demonstrated that for Az, the optically determined $FCVE_0$ values were normally distributed around a mean value, this was close to redox potential determined by conventional CV. The correlation between the two was further verified by varying the pH of the electrolyte solution, which is reflected in a shift of the electrochemical potential of the proteins.

A second factor affecting the FCV output was isolated through variation of the distance between the protein and the electrode surface by means of SAMs of increasing thickness. In this case the width of $FCVE_0$ distribution, rather than the potential value, was found to differ. A lower spread in the thermodynamic potentials measured across the surface was in fact detected at dodecanethiol SAM with respect to octanethiol, suggesting a more homogenous protein response, possibly in correlation with improved SAM quality or with limitation of other affecting factors. Further investigations on the effects of increasing gold-Az distances were undertaken on zinc Az films. In this case the film was not electroactive, thus the fluorescence emission is not FRET-coupled and was locked in an 'ON' state. A smaller FCV response linear with the applied potential was recorded that was attributed to motion of the protein induced by the variation of the interfacial electric field. This hypothesis is supported by reduction of the fluorescence fluctuation observed at higher ionic strength and on thicker insulating alkanethiol monolayers, as a consequence of increased shielding of the proteins superficial charges from the effects of the interfacial electric field.

Application of the FCV method to more complex systems was attempted with the multicopper oxidase Lcs covalently immobilized on a mercaptoundecanoic acid monolayer, and with the FMN-containing Fld, electrostatically physisorbed on a similar SAM. Both systems revealed fluorescence fluctuations, observed on areas estimated to contain few hundred molecules.

The presence of active Lcs molecules on the gold was suggested by both substrate turnover and by the presence of small Faradaic peaks in the voltammograms. However, the fluorescent traces seemed to reproduce what already reported for zinc Az, supporting the electrochemical data that suggest poor electronic coupling between the redox centres and the gold. The potential modulation observed might be caused by movement of the labelled molecules on the gold electrode triggered by the electrostatic effects of the interfacial electric field.

Redox coupled fluorescence switching of Fld was instead observed both upon excitation of the intrinsic fluorescence at 450 nm and upon excitation of the FRET coupled Atto655 label at 633 nm. In this case too, Fld electrochemistry represents a further level of complication with respect to Az, due to the ability of transferring either one or two electrons per molecule and to the known interference of free FMN molecules in the current signal. Free FMN also emits at the same wavelengths and with higher emission rates of the protein-bound FMN, and therefore can affect the FCV signal observed. However at λ_{exc} of 450 nm, the switching potential determined by FCV is closer to the one of the holo-Fld protein rather than the free FMN.

In order to clarify these results, FCV experiments on the labelled Fld molecules were undertaken. FRET dependent switching of the labelled Fld unequivocally confirmed an electrochemically triggered redox reaction between the hydroquinone and semiquinone state of the protein, with an FCVE_0 of -650 mV vs. Ag/AgCl, in good agreement with SWV data and previous report for the E_1 potential of Fld.

The origin of the change in emission upon excitation at 450 nm remains uncertain. The hypothesis of Fld molecules in different oxidation states cannot be completely discarded, as reported by Heering for CV of Fld on glassy carbon surfaces.[283] However, in our case, more detailed studies would be required to identify the species involved in the electrochemical reaction. In particular, in the future, combination of lifetime imaging to FCV traces might help to clarify the sources of the fluorescence variation at shorter wavelengths. However measurements at both wavelengths confirmed the enhanced sensitivity of FCV with respect to normal CV, where Fld Faradaic current peaks could not be distinguished from the background. As for the development of FCV, our study probed the possibility of achieving redox switching at multiple wavelengths on suitable molecules.

Finally, in chapter 8 an application of EIS for the study of the kinetics of electron tunnelling through SAM films to the gold electrode is reported. The test used Az and polycrystalline GDEs covered with SAMs to modulate the electronic coupling. A close relationship was observed between the frequency of the peaks in the Bode plot of the (background corrected) imaginary component of the capacitance and the analysis of the k_{et} obtained by CV. The procedure is therefore proposed as a fast method to evaluate the distribution of electron transfer rates of the surface confined Az population.

9.1 Future Perspectives

Clearly, the number of (bio)electrochemical studies that might benefit from FCV application is enormous when considering the large variety of redox proteins present in nature that may be surface confined for electrochemical studies and the colourful variety of contained redox cofactors, which could be coupled to a variety of appended dyes. The development of more refined bio-conjugation and separation techniques for carefully identifying the position of dyes on the proteins surface at desired distances from redox centre(s) might soon allow study of multicentre enzymes or the effects of multiple labels on the same protein scaffold. Exciting developments will also derive from the rapidly increasing sophistication in the design of surface chemistries, offering enhanced control on the labelled proteins orientation and on their separation from the quenching surface.

In the FCV development project described in this thesis, one of the most problematic aspects was the small amount of photons able to reach the EM-CCD detector due the quenching effect of the gold substrate and the limited transparency of the Au-OTEs. In the experiments presented, the quenching effect was limited by introducing a separating layer between the dye and the gold.

Additional improvement might be obtained by optimizing the contribution to fluorescence mediated by excitation of the surface plasmon of the metallic films. Preliminary studies investigating the effects of varying the thickness and composition of the metallic layer were undertaken in order to evaluate if surface plasmon enhancement (SPE) of the fluorescence could be reached with the available lens system. The angle of SPE occurrence depends on a number of factors including the metal complex refractive index and of the intervening medium, the thickness of the metallic film, the wavelength of illumination and the position of the fluorophore on the surface.[118,135,336] On the basis of simulations based on the CPS theory[118,119], angles of ~ 65-75° from the normal were expected for 40-50 nm thick gold and silver electrodes, thus possibly within reach with the available TIRF objective, which has a N.A. limit of 72.8°.

As shown in Figure 9.1, preliminary results were highly encouraging. In particular two types of electrodes were compared with the previously used 10 nm thick Au-OTE: 50 nm thick silver films and bilayered electrodes with 40 nm thick silver topped by 10 nm gold. These were modified with an octanethiol SAM and a zinc Atto655 layer and images were acquired while moving the laser from 90°(‘epi’) towards θ_{NA} at the glass side of the electrode, as in the insert schematic in Figure 9.1A.

As clearly shown in the Figure 9.1, the experiment confirmed the possibility of reaching the angle for SP excitation on the two surfaces upon illumination at 633 nm with the available 1.45 N.A. objective. The highest increase in fluorescence detection was obtained at silver surfaces, with a epi/SPEF intensity ratio of ~50 and image intensities approaching the epifluorescence values reported on glass for analysis of nanoparticles (data not shown).

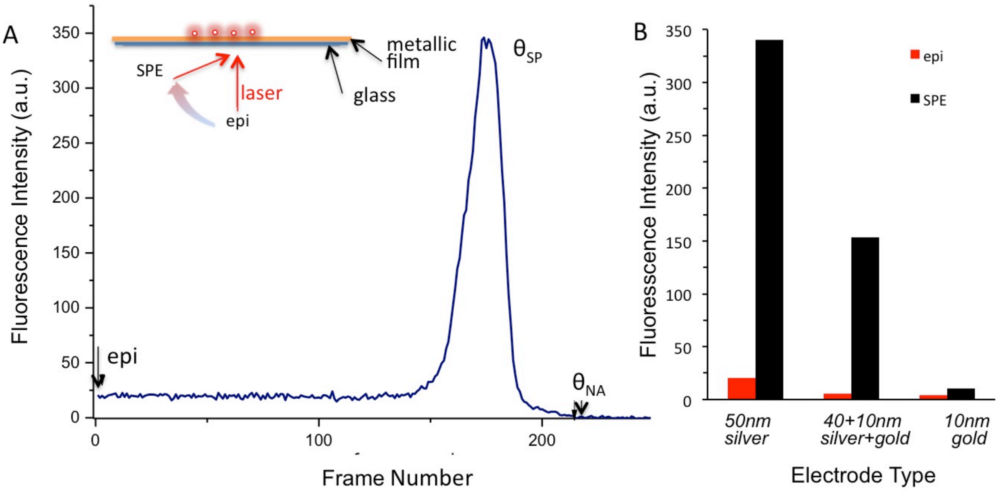

Figure 9.1: A) Fluorescence spectrum collected at the EM-CCD camera as a function of the angle of incidence of the excitation beam (λexc=633 nm) for a sample of Zinc Az labelled with Atto655 and deposited on a SAM modified (octanethiol) 50 nm Ag film; 'epi' indicates positioning of the laser normal to the surface (see insert) and SPE the surface enhancement peak. For comparison purposes the fluorescence emission was normalized to 1ms. B) Comparison of the fluorescence intensity obtained in epi and SPE position for the three electrodes analysed: 50 nm silver electrodes, bilayered and 10 nm thick gold electrodes.

Taking into account the FCV samples of few hundred molecules observed for labelled Az and Fld it is easy to note that a further 50 times increase in sensitivity might result in observation of less than 10 molecules, therefore experiments to evaluate the response of these electrodes in FCV were undertaken. Unfortunately, when the Ag surface was modified with SAMs and with the copper Atto655-Az for FCV investigation, application of the CV potential sweeps resulted in corrosion (associated to luminescence emission) of the film. Brightly emitting areas, coupled to increasing broad Faradaic peaks centred at 50-100 mV vs. SCE, were observed to propagate irreversibly over the imaged area after each CV scan (Figure 9.2). Alignment of the optical and electrochemical data unequivocally associated the nucleation and growth of these spectacular luminescent features on the Ag film with the anodic scan of the CV.

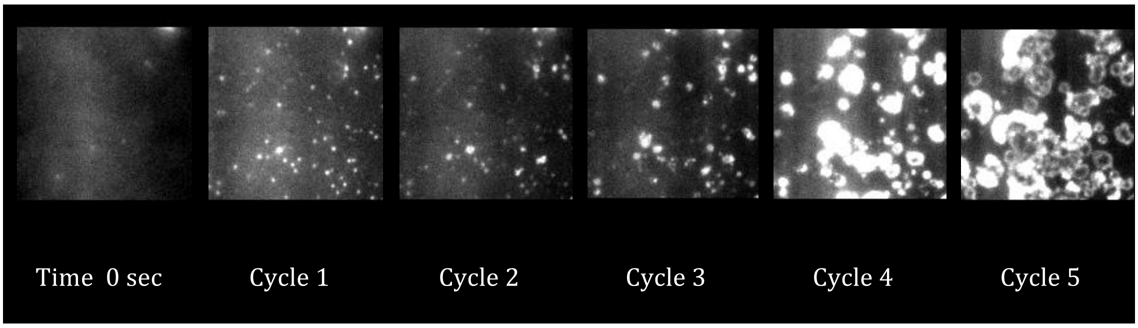

Figure 9.2: EM-CCD camera images showing examples of luminescent emission from a 50 nm silver electrode covered with octanethiol SAMs and Atto655-Az and tested for FCV response in the potential window -0.3 to 0.25V vs. SCE (a DriRef electrode was used to prevent chloride ions to diffuse in the electrolyte solution). At each CV cycle the areas of luminescent emission on the electrode surface were expanding suggesting irreversible corrosion of the electrode surface. The luminescent emission is thought to originate from formation of silver nanostructures occurring during the oxidation process.

Application of a protective layer of gold (10 nm) on the 40 nm silver resulted in a stable film retaining the favourable optical characteristics of the pure silver. However, even in this case the reversible FRET-coupled process was not observed, possibly due to the sensitivity of Az to free Ag^+ ions, which can displace the copper from the T1 coordination site.[337,338]

However in the future SPE on these silver and silver/gold electrodes might be used for FCV investigation of proteins switching at lower potentials, such as Fld molecules, where oxidation of the silver should not interfere with the protein electron transfer.

A further increase in the efficiency of detection would allow a reduction in the optical sampling time, thus opening the possibility of extending the optical detection to other powerful electrochemical techniques, such as chronoamperometry and electrochemical impedance spectroscopy.

Bibliography

(1) Hammerich, O.; Ulstrup, J. *Bioinorganic electrochemistry*; Springer Verlag, 2008.

(2) Bertini, I. In *Handbook on metalloproteins*; 1st ed.; Bertini, I., Siegel, A., Eds.; CRC Press: 2001, p 1118.

(3) Andreini, C.; Bertini, I.; Cavallaro, G.; Holliday, G. L.; Thornton, J. M. *Journal of Biological Inorganic Chemistry* **2008**, *13*, 1205.

(4) Andreini, C.; Bertini, I.; Rosato, A. *Accounts of Chemical Research* **2009**, *42*, 1471.

(5) Cvetkovic, A.; Menon, A. L.; Thorgersen, M. P.; Scott, J. W.; Poole Ii, F. L.; Jenney Jr, F. E.; Lancaster, W. A.; Praissman, J. L.; Shanmukh, S.; Vaccaro, B. J.; Trauger, S. a.; Kalisiak, E.; Apon, J. V.; Siuzdak, G.; Yannone, S. M.; Tainer, J. a.; Adams, M. W. W. *Nature* **2010**, *466*, 779.

(6) Butterfield, S. M.; Goodman, C. M.; Rotello, V. M.; Waters, M. L. *Angewandte Chemie International Edition* **2004**, *43*, 724.

(7) Gilardi, G.; Fantuzzi; Sadeghi, S. J.; Fantuzzi, a. *Current Opinion in Structural Biology* **2001**, *11*, 491.

(8) Discher, B. *Current Opinion in Chemical Biology* **2003**, *7*, 741.

(9) Canters, G. W.; Gilardi, G. *FEBS Lett* **1993**, *325*, 39.

(10) Li, T. T. T.; Weaver, M. J. *Journal of the American Chemical Society* **1984**, *106*, 6107.

(11) Tarlov, M. J.; Bowden, E. F. *Journal of the American Chemical Society* **1991**, *113*, 1847.

(12) Song, S.; Clark, R. A.; Bowden, E. F.; Tarlov, M. J. *The Journal of Physical Chemistry* **1993**, *97*, 6564.

(13) Armstrong, F. A.; Butt, J. N.; Sucheta, A. *Methods in Enzymology* **1993**, *227*, 479.

(14) Armstrong, F. *Russian Journal of Electrochemistry* **2002**, *38*, 49.

(15) Armstrong, F. a.; Heering, H. a.; Hirst, J. *Chemical Society Reviews* **1997**, *26*, 169.

(16) Léger, C.; Lederer, F.; Guigliarelli, B.; Bertrand, P. *Journal of the American Chemical Society* **2006**, *128*, 180.

(17) Wijma; Lars J. C. Jeuken; Martin Ph. Verbeet; Fraser A. Armstrong; Canters, G. W. *Journal of the American Chemical Society* **2007**, *129*, 8557.

(18) Fujita, K.; Nakamura, N.; Ohno, H.; Leigh, B. S.; Niki, K.; Gray, H. B.; Richards, J. H. *Journal of the American Chemical Society* **2004**, *126*, 13954.

(19) Armstrong, F. A.; Camba, R.; Heering, H. A.; Hirst, J.; Jeuken, L. J.; Jones, A. K.; Léger, C.; McEvoy, J. P. *Faraday Discussions* **2000**, 191.

(20) Fleming, B. D.; Praporski, S.; Bond, A. M.; Martin, L. L. *Langmuir* **2007**, *24*, 323.

(21) Hoogvliet, J. *Electrochimica Acta* **2001**, *47*, 599.

(22) Sondag-Huethorst, J. A. M.; Fokkink, L. G. J. *Langmuir* **1992**, *8*, 2560.

(23) Sirohi, R. S.; Genshaw, M. A. *Journal of The Electrochemical Society* **1969**, *116*, 910.

(24) Shan, X.; Patel, U.; Wang, S.; Iglesias, R.; Tao, N. *Science* **2010**, *327*, 1363.

(25) Wang, S.; Huang, X.; Shan, X.; Foley, K. J.; Tao, N. *Analytical Chemistry* **2010**, *82*, 935.

(26) Hildebrandt, P. *Journal of Molecular Structure* **1991**, *242*, 379.

(27) Murgida, D. H.; Hildebrandt, P. *Journal of the American Chemical Society* **2001**, *123*, 4062.

(28) Murgida, D. H.; Hildebrandt, P. *Physical Chemistry Chemical Physics* **2005**, *7*, 3773.

(29) Murgida, D. H.; Hildebrandt, P. *Journal of Molecular Structure* **2001**, *565-566*, 97.

(30) Murgida, D. H.; Hildebrandt, P.; Daniel, H. M. *Accounts of Chemical Research* **2004**, *37*, 854.

(31) Schmauder, R.; Alagaratnam, S.; Chan, C.; Schmidt, T.; Canters, G. W.; Aartsma, T. J. *Journal of Biological Inorganic Chemistry* **2005**, *10*, 683.

(32) Schmauder, R. R.; Librizzi, F.; Fabio; Canters, G. W.; T; Schmidt; Schmidt, T.; Aartsma, T. J. *ChemPhysChem* **2005**, *6*, 1381.

(33) Kuznetsova, S.; Zauner, G.; Schmauder, R.; Mayboroda, O. A.; Deelder, A. M.; Aartsma, T. J.; Canters, G. W. *Analytical Biochemistry* **2006**, *350*, 52.

(34) Clark, R. A.; Bowden, E. F. *Langmuir* **1997**, *13*, 559.

(35) Zhang, Z. *Biophysical chemistry* **1997**, *63*, 133.

(36) Hirst, J.; Armstrong, F. A. *Analytical Chemistry* **1998**, *70*, 5062.

(37) Jeuken, L. J. C.; Armstrong, F. A. *The Journal of Physical Chemistry B* **2001**, *105*, 5271.

(38) Leger, C.; Jones, A. K.; Albracht, S. P. J.; Armstrong, F. A. *The Journal of Physical Chemistry B* **2002**, *106*, 13058.

(39) Lee, C.-Y.; Tan, Y.-J.; Bond, A. M. *Analytical Chemistry* **2008**, *80*, 3873.

(40) Leopold, M. C.; Bowden, E. F. *Langmuir* **2002**, *18*, 2239.

(41) Heering, H. A.; Wiertz, F. G. M.; Dekker, C.; de Vries, S. *Journal of the American Chemical Society* **2004**, *126*, 11103.

(42) Hoeben, F. J. M.; Meijer, F. S.; Dekker, C.; Albracht, S. P. J.; Heering, H. A.; Lemay, S. G. *ACS Nano* **2008**, *2*, 2497.

(43) Zhang, J.; Grubb, M.; Hansen, A. G.; Kuznetsov, A. M.; Boisen, A.; Wackerbarth, H.; Ulstrup, J. *Journal of Physics: Condensed Matter* **2003**, *15*, S1873.

(44) Gell, C.; Brockwell, D.; Smith, A. *Handbook of single molecule fluorescence spectroscopy*; Oxford University Press: Oxford ; New York, 2006.

(45) Nie, S.; Zare, R. N. *Annual Review of Biophysics and Biomolecular Structure* **1997**, *26*, 567.

(46) Xie, X. S.; Trautman, J. K. *Annual Review of Physical Chemistry* **1998**, *49*, 441.

(47) Funatsu, T.; Harada, Y.; Tokunaga, M.; Saito, K.; Yanagida, T. *Nature* **1995**, *374*, 555.

(48) Singh-Zocchi, M. *Proceedings of the National Academy of Sciences of the United States of America* **2003**, *100*, 7605.

(49) Lu, H. P. *Science* **1998**, *282*, 1877.

(50) Schneckenburger, H. *Current Opinion in Biotechnology* **2005**, *16*, 13.

(51) Schapper, F.; Gonçalves, J. T.; Oheim, M. *European Biophysics Journal* **2003**, *32*, 635.

(52) Chon, J. W. M.; Gu, M. *Applied Optics* **2004**, *43*, 1063.

(53) Schneckenburger, H.; Stock, K.; Lyttek, M.; Strauss, W. S. L.; Sailer, R. *Photochemical & Photobiological Sciences* **2004**, *3*, 127.

(54) Lakowicz, J. R. *Principles of fluorescence spectroscopy*; 3rd ed.; Springer New York ; London, 2006.

(55) Hawkridge, F. M.; Kuwana, T. *Analytical Chemistry* **1973**, *45*, 1021.

(56) Nöll, G.; Kozma, E.; Grandori, R.; Carey, J.; Schodl, T.; Hauska, G.; Daub, J. *Langmuir* **2006**, *22*, 2378.

(57) St. Clair, C. S.; Ellis, W. R.; Gray, H. B. *Inorganica Chimica Acta* **1992**, *191*, 149.

(58) Comtat, M.; Durliat, H. *Biosensors and Bioelectronics* **1994**, *9*, 663.

(59) Ash, P. A.; Vincent, K. A. *Chemical Communications* **2012**, *48*, 1400.

(60) Postlethwaite, T. A.; Hutchison, J. E.; Hathcock, K. W.; Murray, R. W. *Langmuir* **1995**, *11*, 4109.

(61) Renault, C.; Harris, K. D.; Brett, M. J.; Balland, V. r.; Limoges, B. Æ. *Chemical communications (Cambridge, England)* **2011**, *47*, 1863.

(62) Rusling, J. F. *Accounts of Chemical Research* **1998**, *31*, 363.

(63) Shi, G.; Sun, Z.; Liu, M.; Zhang, L.; Liu, Y.; Qu, Y.; Jin, L. *Analytical Chemistry* **2007**, *79*, 3581.

(64) Dunphy, D. R.; Mendes, S. B.; Saavedra, S. S.; Armstrong, N. R. *Analytical Chemistry* **1997**, *69*, 3086.

(65) Ashur, I.; Schulz, O.; McIntosh, C. L.; Pinkas, I.; Ros, R.; Jones, A. K. *Langmuir* **2012**, 120322083116009.

(66) Shepherd, J. L.; Bizzotto, D. *Langmuir* **2006**, *22*, 4869.

(67) Shepherd, J. L.; Kell, A.; Chung, E.; Sinclar, C. W.; Workentin, M. S.; Bizzotto, D. *Journal of the American Chemical Society* **2004**, *126*, 8329.

(68) Shepherd, J. L.; Bizzotto, D. *The Journal of Physical Chemistry B* **2003**, *107*, 8524.

(69) Bizzotto, D.; Pettinger, B. *Langmuir* **1999**, *15*, 8309.

(70) Musgrove, A.; Kell, A.; Bizzotto, D. *Langmuir* **2008**, *24*, 7881.

(71) Stoodley, R.; Bizzotto, D. *The Analyst* **2003**, *128*, 552.

(72) Kaiser, W.; Rant, U. *Journal of the American Chemical Society* **2010**, *132*, 7935.

(73) Rant, U. *Proc. Natl Acad. Sci. USA* **2007**, *104*, 17364.

(74) Rant, U.; Arinaga, K.; Fujita, S.; Yokoyama, N.; Abstreiter, G.; Tornow, M. *Langmuir* **2004**, *20*, 10086.

(75) Rant, U. *Nano Letters* **2004**, *4*, 2441.

(76) Murphy, J. N.; Cheng, A. K. H.; Yu, H.-Z.; Bizzotto, D. *Journal of the American Chemical Society* **2009**, *131*, 4042.

(77) Miomandre, F.; Meallet-Renault, R.; Vachon, J.-J.; Pansu, R. B.; Audebert, P. *Chemical Communications* **2008**, 1913.

(78) Miomandre, F.; Allain, C.; Clavier, G.; Audibert, J.-F.; Pansu, R. B.; Audebert, P.; Hartl, F. *Electrochemistry Communications* **2011**, *13*, 574.

(79) Chidsey, C. E. D.; Loiacono, D. N.; H, M. *Langmuir* **1990**, *6*, 682.

(80) Bain, C. D.; Evall, J.; Whitesides, G. M. *Journal of the American Chemical Society* **1989**, *111*, 7155.

(81) Finklea, H. O. *Electroanalytical Chemistry* **1996**, *19*, 110.

(82) Schwartz, D. K. *Annual Review of Physical Chemistry* **2001**, *52*, 107.

(83) Love, J. C.; Estroff, L. A.; Kriebel, J. K.; Nuzzo, R. G.; Whitesides, G. M. *Chemical Reviews* **2005**, *105*, 1103.

(84) Ulman, A. *Chemical Reviews* **1996**, *96*, 1533.

(85) Godin, M.; Williams, P. J.; Tabard-Cossa, V.; Laroche, O.; Beaulieu, L. Y.; Lennox, R. B.; Grütter, P. *Langmuir* **2004**, *20*, 7090.

(86) Laibinis, P. E.; Fox, M. A.; Folkers, J. P.; Whitesides, G. M. *Langmuir* **1991**, *7*, 3167.

(87) Evans, E.; Ritchie, K. *Biophysical Journal* **1997**, *72*, 1541.

(88) Tam-Chang, S.-W.; Biebuyck, H. A.; Whitesides, G. M.; Jeon, N.; Nuzzo, R. G. *Langmuir* **1995**, *11*, 4371.

(89) Biebuyck, H. a.; Bain, C. D.; Whitesides, G. M. *Langmuir* **1994**, *10*, 1825.

(90) Weiss, P. S.; Bumm, L. A.; Dunbar, T. D.; Burgin, T. P.; Tour, J. M.; Allara, D. L.; La, B. *Annals of the New York Academy of Sciences* **1998**, *852*, 145.

(91) Hu, Z. G.; Prunici, P.; Patzner, P.; Hess, P. *The Journal of Physical Chemistry B* **2006**, *110*, 14824.

(92) Folkers, J. P.; Laibinis, P. E.; Whitesides, G. M. *Langmuir* **1992**, *8*, 1330.

(93) Porter, M. D.; Bright, T. B.; Allara, D. L.; Chidsey, C. E. D. *Journal of the American Chemical Society* **1987**, *109*, 3559.

(94) Desikan, R.; Armel, S.; Meyer III, H. M.; Thundat, T. *Nanotechnology* **2007**, *18*, 424028.

(95) Berger, R. *Science* **1997**, *276*, 2021.

(96) Berger, R.; Delamarche, E.; Lang, H. P.; Gerber, C.; Gimzewski, J. K.; Meyer, E. *Applied Physics A: Materials Science & Processing* **1998**, *66*, S55.

(97) Guo, Y.; Zhao, J.; Yin, X.; Gao, X.; Tian, Y. *The Journal of Physical Chemistry C* **2008**, *112*, 6013.

(98) Chi, Q.; Farver, O.; Ulstrup, J. *Proceedings of the National Academy of Sciences of the United States of America* **2005**, *102*, 16203.

(99) Davis, J. J.; Burgess, H.; Zauner, G.; Kuznetsova, S.; Salverda, J.; Aartsma, T.; Canters, G. W. *The Journal of Physical Chemistry B* **2006**, *110*, 20649.

(100) Salverda, J.; Patil, A.; Mizzon, G.; Kuznetsova, S.; Zauner, G.; Akkilic, N.; Canters, G.; Davis, J.; Heering, H.; Aartsma, T. *Angewandte Chemie International Edition* **2010**, *49*, 5776.

(101) Lakowicz, J. R. *Photochemistry and Photobiology* **2000**, *72*, 421.

(102) Pan, C.-P.; Muinaeo, P. L.; Barkley, M. D.; Callis, P. R. *The Journal of Physical Chemistry B* **2011**, *115*, 3245.

(103) Vivian, J. T.; Callis, P. R. *Biophysical Journal* **2001**, *80*, 2093.

(104) Rudolf, R.; Mongillo, M.; Rizzuto, R.; Pozzan, T. *Nature Reviews of Molecular Cell Biology* **2003**, *4*, 579

(105) Tsien, R. Y. *Annual Review of Neuroscience* **1989**, *12*, 227.

(106) Kim, Y.; Ho, S. O.; Gassman, N. R.; Korlann, Y.; Landorf, E. V.; Collart, F. R.; Weiss, S. *Bioconjugate chemistry* **2008**, *19*, 786.

(107) Berlier, J. E.; Rothe, A.; Buller, G.; Bradford, J.; Gray, D. R.; Filanoski, B. J.; Telford, W. G.; Yue, S.; Liu, J.; Cheung, C.-Y.; Chang, W.; Hirsch, J. D.; Beechem, J. M.; Haugland, R. P.; Haugland, R. P. *Journal of Histochemistry and Cytochemistry* **2003**, *51*, 1699.

(108) Hermanson, G. T. *Bioconjugate techniques*; Academic Press: San Diego ; London, 1996.

(109) Förster, T. H. *Annuals of Physics (Leipzig)* **1948**, *437*, 55.

(110) Stryer, L. *Annual Review of Biochemistry* **1978**, *47*, 819.

(111) Rischel, C.; J rgensen, L. Elkj r.; F ldes-Papp, Z. *Journal of Physics: Condensed Matter* **2003**, *15*, S1725.

(112) Taylor, R. M.; Lin, B.; Foubert, T. R.; Burritt, J. B.; Sunner, J.; Jesaitis, A. J. *Analytical Biochemistry* **2002**, *302*, 19.

(113) Barker, S. L. R.; Kopelman, R.; Meyer, T. E.; Cusanovich, M. A. *Analytical Chemistry* **1998**, *70*, 971.

(114) Mertz, J. *Journal of the Optical Society of America B* **2000**, *17*, 1906.

(115) Barnes, W. *Journal of Modern Optics* **1998**, *45*.

(116) Hellen, E. H.; Axelrod, D. *Journal of the Optical Society of America B* **1987**, *4*, 337.

(117) Lakowicz, J. R. *Analytical Biochemistry* **2001**, *298*, 1.

(118) Fort, E.; Grasillon, S. *Journal of Physics D: Applied Physics* **2008**, *41*.

(119) Chance, R. R.; Prock, A.; Silbey, R. *Advances in Chemical Physics* **1978**, *37*, 1.

(120) Persson, B.; Lang, N. *Physical Reviews B* **1982**, *26*, 5409.

(121) Yun, C. S.; Javier, A.; Jennings, T.; Fisher, M.; Hira, S.; Peterson, S.; Hopkins, B.; Reich, N. O.; Strouse, G. F. *Journal of the American Chemical Society* **2005**, *127*, 3115.

(122) Rant, U.; Arinaga, K.; Scherer, S.; Pringsheim, E.; Fujita, S.; Yokoyama, N.; Tornow, M.; Abstreiter, G. *Proceedings of the National Academy of Sciences of the United States of America* **2007**, *104*, 17364.

(123) Rant, U.; Arinaga, K.; Fujita, S.; Yokoyama, N.; Abstreiter, G.; Tornow, M. *Nano Letters* **2004**, *4*, 2441.

(124) Demuro, A.; Parker, I. *Biophysical Journal* **2004**, *86*, 3250.

(125) Buijs, J.; Hlady, V. *Journal of Colloid and Interface Science* **1997**, *190*, 171.

(126) Hoover, D. K.; Lee, E.-J.; Yousaf, M. N. *Langmuir* **2009**, *25*, 2563.

(127) Axelrod, D. *Traffic* **2001**, *2*, 764.

(128) Axelrod, D.; Thompson, N. L.; Burghardt, T. P. *Journal of Microscopy* **1983**, *129*, 19.

(129) Mashanov, G. *Methods* **2003**, *29*, 142.

(130) Fort, E.; Gresillon, S. *Journal of Physics D: Applied Physics* **2008**, *41*.

(131) Aslan, K.; Gryczynski, I.; Malicka, J.; Matveeva, E.; Lakowicz, J. R.; Geddes, C. D. *Current Opinion in Biotechnology* **2005**, *16*, 55.

(132) Knoll, W. *Annual Review of Physical Chemistry* **1998**, *49*, 569.

(133) Liebermann, T.; Knoll, W. *Colloids and Surfaces A: Physicochemical and Engineering Aspects* **2000**, *171*, 115.

(134) Houssen, Y. G.; Balaa, K.; Studer, V.; Lévêque-Fort, S.; Fort, E. *Optical Society of America* **2009**.

(135) Balaa, K.; Fort, E. *Imaging & Microscopy* **2009**, *11*, 55.

(136) Bard, A. J.; Faulkner, L. R. *Electrochemical Methods Fundamentals and applications*; 2 ed.; John Wiley & Sons, 2000; Vol. 677.

(137) Armstrong, F. A. *Journal of Chemical Society, Dalton Transactions* **2002**, 661.

(138) Vincent, K. A.; Armstrong, F. A. *Inorganic Chemistry* **2005**, *44*, 798.

(139) Gray, H. B.; Winkler, J. R. *Quarterly Reviews of Biophysics* **2003**, *36*, 341.

(140) Winkler, J. R.; Angel J. Di Bilio; Neil A. Farrow; Richards, J. H.; Gray, H. B. *Pure and Applied Chemistry* **1999**, *71*, 1753.

(141) Marcus, R. A.; Sutin, N. **1985**, *811*, 265.

(142) Gray, H. B.; Winkler, J. R. *Annual Review of Biochemistry* **1996**, *65*, 537.

(143) Marcus, R. A.; Sutin, N. *Biochimica et Biophysica Acta (BBA) - Reviews on Bioenergetics* **1985**, *811*, 265.

(144) Donner, S.; Li, H. W.; Yeung, E. S.; Porter, M. D. *Analytical Chemistry* **2006**, *78*, 2816.

(145) Van de Kamp, M.; Hali, F. C.; Rosato, N.; Agro, A. F.; Canters, G. W. *Biochimica et Biophysica Acta* **1990**, *1019*, 283.

(146) Riener, C.; Kada, G.; Gruber, H. *Analytical and Bioanalytical Chemistry* **2002**, *373*, 266.

(147) Tkac, J. D., Jason J *Journal of Electroanalytical Chemistry* **2008**, *621*, 117.

(148) Hoogvliet, J. C.; Dijksma, M.; Kamp, B.; van Bennekom, W. P. *Analytical Chemistry* **2000**, *72*, 2016.

(149) Gruber, H. J.; Hahn, C. D.; Kada, G.; Riener, C. K.; Harms, G. S.; Ahrer, W.; Dax, T. G.; Knaus, H.-G. *Bioconjugate chemistry* **2000**, *11*, 696.

(150) Dennison, C. *Coordination Chemistry Reviews* **2005**, *249*, 3025.

(151) Vijgenboom, E.; Busch, J. E.; Canters, G. W. *Microbiology* **1997**, *143*, 2853.

(152) Gaigalas, A. K. A.; Niaura, G. *Journal of Colloid and Interface Science* **1997**, *193*, 60.

(153) Chi, Q.; Zhang, J.; Andersen, J. E. T.; Ulstrup, J. *The Journal of Physical Chemistry B* **2001**, *105*, 4669.

(154) Yokoyama, K.; Leigha, B. S.; Shenga, Y.; Nikia, K.; Nakamura, N.; Ohno, H.; Winkler, J. R.; Gray, H. B.; Richards, J. H. *Inorganica Chimica Acta* **2008**, *361*, 1095.

(155) Jeuken, L. J. C.; Wisson, L.-J.; Armstrong, F. A. *Inorganica Chimica Acta* **2002**, *331*, 216.

(156) Shleev, S.; Wettero, J.; Magnusson, K.; Ruzgas, T. *Biosensors and Bioelectronics* **2006**, *22*, 213.

(157) Davis, J. J.; Morgan, D. A.; Wrathmell, C. L.; Axford, D. N.; Zhao, J.; Wang, N. *Journal of Materials Chemistry* **2005**, *15*, 2160.

(158) Canters, G. W.; van Pouderoyen, G. *Biosensors and Bioelectronics* **1994**, *9*, 637.

(159) Monari, S.; Battistuzzi, G.; Dennison, C.; Borsari, M.; Ranieri, A.; Siwek, M. J. J.; Sola, M. *The Journal of Physical Chemistry C* **2010**, 22322.

(160) Yi Xiao, F. P., 1 Eugenii Katz,1 James F. Hainfeld,2; Willner, I. *Science* **2003**, *299*, 1877.

(161) Fuentes, L.; Oyola, J.; Fernández, M.; Quiñones, E. *Biophysical Journal* **2004**, *87*, 1873.

(162) Leckner, J.; Bonander, N.; Wittung-Stafshede, P.; Malmström, B. G.; Karlsson, B. G. *Biochimica et Biophysica Acta* **1997**, *1342*, 19.

(163) Solomon, E. I.; Penfield, K. W.; Gewirth, A. A. *Inorganica Chimica Acta* **1996**, *243*, 67.

(164) Solomon, E. I.; Szilagyi, R. K.; George, S. D.; Basumallick, L. *Chemical Reviews* **2004**, *104*, 419.

(165) Canters, G. W.; Lommen, A.; Van De Kamp, M.; Hoitink, C. W. G. *Biology of Metals* **1990**, *3*, 67.

(166) Kuznetsova, S.; Zauner, G.; Aartsma, T. J.; Engelkamp, H.; Hatzakis, N.; Rowan, A. E.; Nolte, R. J. M.; Christianen, P. C. M.; Canters, G. W. *Proceedings of the National Academy of Sciences of the United States of America* **2008**, *105*, 3250.

(167) Zauner, G.; Strianese, M.; Bubacco, L.; Aartsma, T. J.; Tepper, A.; Canters, G. W. *Inorganica Chimica Acta* **2008**, *361*, 1116.

(168) Van Amsterdam, I. M.; Ubbink, M.; Einsle, O.; Messerschmidt, A.; Merli, A.; Cavazzini, D.; Rossi, G. L.; Canters, G. W. *Nature Structural Biology* **2002**, *9*, 48.

(169) Van Amsterdam, I. M. C.; Ubbink, M.; Jeuken, L. J. C.; Verbeet, M. P.; Einsle, O.; Messerschmidt, A.; Canters, G. W. *Chemistry - A European Journal* **2001**, *7*, 2398.

(170) Furederkitzmuller, E.; Hesse, J.; Ebner, A.; Gruber, H.; Schutz, G. *Chemical Physics Letters* **2005**, *404*, 13.

(171) Widengren, J.; Schwille, P. *The Journal of Physical Chemistry A* **2000**, *104*, 6416.

(172) Goldberg, M. *Biochemistry* **1976**, *15*, 4197.

(173) Pompa, P. P.; Biasco, A.; Cingolani, R.; Rinaldi, R.; Verbeet, M. P.; Canters, G. W. *Physical Reviews E* **2004**, *69*, 032901.

(174) Krzemiński, Ł.; Cronin, S.; Ndamba, L.; Canters, G. W.; Aartsma, T. J.; Evans, S. D.; Jeuken, L. J. C. *The Journal of Physical Chemistry B* **2011**, *115*, 12607.

(175) Van de Kamp, M.; Floris, R.; Hali, F. C.; Canters, G. W. *Journal of the American Chemical Society* **2002**, *112*, 907.

(176) Jeuken, L. J.; Ubbink, M.; Bitter, J. H.; van Vliet, P.; Meyer-Klaucke, W.; Canters, G. W. *Journal of Molecular Biology* **2000**, *299*, 737.

(177) Khoshtariya, D. E.; Dolidze, T. D.; Shushanyan, M.; Davis, K. L.; Waldeck, D. H.; van Eldik, R. *Proceedings of the National Academy of Sciences of the United States of America* **2010**, *107*, 2757.

(178) Jeuken, L. J. C.; McEvoy, J. P.; Armstrong, F. a. *The Journal of Physical Chemistry B* **2002**, *106*, 2304.

(179) Zudans, I.; Paddock, J. R.; Kuramitz, H.; Maghasi, A. T.; Wansapura, C. M.; Conklin, S. D.; Kaval, N.; Shtoyko, T.; Monk, D. J.; Bryan, S. A.; Hubler, T. L.; Richardson, J. N.; Seliskar, C. J.; Heineman, W. R. *Journal of Electroanalytical Chemistry* **2004**, *565*, 311.

(180) De Angelis, T. P.; Hurst, R. W.; Yacynych, A. M.; Mark, H. B.; Heineman, W. R.; Mattson, J. S. *Analytical Chemistry* **1977**, *49*, 1395.

(181) Mattson, J. S.; Smith, C. A. *Analytical Chemistry* **1975**, *47*, 1122.

(182) Haacke, G. *Annual Review of Materials Science* **1977**, *7*, 73.

(183) Willner, I.; Katz, E. *Angewandte Chemie International Edition* **2000**, *39*, 1180.

(184) Di Milla, P. A.; Folkers, J. P.; Biebuyck, H. A.; Haerter, R.; Lopez, G. P.; Whitesides, G. M. *Journal of the American Chemical Society* **1994**, *116*, 2225.

(185) Wanunu, M.; Vaskevich, A.; Rubinstein, I. *Journal of the American Chemical Society* **2004**, *126*, 5569.

(186) Prostak, A.; Mark, H. B.; Hansen, W. N. *The Journal of Physical Chemistry* **1968**, *72*, 2576.

(187) Kaiser, N. *Applied Optics* **2002**, *41*, 3053.

(188) McCreery, R. L. *Chemical Reviews* **2008**, *108*, 2646.

(189) Hegner, M.; Wagner, P.; Semenza, G. *Surface Science* **1993**, *291*, 39.

(190) Wagner, P.; Hegner, M.; Guentherodt, H.-J.; Semenza, G. *Langmuir* **1995**, *11*, 3867.

(191) Cavalleri, O.; Natale, C.; Stroppolo, M. E.; Relini, A.; Cosulich, E.; Thea, S.; Novi, M.; Gliozzi, A. *Physical Chemistry Chemical Physics* **2000**, *2*, 4630.

(192) Davis, J. J.; Hill, H. A. O. *Chemical Communications (Cambridge, England)* **2002**, 393.

(193) Nowicka, A. M.; Hasse, U.; Sievers, G.; Donten, M.; Stojek, Z.; Fletcher, S.; Scholz, F. *Angewandte Chemie International Edition* **2010**, *49*, 3006.

(194) Hoogvliet, J. C.; Dijksma, M.; Kamp, B.; van Bennekom, W. P. *Analytical Chemistry* **2000**, *72*, 2016.

(195) Aslan, K.; Geddes, C. D. *Chemical Society Reviews* **2009**, *38*, 2556.

(196) Enderlein, J. *Biophysical Journal* **2000**, *78*, 2151.

(197) Burghardt, T. P.; Charlesworth, J. E.; Halstead, M. F.; Tarara, J. E.; Ajtai, K. *Biophysical Journal* **2006**, *90*, 4662.

(198) Davis, J. J.; Bruce, D.; Canters, G. W.; Crozier, J.; Hill, H. A. O. *Chemical Communications (Cambridge, England)* **2003**, *44*, 576.

(199) Rowe, G. K.; Carter, M. T.; Richardson, J. N.; Murray, R. W. *Langmuir* **1995**, *11*, 1797.

(200) Feldberg, S. W.; Rubinstein, I. *Journal of Electroanalytical Chemistry and Interfacial Electrochemistry* **1988**, *240*, 1.

(201) Andolfi, L.; Bizzarri, a.; Cannistraro, S. *Thin Solid Films* **2006**, *515*, 212.

(202) Sokolová, L.; Williamson, H.; Sykora, J.; Hof, M.; Gray, H. B.; Brutschy, B.; Vlcek, A. *The Journal of Physical Chemistry B* **2011**, *115*, 4790.

(203) Patil, A. V.; Davis, J. J. *Journal of the American Chemical Society* **2010**, *132*, 16938.

(204) Vincent, K. A.; Parkin, A.; Armstrong, F. A. *Chemical Reviews* **2007**, *107*, 4366.

(205) Hille, B. *Ion channels of excitable membranes*; Sinauer, 2001.

(206) Laviron, E. *Journal of Electroanalytical Chemistry* **1979**, *101*, 19.

(207) Laviron, E. *Electroanalytical Chemistry and Interfacial Electrochemistry* **1972**, *8*.

(208) Canters, G. W.; Kolczak, U.; Armstrong, F.; Jeuken, L. J.; Camba, R.; Sola, M. *Faraday Discussions* **2000**, 205.

(209) Battistuzzi, G.; Bellei, M.; Borsari, M.; Canters, G. W.; de Waal, E.; Jeuken, L. J.; Ranieri, A.; Sola, M. *Biochemistry* **2003**, *42*, 9214.

(210) Jeuken, L. J. C.; van Vliet, P.; Verbeet, M. P.; Camba, R.; McEvoy, J. P.; Armstrong, F. A.; Canters, G. W. *Journal of the American Chemical Society* **2000**, *122*, 12186.

(211) Dennison, C. *Natural Product Reports* **2008**, *25*, 15.

(212) Li, C.; Sato, K.; Monari, S.; Salard, I.; Sola, M.; Banfield, M. J.; Dennison, C. *Inorganic Chemistry* **2010**, 482.

(213) Adman, E. T.; Canters, G. W.; Hill, H. A.; Kitchen, N. A. *FEBS Letters* **1982**, *143*, 287.

(214) Nar, H.; Messerschmidt, A.; Huber, R.; van de Kamp, M.; Canters, G. W.; Kamp, M. V. D. *Journal of Molecular Biology* **1991**, *221*, 765.

(215) Pascher, T.; Karlsson, B. G.; Nordling, M.; Malmstrom, B. G.; Vanngard, T. *European Journal of Biochemistry* **1993**, *212*, 289.

(216) Vogelsang, J.; Cordes, T.; Forthmann, C.; Steinhauer, C.; Tinnefeld, P. *Proceedings of the National Academy of Sciences of the United States of America* **2009**, *106*, 8107.

(217) Vogelsang, J.; Cordes, T.; Tinnefeld, P. *Photochemical & Photobiological Sciences* **2009**, *8*, 486.

(218) Armstrong, F. A. *Current Opinion in Chemical Biology* **2005**, *9*, 110.

(219) Fleming, B. D.; Barlow, N. L.; Zhang, J.; Bond, A. M.; Armstrong, F. A. *Analytical Chemistry* **2006**, *78*, 2948.

(220) Avila, A.; Gregory, B. W.; Niki, K.; Cotton, T. M. *The Journal of Physical Chemistry B* **2000**, *104*, 2759.

(221) Nar, H.; Huber, R.; Messerschmidt, A.; Filippou, A. C.; Barth, M.; Jaquinod, M.; Kamp, M.; Canters, G. W. *European Journal of Biochemistry* **1992**, *205*, 1123.

(222) De Jongh, T. E.; Van Roon, A.-M. M.; Prud√™ncio, M.; Ubbink, M.; Canters, G. W. *European Journal of Inorganic Chemistry* **2006**, *2006*, 3861.

(223) Bizzotto, D. *Journal of Electroanalytical Chemistry* **2000**, *480*, 233.

(224) Yoshida, H. *Journal of the Chemical Society, Faraday Transactions* **1883**, *43*, 472.

(225) Solomon, E. I.; Sundaram, J. U.; Machonkin, T. E. *Chemical Reviews* **1996** *96*, 2563.

(226) Solomon, E. I.; Chen, P.; Metz, M.; Lee, S.-K.; Palmer, A. E. *Angewandte Chemie International Edition* **2001**, *40*, 4570.

(227) Solomon, E. I.; Augustine, A. J.; Yoon, J. *Dalton transactions* **2008**, *9226*, 3921.

(228) Lee, S. K.; George, S. D.; Antholine, W. E.; Hedman, B.; Hodgson, K. O.; Solomon, E. I. *Journal of the American Chemical Society* **2002**, *124*, 6180.

(229) Xu, F.; Shin, W.; Brown, S. H.; Wahleithner, J. A.; Sundaram, U. M.; Solomon, E. I. *Biochimica et Biophysica Acta* **1996** *1292*, 303.

(230) Couto; Herrera, T. *Biotechnology Advances* **2006**, *24*, 500.

(231) Singh, A. D.; Kumar, S. R. *Applied Biochemistry and Biotechnology* **2009**.

(232) Hilden, K.; Hakala, T. K.; Lundell, T. *Biotechnology Letters* **2009**, *31*, 1117.

(233) Riva, S. *Trends in Biotechnology* **2006**, *24*, 219.

(234) Abadulla, E.; Tzanov, T.; Costa, S.; Robra, K. H.; Cavaco-Paulo, A.; Gubitz, G. M. *Applied and Environmental Microbiology* **2000**, *66*, 3357.

(235) Ghindilis, A. L.; Gavrilova, V. P.; Yaropolov, A. I. *Biosensors and biotechnology* **1992**, *7*, 127.

(236) Morozova, M.; Gorbacheva, A.; Shleev, S. V.; Yaropolov, A. I.; Shumakovich, G. P. *Biochemistry* **2007**, *72*, 1136.

(237) Gianfreda, L.; Xu, C.; Bollag, J. M. *Bioremediation Journal* **1999**, *january*.

(238) Strong, P. J.; Claus, H. *Critical Reviews in Environmental Science and Technology* **2011**, *41*, 373.

(239) Wong, D. W. S. *Applied Biochemistry And Biotechnology* **2008**, *157*, 174.

(240) Martinez-Ortiz, J.; Flores, R.; Vazquez-Duhalt, R. *Biosensors and Bioelectronics* **2011**, *26*, 2626.

(241) Pita, M.; Gutierrez-Sanchez, C.; Olea, D.; Velez, M.; Garcia-Diego, C.; Shleev, S.; Fernandez, V. M.; De Lacey, A. L. *The Journal of Physical Chemistry C* **2011**, 13420.

(242) Vaz-Dominguez, C.; Campuzano, S.; Rüdiger, O.; Pita, M.; Gorbacheva, M.; Shleev, S.; Fernandez, V. M.; De Lacey, A. L. *Biosensors and Bioelectronics* **2008**, *24*, 531.

(243) Deng, L.; Shang, L.; Wang, Y.; Wang, T.; Chen, H.; Dong, S. *Electrochemistry Communications* **2008**, *10*, 1012.

(244) Gallaway, J.; Wheeldon, I.; Atanassov, P.; Banta, S.; Barton, S. C. *Biosensors and Bioelectronics* **2008**, *23*, 1229.

(245) Barton, S. C.; Kim, H.-H.; Binyamin, G.; Zhang, Y.; Heller, A. *The Journal of Physical Chemistry B* **2001**, *105*, 11917.

(246) Blanford, C. F.; Heath, R. S.; Armstrong, F. A. *Chemical Communications* **2007**, 1710.

(247) Haghighi, B.; Rahmati-Panah, A.; Shleev, S.; Gorton, L. *Electroanalysis* **2007**, *19*, 907.

(248) Solná, R.; Skládal, P. *Electroanalysis* **2005**, *17*, 2137.

(249) Vianello, F.; Cambria, A.; Ragusa, S.; Teresa, M.; Zennaro, L.; Rigo, A.; Vianello Ragusa, C. Z.; Rigo, C.; Cambria, M. T. *Biosensors and Bioelectronics* **2004**, *Volume 20*, 315.

(250) Kulys, J.; Vidziunaite, R. *Biosensors and Bioelectronics* **2003**, *18*, 319.

(251) Quan, D.; Shin, W. *Materials Science and Engineering C* **2004**, *24*, 113.

(252) Quan, D.; Shin, W.; Kim, Y. *Journal of Electroanalytical Chemistry* **2004**, *561*, 181.

(253) Claus, H. *Micron* **2004**, *35*, 93.

(254) Shleev, S.; Tkac, J.; Ruzgas, T.; Yaropolov, A. I.; Whittaker, W.; Gorton, L. *Biosensors and Bioelectronics* **2005** *20* 2517.

(255) Battistuzzi, G.; Bellei, M.; Leonardi, A.; Pierattelli, R.; De Candia, A.; Vila, A. J.; Sola, M. *Journal of Biological Inorganic Chemistry* **2005**, *10*, 867.

(256) Thurston, C. F. *Microbiology* **1994**, *140*, 19.

(257) Reinhammar, B. M. *Biochimica et Biophysica Acta* **1972**, *275*, 245.

(258) Call, H. P.; Mücke, I. *Journal of Biotechnology* **1997**, *53*, 163.

(259) Koroljova-Skorobogat'ko, O. V.; Stepanova, E. V.; Gavrilova, V. P.; Morozova, O. V.; Lubimova, N. V.; Dzchafarova, A. N.; Jaropolov, A. I.; Makower, A. *Biotechnology and Applied Biochemistry* **1998**, *28 (Pt 1)*, 47.

(260) Xu, F. *Journal of Biological Chemistry* **1997**, *272*, 924.

(261) Xu, F.; Kulys, J. J.; Duke, K.; Li, K.; Krikstopaitis, K.; Deussen, H. J. W.; Abbate, E.; Galynte, V.; Schenider, P. *Applied and Environmental Microbiology* **2000**, *May 2000*, 2052.

(262) Bertrand, T.; Jolivalt, C.; Briozzo, P.; Caminade, E.; Joly, N.; Madzak, C.; Mougin, C. *Biochemistry* **2002**, *41*, 7325.

(263) Piontek, K.; Antorini, M.; Choinowski, T. *Journal of Biological Chemistry* **2002**, *277*, 37663.

(264) Antorini, M.; Herpoel-Gimbert, I.; Choinowski, T.; Sigoillot, J.-C.; Asther, M.; Winterhalter, K.; Piontek, K. *Biochimica et Biophysica Acta (BBA) - Protein Structure and Molecular Enzymology* **2002**, *1594*, 109.

(265) McGuirl, M. A.; Dooley, D. M. *Current Opinion in Chemical Biology* **1999**, *3*, 138.

(266) Page, C. C.; Moser, C. C.; Chen, X.; Dutton, P. L. *Nature* **1999**, *402*, 47.

(267) Moser, C. C.; Keske, J. M.; Warncke, K.; Farid, R. S.; Dutton, P. L. *Nature* **1992**, *355*, 796.

(268) Pita, M.; Shleev, S.; Ruzgas, T.; Fernandez, V.; Yaropolov, A. I.; Gorton, L. *Electrochemistry Communications* **2006**, *8*, 747.

(269) Gupta, G.; Rajendran, V.; Atanassov, P. *Electroanalysis* **2004**, *Volume 16*, 1182.

(270) Shleev, S.; Christenson, A.; Serezhenkov, V.; Burbaev, D.; Yaropolov, A.; Gorton, L.; Ruzgas, T. *Biochemical Journal* **2005**, *385*, 745.

(271) Shleev, S.; Reimann, C. T.; Serezhenkov, S.; Burbaev, D.; Yaropolov, A. I.; Gorton, L.; Ruzgas, T. *Biochimie* **2006**, *88*, 1275.

(272) Johnson, D. L.; Thompson, J. L.; Brinkmann, S. M.; Schuller, K. A.; Martin, L. L. *Biochemistry* **2003**, *42*, 10229.

(273) Su, X.; Wu, Y.-J.; Knoll, W. *Biosensors and Bioelectronics* **2005**, *21*, 719.

(274) Klis, M.; Maicka, E.; Michota, A.; Bukowska, J.; Sek, S.; Rogalski, J.; Bilewicz, R. *Electrochimica Acta* **2007**, *52*, 5591.

(275) Shleev, S. V.; Morozova, O. V.; Nikitina, O. V.; Gorshina, E. S.; Rusinova, T. V.; Serezhenkov, V. A.; Burbaev, D. S.; Gazaryan, I. G.; Yaropolov, A. I. *Biochimie* **2004**, *86*, 693.

(276) Shleev, S.; Pita, M.; Yaropolov, A. I.; Ruzgas, T.; Gorton, L. *Electroanalysis* **2006**, *18*, 1901.

(277) Wynn, R.; Sarkar, H.; Holwerda, R.; Knaff, D. *FEBS Letters* **1983**, *156*, 23.

(278) Bacci, M.; Baldecchi, M. G.; Fabeni, P.; Linari, R.; Pazzi, G. P. *Biophysical Chemistry* **1983**, *17*, 125.

(279) Hemmerich, P.; Veeger, C.; Wood, H. C. S. *Angewandte Chemie* **1965**, *77*, 699.

(280) Heelis, P. F. *Chemical Society Reviews* **1982**, *11*, 15.

(281) Draper, R. *Archives of Biochemistry and Biophysics* **1968**, *125*, 802.

(282) Vervoort, J.; Heering, D.; Peelen, S.; Van Berkel, W. *Methods in Enzymology* **1985**, *243*, 188.

(283) Heering, H. A.; Hagen, W. R. *Journal of Electroanalytical Chemistry* **1996**, *404*, 249.

(284) Drake, H. L.; Akagi, J. M. *The Journal of Bacteriology* **1977**, *132*, 139.

(285) Sancho, J. *Cellular and Molecular Life Sciences* **2006**, *63*, 855.

(286) Leenders, H. R. M.; Vervoort, J.; Hoek, A.; Visser, A. J. W. G. *European Biophysics Journal* **1990**, *18*.

(287) Ishikita, H. *Biochemistry* **2008**, *47*, 4394.

(288) Chang, C.-W.; He, T.-F.; Guo, L.; Stevens, J. A.; Li, T.; Wang, L.; Zhong, D. *Journal of the American Chemical Society* **2010**, *132*, 12741.

(289) Ai, Y.-j.; Tian, G.; Liao, R.-z.; Zhang, Q.; Fang, W.-h.; Luo, Y. *ChemPhysChem* **2011**, *12*, 2899.

(290) Fantuzzi, A.; Meharenna, Y. T.; Briscoe, P. B.; Guerlesquin, F.; Sadeghi, S. J.; Gilardi, G. *Biochimica et Biophysica Acta (BBA) - Bioenergetics* **2009**, *1787*, 234.

(291) Apiyo, D. *Biochimica et Biophysica Acta - Protein Structure and Molecular Enzymology* **2000**, *1479*, 214.

(292) Swenson, R. P.; Krey, G. D. *Biochemistry* **1994**, *33*, 8505.

(293) Van Dijk, C.; Van Leeuwen, J. W.; Veeger, C.; Schreurs, J. P. G. M.; Barendrecht, E. *Bioelectrochemistry and Bioenergetics* **1982**, *9*, 743.

(294) Armstrong, F. A.; Hill, H. A. O.; Oliver, B. N.; Walton, N. J. *Journal of the American Chemical Society* **1984**, *106*, 921.

(295) Bianco, P.; Haladjian, J.; Manjaoui, A.; Bruschi, M. *Electrochimica Acta* **1988**, *33*, 745.

(296) Steensma, E.; Heering, H. A.; Hagen, W. R.; Van Mierlo, C. P. *European Journal of Biochemistry* **1996**, *235*, 167.

(297) Bagby, S.; Barker, P. D.; Allen, H.; Hill, O.; Sanghera, G. S.; Dunbar, B.; Ashby, G. A.; Eady, R. R.; Thorneley, R. N. F. *Biochemical Journal* **1991**, *277*, 313.

(298) Dubourdieu, M.; Le Gall, J.; Favaudon, V. *Biochimica et Biophysica Acta - Bioenergetics* **1975**, *376*, 519.

(299) Watt, W.; Tulinsky, A.; Swenson, R. P.; Watenpaugh, K. D. *Journal of Molecular Biology* **1991**, *218*, 195.

(300) Kuznetsov, V. Y.; Blair, E.; Farmer, P. J.; Poulos, T. L.; Pifferitti, A.; Sevrioukova, I. F. *Journal of Biological Chemistry* **2005**, *280*, 16135.

(301) Bell, S. G.; Dale, A.; Rees, N. H.; Wong, L.-L. *Applied Microbiology and Biotechnology* **2010**, *86*, 163.

(302) Peterson, J. A.; Lorence, M. C.; Amarneh, B. *Journal of Biological Chemistry* **1990**, *265*, 6066.

(303) Hecht, H. J.; Kalisz, H. M.; Hendle, J.; Schmid, R. D.; Schomburg, D. *Journal of Molecular Biology* **1993**, *229*, 153.

(304) Peng, Y.; Xu, F.; Bell, S. G.; Wong, L.-L.; Rao, Z. *Acta Crystallographica F* **2007**, *63*, 422.

(305) Bentley, E. a.; Astier, Y.; Ji, W. M.; Bell, S. G.; Wong, L.-L.; Hill, H. A. O. *Inorganica Chimica Acta* **2003**, *356*, 343.

(306) Chi, Q.; Zhang, J.; Jensen, P. S.; Christensen, H. E. M.; Ulstrup, J. *Faraday Discussions* **2006**, *131*, 181.

(307) Persson, B. N. J.; Lang, N. D. *Physical Review B* **1982**, *26*, 5409.

(308) Heering, H. A.; Hirst, J.; Armstrong, F. A. *The Journal of Physical Chemistry B* **1998**, *102*, 6889.

(309) Saccucci, T. M.; Rusling, J. F. *The Journal of Physical Chemistry B* **2001**, *105*, 6142.

(310) Hirst, J.; Duff, J. L. C.; Jameson, G. N. L.; Kemper, M. a.; Burgess, B. K.; Armstrong, F. A.; Judy Hirst ,Ä† Guy N. L. Jameson, Ä. M. A. K. Ä. Ä. J. L. C. D.; Barbara K. Burgess, Ä.; Fraser, A. A. *Journal of the American Chemical Society* **1998**, *120*, 7085.

(311) Leger, C.; Elliott, S. J.; Hoke, K. R.; Jeuken, L. J. C.; Jones, A. K.; Armstrong, F. A. *Biochemistry* **2003**, *42*, 8653.

(312) Fourmond, V.; Hoke, K.; Heering, H. A.; Baffert, C.; Leroux, F.; Bertrand, P.; Léger, C. *Bioelectrochemistry* **2009**, *76*, 141.

(313) Lee, C.-Y.; Guo, S.-X.; Bond, A. M.; Oldham, K. B. *Journal of Electroanalytical Chemistry* **2008**, *615*, 1.

(314) Creager, S. E.; Wooster, T. T. *Analytical Chemistry* **1998**, *70*, 4257.

(315) Li, J.; Schuler, K.; Creager, S. E. *Journal of The Electrochemical Society* **2000**, *147*, 4584.

(316) Jonscher, A. K. *Nature* **1977**, *267*, 673.

(317) Jonscher, A. K. *Universal relaxation law*; Chelsea Dielectric Press: London, 1996.

(318) Qiang Feng, Z.; Imabayashi, S.; Kakiuchi, T.; Niki, K. *Journal of the Chemical Society, Faraday Transactions* **1997**, *93*, 1367.

(319) Yue, H.; Khoshtariya, D.; Waldeck, D. H.; Grochol, J.; Hildebrandt, P.; Murgida, D. H.; Hongjun, Y.; D. H. Waldeck*, J. G. P. H.; D. H. Murgida*, D. K. *The Journal of Physical Chemistry B* **2006**, *110*, 19906.

(320) Kranich, A.; Ly, H. K.; Hildebrandt, P.; Murgida, D. H. *Journal of the American Chemical Society* **2008**, *130*, 9844.

(321) Wei, J. J.; Liu, H.; Niki, K.; Margoliash, E.; Waldeck, D. H. *The Journal of Physical Chemistry B* **2004**, *108*, 16912.

(322) Yue, H.; Waldeck, D. *Current Opinion in Solid State and Materials Science* **2005**, *9*, 28.

(323) Tina D. Dolidze; Sandra Rondinini; Alberto Vertova; David H. Waldeck; Dimitri E. Khoshtariya *Biopolymers* **2008**, *87*, 68.

(324) Heering, H. A.; Mondal, M. S.; Armstrong, F. A. *Analytical Chemistry* **1998**, *71*, 174.

(325) Smalley, J. F.; Feldberg, S. W.; Chidsey, C. E. D.; Linford, M. R.; Newton, M. D.; Liu, Y.-P. *The Journal of Physical Chemistry* **1995**, *99*, 13141.

(326) Peters, B., Oxford 2008.

(327) Stan, R., University of Leiden, 2010.

(328) Gorren, A. C.; den Blaauwen, T.; Canters, G. W.; Hopper, D. J.; Duine, J. A. *FEBS Letters* **1996**, *381*, 140.

(329) Den Blaauwen, T.; Canters, G. W. *Journal of the American Chemical Society* **1993**, *115*, 1121.

(330) Jeuken, L. J. C., University of Leiden, 2001.

(331) Dudek, S. P.; Sikes, H. D.; Chidsey, C. E. *Journal of the American Chemical Society* **2001**, *123*, 8033.

(332) Durkut; M. Mas-Torrent; Hadley, P. *The Journal of Chemical Physics* **2006**, *124*.

(333) Sachs, S. B.; Dudek, S. P.; Hsung, R. P.; Sita, L. R.; Smalley, J. F.; Newton, M. D.; Feldberg, S. W.; Chidsey, C. E. D. *J. Am. Chem. Soc* **1997**, *119*, 10563.

(334) Sikes, H. D. *Science* **2001**, *291*, 1519.

(335) Creager, S.; Yu, C. J.; Bamdad, C.; O'Connor, S.; MacLean, T.; Lam, E.; Chong, Y.; Olsen, G. T.; Luo, J.; Gozin, M.; Kayyem, J. F. *Journal of the American Chemical Society* **1999**, *121*, 1059.

(336) Raether, H. *Surface plasmons on smooth and rough surfaces and on gratings*; Springer-V ed.; Springer: Berlin Heidelberg New York London Paris Tokio, 1988.

(337) Tordi, M. G.; Naro, F.; Giordano, R.; Silvestrini, M. C. *BioMetals* **1990**, *3*, 73.

(338) Finazzi-Agro, A.; Giovagnoli, C.; Avigliano, L.; Rotilio, G.; Mondovi, B. *European Journal of Biochemistry* **1973**, *34*; 20

Appendix 1: LC-MS Analysis of Labelled and Unlabelled Azurin

According to the gene analysis, *Pseudomonas* Az consists of 128 amino acids, with an average molecular mass of 13945 Da (14008.5 Da after addition of 63.5Da to account for the copper ion). Evaluation of the number of appended fluorophores was verified by LC-MS. Analysis of the adjacent m/z peaks was performed using the software for LC-MS, MassLynx MS v.4.1.

Unlabelled wt copper and zinc Az: the chromatogram of unmodified copper Az was characterized by the presence of two main peaks, eluted at 7.38 min and 6.24 min (labelled as A and B in Figure A1.3), corresponding to species with molecular weights of 13933Da (A) and 13991Da(B).

The two values are close to the expected MW and suggest that the copper was partially displaced from the binding site upon ionization of the proteins, as already observed by Fukuo et al.[1]

The LC-MS of the unlabelled zinc Az presented only the elution peak at 7.38 min (in Figure A1.4), corresponding to the MW of the peptide backbone only of 13934Da.

The complete loss of the zinc ion during the ionization process is likely to be a consequence of the lower affinity of the protein for zinc ions than for the copper, which in fact was partially retained. This is justified considering the different binding energies of the two ions, documented by Az unfolding studies via chemical and thermal treatments.[2,3]

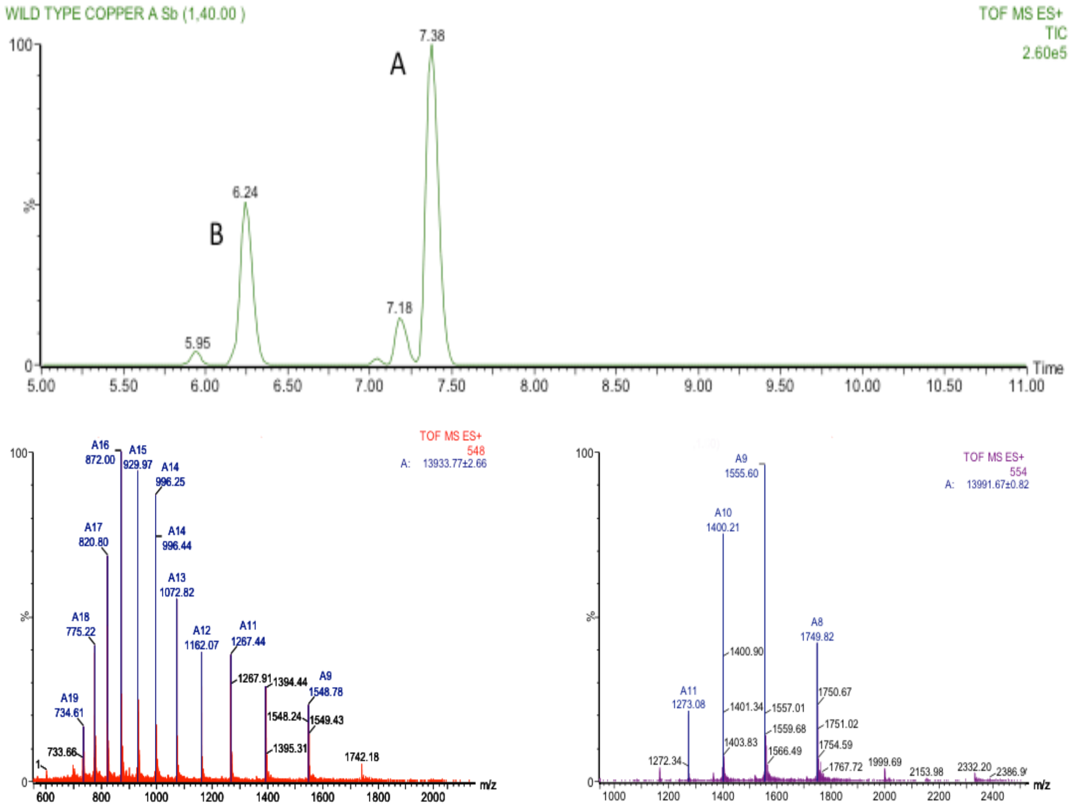

Figure A1.3: LC-MS of a sample of wt copper Az prior to modification with the dye. On top (green line) the elution profile of the HPLC chromatogram in a gradient 5% to 95% of ACN in water in 20 minutes. The two graphs A and B are the positive ionization m/z spectrum of the eluted proteins (labelled as in the upper plot), for which the molecular masses of 13933Da and 13991Da, respectively, were determined from analysis of the adjacent peaks with the software MassLynx MS v.4.1.

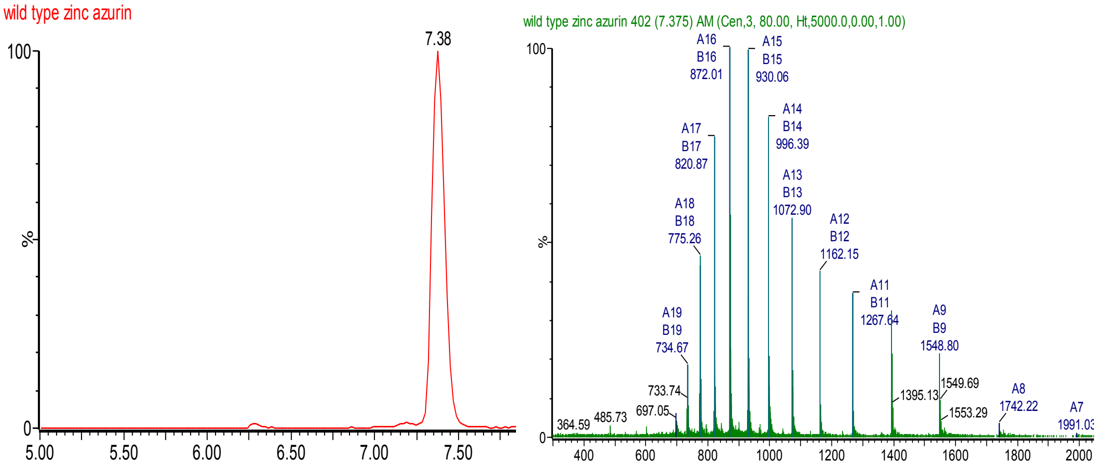

Figure A1.4: Wt zinc Az LC-MS: on top (red line) the elution profile in the same conditions as in the previous figure shows a peak at 7.38 minutes, correspondent to peak A in Figure A1.3. In the bottom part (green line), the positive ionization spectrum of the peak corresponding to a MW of 13934Da.

Labelled wt Az: As expected, after labelling the MW of both zinc and copper Az increased of 600-700 Da, equivalent to the MW of one dye molecule attached, as shown for a sample of zinc Az in Figure A1.5.

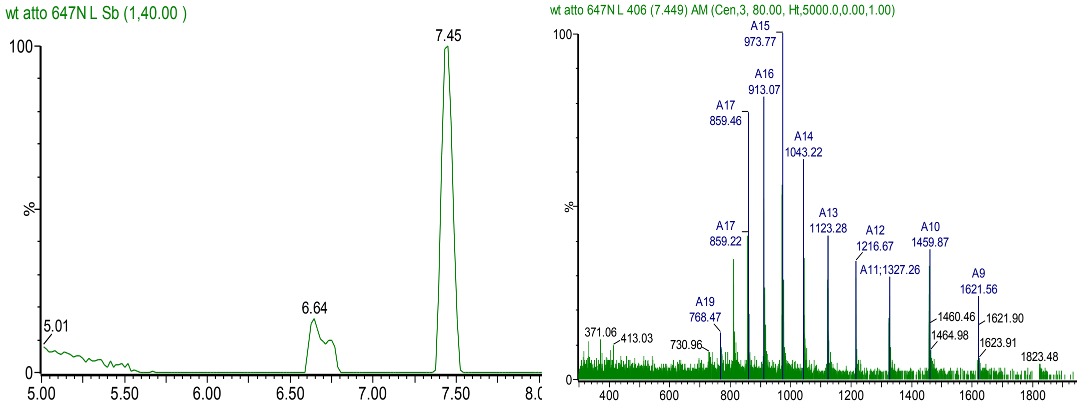

Figure A1.5: N terminal labelling of wt zinc Az with Atto647N. The smaller peak at min. 6.64 (data not shown) was due to residues of unlabelled proteins in the sample with MW~13930.

N42C Az unlabelled:

Having reactive thiols on the surface, in absence of reducing agents and non deareated solutions N42C forms dimers. These are observed by LC-MS. Prior to reduction and labelling, LC-MS of both copper and zinc N42C-Az showed the presence of homo-dimers of ~28 kDa (Figure A1.6). For the copper N42C, two peaks, due to partial leakage of the copper ion from the T1 site were observed, analogously to the wt-Az monomers, while for the zinc only the apo-protein dimers are observed (not shown).

N42C Az labelled:

After reduction of the disulphide bridge and reaction of the C42 with the maleimide functionalized Atto655 and Atto647N dyes, a MW of about (13930+ ~700) Da was noted (Figure A1.5 & Figure A1.7), indicative of the labelling occurring at the exposed SH group.

(1) Fukuo, T.; Kubota, N.; Kataoka, K.; Nakai, M.; Suzuki, S.; Arakawa, R. *Rapid Communications in Mass Spectrometry* **1998**, *12*, 1967.

(2) Wilson, C. J.; Wittung-Stafshede, P. *Biochemistry* **2005**, *44*, 10054.

(3) Leckner, J.; Bonander, N.; Wittung-Stafshede, P.; Malmström, B. G.; Karlsson, B. G. *Biochimica et Biophysica Acta* **1997**, *1342*, 19.

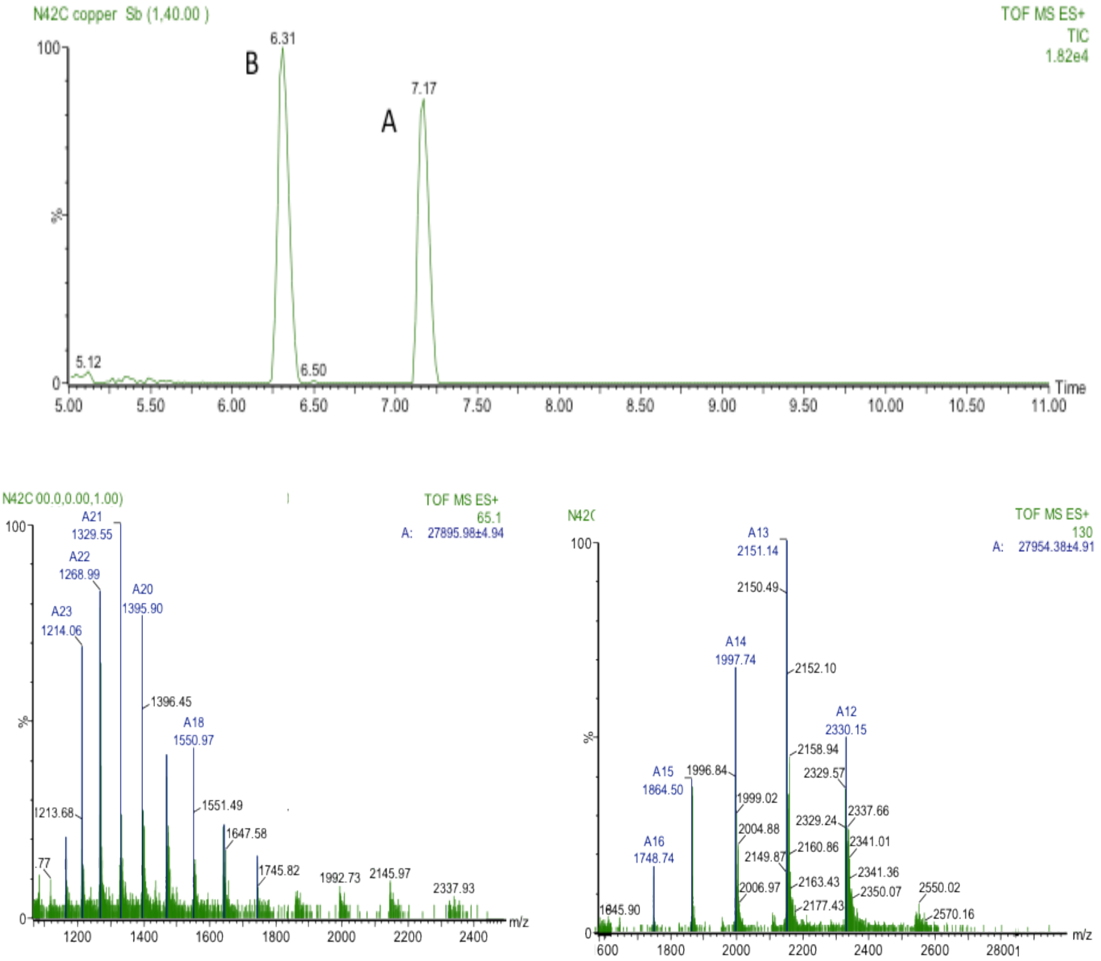

Figure A1.6: LC-MS of the unlabelled copper-reconstituted cysteine mutant of Az, N42C. Top plot: the elution profile shows two peaks at 7.17 (A) and 6.31(B).

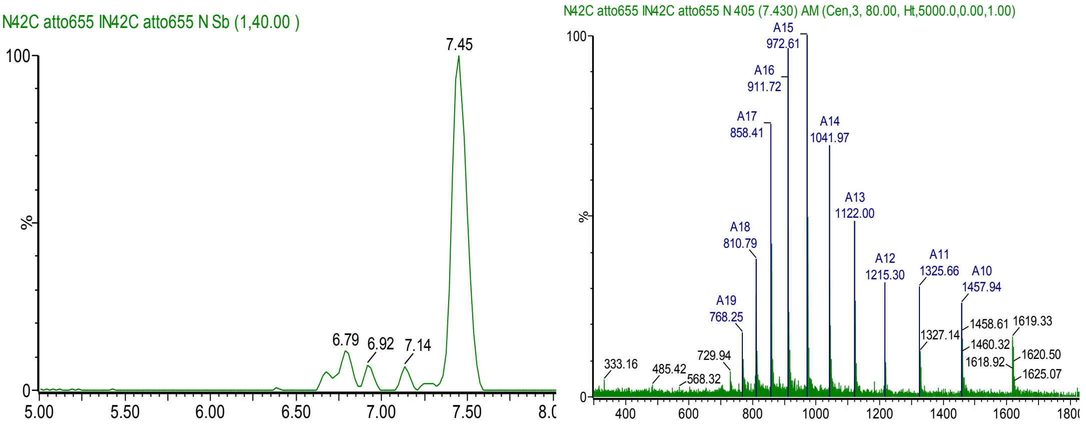

Figure A1.7: On top the chromatogram and ESI spectrum of zinc N42C-Az labelled with A655. The MW=14573Da was obtained by analysis of the adjacent peaks of the spectra, as are reported in B for the main peak eluted at 7.45 minutes in A. The minor peaks between min. 6.70 and 7.14 corresponded to the MW of unlabelled homo-dimer and unlabelled monomers.